Computational and Mathematical Methods in Medicine

Computational and Mathematical Methods in Cardiovascular Diseases

Guest Editors: Elena G. Tolkacheva, Xiaopeng Zhao, Sharon Zlochiver, and Yoichiro Mori

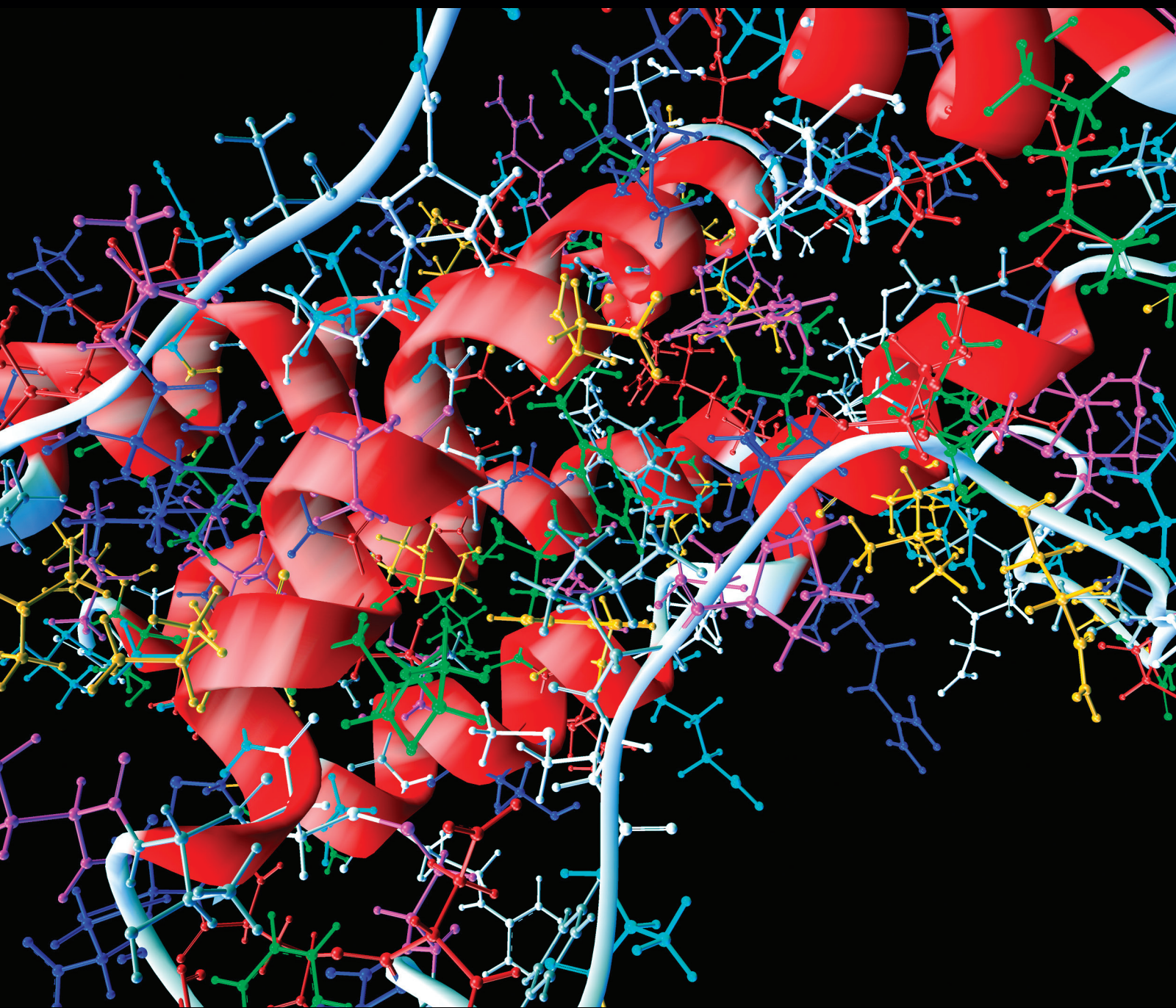

Computational and Mathematical Methods in Cardiovascular Diseases

Computational and Mathematical Methods in Cardiovascular Diseases

Guest Editors: Elena G. Tolkacheva, Xiaopeng Zhao, Sharon Zlochiver, and Yoichiro Mori

Editorial Board

Contents

Hindawi
Computational and Mathematical Methods in Medicine
Volume 2017, Article ID 4205735, 2 pages
http://dx.doi.org/10.1155/2017/4205735

Editorial

Computational and Mathematical Methods in Cardiovascular Diseases

Elena G. Tolkacheva,[1] Xiaopeng Zhao,[2] Sharon Zlochiver,[3] and Yoichiro Mori[4]

[1]*Department of Biomedical Engineering, University of Minnesota, Minneapolis, MN, USA*
[2]*Department of Mechanical, Aerospace, and Biomedical Engineering, University of Tennessee, Knoxville, TN, USA*
[3]*Department of Biomedical Engineering, Tel-Aviv University, Tel Aviv, Israel*
[4]*Department of Mathematics, University of Minnesota, Minneapolis, MN, USA*

Correspondence should be addressed to Elena G. Tolkacheva; talkacal@umn.edu

Received 31 January 2017; Accepted 31 January 2017; Published 19 March 2017

Cardiovascular diseases are a leading cause of death in the world. Computational and mathematical methods provide a useful tool to better understand heart and vessel problems. This special issue focuses on various computational and mathematical methods to model cardiac disorders, to understand the existing mathematical challenges, to explore new directions in modeling of cardiovascular dynamics and cardiac rhythm abnormalities, and to develop cardiac related mathematical applications in clinical and emergency situations.

Several key aspects become the main targets for discussion in the current special issue.

Several authors presented their research aiming to use computational approaches to elucidate the underlying electrophysiological mechanisms of different cardiac diseases leading to increased arrhythmogeneity in the heart. One area of research includes investigating the roles of hyperkalemia and calcium handling components played in the genesis of alternans in ischemia at the cellular level. The results show that hyperkalaemic conditions reduced cell excitability and delayed recovery from inactivation of depolarization currents, thus leading to alternans formation. In addition, sarcoplasmic reticulum calcium-ATPase (SERCA2a) function decreased in ischemia, thus resulting in intracellular Ca (Cai) alternans of small magnitude. Finally, a strong Na^+-Ca^{2+} exchange current (INCX) increased the magnitude of Cai alternans, leading to APD alternans through excitation-contraction coupling. Another research aimed to investigate the combined role of Ca2+/calmodulin-dependent protein kinase II (CaMKII) and β-adrenergic signaling pathway in regulating early afterdepolarization. Early afterdepolarization (EAD) has tremendous relevance for the onset of arrhythmogenesis. Simulations of this kind provide insights on therapy strategies to treat EADs related arrhythmogenesis. Finally, there is an interest to determine the potential antiarrhythmic effects of the green tea catechin Epigallocatechin-3-Gallate (E3G), by employing numerical simulations of cellular and cable models using atrial, Purkinje, and ventricular kinetics. The authors tested the effects of the drug on action potential properties and conduction velocity in the settings of two Na+ channel gain of function mutations that are correlated with hyperexcitability and ectopic premature contractions. They concluded that 30 μM E3G reduces and suppresses cellular electrical abnormalities that are associated with those mutations.

Another important aspect was the development and application of different methods and techniques to various cardiovascular recordings in order to differentiate between diseased and healthy states. Some studies propose to investigate the level of temporal dependency in cardiovascular time series using a copula method. The technique was applied to healthy aging rats as well as aging rats with early developed hypertension. The study shows that copulas and conditional entropy can reveal dependency of streams, to their number and to type. The authors highlighted that antiparallel streams play an important role between systolic blood pressure and

its pulse interval. Another approach is to use a 3D modeling for hemodynamic analysis of fluid structure interaction in intima and adventitia. Combining CT, IVUS, and biplane X-ray angiogram images, the authors calculated deformation of intima and adventitia by catheter insertion and generated vessel bifurcations. Limitations and future directions were also discussed. Finally, a hybrid classification system using the Rough Set and Relief (RSRF) method for diagnosis of heart diseases can be developed. Numerical experiments were conducted using the Statlog data. Results that reported on 10-fold cross validation demonstrate a high classification accuracy.

Several authors used computational approach to study various biomechanical properties and characteristics of the various diseased hearts. Some studies evaluate the pumping efficacy of a left ventricular assist device according to cannulation site in heart failure with valvular regurgitation. They aimed to analyze the contribution of a left ventricular assist device (LVAD) to mitral and aortic valve regurgitation for the following cannulation sites: from the LA to the aorta (LAAO) and from the LV to the aorta (LVAO) under different conditions. The results showed that LVAD with LAAO cannulation is appropriate for recovery of the mitral valve regurgitation heart, and the LVAD with LVAO cannulation is appropriate for treating the aortic valve regurgitation heart. Another approach is to investigate the relationship between endoleak formation and the surrounding pathological flow fields. Endoleak formation is a major complication for abdominal aortic aneurysm patients. Using computational fluid dynamics and image processing techniques, the authors reconstructed 6 patient specific models to study possible endoleak formation in a location with high local wall stress. The developed models may be adapted for other human cardiovascular surgeries, such as cardiopulmonary bypass, where detailed patient-specific hemodynamics is necessary.

Elena G. Tolkacheva
Xiaopeng Zhao
Sharon Zlochiver
Yoichiro Mori

Hindawi
Computational and Mathematical Methods in Medicine
Volume 2017, Article ID 9807617, 13 pages
http://dx.doi.org/10.1155/2017/9807617

Research Article

Reconstruction of Intima and Adventitia Models into a State Undeformed by a Catheter by Using CT, IVUS, and Biplane X-Ray Angiogram Images

Jinwon Son and Young Choi

School of Mechanical Engineering, Chung-Ang University, 221 Heukseok-dong, Dongjak-gu, Seoul 156-756, Republic of Korea

Correspondence should be addressed to Young Choi; yychoi@cau.ac.kr

Received 28 October 2016; Accepted 6 December 2016; Published 5 January 2017

Academic Editor: Xiaopeng Zhao

The number of studies on blood flow analysis using fluid-structure interaction (FSI) analysis is increasing. Though a 3D blood vessel model that includes intima and adventitia is required for FSI analysis, there are difficulties in generating it using only one type of medical imaging. In this paper, we propose a 3D modeling method for accurate FSI analysis. An intravascular ultrasound (IVUS) image is used with biplane X-ray angiogram images to calculate the position and orientation of the blood vessel. However, these images show that the blood vessel is deformed by the catheter inserted into the blood vessel for IVUS imaging. To eliminate such deformation, a CT image was added and the two models were registered. First, a 3D model of the undeformed intima was generated using a CT image. In the second stage, a model of intima and adventitia deformed by the catheter was generated by combining the IVUS image and the X-ray angiogram images. A 3D model of intima and adventitia with the deformation caused by insertion of the catheter eliminated was generated by matching these 3D blood vessel models in different states. In addition, a 3D blood vessel model including bifurcation was generated using the proposed method.

1. Introduction

Thanks to the advances in computing and analysis techniques, studies on circulatory diseases using CFD (computational fluid dynamics) analysis are now using FSI (fluid-structure interaction) analysis that can take into account the movement of blood vessel walls [1–4]. As opposed to CFD analysis that requires only a 3D model of intima, a 3D model containing information about the blood vessel thickness is required to analyze the blood flow inside the blood vessel and the forces applied to the blood vessel wall using FSI analysis [5–9]. However, there are difficulties in generating a 3D model of blood vessel that includes both the intima and adventitia using only a single type of medical image, owing to the characteristics of the imaging techniques. To achieve this, many studies have proposed 3D modeling methods of blood vessels that include intima and adventitia by combining different imaging techniques or by making assumptions. The representative imaging techniques used for such blood vessel modeling methods are CT (computed tomography) and IVUS (intravascular ultrasound).

Though the shape of a blood vessel intima can be easily obtained using a CT image, no information can be obtained about the blood vessel adventitia. In addition, owing to the low accuracy of CT images, the blood vessel intima model generated using a CT image will have an uneven surface. Antiga has proposed a method of calculating the centerline of the blood vessel model to resolve the problem of the blood vessel model generated using such a CT image [10, 11]. A 3D blood vessel model generated using a CT image was automatically corrected using the centerline of the 3D blood vessel model, and a 3D blood vessel model that includes the intima and adventitia was generated with the assumption that the thickness of a blood vessel wall is proportional to the inner diameter.

An IVUS image is an image that shows the cross section of a blood vessel by inserting a microminiaturized ultrasonic instrument into the blood vessel. As an IVUS image is

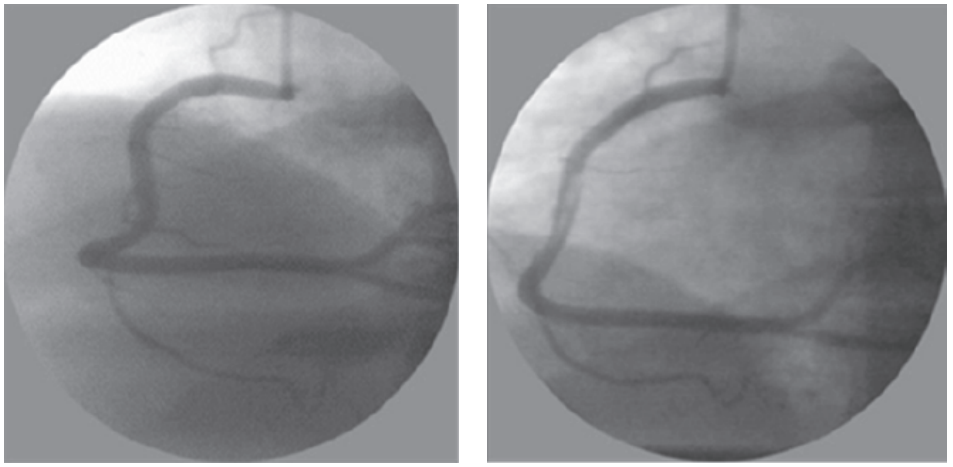

(a) (b)

Figure 1: (a) Shape of blood vessel before catheter insertion. (b) Shape of blood vessel after catheter insertion [19].

taken around a blood vessel, a lot more detailed information about the blood vessel can be obtained than that with a CT image. In addition, because an ultrasonic wave is used, it has the advantage that the information about the blood vessel adventitia can also be obtained. However, an IVUS image only shows the cross section of a blood vessel without showing the position and direction at which the IVUS image is taken. Whale has proposed a sequential triangulation method that calculates the position and orientation of an IVUS image using biplane X-ray angiogram images [12–17]. The 3D path along which IVUS images were taken was generated using biplane X-ray angiogram images, and the positions and orientations of these IVUS images were calculated using only the geometric shape of this path.

However, the catheter inserted to take the IVUS image heavily deforms the blood vessel, as shown in Figure 1. Accordingly, the IVUS image and the biplane X-ray angiogram images taken with the catheter inserted show the information about the blood vessel deformed by the catheter insertion. In addition, the blood vessel model generated by combining these images will also be in a deformed state.

The initial state of the blood vessel has a great effect on the analysis result of the blood vessel model. Accordingly, in this study, we propose a 3D modeling method of intima and adventitia with the deformation caused by insertion of a catheter eliminated for accurate FSI analysis.

2. Overview

Figure 2 shows the overall flow of the 3D blood vessel modeling method proposed in this study.

This method can be largely divided into three stages.

First, a 3D model of the undeformed intima is generated using a CT image. CT images only require a contrast medium to be administered and thus do not have any deformation caused by insertion of a catheter.

Then, a 3D intima and adventitia model in a state deformed by a catheter is generated by combining IVUS and biplane X-ray angiogram images. As explained earlier, IVUS images and biplane X-ray angiogram images show information about the blood vessel in a state deformed by insertion of a catheter.

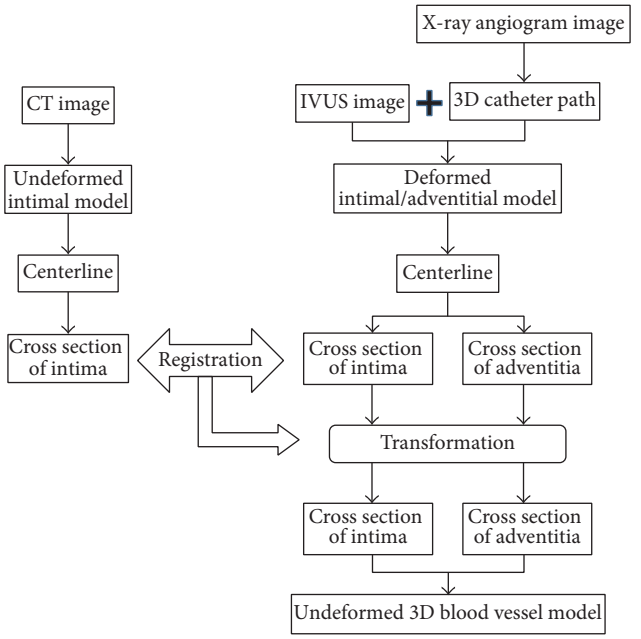

Figure 2: Overview of the proposed blood vessel modeling method.

The last stage involves converting the 3D model of the deformed intima and adventitia into a 3D model of the undeformed intima and adventitia through registration.

The last stage involves converting the 3D model of the deformed intima and adventitia into a 3D model of the undeformed intima and adventitia through registration. For this, the cross sections of the 3D models are extracted and registered. First, as the intimae exist in different states, the deformed intima is registered with the undeformed intima.

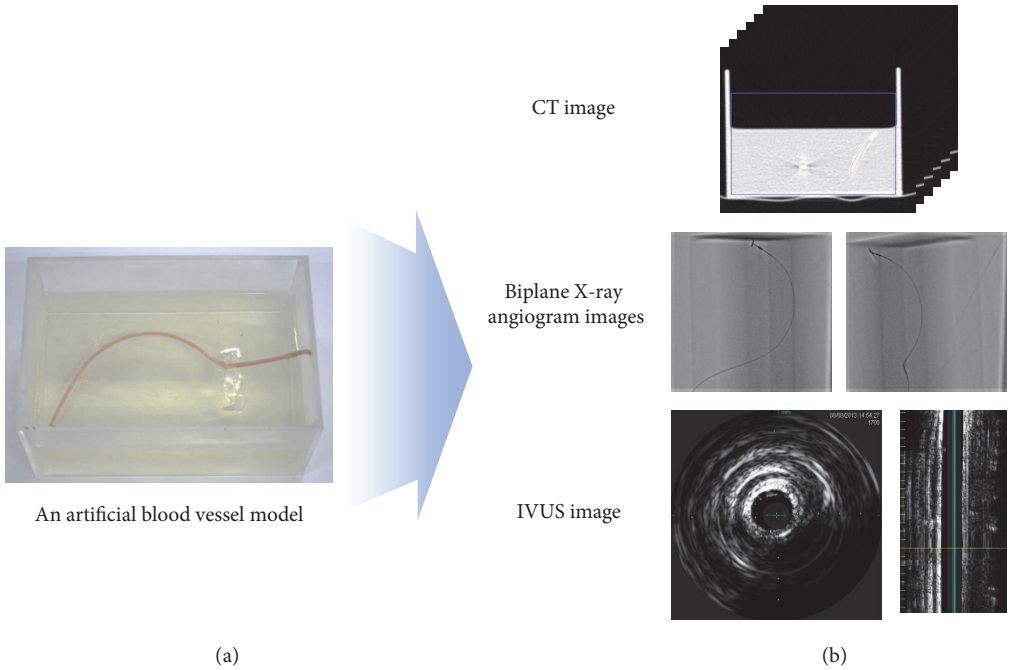

Figure 3: (a) Blood vessel replica. (b) CT, IVUS, and biplane X-ray angiogram images of the replica.

The cross sections of the undeformed intima and adventitia are calculated by applying the registration result to the cross section of the deformed adventitia.

A blood vessel replica was produced as shown in Figure 3(a) to facilitate acquisition of the medical images required for the method proposed in this paper. A silicone tube was used as the replica blood vessel and gelatin was used to fix it and to enable it to be deformed when a catheter was inserted. Figure 3(b) shows the CT, IVUS, and biplane X-ray images taken using the blood vessel replica.

3. Reconstruction of Undeformed Intima Model

A CT image can be obtained without inserting a catheter into the blood vessel by administering a contrast medium and thus shows the undeformed shape of the blood vessel. However, as it only shows the contrast medium passing through the blood vessel, no information about the adventitia of the blood vessel can be acquired. Accordingly, we intended to utilize the overall shape of the blood vessel without the catheter-induced deformation by using such characteristics of CT images. For this, a 3D intima model with no catheter-induced deformation was generated using the CT image of the blood vessel replica.

A CT image consists of voxel data produced by stacking tomograms of a human body. To generate a 3D blood vessel model, a process of extracting the polygon data corresponding to the blood vessel from the voxel data is required. To generate the polygon data of the blood vessel from the voxel data, the isosurfaces that have the same intensity value as that of the section corresponding to the blood vessel were extracted from each tomogram. A polygon model of the blood vessel was generated by stacking these isosurfaces and approximating the NURB surfaces. Figure 4 shows the 3D model of the undeformed intima generated using the CT image of the blood vessel replica.

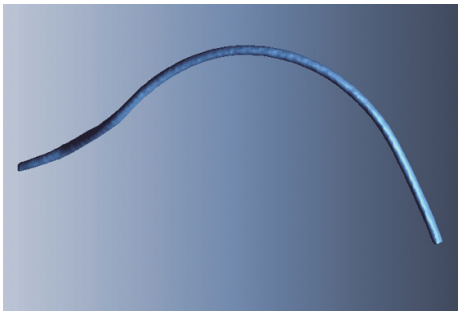

Figure 4: Generated 3D undeformed intima model of replica.

4. Reconstruction of Deformed Intima and Adventitia Model

4.1. Extraction of the Blood Vessel Intima and Adventitia Cross Sections in a Deformed State. An IVUS image shows the inside of a blood vessel in greater detail than a CT image as it is obtained by imaging the inside of the blood vessel with an ultrasonic device inserted into the blood vessel. Moreover, it provides information about the shape of the blood vessel adventitia. Figure 5 shows the cross sections of blood vessel intima and adventitia extracted from an IVUS image.

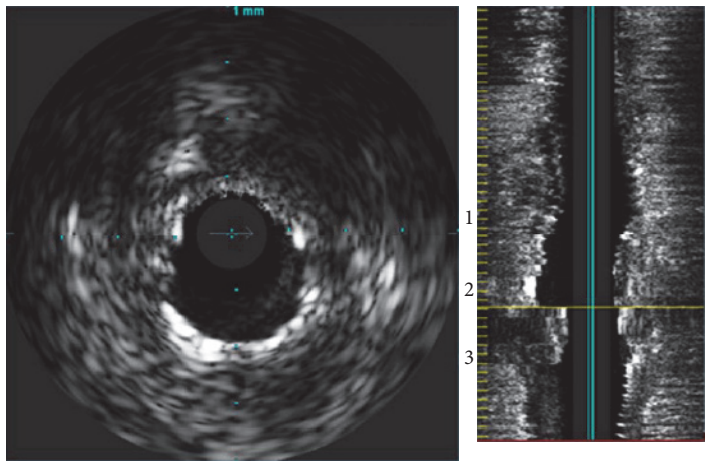

Figure 5: IVUS image of blood vessel.

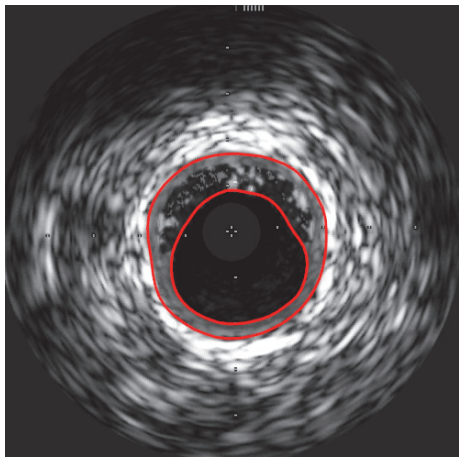

Figure 6: Segmented intima and adventitia contours from IVUS image.

As an IVUS image does not include color values but has points with gray scale values, there are difficulties in automatically extracting the areas corresponding to the intima and the adventitia of a blood vessel. Accordingly, in this study, we checked the IVUS image and manually segmented the sections corresponding to the intima and adventitia of the blood vessel, respectively, as shown in Figure 6.

4.2. Restoration of 3D Catheter Path. Though an IVUS image contains information about cross section of a blood vessel, the position and orientation at which the image was acquired are unknown. Accordingly, to generate a 3D blood vessel model using the cross sections of the blood vessel intima and adventitia extracted earlier from an IVUS image, the position and orientation where the IVUS image has been actually taken should be conjectured using other medical imaging techniques. For this, biplane X-ray angiogram images were used in this study.

When taking IVUS images, the path along which the IVUS images are to be taken is secured by inserting a catheter in advance to place an IVUS ultrasonic device at the place where the imaging is to be started. When the IVUS ultrasonic device arrives at the desired position, it follows the catheter and acquires images of the blood vessel cross sections, with the path of the IVUS images matching the path of the catheter. To obtain the catheter path, X-ray angiograms were taken from different directions immediately before the IVUS ultrasonic device was pulled back to take images. The 3D catheter path was generated as shown in Figure 7 using the two 2D catheter paths extracted from the biplane X-ray angiogram images.

4.3. Calculation of IVUS Image Position and Orientation. When IVUS images are acquired, the IVUS ultrasonic device moves out of the catheter at a constant speed using the IVUS pullback device. Accordingly, if the 3D catheter path restored using the biplane X-ray angiogram images is divided into as many parts as the number of the IVUS images using the same interval, the positions where the IVUS images have been acquired can be easily calculated. However, as the IVUS ultrasonic device rotates around the catheter when it travels around a bent blood vessel, the IVUS image acquired at this time is in a rotated state.

Whale has proposed the sequential triangulation method that can determine the twist angles of IVUS images using the characteristics of such IVUS images. With this method, the orientations of IVUS images were calculated using only the geometric shape of the catheter restored in 3D. A 3D catheter path was divided into small pieces assuming that it is comprised of innumerable joints and links. The positions and orientations of IVUS images were determined as shown in Figure 8 using the 3 consecutive points on the 3D path divided into smaller pieces. The orientation of each IVUS

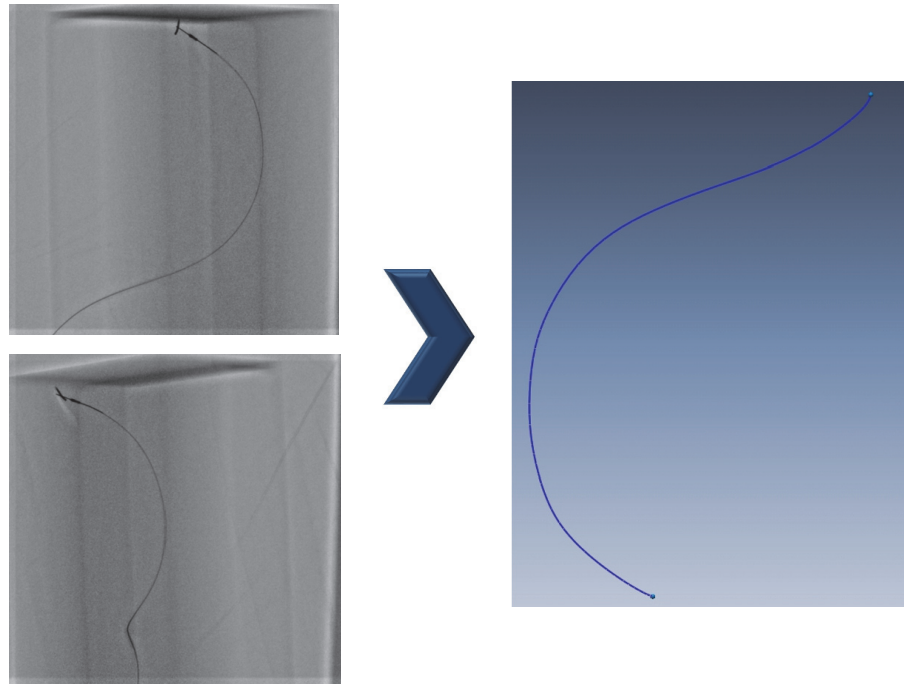

(a) (b)

Figure 7: (a) Biplane X-ray angiogram images of IVUS catheter. (b) Restored IVUS catheter path in 3D space.

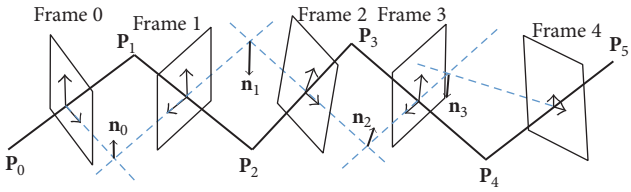

Figure 8: Sequential triangulation method [15].

image is determined by the plane made of the 3 consecutive points existing on the catheter. **P** is the position of each point, and **S**, which is the position of an IVUS image, is the center of the two points as shown in the following [12–17]:

$$\mathbf{S}_i = \frac{(\mathbf{P}_i + \mathbf{P}_{i+1})}{2}, \qquad \mathbf{S}_{i+1} = \frac{(\mathbf{P}_{i+1} + \mathbf{P}_{i+2})}{2}. \tag{1}$$

Also, the tangent vector $\vec{\mathbf{t}}$ at **P** is calculated as follows:

$$\vec{\mathbf{t}}_i = \mathbf{P}_{i+1} - \mathbf{P}_i, \qquad \vec{\mathbf{t}}_{i+1} = \mathbf{P}_{i+2} - \mathbf{P}_{i+1}. \tag{2}$$

The normal vector $\vec{\mathbf{n}}$, which is each of the y-axis directions of the 2D IVUS images, was calculated by calculating the outer products of the two neighboring tangent vectors $\vec{\mathbf{t}}$:

$$\vec{\mathbf{n}} = \vec{\mathbf{t}}_i \times \vec{\mathbf{t}}_{i+1}. \tag{3}$$

Through such a method, the position and orientation where an IVUS image was taken were determined from the 3D path of the catheter. Figure 9(a) shows the result of applying the position and orientation calculated using the sequential triangulation method to the cross sections of the blood vessel intima and adventitia extracted from a 2D IVUS image, and Figure 9(b) shows the polygon model generated using the points in 3D space. As these models were generated by combining the IVUS and biplane X-ray angiogram images taken in a state deformed by a catheter, they are the blood vessel intima and adventitia models deformed by insertion of a catheter.

5. Computation of Undeformed Intima and Adventitia Model by Registration

In this chapter, we intend to compute a 3D intima and adventitia model without the catheter-induced deformation. To achieve this, the 3D model of deformed intima and adventitia generated by combining the IVUS and biplane X-ray angiogram images was registered with the 3D model of the undeformed intima generated using a CT image. As these two 3D models do not only exist on different coordinate systems but also have different scales, there are difficulties in directly registering these 3D models. Accordingly, in this study, we

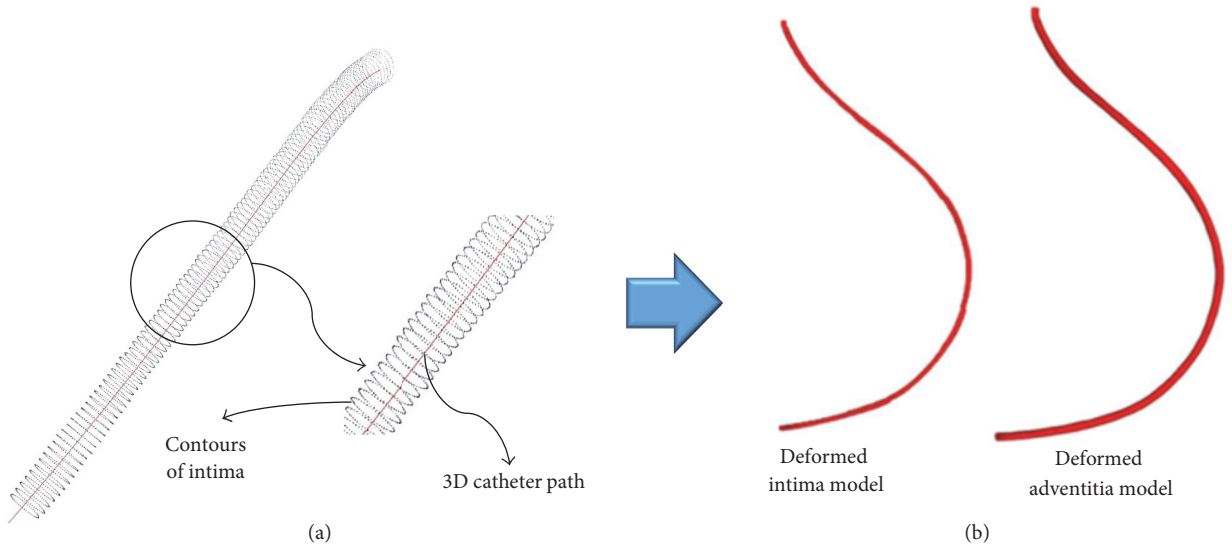

Figure 9: (a) A series of deformed intima cross sections. (b) A polygon model of deformed intima and adventitia model.

propose a method of determining the corresponding relation between the two 3D blood vessel models to extract the cross sections at the corresponding positions and matching them.

5.1. Calculation of Centerline and Extraction of Cross Section. To define a plane required for extraction of 2D cross sections from the 3D blood vessel intima model in a tube form, one 3D point and normal vector are required. For this, the centerline that could well express the shape of the blood vessel should be calculated.

In the study carried out by Luca, the centerline existing between two points within a model in a tube form was defined to be the line farthermost from the boundary. Accordingly, the centerline of an object $\mathbf{\Omega}$ existing in a 3D space can be expressed as the path $\mathbf{C} = \mathbf{C}(\mathbf{s})$ between two points $\mathbf{P}_1$ and $\mathbf{P}_2$ which minimizes

$$\mathbf{E}_{\text{centerline}}(\mathbf{C}) = \int_{\mathbf{0}=\mathbf{C}^{-1}(\mathbf{P}_0)}^{\mathbf{L}=\mathbf{C}^{-1}(\mathbf{P}_1)} \mathbf{F}(\mathbf{C}(\mathbf{s}))\, ds. \tag{4}$$

For this, the Delaunay triangulation of the object $\mathbf{\Omega}$ was calculated, through which the maximum spheres inscribed in the blood vessel model were calculated. The centerline of the 3D blood vessel model was extracted using the center points of these spheres.

5.2. Correspondence Definition between 3D Blood Vessel Models and Extraction of Cross Sections. To register two blood vessel models in different states, correspondence between the two models should be defined first. For this, the centerlines of the two intima models calculated earlier were used. Because the CT, IVUS, and biplane X-ray angiogram images were all obtained by imaging the same section of the blood vessel replica, the 3D blood vessel models generated earlier model the same section of the blood vessel though they are in different states. Accordingly, the corresponding relation between these two intima models was defined by dividing the center curves of these two intima models into the same number of lines using the same interval, and the cross sections of the 3D models were extracted at the defined positions.

5.3. Registering between Cross Sections in Different States. In this study, we intend to generate a 3D intima and adventitia model from which the catheter-induced deformation is removed through registration. Accordingly, we attempted to convert the cross sections of the deformed intima and adventitia extracted earlier into the cross sections of the undeformed intima and adventitia. For this, the cross sections of the deformed intima and adventitia were registered with the cross sections of the undeformed intima.

Registration is the calculation of the coordinate transformation that can minimize the distance between two point sets. Accordingly, registration in this study is to calculate the translation (x, y), rotation (θ), and scale (s) that minimizes the distance between the two point sets ($\mathbf{X}$: target point cloud, $\mathbf{Y}$: source point cloud), which compose the 2D blood vessel cross sections. In this study, the coordinate transformation matrix $\mathbf{T}_0$ that minimizes the distance between the two point sets $\mathbf{X}$ and $\mathbf{Y}$ was calculated using the optimization method after setting these 4 elements as the variables. In addition, to make a result linear to the rotation value of the previous frame when registering cross sections, the value closest to the rotation value θ of the previous frame was calculated.

$$\mathbf{T}_0 = \min\left(\sum \text{dist}\left(\mathbf{X}, \mathbf{Y}'\right)\right), \tag{5}$$

where

$$\mathbf{Y}' = \mathbf{T}(x, y, \theta, s)\,\mathbf{Y}. \tag{6}$$

To achieve this, the multiminimizer function of the GNU Scientific Library was used [18]. Figure 10 shows the registration result of the two intima cross sections.

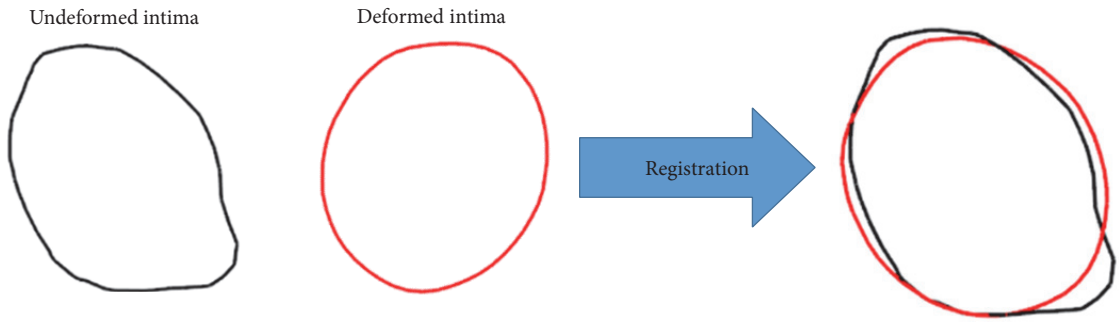

Figure 10: Registration between undeformed and deformed intima contours using the proposed method.

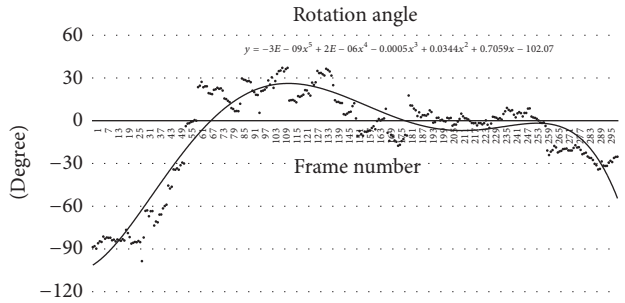

Figure 11: Trend line of rotation angle result.

The x, y, θ, and s calculated through the registration between intima cross sections are the values at which the deformed intima cross section changes to the undeformed intima cross section. Accordingly, the calculated x, y, θ, and s were equally applied to change the deformed adventitia cross section to the undeformed adventitia cross section. Figure 11 shows the rotation values of all the cross sections registered using the optimization method. To more linearly transform such rotation values, the trend line was calculated using all the rotation values, and the rotation value of each cross section was corrected to the trend line value.

5.4. Generation of an Undeformed Intima and Adventitia Model. The cross sections of the undeformed intima and adventitia were calculated through a process similar to that above. To finally generate a model in an undeformed state using such cross sections, the cross sections should be located at the proper positions and in proper orientation. For this, the centerline extracted from the 3D model of the intima not deformed by a catheter, which was generated from a CT image, was used. A 3D blood vessel polygon model, which included the intima and adventitia as shown in Figure 12, was generated by placing the calculated cross sections of the undeformed intima and adventitia on the undeformed centerline.

6. Bifurcated Blood Vessel Model

In fact, human blood vessels are not comprised of single blood vessels but a combination of blood vessels with many

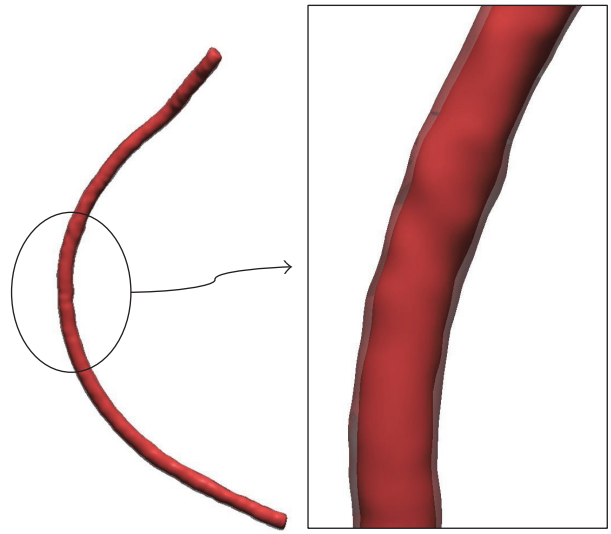

Figure 12: Generated 3D blood vessel model including intima and adventitia.

branches. Accordingly, to actually model the blood vessel of a patient, not a single blood vessel model but a 3D blood vessel model that includes branches should be generated. Accordingly, a 3D blood vessel model including branches not deformed by a catheter was generated using the proposed blood vessel modeling method in this chapter. For this, a blood vessel replica including branches was produced as shown in Figure 13. Different from the case of a single blood vessel, this replica was produced by creating a 3D model using the CT images of an actual patient and producing a mold using a 3D printer. A blood vessel replica of the desired form was produced by injecting silicon into this mold. For this replica, gelatin was again used to fix the blood vessel tube.

The CT, IVUS, and biplane X-ray angiogram images were taken using the produced blood vessel replica as per the case of a single blood vessel. As the replica includes branches, the IVUS images and the X-ray angiogram images of each blood vessel branch were taken. Figure 14 shows the medical images taken using the blood vessel replica.

6.1. Generation of a 3D Intima Model Including Branches Not Deformed by a Catheter and Extraction of Cross Sections. In

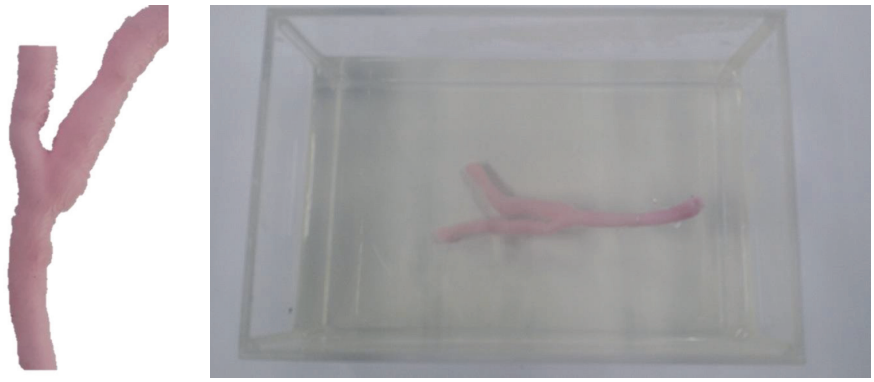

Figure 13: Replica of blood vessel.

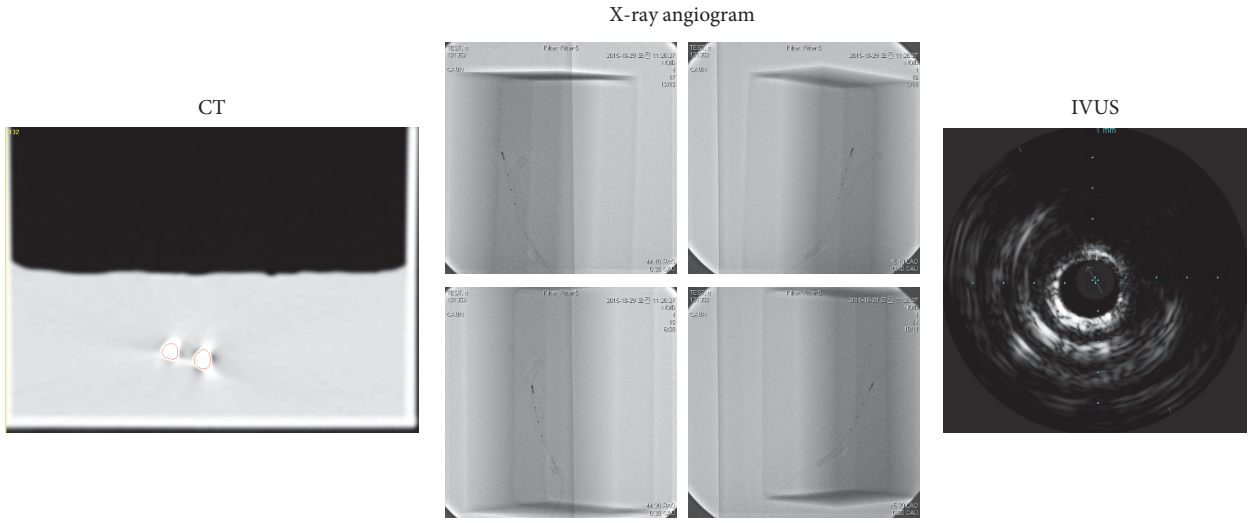

Figure 14: CT, biplane X-ray angiogram, and IVUS images of replica.

the case of the blood vessel that includes branches, a 3D model of the intima not deformed by a catheter was also generated using the CT image as per the single blood vessel. Figure 15 shows the 3D model of the intima not deformed by a catheter, which was generated using a CT image.

To extract the cross sections of the 3D intima models, the centerline of each branch was calculated using a 3D Voronoi diagram. Figure 16 shows the centerline of each branch and the cross sections extracted using them.

6.2. Generation of a 3D Model of the Intima and Adventitia Not Deformed by a Catheter That Includes Branches and Extraction of Cross Sections. To generate a blood vessel model that includes branches, the IVUS images of all the blood vessel branches should be taken to obtain data about the intima and adventitia of each blood vessel branch. In addition, to calculate the position and orientation of the IVUS image of each branch, when the IVUS image of each blood vessel branch is taken, the inserted catheter should be photographed from different directions. Accordingly, as the blood vessel replica used in this study had two blood vessel branches, 2

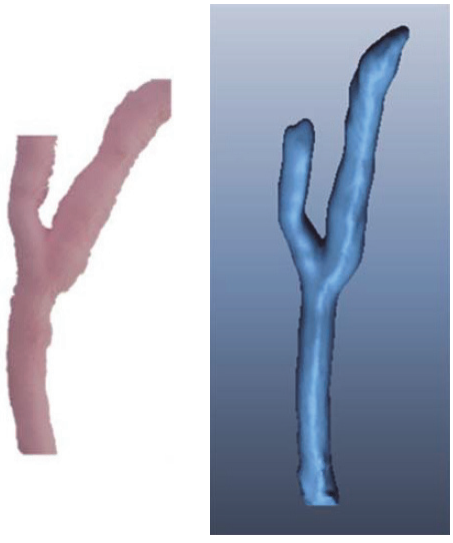

(a) (b)

Figure 15: (a) Bifurcated artificial blood vessel model. (b) Generated undeformed 3D intima model.

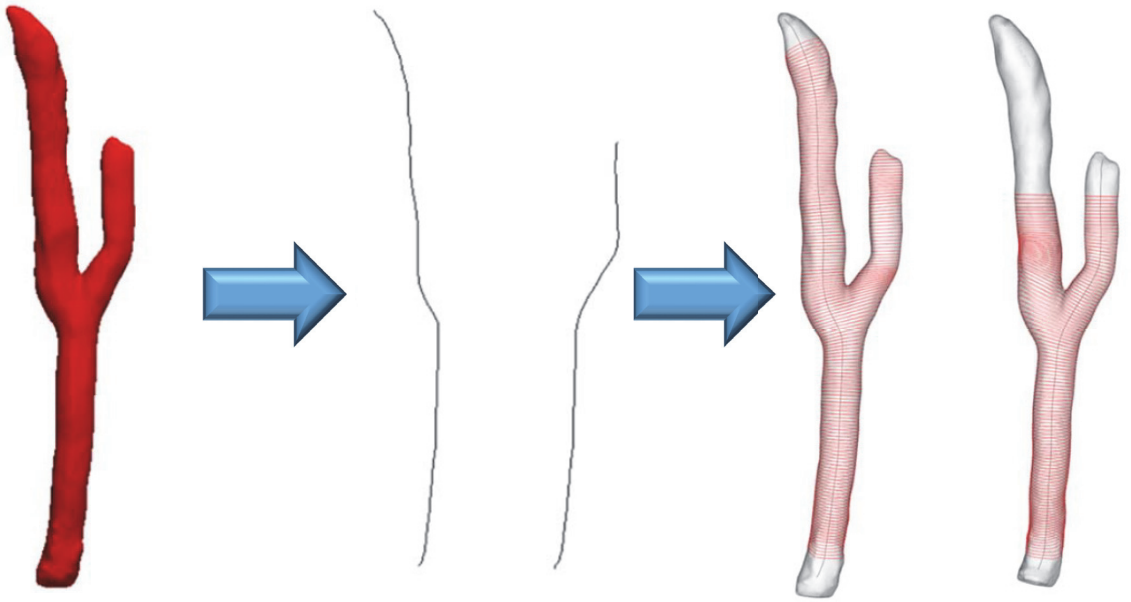

Figure 16: (a) Undeformed intima model. (b) Centerlines of each branch. (c) Extracted cross sections using each centerline.

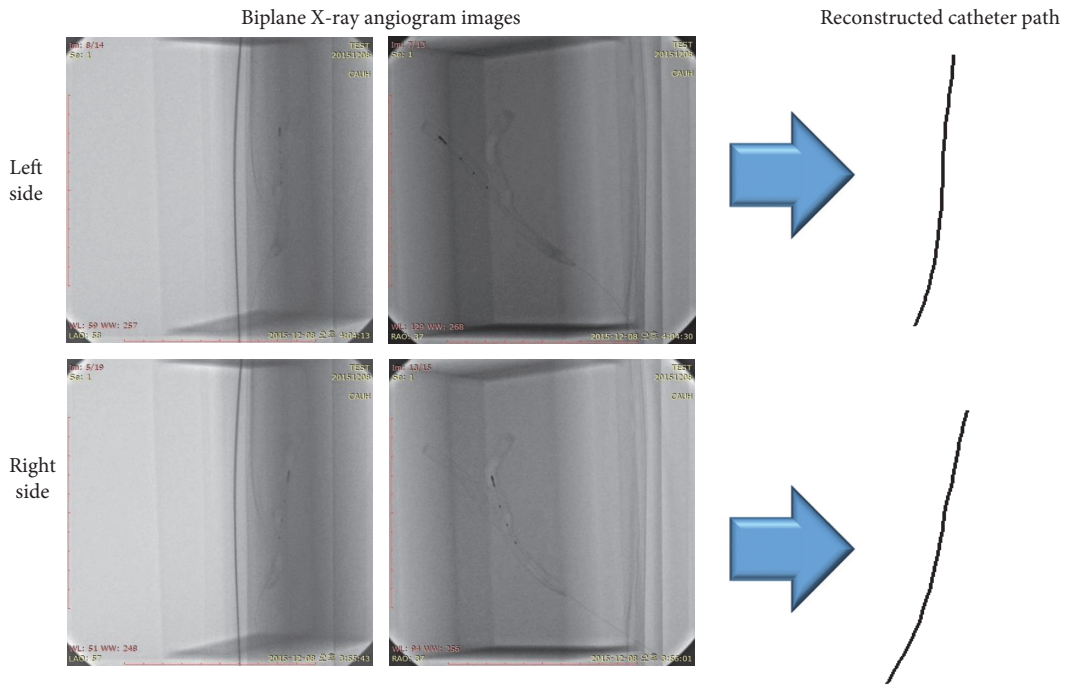

Figure 17: Reconstructed 3D catheter path of each branch.

sets of biplane X-ray angiogram images were acquired by photographing the catheter inserted into each blood vessel branch twice from different directions, which were used to generate two 3D paths of the catheter as shown in Figure 17.

In addition, to acquire the detailed shape of the blood vessel, the two sets of IVUS images obtained by imaging each blood vessel branch were used. In the case that branches are included, as in the case of the CT images, the IVUS images also show the sections where the blood vessel is bifurcated as shown in Figure 18. When the cross sections in the IVUS images were registered with the cross sections extracted from the CT images, the cross sections of the relevant intima and adventitia were all extracted from the IVUS images so that the branched sections can be accurately matched. Furthermore, even when the shapes of the blood vessel intima and adventitia on the other side are not perfectly obtained,

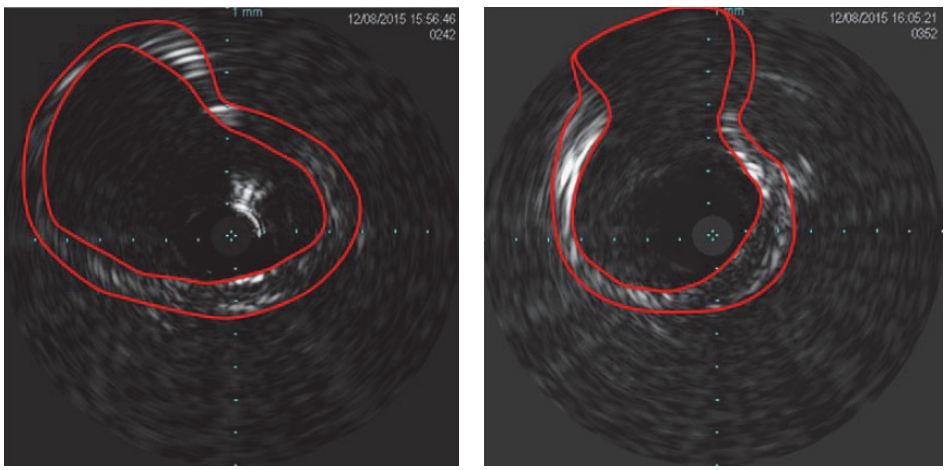

Figure 18: Segmented intima and adventitia contours from IVUS image at bifurcation.

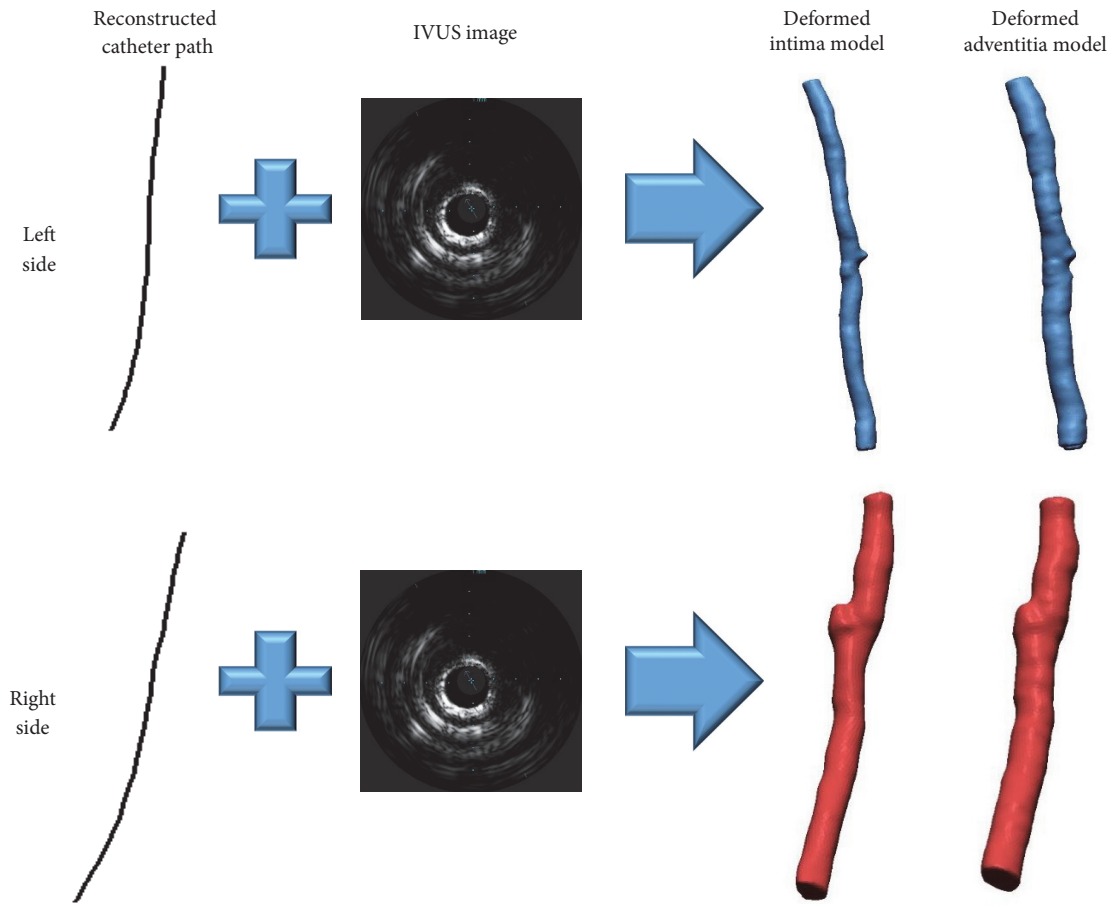

Figure 19: Reconstructed deformed 3D intima and adventitia models of each branch.

the shapes of the intima and adventitia were extracted by overlapping them as shown in Figure 18.

A 3D model of the intima and adventitia not deformed by the catheter inserted was generated as shown in Figure 19 by applying the result of the sequential triangulation method using each 3D catheter path to each cross section of the intima and adventitia extracted from the IVUS images.

6.3. Computation of a 3D Model of the Intima and Adventitia Including Branches with the Deformation Caused by the

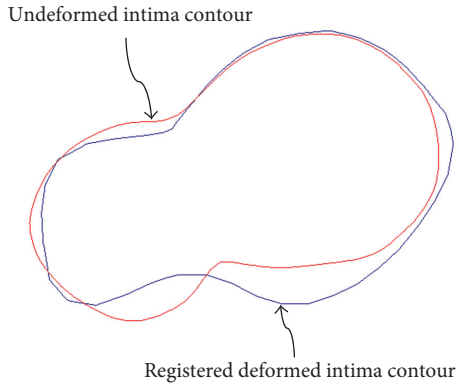

Figure 20: Comparison undeformed intima contour with registered deformed intima contour.

Catheter Eliminated through Registration. In the case of a blood vessel that includes bifurcation, a 3D model of intima and adventitia deformed by a catheter is generated in the form of a single blood vessel for each branch, and the cross sections are also found to be similar to the case of a single blood vessel. Accordingly, to carry out registration using these cross sections, the intima cross sections extracted from each branch in the undeformed intima model, which had been generated through the CT images earlier, were used directly. The cross sections of the undeformed intima and adventitia were calculated by registering the cross sections of the deformed intima and adventitia with the cross sections of the undeformed intima that included these branch points. Figure 20 shows the result of registration between the cross sections of the undeformed and deformed intima at a branch point. It can be seen that even when branch points are included, cross sections can be properly matched using the proposed registration method in this study.

The rotation values of the registered cross sections were corrected to enable the rotation variations of the cross sections to be linear using the trend line equations of the rotation values of the cross sections when all the cross sections of the right and left blood vessel branches are registered. After transforming the cross sections of the intima and adventitia in a deformed state into the cross sections of the intima and adventitia in an undeformed state through such a registration process, all the cross sections were placed on the centerline extracted from the 3D model in an undeformed state as shown in Figure 21(a). A model of the intima and the adventitia that included a branch point was generated as shown in Figure 21(b), using all the points corresponding to the left and right blood vessel branches, which were used to generate a 3D blood vessel model that included intima and adventitia.

7. Conclusion and Discussion

In this paper, we have proposed a method for generating a 3D model of intima and adventitia for accurate FSI analysis that eliminates the deformation caused by insertion of a catheter. The method of combining IVUS images and biplane X-ray angiogram images is widely used for generation of 3D blood vessel models and generates a 3D model of the intima and adventitia that is deformed by the inserted catheter. To eliminate such deformation, a 3D model of the intima without catheter-induced deformation was additionally generated from CT images, and these two models were registered to eliminate the catheter-induced deformation.

In the registration, the 3D models were not directly registered but the cross sections of each model were registered. The cross sections of the deformed intima were registered with the cross sections of the undeformed intima, and the cross sections of the undeformed adventitia were converted by applying the registration result to the cross sections of the deformed adventitia. A 3D blood vessel model that included the undeformed intima and adventitia was finally generated by placing the cross sections of the undeformed intima and adventitia calculated through such a process on the centerline extracted from the undeformed intima model.

The method of modeling a 3D blood vessel proposed in this study has various limitations. To determine the position and direction of the intima and adventitia cross sections extracted from IVUS images, these cross sections were registered with the cross sections of the intima extracted from CT images. The values of movement (x, y), rotation (θ), and scale (s) calculated through the registration between the two intima cross sections were equally applied to the cross sections of the adventitia extracted from IVUS images. However, such a method calculates an ideal result without considering the material properties of the blood vessel. In the case of an actual blood vessel, the intima and the adventitia will not equally deform because of the material properties of the blood vessel wall. In addition, for a patient with atherosclerosis, the blood vessel wall will not be isotropic owing to the plague existing on the blood vessel wall. Accordingly, the intima and adventitia model calculated using the method proposed in this study contains such errors.

Another limitation is that it is difficult to accurately evaluate the accuracy of the blood vessel model generated through the proposed method. This is because the only medical image through which the information about blood vessel adventitia can be obtained is IVUS image.

If OCT (Optical Coherence Tomography) that can photograph lumen more clearly than IVUS is used to further this study, more accurate information about blood vessel intima can be obtained. However, as OCT uses light, there are difficulties in obtaining accurate information about adventitia unlike IVUS that uses ultrasound. Accordingly, more precise 3D blood vessel models are expected to be generated by using OCT to obtain intima data and IVUS to obtain adventitia data.

Competing Interests

The authors declare that there is no conflict of interests regarding the publication of this paper.

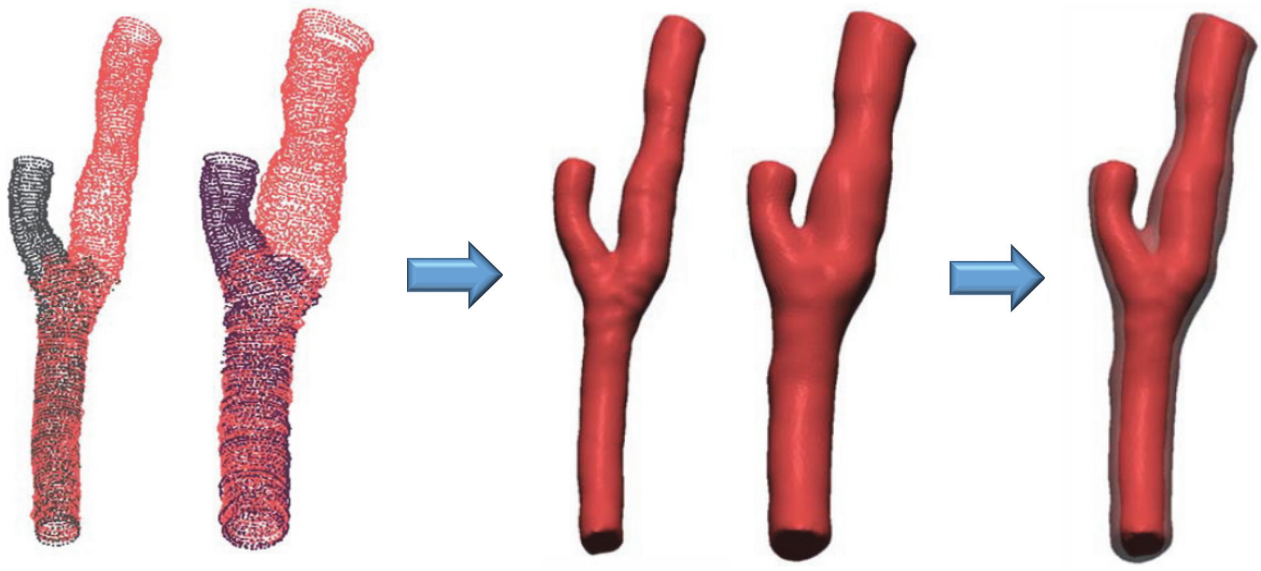

(a) (b) (c)

Figure 21: (a) Intima and adventitia point sets placed on undeformed centerline. (b) Computed undeformed intima and adventitia model. (c) Three-dimensional blood vessel model including intima and adventitia.

Acknowledgments

This research was supported by Basic Science Research Program through the National Research Foundation of Korea (NRF) funded by the Ministry of Science, ICT and Future Planning (NRF-2012R1A2A2A01047366 and NRF-2015R1D1A1A01060486).

References

[1] K. Dumont, J. Vierendeels, R. Kaminsky, G. Van Nooten, P. Verdonck, and D. Bluestein, "Comparison of the hemodynamic and thrombogenic performance of two bileaflet mechanical heart valves using a CFD/FSI model," *Journal of Biomechanical Engineering*, vol. 129, no. 4, pp. 558–565, 2007.

[2] P. Reymond, P. Crosetto, S. Deparis, A. Quarteroni, and N. Stergiopulos, "Physiological simulation of blood flow in the aorta: comparison of hemodynamic indices as predicted by 3-D FSI, 3-D rigid wall and 1-D models," *Medical Engineering and Physics*, vol. 35, no. 6, pp. 784–791, 2013.

[3] X. Huang, C. Yang, J. Zheng et al., "Higher critical plaque wall stress in patients who died of coronary artery disease compared with those who died of other causes: a 3D FSI study based on ex vivo MRI of coronary plaques," *Journal of Biomechanics*, vol. 47, no. 2, pp. 432–437, 2014.

[4] H. A. Pakravan, M. S. Saidi, and B. Firoozabadi, "FSI simulation of a healthy coronary bifurcation for studying the mechanical stimuli of endothelial cells under different physiological conditions," *Journal of Mechanics in Medicine and Biology*, vol. 15, no. 5, Article ID 1550089, 28 pages, 2015.

[5] A. Valenciaa, F. Muñoza, S. Arayaa, R. Riverab, and E. Bravob, "Comparison between computational fluid dynamics, fluid–structure interaction and computational structural dynamics predictions of flow-induced wall mechanics in an anatomically realistic cerebral aneurysm model," *International Journal of Computational Fluid Dynamics*, vol. 23, no. 9, pp. 649–666, 2009.

[6] J. Knight, S. Baumüller, V. Kurtcuoglu et al., "Long-term follow-up, computed tomography, and computational fluid dynamics of the Cabrol procedure," *Journal of Thoracic and Cardiovascular Surgery*, vol. 139, no. 6, pp. 1602–1608, 2010.

[7] Y. Qian, J. L. Liu, K. Itatani, K. Miyaji, and M. Umezu, "Computational hemodynamic analysis in congenital heart disease: simulation of the Norwood procedure," *Annals of Biomedical Engineering*, vol. 38, no. 7, pp. 2302–2313, 2010.

[8] K. M. Tse, P. Chiu, H. P. Lee, and P. Ho, "Investigation of hemodynamics in the development of dissecting aneurysm within patient-specific dissecting aneurismal aortas using computational fluid dynamics (CFD) simulations," *Journal of Biomechanics*, vol. 44, no. 5, pp. 827–836, 2011.

[9] W. Lee, H. S. Ryou, S. Kim, J. W. Nam, W. S. Lee, and S. W. Cho, "Study of hemodynamic parameters to predict coronary artery disease using assumed healthy arterial models," *Journal of Mechanical Science and Technology*, vol. 29, no. 3, pp. 1319–1325, 2015.

[10] L. Antiga, *Patient-Specific Modeling of Geometry and Blood Flow in Large Arteries*, Politecnico di Milano, Milan, Italy, 2002.

[11] L. Antiga, B. Ene-Iordache, and A. Remuzzi, "Computational geometry for patient-specific reconstruction and meshing of blood vessels from MR and CT angiography," *IEEE Transactions on Medical Imaging*, vol. 22, no. 5, pp. 674–684, 2003.

[12] A. Wahle, H. Oswald, and E. Fleck, "New 3-D attributed data model for archiving and interchanging of coronary vessel systems," in *Computers in Cardiology*, 1993.

[13] A. Wahle, E. Wellnhofer, I. Mugaragu, H. U. Sauer, H. Oswald, and E. Fleck, "Quantitative volume analysis of coronary vessel systems by 3-D reconstruction from biplane angiograms," in

Proceedings of the IEEE Nuclear Science Symposium & Medical Imaging Conference, pp. 1217–1221, November 1994.

[14] A. Wahle, E. Wellnhofer, I. Mugaragu, H. U. Sauer, H. Oswald, and E. Fleck, "Assessment of diffuse coronary artery disease by quantitative analysis of coronary morphology based upon 3-d reconstruction from biplane angiograms," *IEEE Transactions on Medical Imaging*, vol. 14, no. 2, pp. 230–241, 1995.

[15] A. Wahle, G. P. M. Prause, S. C. DeJong, and M. Sonka, "3-D fusion of biplane angiography and intravascular ultrasound for accurate visualization and volumetry," in *Medical Image Computing and Computer-Assisted Intervention—MICCAI '98: First International Conference Cambridge, MA, USA, October 11–13, 1998 Proceedings*, vol. 1496 of *Lecture Notes in Computer Science*, pp. 146–155, Springer, Berlin, Germany, 1998.

[16] A. Wähle, "Geometrically correct 3-D reconstruction of intravascular ultrasound images by fusion with biplane angiography-methods and validation," *IEEE Transactions on Medical Imaging*, vol. 18, no. 8, pp. 686–699, 1999.

[17] A. Wahle, S. C. Mitchell, M. E. Olszewski, R. M. Long, and M. Sonka, "Accurate visualization and quantification of coronary vasculature by 3-D/4-D fusion from biplane angiography and intravascular ultrasound," in *Proceedings of the Biomonitoring and Endoscopy Technologies*, Proceedings of SPIE, pp. 144–155, Amsterdam, Netherlands, July 2001.

[18] B. Gough, *GNU Scientific Library Reference Manual*, Network Theory Ltd, Godalming, UK, 2009.

[19] P. Schoenhagen, S. E. Nissen, and E. Murat, *IVUS Made Easy*, Informa Health Care, 2005.

Hindawi
Computational and Mathematical Methods in Medicine
Volume 2017, Article ID 2082351, 17 pages
http://dx.doi.org/10.1155/2017/2082351

Research Article

Dependency Structures in Differentially Coded Cardiovascular Time Series

Tatjana Tasic,[1] Sladjana Jovanovic,[2] Omer Mohamoud,[3] Tamara Skoric,[3] Nina Japundzic-Zigon,[1] and Dragana Bajic[3]

[1]*School of Medicine, Laboratory for Cardiovascular Pharmacology, University of Belgrade, Dr. Subotica 1, 11000 Belgrade, Serbia*
[2]*Telecom Serbia, Network and Services Planning and Development Function, Bulevar Umetnosti 16a, 11070 Novi Beograd, Serbia*
[3]*Faculty of Technical Sciences, Center of Excellence CEVAS, University of Novi Sad, Trg Dositeja Obradovica 6, 21000 Novi Sad, Serbia*

Correspondence should be addressed to Dragana Bajic; dragana.bajic@gmail.com

Received 26 August 2016; Revised 11 November 2016; Accepted 22 November 2016; Published 3 January 2017

Academic Editor: Xiaopeng Zhao

Objectives. This paper analyses temporal dependency in the time series recorded from aging rats, the healthy ones and those with early developed hypertension. The aim is to explore effects of age and hypertension on mutual sample relationship along the time axis. *Methods*. A copula method is applied to raw and to differentially coded signals. The latter ones were additionally binary encoded for a joint conditional entropy application. The signals were recorded from freely moving male Wistar rats and from spontaneous hypertensive rats, aged 3 months and 12 months. *Results*. The highest level of comonotonic behavior of pulse interval with respect to systolic blood pressure is observed at time lags $\tau = 0$, 3, and 4, while a strong counter-monotonic behavior occurs at time lags $\tau = 1$ and 2. *Conclusion*. Dynamic range of aging rats is considerably reduced in hypertensive groups. Conditional entropy of systolic blood pressure signal, compared to unconditional, shows an increased level of discrepancy, except for a time lag 1, where the equality is preserved in spite of the memory of differential coder. The antiparallel streams play an important role at single beat time lag.

1. Introduction

Interaction of blood pressure (BP) and pulse interval (PI) are complex, governed by numerous homeostatic mechanisms, including the autonomic nervous system [1–3]. Alterations in their functioning either initiate or worsen cardiovascular diseases [4–6]. As a main blood pressure corrector, baroreflex is a subject of numerous studies. A range of methods for estimating its parameters has been developed, both in time domain [7–9] and in frequency domain [10, 11]. Other approaches include the models based on information domain and on nonlinear nature of the systolic BP (SBP) and heart period interactions [12–16]. The comparative analysis is abundant as well, for example, [6, 17]. Besides the baroreflex as a feedback pathway, SBP-PI loop also includes a mechanical feedforward pathway, as PI influences SBP via Frank-Starling law and diastolic runoff [18].

A time delay (lag) of pulse interval (PI) with respect to SBP was included into the baroreflex studies via cross-correlation baroreflex sensitivity (xBRS), where the cross-correlation is applied for assessing the time delay that corresponds to the maximum SBP-PI interaction [9]. This lag is actually a delay of PI response with respect to changes in SBP, caused by the signal propagation, as well as processing in the autonomic nervous system. This delay also presents an important clinical marker [6, 19]. A longer delay indicates a weaker response of the parasympathetic and stronger response of sympathetic nervous system and vice versa. It is changeable according to the physiological state; for example, it is longer in standing than in lying position and it increases with the increase of heart rate and age [20]. Time delay is also affected by a reduction of baroreflex sensitivity, heart failure [21], and syncope [22].

One of the most widely used techniques for studying the spontaneous BRR without pharmacological or mechanical interventions is the sequence method [19, 20]. Sequences are the streams of consecutive beats in which progressive increases (or decreases) in systolic blood pressure (a SBP ramp) are followed by progressive increases (or decreases) in pulse interval (a PI ramp), delayed by a time lag that heavily depends on species [21–29]. The ramps and streams in physiological time series can be a consequence of physiological interactions and of mere random occurrence. Short random streams may be indistinguishable from the physiological ones due to the large coefficient of correlation (a consequence of shortness). Long streams, on the other hand, are characteristics of real physiological data only, since their number in random time series is negligible [30]. For this reason, only the streams of length that surpass a predefined threshold, usually three or four beats, are considered as "sequences" [17]. So, to avoid the ambiguity, the term "sequence" would be reserved for a stream with a length that exceeds the threshold.

This paper analyses the level of temporal dependency in time series recorded from aging rats: the healthy ones and the ones with early developed hypertension. The aim is to find a time span (time lag) along which a change in one signal sample affects the changes of other samples from the same or from the related time series and to explore whether the increased age and hypertension affect the mutual sample relationship. Among the tools that measure statistical dependency at signal level investigated in [31] (e.g., Pearson's product-moment correlation that measures linear relationship, Spearman's correlation that measures the monotonic relationships, and Kendall's correlation that reflects the number of concordances and discordances in time series, as well as the classical correlation) we opted to use copula, and among the numerous copula families we opted for the Frank copula, since it was shown to be well suited to cardiovascular time series [31]; it distinguishes comonotonic and counter-monotonic behavior in bivariate signals. The analysis is applied to the source signals and to the differentially coded signals that process the real numbers. Novel applications require on-line analysis in battery-operated devices, implying computationally more efficient procedures. It brings binary operations to the fore, so we applied binary conditional entropy as well. Application range include crowdsensing [32], as well as self-monitoring during the exercise.

2. Materials and Methods

2.1. Experimental Protocol and Signal Acquisition. All experimental protocols were approved by the Faculty of Medicine University of Belgrade Experimental Animals' Ethics Committee. All procedures conformed to EEC Directive 86/609 and the School of Medicine University of Belgrade Guidelines on Animal Experimentation.

2.1.1. Animals. Experiments were performed in 3- and 12-week-old male Wistar normotensive and spontaneous hypertensive (SHR) rats, weighing 260–400 g. Total number of rats was $n = 24$. Animals were equipped with a right femoral artery catheter for blood pressure recording. Rats were kept in Plexiglas cages (21 cm × 37 cm × 19 cm) under controlled laboratory conditions (temperature 22 ± 1°C, humidity of 65 ± 1%, 7:00 h–19:00 h light-dark cycle) with tap water and pelleted food available ad libitum. The number of animals per experimental group (6) was calculated using software "Power and Sample Size Calculations" for a given power 90% and type I error probability of 0.05 freely downloadable at http://ps-power-and-sample-size-calculation.software.informer.com/.

2.1.2. Surgery. Under combined xylazine 2% (10 mg/kg i.p.) and ketamine 10% (90 mg/kg; i.p.) anesthesia, a polyethylene catheter (OD = 0.90, ID = 0.58, Smiths Medical International Ltd., Kent, UK) prefilled with heparinized saline (50 IU/mL) was inserted in the right femoral artery and tunneled subcutaneously between scapulae for BP recording. Perioperatively rats received gentamicin (25 mg/kg, i.m.) to prevent infection and carprofen (5 mg/kg, s.c.) for pain relief. The sutures in the inguinal and interscapular regions were sprayed with topical antibiotics. After surgery, each rat was housed individually in Plexiglas cages (30 cm × 30 cm × 30 cm) under standard laboratory conditions and left to recover for two days.

2.1.3. Cardiovascular Signal Acquisition and Preprocessing. Arterial blood pressure was recorded for 30 minutes on polygraph (Hugo Sachs Electronics D79232, Freiburg, Germany) and digitalized at 1000 Hz. Systolic (SBP) and diastolic BP (DBP) and pulse interval (PI) were derived from the arterial pulse pressure as maximum, minimum, and interbeat interval, respectively. The derived signals were inspected for misdetections and artifacts and manually corrected. For each registration period, mean value of SBP, DBP, and PI was calculated and again averaged for the whole experimental group. Other usual analytical methods include Poincaré Plots (PPlots) and cross-approximate entropy (X*ApEn*). PPlot is primarily a visual method; its spotted images correspond to the 2D joint probability distribution function. The PPlot quantitative parameters are standard deviations of signals $x_{1i} = \sqrt{2^{-1}} \cdot (\mathrm{PI}_{i+1} - \mathrm{PI}_i)$ and $x_{2i} = \sqrt{2^{-1}} \cdot (\mathrm{PI}_{i+1} + \mathrm{PI}_i)$, $i = 1, \ldots, N-1$, describing short and long term variability of the pulse interval time series [33]:

$$\begin{aligned}
\mathrm{SD1} &= C_{\mathrm{PI}}(0) - C_{\mathrm{PI}}(1) \\
&= E\left\{\left(\mathrm{PI}_i - E\{\mathrm{PI}\}\right)^2\right\} \\
&\quad - E\left\{\left(\mathrm{PI}_i - E\{\mathrm{PI}\}\right) \cdot \left(\mathrm{PI}_{i+1} - E\{\mathrm{PI}\}\right)\right\}, \\
\mathrm{SD2} &= C_{\mathrm{PI}}(0) + C_{\mathrm{PI}}(1) \\
&= E\left\{\left(\mathrm{PI}_i - E\{\mathrm{PI}\}\right)^2\right\} \\
&\quad + E\left\{\left(\mathrm{PI}_i - E\{\mathrm{PI}\}\right) \cdot \left(\mathrm{PI}_{i+1} - E\{\mathrm{PI}\}\right)\right\},
\end{aligned} \tag{1}$$

where $E\{\}$ is an expectation operator, $C()$ is a covariance function, N is the time series length, SD is standard deviation, and the subscript in $E\{\mathrm{PI}\}$ is omitted since the signals are assumed to be wide sense stationary (WSS). X*ApEn* [34]

is a classical static measure of the mutual interreaction of parallel time series. In brief, X*ApEn* procedure divides each time series into $N - m + 1$ overlapping vectors of length m. A selected vector from the first series is compared to each one of the $N - m + 1$ vectors from the second series, to estimate the probability that their absolute distance is below the specified threshold. It is repeated for each one of the $N - m + 1$ vectors from the first series, and the logarithms of the estimated probabilities are averaged (the first average). Then the procedure is repeated for the vectors of length $m+1$. The obtained second average is subtracted from the first one, yielding X*ApEn* estimate [34].

As a control, pseudorandom and randomized signals were implemented. Pseudorandom signals include series of independent and identically distributed (i.i.d.) random variables with normal and uniform distribution. Randomized signals include surrogate data series [35]. Isodistributional surrogates randomize the temporal order of the observed time series and destroys the sample dependency but preserve the signal distributional function. Isospectral surrogates operate in transform domain, either randomizing the existing signal phases, or substituting them with pseudorandom i.i.d. phase samples with uniform distribution. In both cases, the power spectral density remains unchanged and, according to the Wiener-Khinchin theorem, the same applies to the autocorrelation function, so the intersample connections are preserved [36].

2.1.4. Drugs. Ketamine, xylazine, and carprofen (Rimadyl®) as well as the combination of embutramide, mebezonium, and tetracaine (T61®) injections were purchased from Marlo-Farma (Belgrade, RS). Gentamicin injection and bacitracin neomycin spray (Bivacyn®) were purchased from Hemofarm (Vršac, RS).

2.1.5. Statistical Analysis. Results are shown as mean ± standard error of the mean. Statistical comparison between experimental groups was done using Mann–Whitney test in GraphPad Prism 4 software (GraphPad Software Inc., San Diego, CA, USA). The level of significance was set at $p < 0.05$.

2.2. Analytical Methods. The level of dependence inherent to SBP and PI time series is assessed in two ways: using copula analysis of original and differentially coded data and estimating mutual uncertainty using computationally efficient binary conditional entropy, applied to binary differentially coded time series. The inclusion of the second analysis is initiated by the increasing number of battery-operated wearable monitoring devices.

A copula is a mathematical concept that decomposes a multivariate (in this case: bivariate) distribution functions into its univariate marginals, measuring the global statistical dependency among the components. Its release in [37] initiated an extensive implementation within the various fields, but the applications in biomedical studies are rare, including imaging-based diagnostic classifiers for neuropsychiatric disorders [38], the aortic regurgitation [39], and a drug sensitivity prediction [40]. The possibility of applying a copula for cardiovascular signals is pointed out in [41], while its pharmacological validation is performed in [31]. In brief, observing a set of NV variables (RV) x_i with a joint distribution function $J(x_1, x_2, \ldots, x_{NV})$ and with respective marginal distribution functions $F_1, F_2, \ldots, F_{NV}$, a new set of variables u_i, uniformly distributed on $[0,1]^{NV}$ [42, 43], can be derived as $u_i = F_i(x_i)$, $i = 1, \ldots, NV$. The corresponding copula is defined as

$$C(u_1, u_2, \ldots, u_{NV}) = J\left(F_1^{-1}(u_1), F_2^{-1}(u_2), \ldots, F_{NV}^{-1}(u_{NV})\right). \quad (2)$$

or

$$J(x_1, x_2, \ldots, x_{NV}) = C(F_1(x_1), F_2(x_2), \ldots, F_{NV}(x_{NV})). \quad (3)$$

It was shown that Frank copula is the most suitable for cardiovascular signals [31]: it is unbounded and symmetric with value zero in absence of dependence, its sensitivity for SBP-PI signal is the best, and, for a bivariate case, it permits modelling both comonotonic and counter-monotonic dependence. The Frank copula distribution is given by the following relation:

$$C^{(F)}(u_1, u_2, \ldots, u_N) = -\theta^{-1} \cdot \log\left[1 + \frac{\prod_{i=1}^{N}\left(e^{-\theta \cdot u_i} - 1\right)}{\left(e^{-\theta} - 1\right)^{N-1}}\right]. \quad (4)$$

The copula parameter θ shows the level of statistical dependence and in Frank case it is set to zero if the variables are completely independent.

The copula concept is clarified considering a simple example of two ($NV = 2$) jointly observed time series: pulse interval PI_i as the first one and a beat delayed counterpart PI_{i+1} as the second time series, $i = 1, \ldots, N-1$. Then both the joint empirical probability density function (pdf) and the corresponding empirical marginal pdfs are estimated and shown in Figures 1(a) and 1(d), respectively. The second step in copula procedure is to apply the theory of inverse transform methods [44]. In brief, a random variable (RV) x with arbitrary distribution can be transformed into a RV with uniform distribution u, using its own distribution function $F(x)$ for transformation, as explained in Figure 2. Such a transformation yields an empirical copula density function, shown in Figures 1(b) and 1(e): the transform has eliminated the marginal distributions, so only the dependency structure is preserved, revealing that in this example the tail (corner) samples are the ones that exhibit the maximal dependency and not the samples with the most frequent values. The last step of the procedure is to find an analytical copula that is the closest to the obtained empirical one. After choosing the copula family, the analytical copulas for a range of parameter θ are generated, and the one that is the closest in a maximum likelihood sense to the empirical one is chosen as a representative copula. This copula density, as well as its uniform marginal, is shown in Figures 1(c) and 1(f).

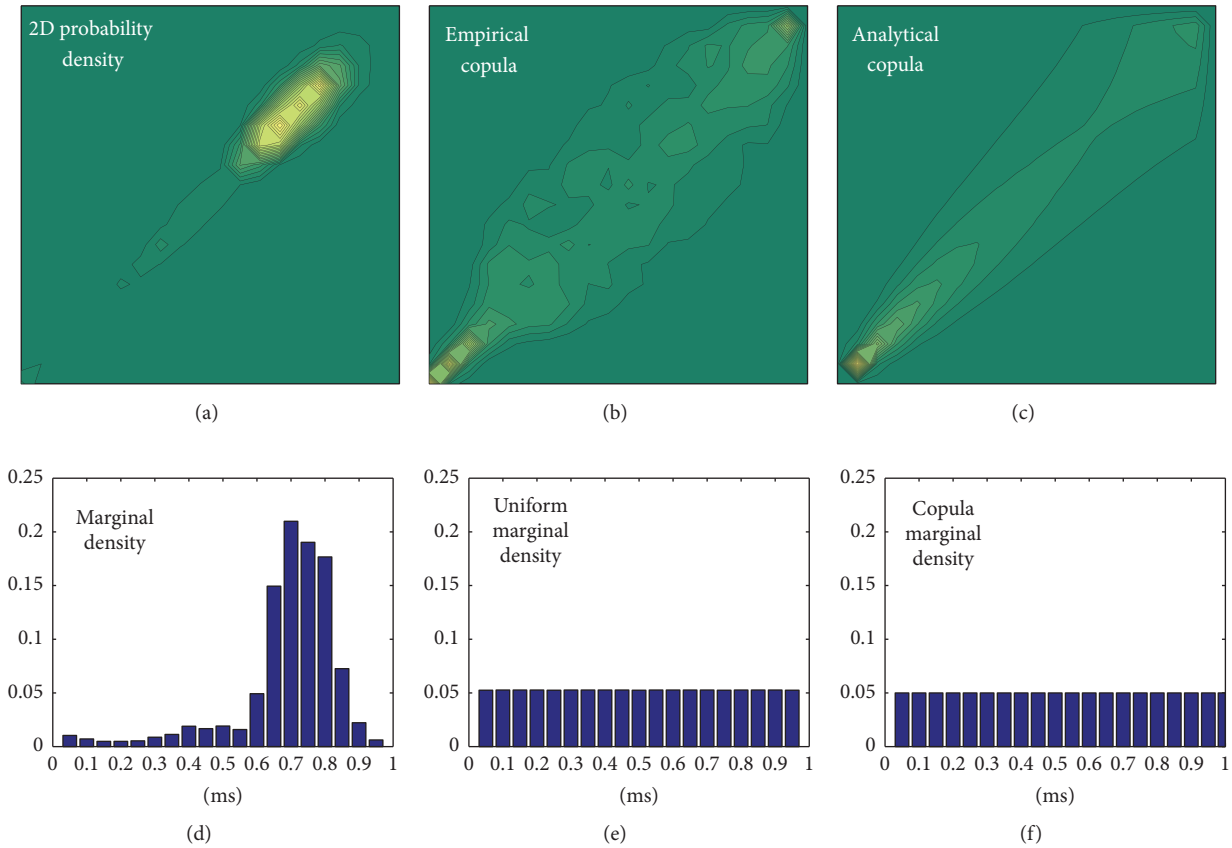

FIGURE 1: Visualization of the copula process. (a) Estimated joint pulse interval density function with time lag 1 (it corresponds to PPlot); (b) estimated copula density showing the level of the dependency structure in $[0, 1]^2$ plane; (c) the best fit theoretical copula (Clayton, $\theta = 4.2617$, 20 bins). (d, e, f) 1D marginal densities; (d) PI time series; (e) and (f) transformed and calculated uniform density.

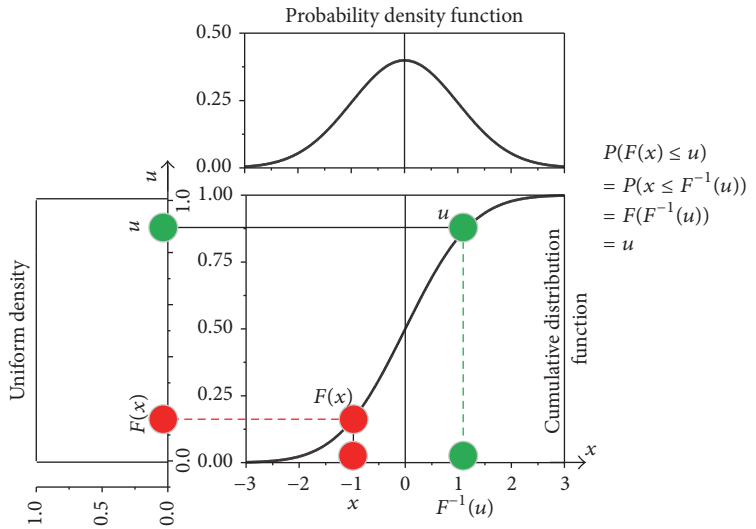

FIGURE 2: Transformation of a random variable x with an arbitrary distribution function $F(x)$ into a random variable u with uniform distribution using $F(x)$ for transform. The relationship $x \leq F^{-1}(u)$ along the x-axis and $F(x) \leq u$ along the u-axis are unaltered by $F(x)$ transform, so $P(F(x) \leq u) = u$, which holds for the uniform distribution with RV defined on $[0, 1]$.

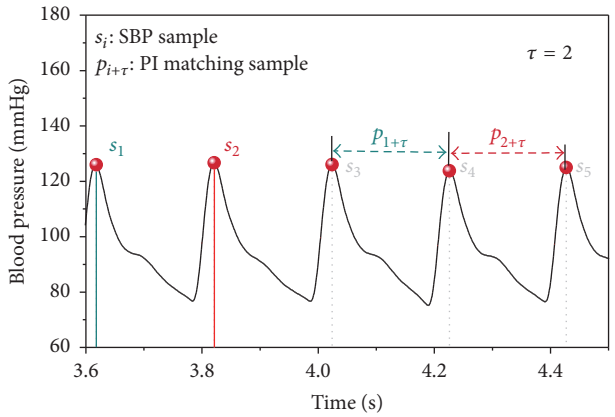

FIGURE 3: Blood pressure waveform (black line), SBP signal samples (red dots), and PI signal samples at the time lag $\tau = 2$; the matching s_i-$p_{i+\tau}$ signal sample pairs are denoted using the same color.

The joint 2D density in Figure 1(a) visually corresponds to PPlot. Indeed, both techniques start from the same visual presentations. Their further development is different: PPlot is devoted to the short and long term signal variability, expressed through the respective standard deviations SD1 and SD2; copula shows the level of statistical dependence, expressed through the copula parameter θ. The copula in this study is applied to bivariate data, to the SBP and PI time series. A level of freedom is a time lag τ of PI samples p_i, $i = 1, \ldots, N$, with respect to SBP samples s_i, $i = 1, \ldots, N$, so the empirical joint distribution function J is estimated over the delayed sample pairs: s_i-$p_{i+\tau}$, $i = 1, \ldots, N - \tau$, as shown in Figure 3.

The estimated copula density shows a structure of mutual relationship of the SBP and PI time series, that is, the regions where the signal dependency is the strongest. A fitting procedure quantifies the overall dependency level, reducing the copula to a static single value θ. But if the time series comprise sufficient amount of data, a dynamic tracking can be performed as well. Time series can be partitioned into the overlapping segments of size d, and for each segment a copula dependency parameter θ can be evaluated. A series of adjacent θ values show the dynamic changes of dependency parameter in time that can be associated with the behavior of the observed subject. Typical segment lengths are 300 to 500 samples, while the overlapping level of adjacent segments is typically $d/10$.

Copula can be applied to the differentially coded signals as well. The differentially coded SBP signal s_i and PI signal p_i, $i = 1, \ldots, N$, are expressed as

$$xD_i = x_{i+1} - x_i, \quad i = 1, \ldots, N-1, \; x \in \{s, p\}. \tag{5}$$

In applications where power and processor resources are limited, it is more appropriate to work with binary signals. Binary differentially coded counterparts of the signals from (5) are expressed as

$$xB_i = \begin{cases} 0 & xD_i \le 0 \\ 1 & xD_i > 0, \end{cases} \quad i = 1, \ldots, N-1, \; x \in \{s, p\}. \tag{6}$$

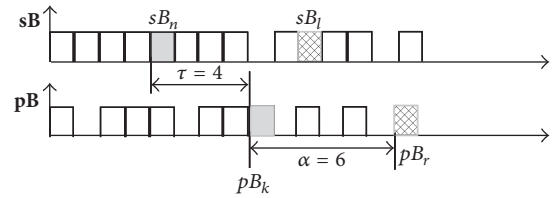

FIGURE 4: Levels of freedom for mutual positions of binary symbols in (7) and (8): τ is time lag between the bit sB_n from SBP and its delayed counterpart pB_k from PI series; α is time lag between the bits sB_n and sB_l (pB_k and pB_r) within the SBP (PI) time series.

Copulas cannot be applied to the time series transformed into a binary form, but the similar goal can be achieved by unconditional and conditional entropy of a single time series ($H(\mathbf{xB})$ and $H(\mathbf{xB} \mid \mathbf{xB})$) and of the joint time series ($H(\mathbf{sB}, \mathbf{pB})$ and $H(\mathbf{sB}, \mathbf{pB} \mid \mathbf{sB}, \mathbf{pB})$) as follows:

$$\begin{aligned} H(\mathbf{xB}) &= -\sum_{n=0}^{1} P(xB_n) \cdot \ln\left(P(xB_n)\right), \\ &\qquad x \in \{s, p\}, \; xB_n \in \{0, 1\}. \\ H(\mathbf{xB} \mid \mathbf{xB}) &= -\sum_{k=0}^{1} P(xB_k) \cdot \sum_{n=0}^{1} P(xB_n \mid xB_k) \\ &\quad \cdot \ln\left(P(xB_n \mid xB_k)\right), \\ &\qquad x \in \{s, p\}, \; xB_n, xB_k \in \{0, 1\}. \end{aligned} \tag{7}$$

$$\begin{aligned} H(\mathbf{sB}, \mathbf{pB}) &= -\sum_{n=0}^{1} \sum_{k=0}^{1} P(sB_n, pB_k) \cdot \ln\left(P(sB_n, pB_k)\right), \\ &\qquad sB_n, pB_k \in \{0, 1\}. \\ H(\mathbf{sB}, \mathbf{pB} \mid \mathbf{sB}, \mathbf{pB}) &= -\sum_{k=0}^{1} \sum_{n=0}^{1} P(sB_n, pB_k) \\ &\quad \cdot \sum_{l=0}^{1} \sum_{r=0}^{1} P(sB_l, pB_r \mid sB_n, pB_k) \\ &\quad \cdot \ln\left(P(sB_l, pB_r \mid sB_n, pB_k)\right), \\ &\qquad sB_n, pB_k, sB_l, pB_r \in \{0, 1\}. \end{aligned} \tag{8}$$

In the above equations, $P(x)$, $P(x, y)$, and $P(x \mid y)$ denote a probability, a joint probability, and a conditional probability. Since entropy, as a rule, is a relative measure, conditional entropy (lower parts of (7) and (8)) is usually presented in percentage of its unconditional counterpart (upper part of the same equations). The relationship between the binary symbols in (7) and (8) is shown in Figure 4.

There are two levels of freedom for estimating the joint entropy: time lag τ between the pairs of bits from SBP and PI time series and time lag α within the bits of that belong to the same time series (either SBP or PI). It should be noted that indices n, k, l, and r in Figure 4 correspond to (7) and (8), that is, to the binary symbols and not to the time axis. For example,

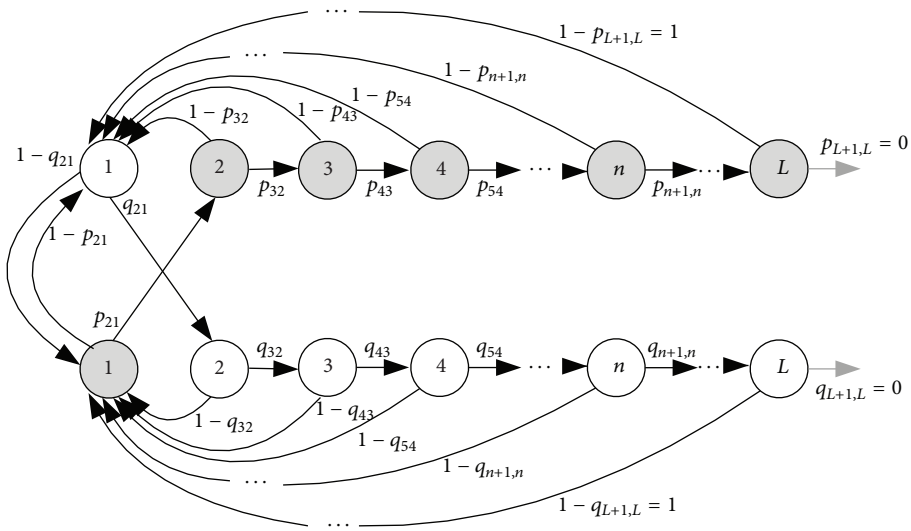

FIGURE 5: A two-branch counter; states correspond to the successive positive and negative differential signal (5), that is, to the successive increasing and decreasing amplitudes.

if the bit sB_n in Figure 4 is the ith bit along the time axis, then the bits pB_k, sB_l, and pB_r would be at the positions $i+\tau$, $i+\alpha$, and $i+\tau+\alpha$.

Figure 5 presents a two-branch counter [30] with states corresponding to the successive positive signal differences, that is, successive increasing signal amplitudes (branch with gray states) and successive decreasing signal amplitudes (branch with white states). If the counter is in the state denoted "k," it means that k signal differences of the same sign have already occurred in a row. It is in a form of a finite ergodic Markov chain and it models the increasing and decreasing ramps of differentially encoded signal samples.

If a ramp in SBP signal is followed by a ramp in PI signal at a particular time lag τ and if the ramps comprise either increasing or decreasing differences, such ramps form a "parallel stream." Similarly, antiparallel stream may be defined as an increasing SBP ramp followed by decreasing PI ramp at a time lag τ (and vice versa). The occurrence of parallel and antiparallel streams will be of importance for dynamic tracking and explanation of copula parameters.

The model shown in Figure 5, aided with the theory of Markov chains, enables analytical evaluation of parameters, such as the exact number of ramps and streams in i.i.d. random data, as well as the state transition probabilities evaluation:

$$N_{\mathrm{RAMP}}(n) = (N-1)\cdot\frac{(n+1)^2+n}{(n+3)!},$$

$$N_{\mathrm{SEQ}}(n) = (N-1)\cdot\frac{2\cdot\left[(n+1)^2\cdot(n+3)^2-(n+2)^2\right]}{[(n+3)!]^2}, \tag{9}$$

$$p_{n+1,n}(n) = \frac{(n+2)}{(n+1)\cdot(n+3)}.$$

The detailed mathematical derivation of the expressions (9) is given in [30].

3. Results and Discussion

3.1. Static Results. The results of the conventional analyses are presented in Table 1. While the PI statistics and the corresponding Poincaré Plot measures SD1 and SD2 were statistically the same in all four groups, blood pressure, both SBP and DBP, was high in spontaneous hypertensive (SHR) rats, and, with their increasing age, pressure significantly increased. X*ApEn* could not make any distinction between the observed groups. Further on, although X*ApEn* is frequently used in assessing the level of interrelations of time series, it has no possibility to observe if one time series is delayed with respect to another: X*ApEn*, by definition, compares all possible combinations of m-sized partitions of both time series, producing always the same result, regardless of time lag τ.

Copula, however, can take the time lag τ between the observed time series into account. Figure 6 presents a static copula measure, calculated over 4000 SBP-PI pairs, as a function of a particular time lag τ. (a, b) show the dependency estimated from the original detrended [45] signals, while (c, d) show dependency estimated from the differentially coded signals (5). Copula parameters derived from differentially coded signals show that the statistical dependency induced by signal changes are consistent with time lags in all four experimental groups: the highest dependence is observed at lags $\tau = 0$ and $\tau = 3$, while a strong negative dependency occurs at time lag $\tau = 1$. While the dependency of SBP-PI changes remained intact in healthy rats with increased age (c), small values of θ, almost close to zero, in aging hypertensive rats show loosening the SBP-PI connections (b), also emphasized by decreased dynamic range dependency level of SBP-PI changes (d).

Table 1: Mean and s.e.m. of measured time series, classical variability analysis.

	SBP [mmHg]	DBP [mmHg]	PI [ms]	Poincaré plot		X*ApEn*
				SD1 [ms]	SD2 [ms]	
SHR 3	172.04 ± 4.25	117.53 ± 4.93	184.13 ± 6.04	2.42 ± 0.28	11.01 ± 1.78	1.59 ± 0.10
SHR 12	200.47 ± 5.01**	134.10 ± 2.59*	197.05 ± 6.10	3.8 ± 0.97	14 ± 2.16	1.39 ± 0.17
WIS 3	123.99 ± 3.82	77.66 ± 4.32	174.02 ± 4.69	2.63 ± 0.37	10.1 ± 1.4	1.38 ± 0.08
WIS 12	132.81 ± 2.44	87.51 ± 1.14	174.18 ± 3.38	3.15 ± 0.45	11.09 ± 1.64	1.49 ± 0.12

Data are expressed as mean ± s.e.m. $* < 0.05$ versus SHR3. $** < 0.01$ versus SHR3.

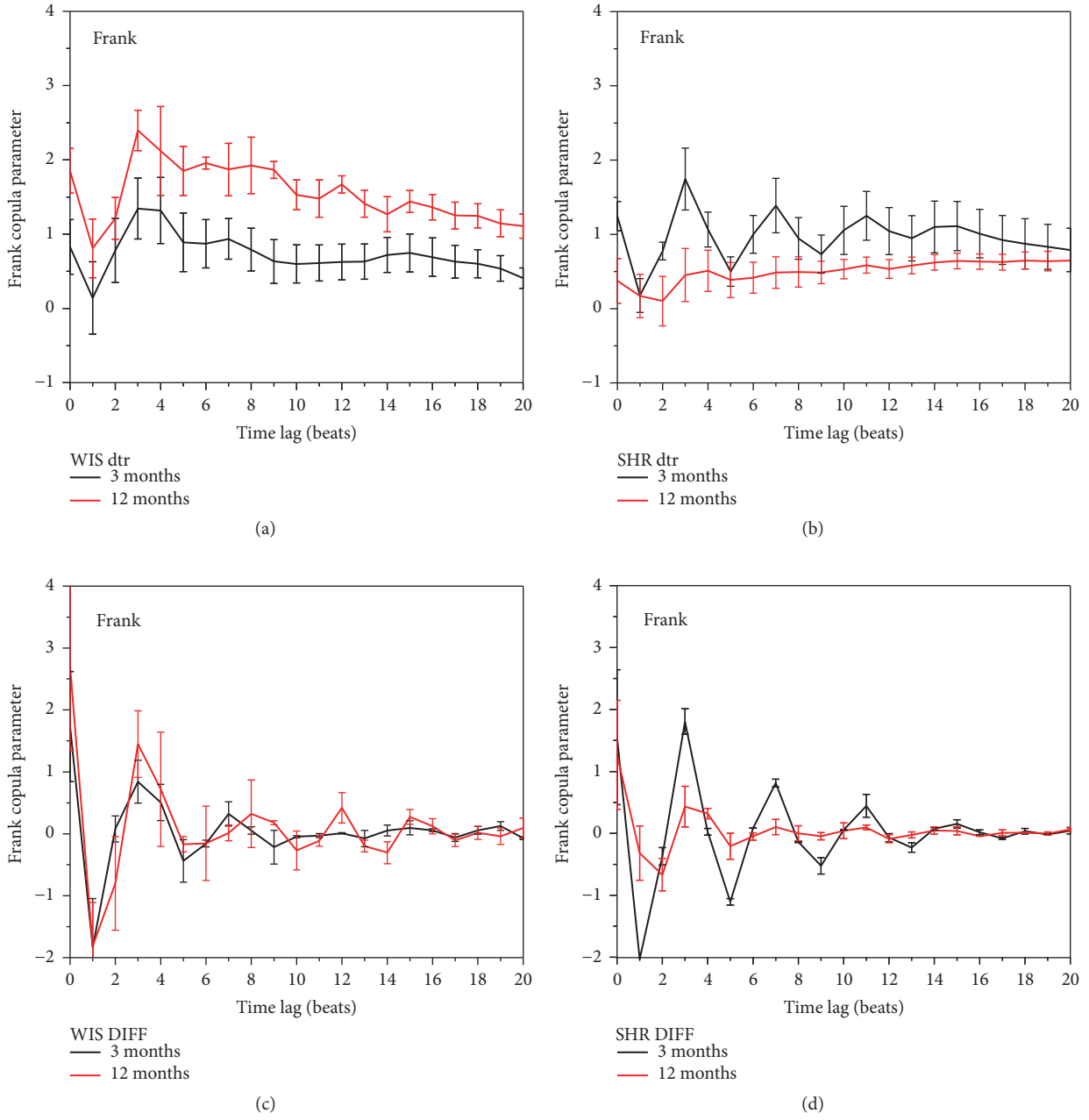

Figure 6: A static copula dependency measure estimated from the original signals with trend removed and from the differentially coded signals ((a–d), resp.); (a, c) correspond to Wistar normotensive rats; (b, d) correspond to spontaneous hypertensive rats.

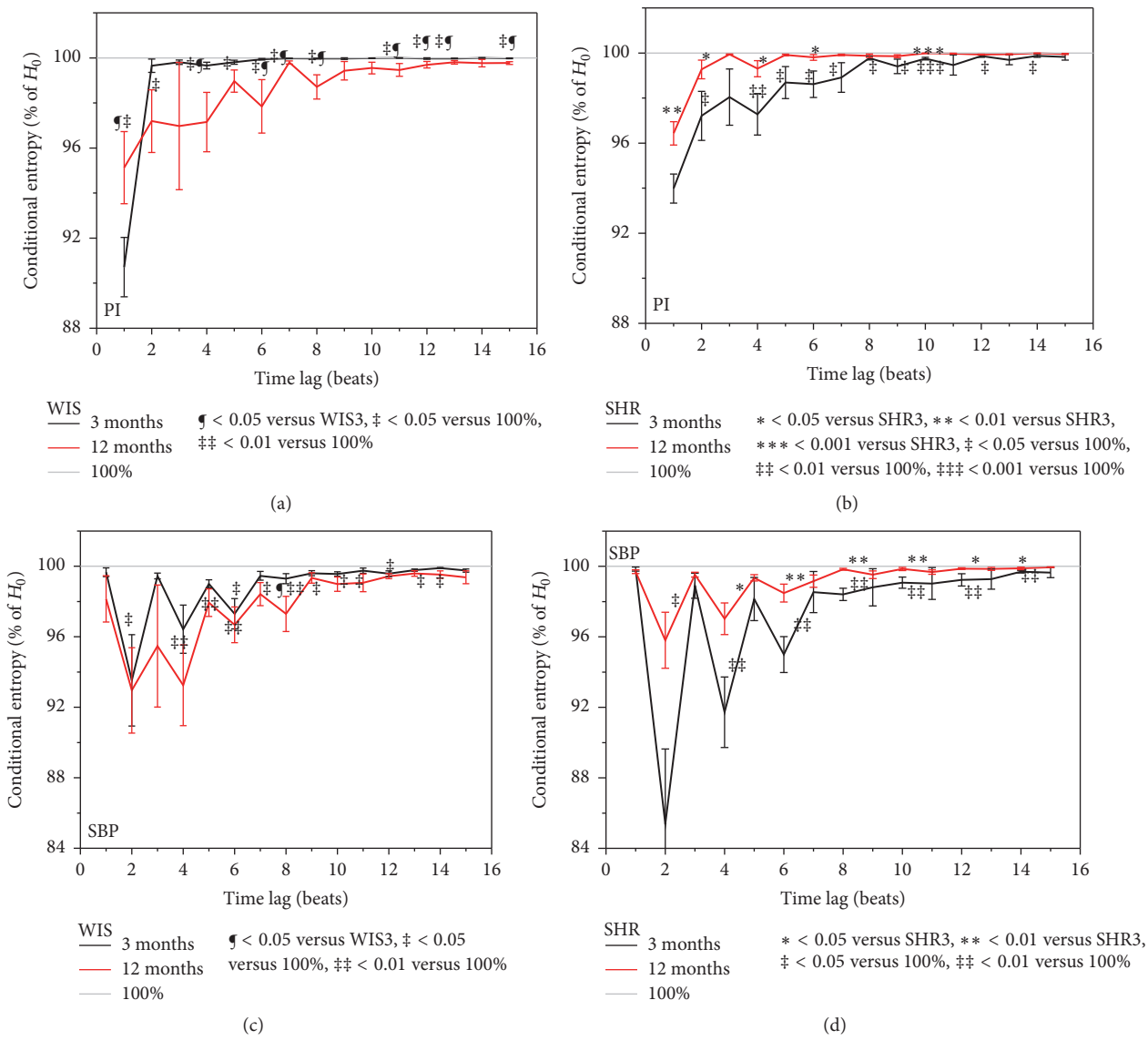

Figure 7: Relative conditional entropy estimates from binary differentially coded PI signals (a, b) and SBP signal (c, d).

Conditional entropy defined over the binary differentially coded signals (6) operates over coarsely coded signals, but it is computationally less demanding. The relative conditional entropy of signals taken from the same time series is presented in Figure 7.

Except for the time lag $\alpha = 1$ (to be explained later on), conditional entropy of PI signals in young healthy Wistar rats is equal to its statistically independent counterpart. As the age increases, the PI signals exhibit more order (inputs are attenuated) and more mutual dependency so the entropy slightly decreases. Surprisingly, hypertensive rats (b, d) showed just opposite results: conditional and unconditional entropies were equal in aging rats, while young ones had a slight increase of statistical dependency between the signal samples at the time lag α, and the corresponding entropy was slightly lower. Considering the binary samples of SBP signals (c, d), the discrepancy of conditional entropy with respect to its unconditional counterpart is considerably enlarged. This discrepancy diminishes at time lag $\alpha = 10$ (12 in hypertensive young rats); that is, there is no statistical dependency between the changes in blood pressure if the observed samples are at time lag of 10 (12) beats one from another.

The dependency at the time lag of $\alpha = 1$ (adjacent symbols) is different as it is not related to the physiological constraints of PI and SBP signals. It is predominantly a consequence of the differential coding procedure: the adjacent samples of differentially coded signal both comprise the same original signal sample x_{i+1} (5). In the first differential sample x_{i+1} is a minuend, $xD_i = x_{i+1} - x_i$, and in the second differential sample x_{i+1} is a subtrahend, $xD_{i+1} = x_{i+2} - x_{i+1}$. The conditional entropy at time lag $\alpha = 1$ is shown in Figure 8, including the entropy estimates of real signals (red bars) and, as a control, estimates taken from the surrogate signals. Isodistributional surrogates randomize the order of the original signal samples,

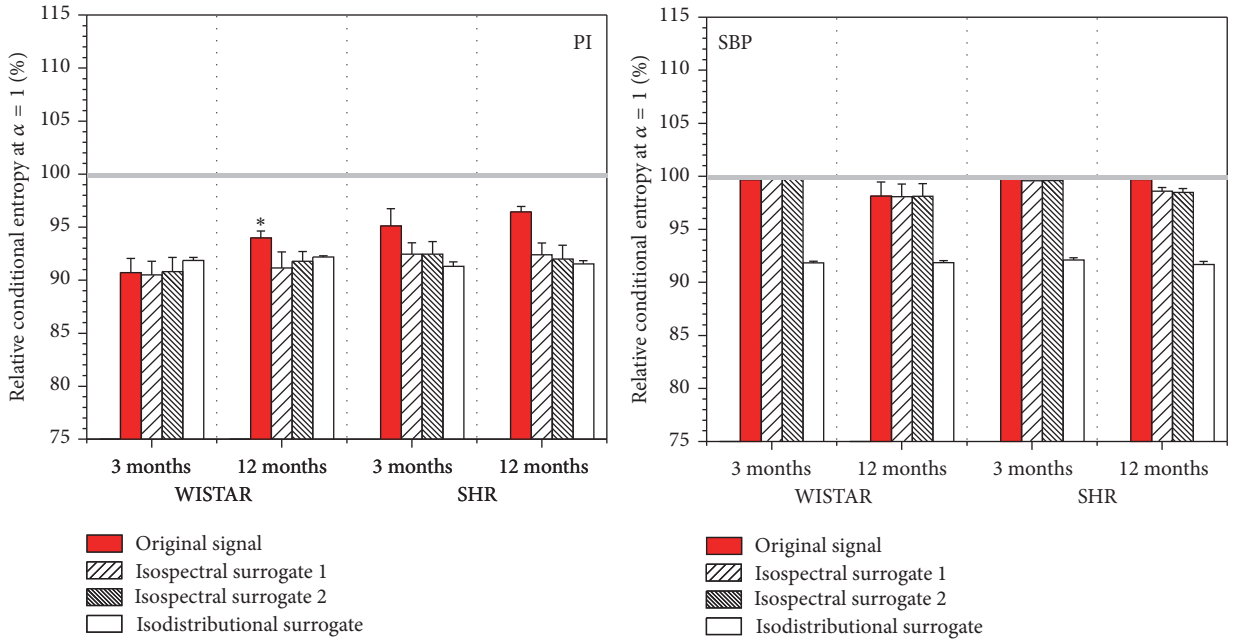

FIGURE 8: Relative conditional entropy estimated at time lag $\alpha = 1$ from the original PI signals, original SBP signals, and the three types of surrogate control signals. The results are expressed as mean ± s.e.m; $* < 0.05$ versus 3-month-old animals. Gray line shows the value of unconditional entropy.

thus destroying their dependency but preserving the distribution function. Isospectral surrogates randomize the signal phase thus altering the samples and their distribution, but preserving the spectral density, autocorrelation function, and, consequently, intersample relationship.

Even if the signals are random and independent, their differentially coded counterparts are not. Differential coding forces the conditional entropy estimates of randomized data (isodistributional surrogates) to lose 8 to 9% of their values (white bars in Figure 8). These simulation results are in a perfect accordance with theoretical entropy loss that is equal to 8.17%, as shown in Appendix. Conditional entropy of PI signal and all of its control surrogates follow the theoretical constraints induced by differential coding. The same holds for isodistributional controls of SBP signals, since the random scrambling destroys intersample relationship. But SBP signals seems to be resilient to the coding-induced dependency, preserving the entropy value that, according to the theory, should be reserved for statistically independent binary data. The same applies to SBP Isospectral surrogates, since the phase randomization does not affect the intersample relationship. Seemingly, the regulatory mechanisms of systolic blood pressure are so firm and manage to oppose coding-induced dependency so well that the conditional entropy does not differ from its unconditional counterpart. It is also in accordance with the finding that the transition probabilities of differentially coded SBP samples (model in Figure 5) follow the Bernoulli distribution: the probabilities that the next SBP sample amplitude would increase or decrease are the same; that is, the transition probabilities for the model in Figure 5 are equal to $p_{n+1,n} = 0.5$ (Figure 9).

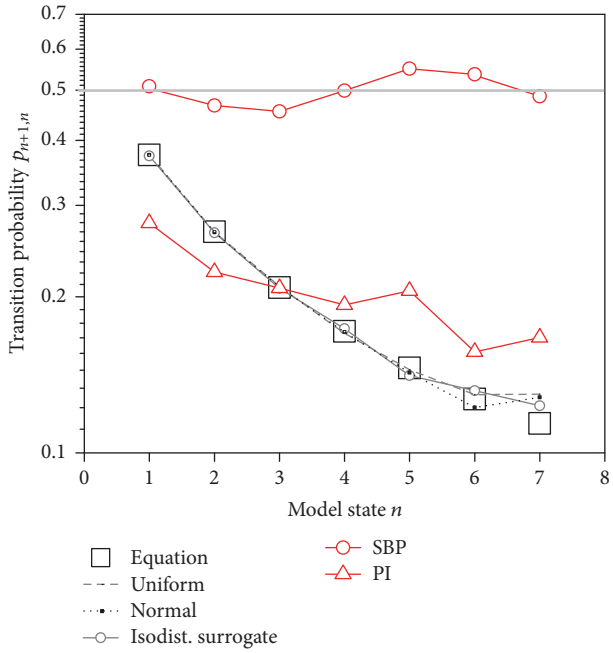

FIGURE 9: Transition probabilities of binary differentially coded signal samples (Figure 5), estimated from all the subjects. SBP probabilities are in a vicinity of 0.5. Probabilities estimated from random and randomized signals are in an excellent accordance with the probability in (8). PI probabilities differ from the previous groups.

3.2. Dynamic Measures. Dynamic observation of copulas imply, as already said, an analysis of the overlapping segments of data and plotting the results obtained from each particular

segment along the time axis (Figure 10(e)), keeping time lag τ as a parameter along the ordinate.

The changes in copula parameter might be a consequence of the appearance of parallel and antiparallel streams, so the occurrence of streams is plotted along the same time axis. (Figures 10(a), 10(b), and 10(c)). The plot distinguishes length of streams, marked by the corresponding amplitude in plot. Type of the stream, parallel and antiparallel, is marked black and red, respectively.

For time lags $\tau = 0$ and $\tau = 4$ parallel streams (black) are dominant (a) and (c). For time lag $\tau = 4$, antiparallel streams (red (b)) outnumber the parallel ones. These observations are in a perfect accordance with the dynamic copula parameter in (e): at the time lags $\tau = 0$ and $\tau = 4$ dependency is expressed as a horizontal red line along the time axis, showing a strong positive dependence; at the time lag $\tau = 2$, the dependence is negative (horizontal dark blue line). A temporary increased concentration of parallel streams between the seconds 400 and 500 (encircled region at $\tau = 2$, (b)) is reflected in short drop of dependency strength marked with lighter blue color of short duration, encircled in (e).

Conditional entropy is estimated from a coarsely coded binary signal. Yet, as a method, it distinguishes the changes in entropy values at the time lags τ, shown by light red horizontal stripes in (d). The entropy changes have lower dynamic range as the coding itself is coarse, reducing 4096 levels of the original data to binary symbols. However, joint conditional entropy suffers a methodical drawbacks when the results are presented simultaneously in α-τ plane: levels of freedom α and τ shown in Figure 3 enable a deterministic sample overlap and induce a dependence that result in diagonal artifacts in Figure 10(d), that may cause an ambiguity in results.

Unconditional entropy as defined in the upper part of (8) corresponds to Shannon entropy $\mathrm{JSD}_{\mathrm{Sh}}$ with $m = 1$, defined within the concept of joint symbolic dynamics (JSD) [46, 47]. JSD forms joint "words" taking m bits from each one of the observed time series, and, among the other parameters, it calculates unconditional entropy $\mathrm{JSD}_{\mathrm{Sh}}$. Typically, m is equal to 3, so the cardinality of words is equal to 64, making conditional entropy difficult to achieve word-by-word estimation of the required 4096 transition probabilities, which is not suited with the concept of limited power resources that are the reason for including the binary operations [48].

Figure 11 illustrates the characteristic cases. (a) corresponds to signals without exposed statistical dependency. Except for the unwanted but deterministic diagonal artifacts, increase of dependency in α-τ plane is registered only at $\tau = 1$, for the adjacent SBP-PI pairs only, and the same applies for copula parameter estimated from differentially coded signals. Copula estimated from the raw signals, however, changes along the time axis. (b) corresponds to signals with strong statistical dependency. Entropy in α-τ plane, although with visible horizontal and vertical lines (the changes of dependency due to lags τ and α, resp.), also exhibits too many diagonal artifacts that make the image difficult to interpret. Dependency estimated by copula, from both raw data and differentially coded data, exhibits strong comonotonic and counter-monotonic relation at the characteristic time lags, shown by dark red and dark blue horizontal lines. Copulas also reveal an interesting phenomenon: statistical dependency can decrease, change the sign, or completely vanish along the time axis (middle and especially lower panels in Figure 11). That might point out a short temporary loss of these portions of neural connection that can be measured by SBP-PI interdependency.

To explore the relationship between the copula parameters and streams, the number of parallel and antiparallel streams at different time lags is shown in Table 2. Antiparallel streams are considered as "increasing" if SBP samples increase and PI samples decrease.

The statistically significant differences exist between the numbers of parallel and antiparallel streams, but not between the different groups of animals. The average number of parallel streams is extremely small at time lags $\tau = 1$ and 5, while it is extremely large for time lag $\tau = 0$. It is in accordance with the mean copula values shown in Figure 6. The streams are further connected with copula parameters in Figure 12: for each rat a copula parameter is estimated and the number of parallel and antiparallel streams are counted. The x-axis of the obtained plots presents a copula parameter, while the y-axis presents the number of streams. A visual inspection of plots reveals that the same number of parallel and antiparallel streams in one rat produce positive dependence with $\theta = 1$ and in the other rat negative dependence with $\theta = -1$. Therefore, the copula value is related to the number of parallel and antiparallel streams, but loosely, and the dependency that copula reveals is more complex to be explained by the occurrences of SBP and PI ramps that change their amplitudes in the same or in the opposite direction.

4. Conclusion

The aim of this paper was to explore a time lag along which a change in one signal sample affects the changes of other samples in rats with hypertension and with increased age. Healthy Wistar rats, young and aging, were used as control. The dependency is measured using copula method at signal level (both raw signal and differentially coded signal) and at the binary level (binary differentially coded signals). Tools for assessing dependency were copulas within the field of real numbers and conditional entropy within the binary field.

Copulas applied as a static measure of SBP-PI dependency showed that the highest level of comonotonic behavior of PI with respect to SBP is observed at time lags $\tau = 0$, 3, and 4, while a strong counter-monotonic behavior occurs at time lags $\tau = 1$ and 2 in all four animal groups and is observable both for raw and for differentially coded signals. Dynamic range of copula parameter in aging rats was considerably reduced in hypertensive groups, showing a reduced capability for SBP-PI responses along the time axis. Contrary to this, dynamic range in healthy rats remained intact. Copula parameter observed along the time axis can be loosely related to the number of parallel and antiparallel streams and, indeed, the time lags with considerably increased average number of parallel streams correspond to the time lags that exhibits the strongest (averaged) comonotonic dependence and vice versa, the lags with increased number of antiparallel streams are the ones with lowest copula parameter. The number

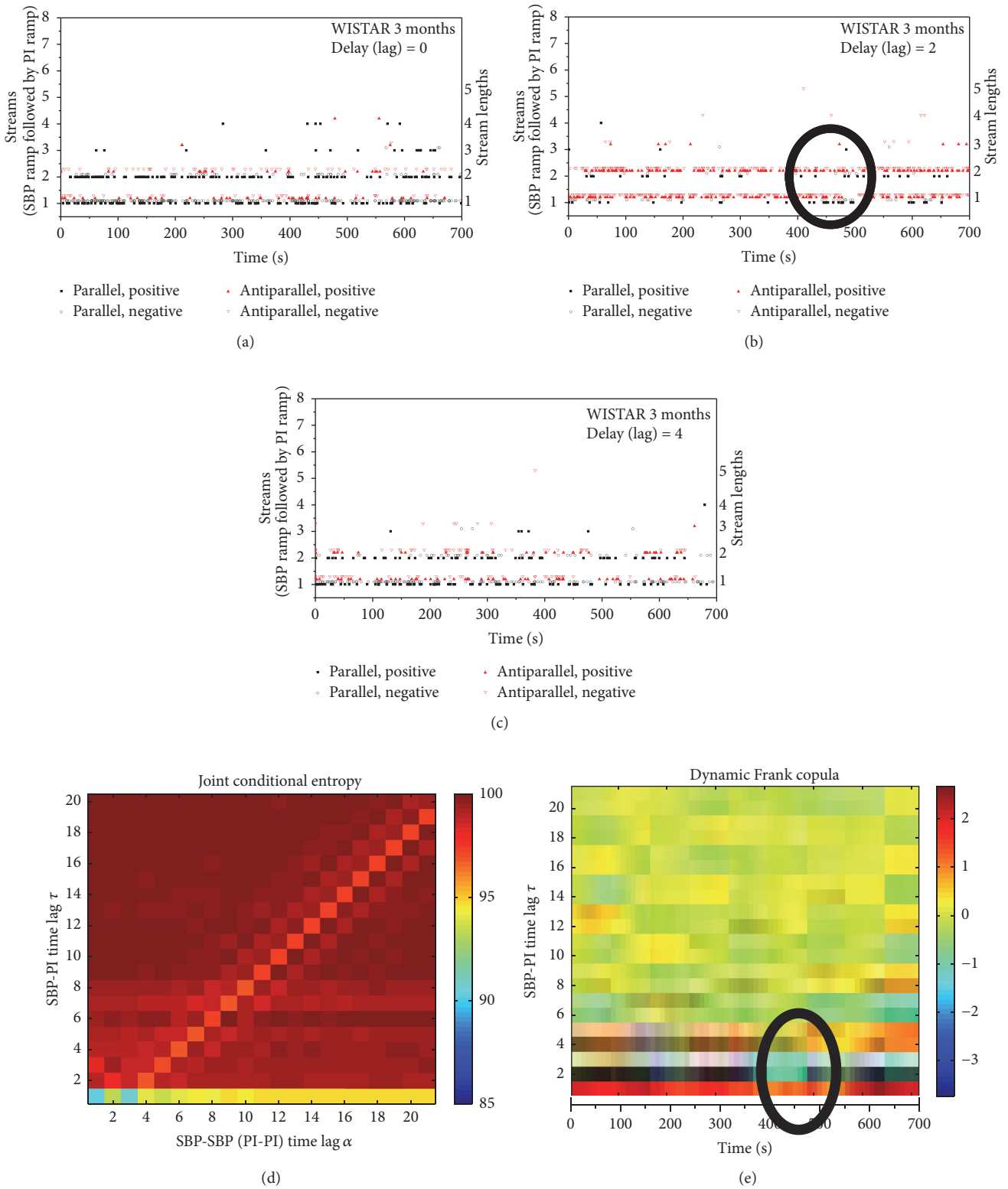

FIGURE 10: Dynamic observation of streams and copula; (a, b, c) show the position of a particular stream at the time axis; length of sequence is marked in the right, while the type of sequence is marked by a different symbol and a slight amplitude offset. (d) shows joint relative cross-entropy for different time lags τ and α, while (e) shows a copula plot, change of copula along the time axis.

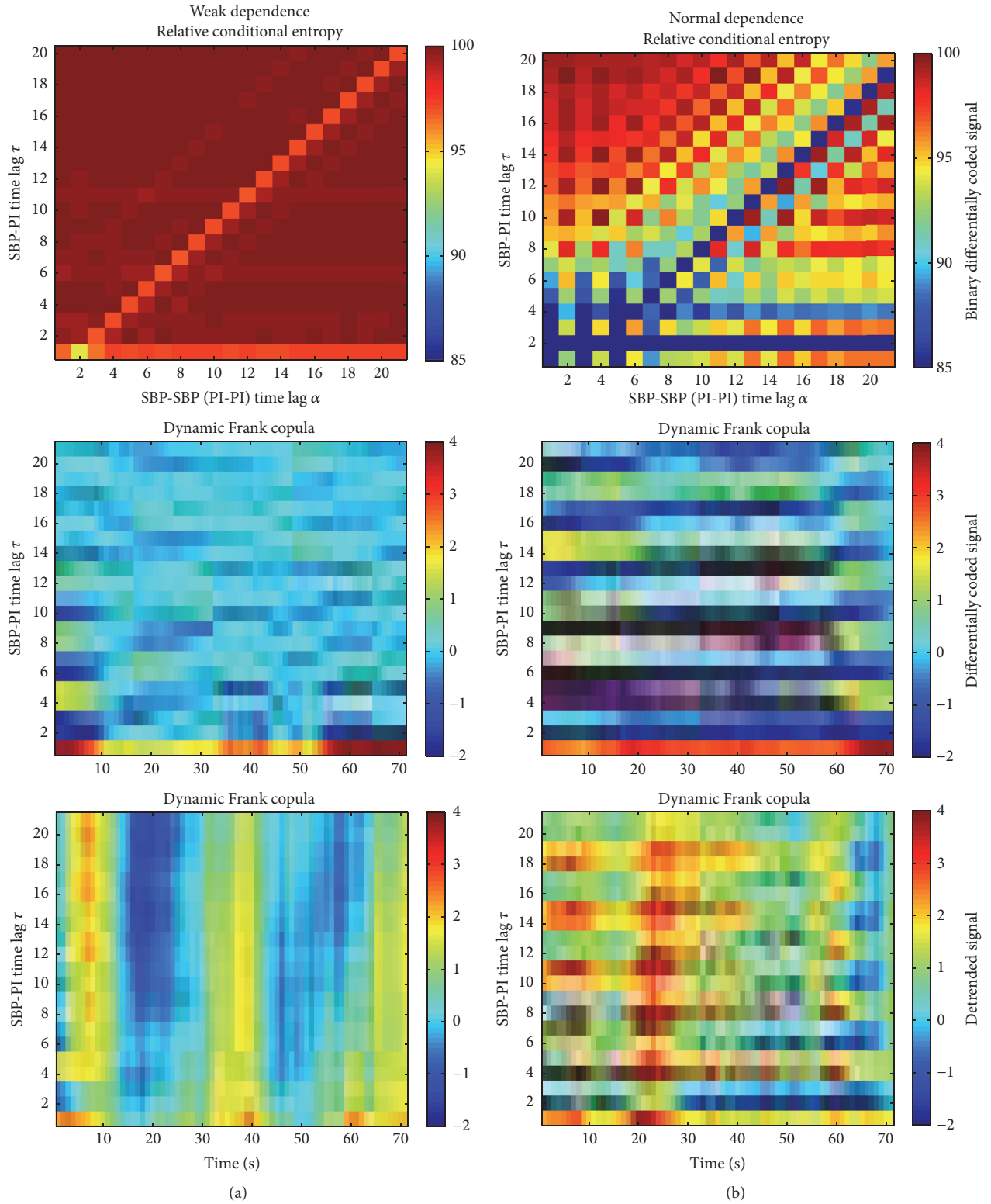

Figure 11: Joint conditional entropy and copula parameter observed along the time axis, (a) signals with poor statistical dependency; (b) signals with strong dependency (horizontal lines).

Table 2: Mean number of streams ± s.e.m. at different SBB-PI time lags τ. Streams have two attributes: parallel or antiparallel, positive or negative.

	Parallel+	Parallel−	Antipar+	Antipar−	Parallel+	Parallel−	Antipar+	Antipar−
		Lag $\tau = 0$				Lag $\tau = 1$		
SHR 3	213.16 ± 34.27	227.33 ± 28.67	70.33 ± 18.98	67 ± 21.11	74.16 ± 24.88	62.83 ± 22.12	276.66 ± 50	356.16 ± 62.89
SHR 12	268.33 ± 43.27	241.16 ± 40.46	86.66 ± 19.66	79.15 ± 12.81	120 ± 23.87	112 ± 13.55	157 ± 30.79	211.66 ± 34.06
WIS 3	268.833 ± 25.44	277.83 ± 24.96	62.5 ± 6.42	74.5 ± 5.89	63.66 ± 7.16	54.3 ± 6.95	238 ± 33.78	289.333 ± 24.02
WIS 12	288.66 ± 87.92	286.33 ± 86.19	57 ± 15/3	70 ± 12.8	59.33 ± 13.98	61.666 ± 8.3	245.66 ± 48.85	302.833 ± 30.35
		Lag $\tau = 2$				Lag $\tau = 3$		
SHR 3	121.5 ± 12.59	129.5 ± 12	130.83 ± 14.35	136.16 ± 15.46	306.66 ± 42.42	233 ± 25.9	76.16 ± 19,97	108.33 ± 20.17
SHR 12	109.83 ± 3.42	121.66 ± 6.24	156 ± 13.1	165.83 ± 4.27	211.16 ± 28.07	176 ± 25.77	121.16 ± 9,06	135.33 ± 10.21
WIS 3	155 ± 15.08	169.166 ± 18,99	122.33 ± 10.97	131.5 ± 11.72	212.16 ± 18.19	181.33 ± 16.05	101.5 ± 14.42	140.83 ± 12.46
WIS 12	111.5 ± 18.21	96.333 ± 26.86	156 ± 25.35	172.66 ± 24.28	275.66 ± 72.40	227.333 ± 74.06	88 ± 17.14	112.66 ± 25.24
		Lag $\tau = 4$				Lag $\tau = 5$		
SHR 3	144.16 ± 15.09	131.33 ± 13.12	159.16 ± 16.73	155.16 ± 10.89	98 ± 22.63	100.16 ± 20.30	195.83 ± 23.51	236.16 ± 26.38
SHR 12	170.83 ± 19,82	155.33 ± 10.88	119.83 ± 2.85	132.16 ± 4.222	141.5 ± 15,12	134.5 ± 6.13	145.833 ± 15.89	174.33 ± 18,49
WIS 3	191.66 ± 11.68	175.333 ± 5.85	126.83 ± 19.91	152.333 ± 13.60	119.5 ± 15.18	127.16 ± 21.23	151.166 ± 12.22	193.83 ± 13.95
WIS 12	187.33 ± 32,59	164 ± 23.96	137.5 ± 59.07	150.66 ± 53.56	131.5 ± 20.76	121.833 ± 17.64	153.16 ± 22	195.5 ± 30.81

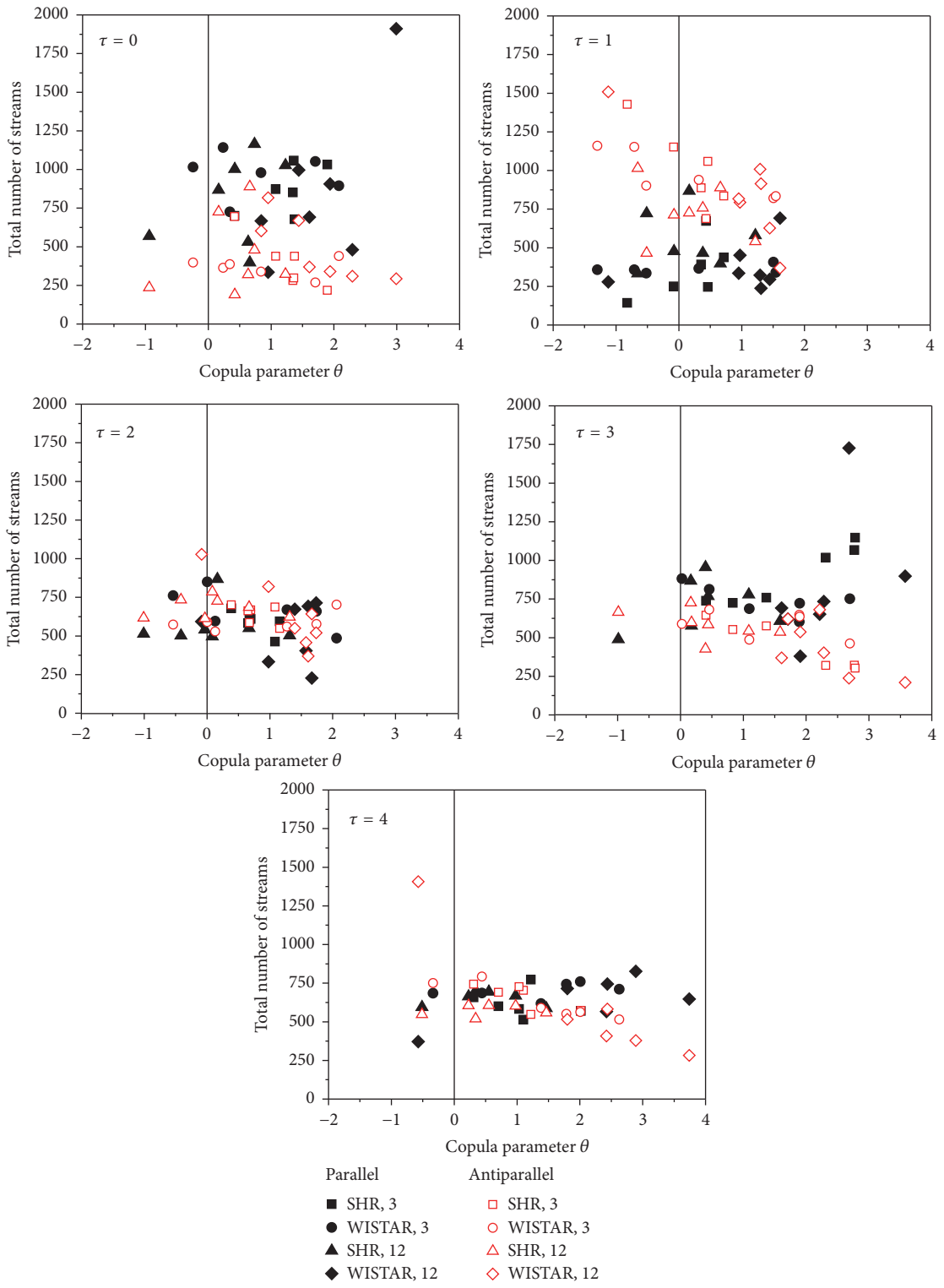

FIGURE 12: Number of parallel streams (black) and antiparallel streams (red) plotted against the copula parameter θ. Each point is estimated from 4000 SBP-PI signal samples.

of streams has not shown statistically significant difference among the experimental groups but did show the difference at different time lags. When the copula parameter is related to the number of streams for each rat separately, it turned out that the same number of parallel and antiparallel streams produced positive dependency in one rat and negative dependency in another rat for the same time lag. It shows that the dependency that copula reveals is more complex to be

explained by mere occurrences of parallel and antiparallel SBP-PI streams. This conclusion is also confirmed with decreased dynamic range of copula parameter: it was considerably attenuated in hypertensive rat with an increased age, although no significant change in number of streams is observed.

Conditional entropy is a measure applicable to the binary data, important for applications in wearable battery-operated devices (crowdsensing, self-monitoring), where saving the processor power and increased computing efficiency are the ultimate goal. Although the binary coding is extremely coarse, conditional entropy can observe the changes in sample dependency. The sensitivity is slightly reduced, due to the reduced number of amplitude levels of the observed signals. Conditional and unconditional entropy of PI signals in young healthy Wistar rats are equal, revealing the sample independence. As the age increases, the PI signals exhibit more order (inputs are attenuated) and more mutual dependency so the entropy slightly decreases. Surprisingly, hypertensive rats showed just opposite results: conditional and unconditional entropies were equal in aging rats, while young ones had a slight increase of statistical dependency. Conditional entropy of SBP signals shows a considerable discrepancy with respect to unconditional counterparts that diminishes at time lag $\alpha = 12$ in hypertensive young rats and at time lag $\alpha = 10$ in all the other groups. Simultaneous observation of entropy changes in τ-α plane is not recommended, as the artifacts due to the signal overlap occur. The level of conditional entropy at time lag $\alpha = 1$ (adjacent symbols) is reduced by a theoretical value of 8.17%, induced by the constraints of differential coding. This applies if the raw data are random and statistically independent, and this also applies to PI signals, to their isospectral surrogates, and to isodistributional surrogates of all the signals. SBP signals, however, preserve the equality of conditional and unconditional entropy in spite of dependency induced by differential coding. Seemingly, the regulatory mechanisms of systolic blood pressure are so firm and manage to oppose coding-induced dependency.

Dynamic tracing the dependency parameters shows that, occasionally, SBP and PI signals may become unconnected. A future task would include quantification of these occurrences and mode of their exploitation. Another goal of the future research would be to include multivariable time series (respiratory rate, such as in [49], or temperature), since the copula method allows creation of dependency structures among multidimensional signals.

Appendix

The purpose of this appendix is to derive an exact amount of conditional entropy loss if a random and statistically independent signal is submitted to the binary differential coding.

The probability that the adjacent binary differentially coded samples would be both equal to zero is equal to

$$\begin{aligned} P\left(xB_i = 1, xB_{i+1} = 1\right) &= P\left(xD_i < 0, xD_{i+1} < 0\right) \\ &= P\left(x_{i+1} - x_i < 0, x_{i+2} - x_{i+1} < 0\right). \end{aligned} \tag{A.1}$$

The notation is taken from (5), (6), and (7).

If x_i are independent and identically distributed random variables (i.i.d. RVs) with probability distribution function $f(x_i)$, then the probability (A.1) can be obtained as follows:

$$\begin{aligned} &P\left(xB_i = 1, xB_{i+1} = 1\right) \\ &\quad = E\left\{P\left(x_{i+1} < x_i, x_{i+2} < x_{i+1}\right)\right\} \\ &\quad = E\left\{P\left(x_{i+1} < x_i\right) \cdot \left(x_{i+2} < x_{i+1}\right)\right\} \\ &\quad = E\left\{\left(\int_{-\infty}^{x_{i+1}} f\left(x_{i+2}\right) \cdot \mathrm{d}x_{i+2}\right)\right. \\ &\quad \left.\cdot \left(\int_{x_{i+1}}^{\infty} f\left(x_i\right) \cdot \mathrm{d}x_i\right)\right\} = \int_{-\infty}^{\infty} f\left(x_{i+1}\right) \\ &\quad \cdot \left(\left(\int_{-\infty}^{x_{i+1}} f\left(x_{i+2}\right) \cdot \mathrm{d}x_{i+2}\right) \cdot \left(\int_{x_{i+1}}^{\infty} f\left(x_i\right) \cdot \mathrm{d}x_i\right)\right) \\ &\quad \cdot \mathrm{d}x_{i+1}. \end{aligned} \tag{A.2}$$

Similarly,

$$\begin{aligned} &P\left(xB_i = 0, xB_{i+1} = 0\right) = \int_{-\infty}^{\infty} f\left(x_{i+1}\right) \\ &\quad \cdot \left(\left(\int_{x_{i+1}}^{\infty} f\left(x_{i+2}\right) \cdot \mathrm{d}x_{i+2}\right) \cdot \left(\int_{-\infty}^{x_{i+1}} f\left(x_i\right) \cdot \mathrm{d}x_i\right)\right) \\ &\quad \cdot \mathrm{d}x_{i+1}, \\ &P\left(xB_i = 0, xB_{i+1} = 1\right) = \int_{-\infty}^{\infty} f\left(x_{i+1}\right) \\ &\quad \cdot \left(\left(\int_{-\infty}^{x_{i+1}} f\left(x_{i+2}\right) \cdot \mathrm{d}x_{i+2}\right) \cdot \left(\int_{-\infty}^{x_{i+1}} f\left(x_i\right) \cdot \mathrm{d}x_i\right)\right) \\ &\quad \cdot \mathrm{d}x_{i+1}, \\ &P\left(xB_i = 1, xB_{i+1} = 0\right) = \int_{-\infty}^{\infty} f\left(x_{i+1}\right) \\ &\quad \cdot \left(\left(\int_{x_{i+1}}^{\infty} f\left(x_{i+2}\right) \cdot \mathrm{d}x_{i+2}\right) \cdot \left(\int_{x_{i+1}}^{\infty} f\left(x_i\right) \cdot \mathrm{d}x_i\right)\right) \\ &\quad \cdot \mathrm{d}x_{i+1}, \\ &P\left(xB_i = 0\right) = \int_{-\infty}^{\infty} f\left(x_{i+1}\right) \cdot \left(\int_{-\infty}^{x_{i+1}} f\left(x_i\right) \cdot \mathrm{d}x_i\right) \\ &\quad \cdot \mathrm{d}x_{i+1}, \\ &P\left(xB_i = 1\right) = \int_{-\infty}^{\infty} f\left(x_{i+1}\right) \cdot \left(\int_{x_{i+1}}^{\infty} f\left(x_i\right) \cdot \mathrm{d}x_i\right) \\ &\quad \cdot \mathrm{d}x_{i+1}. \end{aligned} \tag{A.3}$$

For i.i.d. RVs with uniform probability density function $f(x) = 1/a$, $0 \le x \le a$, and $f(x) = 0$ elsewhere, the probabilities defined with (A.3) are equal to $P(00) = P(11) = 1/3$, $P(10) = P(01) = 1/6$, and $P(0) = P(1) = 0.5$. Conditional probabilities that follow are $P(0 \mid 0) = P(1 \mid 1) = 2/3$ and $P(1 \mid 0) = P(0 \mid 1) = 1/3$. All four conditional probabilities

in statistically independent data are equal to 0.5. Implementing (7), lower part, entropy values (conditional and unconditional) are 0.27643 and 0.30103, while their relative measure is 91.92968, perfectly in accordance with the values estimated from randomized signal (isodistributional surrogate data). This conclusion is general, since it was proven [30] that the differentially coded samples of i.i.d. RVs (including the isodistributional surrogates) statistically follow the same distribution.

Competing Interests

The authors declare that there is no conflict of interests regarding the publication of this paper.

Acknowledgments

The authors are grateful to Professor Dr. Harald Straus, University of Iowa, and to Professor Dr. Suave Lobodzinski, UCLA, for the inspiring discussion during and after Neurocard 2016. This work was supported by the Serbian Ministry of Education, Science and Technology Development, under Grants TR32040 and III41013. The paper is an outcome of EU COST Action CA15104-Body Communications group.

References

[1] W. W. Holbein, J. K. Limberg, N. Covassin, M. J. Joyner, and V. K. Somers, "Experimental sleep restriction blunts baroreflex sensitivity in healthy individuals," *Autonomic Neuroscience*, vol. 192, p. 109, 2015.

[2] M. J. Goldberg, S. H. Boutcher, and Y. N. Boutcher, "The effect of 4 weeks of aerobic exercise on vascular and baroreflex function of young men with a family history of hypertension," *Journal of Human Hypertension*, vol. 26, no. 11, pp. 644–649, 2012.

[3] D. Bajic, T. Loncar-Turukalo, and S. Stojicic, "Temporal analysis of the spontaneous baroreceptor reflex during mild emotional stress in the rat," *Stress*, vol. 13, no. 2, pp. 142–154, 2010.

[4] G. Nollo, A. Porta, L. Faes, M. Del Greco, M. Disertori, and F. Ravelli, "Causal linear parametric model for baroreflex gain assessment in patients with recent myocardial infarction," *American Journal of Physiology—Heart and Circulatory Physiology*, vol. 280, no. 4, pp. H1830–H1839, 2001.

[5] O. Ormezzano, J. L. Cracowski, and H. Quesada, "Evaluation of the prognostic value of baroreflex sensitivity in hypertensive patients: the EUROBAVAR study," *Journal of Hypertension*, vol. 26, no. 7, pp. 1373–1378, 2008.

[6] M. Javorka, Z. Lazarova, I. Tonhajzerova et al., "Baroreflex analysis in diabetes mellitus: linear and nonlinear approaches," *Medical & Biological Engineering & Computing*, vol. 49, no. 3, pp. 279–288, 2011.

[7] T. Turukalo, N. Japundzic-Zigon, and D. Bajić, "BP and HRV interactions: spontaneous baroreflex sensitivity assessment," in *Engineering and Medicine*, H. Jelinek, A. Khandoker, and D. Cornforth, Eds., ECG Time Series Variability Analysis, chapter 9, CRC Press, Boca Raton, Fla, USA, 2016.

[8] D. Laude, V. Baudrie, and J.-L. Elghozi, "Tuning of the sequence technique," *IEEE Engineering in Medicine and Biology Magazine*, vol. 28, no. 6, pp. 30–34, 2009.

[9] B. E. Westerhof, J. Gisolf, W. J. Stok, K. H. Wesseling, and J. M. Karemaker, "Time-domain cross-correlation baroreflex sensitivity: performance on the EUROBAVAR data set," *Journal of Hypertension*, vol. 22, no. 7, pp. 1371–1380, 2004.

[10] H. W. J. Robbe, L. J. M. Mulder, H. Rüddel, W. A. Langewitz, J. B. P. Veldman, and G. Mulder, "Assessment of baroreceptor reflex sensitivity by means of spectral analysis," *Hypertension*, vol. 10, no. 5, pp. 538–543, 1987.

[11] M. T. La Rovere, G. D. Pinna, and G. Raczak, "Baroreflex sensitivity: measurement and clinical implications," *Annals of Noninvasive Electrocardiology*, vol. 13, no. 2, pp. 191–207, 2008.

[12] R. Barbieri, E. C. Matten, A. A. Alabi, and E. N. Brown, "A point-process model of human heartbeat intervals: new definitions of heart rate and heart rate variability," *American Journal of Physiology—Heart and Circulatory Physiology*, vol. 288, no. 1, pp. H424–H435, 2005.

[13] G. Baselli, S. Cerutti, S. Civardi, A. Malliani, and M. Pagani, "Cardiovascular variability signals: towards the identification of a closed-loop model of the neural control mechanisms," *IEEE Transactions on Biomedical Engineering*, vol. 35, no. 12, pp. 1033–1046, 1988.

[14] A. Porta, P. Castiglioni, M. Di Rienzo et al., "Information domain analysis of the spontaneous baroreflex during pharmacological challenges," *Autonomic Neuroscience: Basic and Clinical*, vol. 178, no. 1-2, pp. 67–75, 2013.

[15] A. Porta, S. Guzzetti, N. Montano et al., "Information domain analysis of cardiovascular variability signals: evaluation of regularity, synchronisation and co-ordination," *Medical and Biological Engineering and Computing*, vol. 38, no. 2, pp. 180–188, 2000.

[16] A. Voss, S. Schulz, R. Schroeder, M. Baumert, and P. Caminal, "Methods derived from nonlinear dynamics for analysing heart rate variability," *Philosophical Transactions of the Royal Society*, vol. 367, no. 1887, pp. 277–296, 2009.

[17] D. Laude, J.-L. Elghozi, A. Girard et al., "Comparison of various techniques used to estimate spontaneous baroreflex sensitivity (the EuroBaVar study)," *American Journal of Physiology—Regulatory Integrative and Comparative Physiology*, vol. 286, no. 1, pp. R226–R231, 2004.

[18] A. Porta, R. Furlan, O. Rimoldi, M. Pagani, A. Malliani, and P. van de Borne, "Quantifying the strength of the linear causal coupling in closed loop interacting cardiovascular variability signals," *Biological Cybernetics*, vol. 86, no. 3, pp. 241–251, 2002.

[19] D. Laude, V. Baudrie, and J.-L. Elghozi, "Applicability of recent methods used to estimate spontaneous baroreflex sensitivity to resting mice," *American Journal of Physiology—Regulatory Integrative and Comparative Physiology*, vol. 294, no. 1, pp. R142–R150, 2008.

[20] G. Parati, J. P. Saul, and P. Castiglioni, "Assessing arterial baroreflex control of heart rate: new perspectives," *Journal of Hypertension*, vol. 22, no. 7, pp. 1259–1263, 2004.

[21] A. Cividjian, E. Toader, K. H. Wesseling, J. M. Karemaker, R. McAllen, and L. Quintin, "Effect of clonidine on cardiac baroreflex delay in humans and rats," *American Journal of Physiology—Regulatory Integrative and Comparative Physiology*, vol. 300, no. 4, pp. R949–R957, 2011.

[22] J. Alvarez-Ramirez, E. Rodriguez, and J. C. Echeverría, "Delays in the human heartbeat dynamics," *Chaos*, vol. 19, no. 2, 2009.

[23] G. Gulli, V. E. Claydon, V. L. Cooper, and R. Hainsworth, "R–R interval–blood pressure interaction in subjects with different tolerances to orthostatic stress," *Experimental Physiology*, vol. 90, no. 3, pp. 367–375, 2005.

[24] M. Di Rienzo, G. Parati, P. Castiglioni, R. Tordi, G. Mancia, and A. Pedotti, "Baroreflex effectiveness index: an additional measure of baroreflex control of heart rate in daily life," *American Journal of Physiology—Regulatory Integrative and Comparative Physiology*, vol. 280, no. 3, pp. R744–R751, 2001.

[25] J. Oosting, H. A. J. Struijker-Boudier, and B. J. A. Janssen, "Validation of a continuous baroreceptor reflex sensitivity index calculated from spontaneous fluctuations of blood pressure and pulse interval in rats," *Journal of Hypertension*, vol. 15, no. 4, pp. 391–399, 1997.

[26] D. Laude, J.-L. Elghozi, A. Girard et al., "Comparison of various techniques used to estimate spontaneous baroreflex sensitivity (the EuroBaVar Study)," *American Journal of Physiology—Regulatory Integrative and Comparative Physiology*, vol. 286, no. 1, pp. R226–R231, 2004.

[27] G. Bertinieri, M. di Rienzo, A. Cavalazzi, A. U. Ferrari, A. Pedotti, and G. Mancia, "Evaluation of baroreceptor reflex by blood pressure monitoring in anaesthetized cats," *American Journal of Physiology*, vol. 254, no. 2, part 2, pp. H377–H383, 1988.

[28] A. P. Blaber, Y. Yamamoto, and R. L. Hughson, "Methodology of spontaneous baroreflex relationship assessed by surrogate data analysis," *American Journal of Physiology—Heart and Circulatory Physiology*, vol. 268, no. 4, pp. H1682–H1687, 1995.

[29] G. Baselli, S. Cerutti, F. Badilini et al., "Model for the assessment of heart period and arterial pressure variability interactions and of respiration influences," *Medical & Biological Engineering & Computing*, vol. 32, no. 2, pp. 143–152, 1994.

[30] T. L. Turukalo, D. Bajic, and N. J. Zigon, "Temporal sequence parameters in isodistributional surrogate data: model and exact expressions," *IEEE Transactions on Biomedical Engineering*, vol. 58, no. 1, pp. 16–24, 2011.

[31] S. Jovanovic, T. Skoric, O. Sarenac, S. Milutinovic-Smiljanic, N. Japundzic-Zigon, and D. Bajic, "Applying copula as a dynamic SBP-PI dependency measure," *Proceedings of NEUROCARD*, vol. 8, no. 1, pp. 34–37, 2016.

[32] S. Chessa, A. Corradi, L. Foschini, and M. Girolami, "Empowering mobile crowdsensing through social and ad hoc networking," *IEEE Communications Magazine*, vol. 54, no. 7, pp. 108–114, 2016.

[33] M. Brennan, M. Palaniswami, and P. Kamen, "Do existing measures of Poincaré plot geometry reflect nonlinear features of heart rate variability?" *IEEE Transactions on Biomedical Engineering*, vol. 48, no. 11, pp. 1342–1347, 2001.

[34] S. M. Pincus, "Approximate entropy as a measure of system complexity," *Proceedings of the National Academy of Sciences of the United States of America*, vol. 88, no. 6, pp. 2297–2301, 1991.

[35] L. Faes, G. D. Pinna, A. Porta, R. Maestri, and G. Nollo, "Surrogate data analysis for assessing the significance of the coherence function," *IEEE Transactions on Biomedical Engineering*, vol. 51, no. 7, pp. 1156–1166, 2004.

[36] J. G. Proakis and M. Salehi, *Fundamentals of Communication Systems*, Pearson, 2nd edition, 2013.

[37] A. Sklar, *Fonctions de Repartition a n Dimensions et Leursmarges*, vol. 8, Publications de l'Institut de Statistique de l'Université de Paris, Paris, France, 1959.

[38] R. Bansal, X. J. Hao, J. Liu, and B. S. Peterson, "Using Copula distributions to support more accurate imaging-based diagnostic classifiers for neuropsychiatric disorders," *Magnetic Resonance Imaging*, vol. 32, no. 9, pp. 1102–1113, 2014.

[39] P. Kumar and M. M. Shoukri, "Copula based prediction models: an application to an aortic regurgitation study," *BMC Medical Research Methodology*, vol. 7, article 21, 9 pages, 2007.

[40] M. Han and X. Liu, "Feature selection techniques with class separability for multivariate time series," *Neurocomputing*, vol. 110, pp. 29–34, 2013.

[41] D. Bajic, T. Loncar-Turukalo, T. Skoric, and N. Japundzic-Zigon, "Blood pressure and pulse interval coupling: a copula approach," in *Proceedings of the 37th Annual International Conference of the IEEE Engineering in Medicine and Biology Society (EMBC '15)*, pp. 7696–7699, Milan, Italy, August 2015.

[42] H. Joe, *Multivariate models and dependence concepts*, vol. 73 of *Monographs on Statistics and Applied Probability*, Chapman & Hall, London, UK, 1997.

[43] P. Jaworski, F. Durante, W. Härdle, and T. Rychlik, "Copula theory and its applications," in *Proceedings of the Workshop Held in Warsaw*, Lecture Notes in Statistics, pp. 25–26, Springer, Warsaw, Poland, September 2009.

[44] P. Embrechts and M. Hofert, "A note on generalized inverses," *Mathematical Methods of Operations Research*, vol. 77, no. 3, pp. 423–432, 2013.

[45] M. P. Tarvainen, P. O. Ranta-Aho, and P. A. Karjalainen, "An advanced detrending method with application to HRV analysis," *IEEE Transactions on Biomedical Engineering*, vol. 49, no. 2, pp. 172–175, 2002.

[46] M. Baumert, V. Baier, S. Truebner, A. Schirdewan, and A. Voss, "Short- and long-term joint symbolic dynamics of heart rate and blood pressure in dilated cardiomyopathy," *IEEE Transactions on Biomedical Engineering*, vol. 52, no. 12, pp. 2112–2115, 2005.

[47] A. Porta, A. Marchi, V. Bari et al., "Conditional symbolic analysis detects nonlinear influences of respiration on cardiovascular control in humans," *Philosophical Transactions of the Royal Society of London A: Mathematical, Physical and Engineering*, vol. 373, no. 2034, 2014.

[48] O. Mohamoud, T. Loncar-Turukalo, O. Sarenac, N. Japundzic-Zigon, and D. Bajic, "On symbol entropy of joint time series," in *Proceedings of the 7th European Study Group on Cardiovascular Oscilations*, Kazimierz Dolny, Poland, 2012.

[49] A. Porta, T. Bassani, V. Bari, G. D. Pinna, R. Maestri, and S. Guzzetti, "Accounting for respiration is necessary to reliably infer granger causality from cardiovascular variability series," *IEEE Transactions on Biomedical Engineering*, vol. 59, no. 3, pp. 832–841, 2012.

Hindawi
Computational and Mathematical Methods in Medicine
Volume 2017, Article ID 8272091, 11 pages
http://dx.doi.org/10.1155/2017/8272091

Research Article

A Hybrid Classification System for Heart Disease Diagnosis Based on the RFRS Method

Xiao Liu,[1] Xiaoli Wang,[1] Qiang Su,[1] Mo Zhang,[2] Yanhong Zhu,[3] Qiugen Wang,[4] and Qian Wang[4]

[1]*School of Economics and Management, Tongji University, Shanghai, China*
[2]*School of Economics and Management, Shanghai Maritime University, Shanghai, China*
[3]*Department of Scientific Research, Shanghai General Hospital, School of Medicine, Shanghai Jiaotong University, Shanghai, China*
[4]*Trauma Center, Shanghai General Hospital, School of Medicine, Shanghai Jiaotong University, Shanghai, China*

Correspondence should be addressed to Xiaoli Wang; xiaoli-wang@tongji.edu.cn

Received 19 March 2016; Revised 12 July 2016; Accepted 1 August 2016; Published 3 January 2017

Academic Editor: Xiaopeng Zhao

Heart disease is one of the most common diseases in the world. The objective of this study is to aid the diagnosis of heart disease using a hybrid classification system based on the ReliefF and Rough Set (RFRS) method. The proposed system contains two subsystems: the RFRS feature selection system and a classification system with an ensemble classifier. The first system includes three stages: (i) data discretization, (ii) feature extraction using the ReliefF algorithm, and (iii) feature reduction using the heuristic Rough Set reduction algorithm that we developed. In the second system, an ensemble classifier is proposed based on the C4.5 classifier. The Statlog (Heart) dataset, obtained from the UCI database, was used for experiments. A maximum classification accuracy of 92.59% was achieved according to a jackknife cross-validation scheme. The results demonstrate that the performance of the proposed system is superior to the performances of previously reported classification techniques.

1. Introduction

Cardiovascular disease (CVD) is a primary cause of death. An estimated 17.5 million people died from CVD in 2012, representing 31% of all global deaths (http://www.who.int/mediacentre/factsheets/fs317/en/). In the United States, heart disease kills one person every 34 seconds [1].

Numerous factors are involved in the diagnosis of heart disease, which complicates a physician's task. To help physicians make quick decisions and minimize errors in diagnosis, classification systems enable physicians to rapidly examine medical data in considerable detail [2]. These systems are implemented by developing a model that can classify existing records using sample data. Various classification algorithms have been developed and used as classifiers to assist doctors in diagnosing heart disease patients.

The performances obtained using the Statlog (Heart) dataset [3] from the UCI machine learning database are compared in this context. Lee [4] proposed a novel supervised feature selection method based on the bounded sum of weighted fuzzy membership functions (BSWFM) and Euclidean distances and obtained an accuracy of 87.4%. Tomar and Agarwal [5] used the F-score feature selection method and the Least Square Twin Support Vector Machine (LSTSVM) to diagnose heart diseases, obtaining an average classification accuracy of 85.59%. Buscema et al. [6] used the Training with Input Selection and Testing (TWIST) algorithm to classify patterns, obtaining an accuracy of 84.14%. The Extreme Learning Machine (ELM) has also been used as a classifier, obtaining a reported classification accuracy of 87.5% [7]. The genetic algorithm with the Naïve Bayes classifier has been shown to have a classification accuracy of 85.87% [8]. Srinivas et al. [9] obtained an 83.70% classification accuracy using Naïve Bayes. Polat and Güneş [10] used the RBF kernel F-score feature selection method to detect heart disease. The LS-SVM classifier was used, obtaining a classification accuracy of 83.70%. In [11], the GA-AWAIS method was used for heart disease detection, with

a classification accuracy of 87.43%. The Algebraic Sigmoid Method has also been proposed to classify heart disease, with a reported accuracy of 85.24% [12]. Wang et al. [13] used linear kernel SVM classifiers for heart disease detection and obtained an accuracy of 83.37%. In [14], three distance criteria were applied in simple AIS, and the accuracy obtained on the Statlog (Heart) dataset was 83.95%. In [15], a hybrid neural network method was proposed, and the reported accuracy was 86.8%. Yan et al. [16] achieved an 83.75% classification accuracy using ICA and SVM classifiers. Şahan et al. [17] proposed a new artificial immune system named the Attribute Weighted Artificial Immune System (AWAIS) and obtained an accuracy of 82.59% using the k-fold cross-validation method. In [18], the k-NN, k-NN with Manhattan, feature space mapping (FSM), and separability split value (SSV) algorithms were used for heart disease detection, and the highest classification accuracy (85.6%) was obtained by k-NN.

From these works, it can be observed that feature selection methods can effectively increase the performance of single classifier algorithms in diagnosing heart disease [19]. Noisy features and dependency relationships in the heart disease dataset can influence the diagnosis process. Typically, there are numerous records of accompanied syndromes in the original datasets as well as a large number of redundant symptoms. Consequently, it is necessary to reduce the dimensions of the original feature set by a feature selection method that can remove the irrelevant and redundant features.

ReliefF is one of the most popular and successful feature estimation algorithms. It can accurately estimate the quality of features with strong dependencies and is not affected by their relations [20]. There are two advantages to using the ReliefF algorithm: (i) it follows the filter approach and does not employ domain specific knowledge to set feature weights [21, 22], and (ii) it is a feature weighting (FW) engineering technique. ReliefF assigns a weight to each feature that represents the usefulness of that feature for distinguishing pattern classes. First, the weight vector can be used to improve the performance of the lazy algorithms [21]. Furthermore, the weight vector can also be used as a method for ranking features to guide the search for the best subset of features [22–26]. The ReliefF algorithm has proved its usefulness in FS [20, 23], feature ranking [27], and building tree-based models [22], with an association rules-based classifier [28], in improving the efficiencies of the genetic algorithms [29] and with lazy classifiers [21].

ReliefF has excellent performance in both supervised and unsupervised learning. However, it does not help identify redundant features [30–32]. ReliefF algorithm estimates the quality of each feature according to its weight. When most of the given features are relevant to the concept, this algorithm will select most of them even though only some fraction is necessary for concept description [32]. Furthermore, the ReliefF algorithm does not attempt to determine the useful subsets of these weakly relevant features [33].

Redundant features increase dimensionality unnecessarily [34] and adversely affect learning performance when faced with shortage of data. It has also been empirically shown that removing redundant features can result in significant performance improvement [35]. Rough Set (RS) theory is a new mathematical approach to data analysis and data mining that has been applied successfully to many real-life problems in medicine, pharmacology, engineering, banking, financial and market analysis, and others [36]. The RS reduction algorithm can reduce all redundant features of datasets and seek the minimum subset of features to attain a satisfactory classification [37].

There are three advantages to combining ReliefF and RS (RFRS) approach as an integrated feature selection system for heart disease diagnosis.

(i) The RFRS method can remove superfluous and redundant features more effectively. The ReliefF algorithm can select relevant features for disease diagnosis; however, redundant features may still exist in the selected relevant features. In such cases, the RS reduction algorithm can remove remaining redundant features to offset this limitation of the ReliefF algorithm.

(ii) The RFRS method helps to accelerate the RS reduction process and guide the search of the reducts. Finding a minimal reduct of a given information system is an NP-hard problem, as was demonstrated in [38]. The complexity of computing all reducts in an information system is rather high [39]. On one hand, as a data preprocessing tool, the features revealed by the ReliefF method can accelerate the operation process by serving as the input for the RS reduction algorithm. On the other hand, the weight vector obtained by the ReliefF algorithm can act as a heuristic to guide the search for the reducts [25, 26], thus helping to improve the performance of the heuristic algorithm [21].

(iii) The RFRS method can reduce the number and improve the quality of reducts. Usually, more than one reduct exists in the dataset; and larger numbers of features result in larger numbers of reducts [40]. The number of reducts will decrease if superfluous features are removed using the ReliefF algorithm. When unnecessary features are removed, more important features can be extracted, which will also improve the quality of reducts.

It is obvious that the choice of an efficient feature selection method and an excellent classifier is extremely important for the heart disease diagnosis problem [41]. Most of the common classifiers from the machine learning community have been used for heart disease diagnosis. It is now recognized that no single model exists that is superior for all pattern recognition problems, and no single technique is applicable to all problems [42]. One solution to overcome the limitations of a single classifier is to use an ensemble model. An ensemble model is a multiclassifier combination model that results in more precise decisions because the same problem is solved by several different trained classifiers, which reduces the variance of error estimation [43]. In recent years, ensemble learning has been employed to increase classification accuracies beyond the level that can be achieved by individual classifiers [44, 45]. In this paper, we used an ensemble classifier to evaluate the feature selection model.

To improve the efficiency and effectiveness of the classification performance for the diagnosis of heart disease, we propose a hybrid classification system based on the ReliefF and RS (RFRS) approach in handling relevant and redundant

features. The system contains two subsystems: the RFRS feature selection subsystem and a classification subsystem. In the RFRS feature selection subsystem, we use a two-stage hybrid modeling procedure by integrating ReliefF with the RS (RFRS) method. First, the proposed method adopts the ReliefF algorithm to obtain feature weights and select more relevant and important features from heart disease datasets. Then, the feature estimation obtained from the first phase is used as the input for the RS reduction algorithm and guide the initialization of the necessary parameters for the genetic algorithm. We use a GA-based search engine to find satisfactory reducts. In the classification subsystem, the resulting reducts serve as the input for the chosen classifiers. Finally, the optimal reduct and performance can be obtained.

To evaluate the performance of the proposed hybrid method, a confusion matrix, sensitivity, specificity, accuracy, and ROC were used. The experimental results show that the proposed method achieves very promising results using the jack knife test.

The main contributions of this paper are summarized as follows.

(i) We propose a feature selection system to integrate the ReliefF approach with the RS method (RFRS) to detect heart disease in an efficient and effective way. The idea is to use the feature estimation from the ReliefF phase as the input and heuristics for the RS reduction phase.

(ii) In the classification system, we propose an ensemble classifier using C4.5 as the base classifier. Ensemble learning can achieve better performance at the cost of computation than single classifiers. The experimental results show that the ensemble classifier in this paper is superior to three common classifiers.

(iii) Compared with three classifiers and previous studies, the proposed diagnostic system achieved excellent classification results. On the Statlog (Heart) dataset from the UCI machine learning database [3], the resulting classification accuracy was 92.59%, which is higher than that achieved by other studies.

The rest of the paper is organized as follows. Section 2 offers brief background information concerning the ReliefF algorithm and RS theory. The details of the diagnosis system implementation are presented in Section 3. Section 4 describes the experimental results and discusses the proposed method. Finally, conclusions and recommendations for future work are summarized in Section 5.

2. Theoretical Background

2.1. Basic Concepts of Rough Set Theory. Rough Set (RS) theory, which was proposed by Pawlak, in the early 1980s, is a new mathematical approach to addressing vagueness and uncertainty [46]. RS theory has been applied in many domains, including classification system analysis, pattern reorganization, and data mining [47]. RS-based classification algorithms are based on equivalence relations and have been used as classifiers in medical diagnosis [37, 46]. In this paper, we primarily focus on the RS reduction algorithm, which can reduce all redundant features of datasets and seek the minimum subset of features necessary to attain a satisfactory classification [37]. A few basic concepts of RS theory are defined [46, 47] as follows.

Definition 1. U is a certain set that is referred to as the universe; R is an equivalence relation in U. The pair $A = (U, R)$ is referred to as an approximation space.

Definition 2. $P \subset R$, $\cap P$ (the intersection of all equivalence relations in P) is an equivalence relation, which is referred to as the R-indiscernibility relation, and it is represented by $\mathrm{Ind}(R)$.

Definition 3. Let X be a certain subset of U. The least composed set in R that contains X is referred to as the best upper approximation of X in R and represented by $R^{-}(X)$; the greatest composed set in R contained in X is referred to as the best lower approximation of X in R, and it is represented by $R\_(X)$.

$$\begin{aligned} R\_(X) &= \{x \in U : [x]_R \subset X\}, \\ R^{-}(X) &= \{x \in U : [x]_R \cap X \neq \phi\}. \end{aligned} \tag{1}$$

Definition 4. An information system is denoted as

$$S = (U, A, V, F), \tag{2}$$

where U is the universe that consists of a finite set of n objects, $A = \{C \cup D\}$, in which C is a set of condition attributes and D is a set of decision attributes, V is the set of domains of attributes, and F is the information function for each $a \in A$, $x \in U$, $F(x, a) \in V_a$.

Definition 5. In an information system, C and D are sets of attributes in U. $X \in U/\mathrm{ind}(Q)$, and $\mathrm{pos}_p(Q)$, which is referred to as a positive region, is defined as

$$\mathrm{pos}_p(Q) = \cup P\_(X). \tag{3}$$

Definition 6. P and Q are sets of attributes in U, $P, Q \subseteq A$, and the dependency $r_p(Q)$ is defined as

$$r_p(Q) = \frac{\mathrm{card}\left(\mathrm{pos}_p(Q)\right)}{\mathrm{card}(U)}. \tag{4}$$

Card (X) denotes the cardinality of X. $0 \leq r_p(Q) \leq 1$.

Definition 7. P and Q are sets of attributes in U, $P, Q \subseteq A$, and the significance of a_i is defined as

$$\mathrm{sig}(\{a_i\}) = r_p(Q) - r_{p-a_i}(Q). \tag{5}$$

2.2. ReliefF Algorithm. Many feature selection algorithms have been developed; ReliefF is one of the most widely used and effective algorithms [48]. ReliefF is a simple yet efficient procedure for estimating the quality of features in problems with dependencies between features [20]. The pseudocode of ReliefF algorithm is listed in Algorithm 1.

ReliefF algorithm
Input: A decision table $S = (U, P, Q)$
Output: the vector W of estimations of the qualities of features
(1) set all weights $W[A] := 0.0$;
(2) for $i := 1$ to m do begin
(3) randomly select a sample R_i;
(4) find k nearest hits H_j;
(5) for each class $C \neq \text{class}(R_i)$ do
(6) from class C find k nearest misses $M_j(C)$;
(7) for $A := 1$ to a do
(8) $W[A] := W[A] - \sum_{j=1}^{k} \text{diff}(A, R_i, H_j)/mk + \sum_{C \neq \text{class}(R_i)} [P(C)/1 - P(\text{class}(R_i)) \sum_{j=1}^{k} \text{diff}(A, R_i, M_j(C))]/mk$;
(9) end;

Algorithm 1: Pseudocode of ReliefF.

3. Proposed System

3.1. Overview. The proposed hybrid classification system consists of two main components: (i) feature selection using the RFRS subsystem and (ii) data classification using the classification system. A flow chart of the proposed system is shown in Figure 1. We describe the preprocessing and classification systems in the following subsections.

3.2. RFRS Feature Selection Subsystem. We propose a two-phase feature selection method based on the ReliefF algorithm and the RS (RFRS) algorithm. The idea is to use the feature estimation from the ReliefF phase as the input and heuristics for the subsequent RS reduction phase. In the first phase, we adopt the ReliefF algorithm to obtain feature weights and select important features; in the second phase, the feature estimation obtained from the first phase is used to guide the initialization of the parameters required for the genetic algorithm. We use a GA-based search engine to find satisfactory reducts.

The RFRS feature selection subsystem consists of three main modules: (i) data discretization, (ii) feature extraction using the ReliefF algorithm, and (iii) feature reduction using the heuristic RS reduction algorithm we propose.

3.2.1. Data Discretization. RS reduction requires categorical data. Consequently, data discretization is the first step. We used an approximate equal interval binning method to bin the data variables into a small number of categories.

3.2.2. Feature Extraction by the ReliefF Algorithm. Module 2 is used for feature extraction by the ReliefF algorithm. To deal with incomplete data, we change the diff function. Missing feature values are treated probabilistically [20]. We calculate the probability that two given instances have different values for a given feature conditioned over the class value [20]. When one instance has an unknown value, then

$$\text{diff}(A, I_1, I_2) = 1 - P(\text{value}(A, I_2) \mid \text{class}(I_1)). \quad (6)$$

When both instances have unknown values, then

$$\text{diff}(A, I_1, I_2) = 1 - \sum_{V}^{\#\text{values}(A)} (P(V \mid \text{class}(I_1)) \times P(V \mid \text{class}(I_2))). \quad (7)$$

Conditional probabilities are approximated by relative frequencies in the training set. The process of feature extraction is shown as follows.

The Process of Feature Extraction Using ReliefF Algorithm

Input. A decision table $S = (U, P, Q)$, $P = \{a_1, a_2, \ldots, a_m\}$, $Q = \{d_1, d_2, \ldots, d_n\}$ $(m \geq 1, n \geq 1)$.

Output. The selected feature subset $K = \{a_1, a_2, \ldots, a_k\}(1 \leq k \leq m)$.

Step 1. Obtain the weight matrix of each feature using ReliefF algorithm$W = \{w_1, w_2, \ldots, w_i, \ldots, w_m\}$ $(1 \leq i \leq m)$.

Step 2. Set a threshold, δ.

Step 3. If $w_i > \delta$, then feature a_i is selected.

3.2.3. Feature Reduction by the Heuristic RS Reduction Algorithm. The evaluation result obtained by the ReliefF algorithm is the feature rank. A higher ranking means that the feature has stronger distinguishing qualities and a higher weight [30]. Consequently, in the process of reduct searching, the features in the front rank should have a higher probability of being selected.

We proposed the RS reduction algorithm by using the feature estimation as heuristics and a GA-based search engine to search for the satisfactory reducts. The pseudocode of the algorithm is provided in Algorithm 2. The algorithm was implemented in MATLAB R2014a.

3.3. Classification Subsystem. In the classification subsystem, the dataset is split into training sets and corresponding test

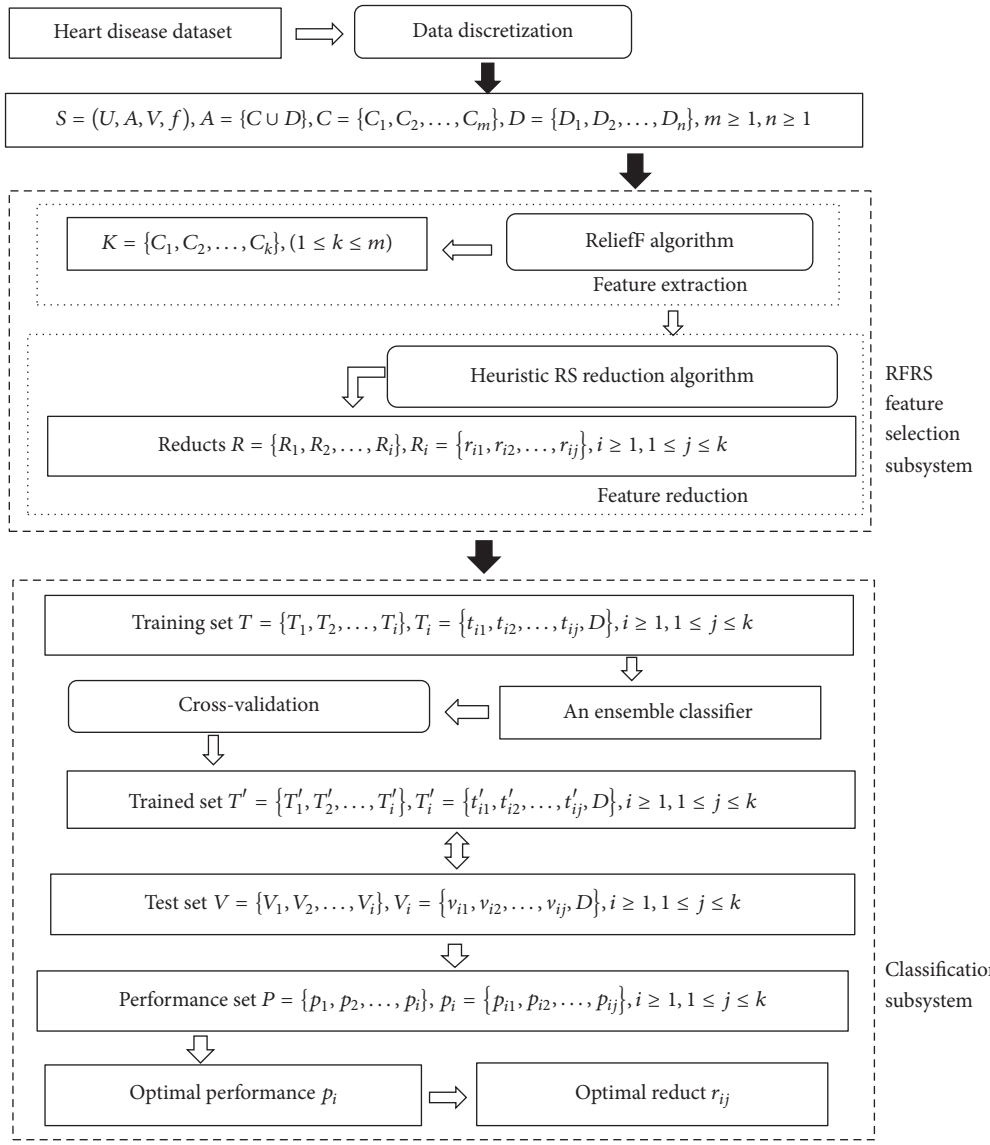

Figure 1: Structure of RFRS-based classification system.

sets. The decision tree is a nonparametric learning algorithm that does not need to search for optimal parameters in the training stage and thus is used as a weak learner for ensemble learning [49]. In this paper, the ensemble classifier uses the C4.5 decision tree as the base classifier. We use the boosting technique to construct ensemble classifiers. Jackknife cross-validation is used to increase the amount of data for testing the results. The optimal reduct is the reduct that obtains the best classification accuracy.

4. Experimental Results

4.1. Dataset. The Statlog (Heart) dataset used in our work was obtained from the UCI machine learning database [3]. This dataset contains 270 observations and 2 classes: the presence and absence of heart disease. The samples include 13 condition features, presented in Table 1. We denote the 13 features as C_1 to C_{13}.

4.2. Performance Evaluation Methods

4.2.1. Confusion Matrix, Sensitivity, Specificity, and Accuracy. A confusion matrix [50] contains information about actual and predicted classifications performed by a classification system. The performance of such systems is commonly evaluated using the data in the matrix. Table 2 shows the confusion matrix for a two-class classifier.

In the confusion matrix, TP is the number of true positives, representing the cases with heart disease that are correctly classified into the heart disease class. FN is the number of false negatives, representing cases with heart disease that

Heuristic RS reduction algorithm
Input: a decision table $S = (U, C, D)$, $C = \{c_1, c_2, \ldots, c_m\}$, $D = \{d_1, d_2, \ldots, d_n\}$
Output: Red
Step 1. Return Core
(1) Core $\leftarrow$ {}
(2) For $i = 1$ to m
(3) Select c_i from C;
(4) Calculate Ind(C), Ind($C - c_i$) and Ind(D);
(5) Calculate $\text{pos}_C(D)$, $\text{pos}_{C-c_i}(D)$ and $r_C(D)$;
(6) Calculate Sig($\{a_i\}$), Sig($\{a_i\}$) $= r_C(D) - r_{C-c_i}(D)$;
(7) If sig($\{c_i\}$) $\neq 0$
(8) core = core $\cup$ $\{c_i\}$;
(9) End if
(10) End for
Step 2. Return Red
(1) Red = Core
(2) $C' = C -$ Red
(3) While Sig(Red, D) $\neq$ Sig(C, D) do
Compute the weight of each feature c in C' using the ReliefF algorithm;
Select a feature c according to its weight, let Red=Red $\cup$ $\{c\}$;
Initialize all the necessary parameters for the GA-based search engine according to the results of the last step and search for satisfactory reducts;
End while

Algorithm 2: Pseudocode of heuristic RS reduction algorithm.

are classified into the healthy class. TN is the number of true negatives, representing healthy cases that are correctly classified into the healthy class. Finally, FP is the number of false positives, representing the healthy cases that are incorrectly classified into the heart disease class [50].

The performance of the proposed system was evaluated based on sensitivity, specificity, and accuracy tests, which use the true positive (TP), true negative (TN), false negative (FN), and false positive (FP) terms [33]. These criteria are calculated as follows [41]:

$$\begin{aligned}
\text{Sensitivity (Sn)} &= \frac{\text{TP}}{\text{TP} + \text{FN}} \times 100\%, \\
\text{Specificity (Sp)} &= \frac{\text{TN}}{\text{FP} + \text{TN}} \times 100\%, \\
\text{Accuracy (Acc)} &= \frac{\text{TP} + \text{TN}}{\text{TP} + \text{TN} + \text{FP} + \text{FN}} \times 100\%.
\end{aligned} \tag{8}$$

4.2.2. Cross-Validation. Three cross-validation methods, namely, subsampling tests, independent dataset tests, and jackknife tests, are often employed to evaluate the predictive capability of a predictor [51]. Among the three methods, the jackknife test is deemed the least arbitrary and the most objective and rigorous [52, 53] because it always yields a unique outcome, as demonstrated by a penetrating analysis in a recent comprehensive review [54, 55]. Therefore, the jackknife test has been widely and increasingly adopted in many areas [56, 57].

Accordingly, the jackknife test was employed to examine the performance of the model proposed in this paper. For jackknife cross-validation, each sequence in the training dataset is, in turn, singled out as an independent test sample and all the parameter rules are calculated based on the remaining samples, without including the one being treated as the test sample.

4.2.3. Receiver Operating Characteristics (ROC). The receiver operating characteristic (ROC) curve is used for analyzing the prediction performance of a predictor [58]. It is usually plotted using the true positive rate versus the false positive rate, as the discrimination threshold of classification algorithm is varied. The area under the ROC curve (AUC) is widely used and relatively accepted in classification studies because it provides a good summary of a classifier's performance [59].

4.3. Results and Discussion

4.3.1. Results and Analysis on the Statlog (Heart) Dataset. First, we used the equal interval binning method to discretize the original data. In the feature extraction module, the number of k-nearest neighbors in the ReliefF algorithm was set to 10, and the threshold, δ, was set to 0.02. Table 3 summarizes the results of the ReliefF algorithm. Based on these results, C_5 and C_6 were removed. In Module 3, we obtained 15 reducts using the heuristic RS reduction algorithm implemented in MATLAB 2014a.

Trials were conducted using 70%–30% training-test partitions, using all the reduced feature sets. Jackknife cross-validation was performed on the dataset. The number of desired base classifiers k was set to 50, 100, and 150. The calculations were run 10 times, and the highest classification

Table 1: Feature information of Statlog (Heart) dataset.

Feature	Code	Description	Domain	Data type	Mean	Standard deviation
Age	C_1	—	29–77	Real	54	9
Sex	C_2	Male, female	0, 1	Binary	—	—
Chest pain type	C_3	Angina, asymptomatic, abnormal	1, 2, 3, 4	Nominal	—	—
Resting blood pressure	C_4	—	94–200	Real	131.344	17.862
Serum cholesterol in mg/dl	C_5	—	126–564	Real	249.659	51.686
Fasting blood sugar > 120 mg/dl	C_6	—	0, 1	Binary	—	—
Resting electrocardiographic results	C_7	Norm, abnormal, hyper	0, 1, 2	Nominal	—	—
Maximum heart rate achieved	C_8	—	71–202	Real	149.678	23.1666
Exercise-induced angina	C_9	—	0, 1	Binary	—	—
Old peak = ST depression induced by exercise relative to rest	C_{10}	—	0–6.2	Real	1.05	1.145
Slope of the peak exercise ST segment	C_{11}	Up, flat, down	1, 2, 3	Ordered	—	—
Number of major vessels (0–3) colored by fluoroscopy	C_{12}	—	0, 1, 2, 3	Real	—	—
Thal	C_{13}	Normal, fixed defect, reversible defect	3, 6, 7	Nominal	—	—

Table 2: The confusion matrix.

	Predicted patients with heart disease	Predicted healthy persons
Actual patients with heart disease	True positive (TP)	False negative (FN)
Actual healthy persons	False positive (FP)	True negative (TN)

performances for each training-test partition are provided in Table 4.

In Table 4, R_2 obtains the best test set classification accuracy (92.59%) using the ensemble classifiers when k = 100. The training process is shown in Figure 2. The training and test ROC curves are shown in Figure 3.

4.3.2. Comparison with Other Classifiers. In this section, our ensemble classification method is compared with the individual C4.5 decision tree and Naïve Bayes and Bayesian Neural Networks (BNN) methods. The C4.5 decision tree and Naïve Bayes are common classifiers. Bayesian Neural Networks (BNN) is a classifier that uses Bayesian regularization to train feed-forward neural networks [60] and has better performance than pure neural networks. The classification accuracy results of the four classifiers are listed in Table 5. The ensemble classification method has better performance than the individual C4.5 classifier and the other two classifiers.

4.3.3. Comparison of the Results with Other Studies. We compared our results with the results of other studies. Table 6 shows the classification accuracies of our study and previous methods.

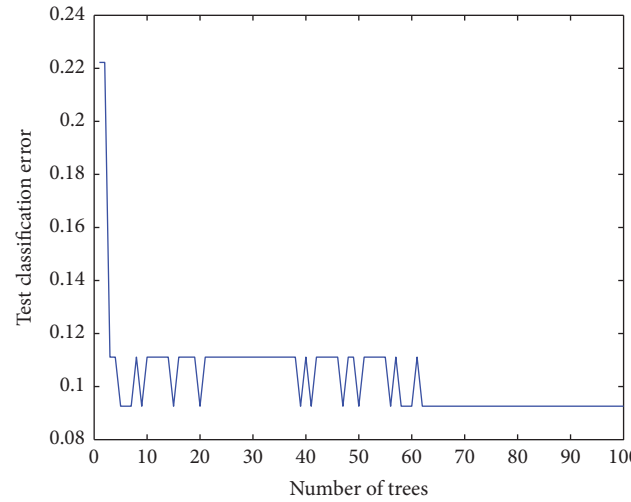

Figure 2: Training process of R_7.

The results show that our proposed method obtains superior and promising results in classifying heart disease patients. We believe that the proposed RFRS-based classification system can be exceedingly beneficial in assisting physicians in making accurate decisions.

Table 3: Results of the ReliefF algorithm.

Feature	C_2	C_{13}	C_7	C_{12}	C_9	C_3	C_{11}	C_{10}	C_8	C_4	C_1	C_6	C_5
Weight	0.172	0.147	0.126	0.122	0.106	0.098	0.057	0.046	0.042	0.032	0.028	0.014	0.011

Table 4: Performance values for different reduced subset.

Code	Reduct	Number	Test classification accuracy (%) Ensemble classifier		
			K	Sn	Sp	ACC
R_1	$C_3, C_4, C_7, C_8, C_{10}, C_{12}, C_{13}$	7	50	83.33	87.5	85.19
			100	83.33	95.83	88.89
			150	86.67	83.33	85.19
R_2	$C_1, C_3, C_7, C_8, C_{11}, C_{12}, C_{13}$	7	50	86.67	91.67	88.89
			100	93.33	87.50	92.59
			150	93.33	87.04	90.74
R_3	$C_1, C_2, C_4, C_7, C_8, C_9, C_{12}$	7	50	86.67	83.33	85.19
			100	93.33	79.17	87.04
			150	80	91.67	85.19
R_4	$C_1, C_4, C_7, C_8, C_{10}, C_{11}, C_{12}, C_{13}$	8	50	86.67	83.33	85.19
			100	93.33	83.33	88.89
			150	86.67	87.5	87.04

Table 5: Classification results using the four classifiers.

Classifiers	Test classification accuracy of R_2 (%)		
	Sn	Sp	Acc
Ensemble classifier (k = 50)	86.67	91.67	88.89
Ensemble classifier (k = 100)	93.33	87.50	92.59
Ensemble classifier (k = 150)	93.33	87.04	90.74
C4.5 tree	93.1	80	87.03
Naïve Bayes	93.75	68.18	83.33
Bayesian Neural Networks (BNN)	93.75	72.72	85.19

5. Conclusions and Future Work

In this paper, a novel ReliefF and Rough Set- (RFRS-) based classification system is proposed for heart disease diagnosis. The main novelty of this paper lies in the proposed approach: the combination of the ReliefF and RS methods to classify heart disease problems in an efficient and fast manner. The RFRS classification system consists of two subsystems: the RFRS feature selection subsystem and the classification subsystem. The Statlog (Heart) dataset from the UCI machine learning database [3] was selected to test the system. The experimental results show that the reduct R_2 (C_1, C_3, C_7, C_8, C_{11}, C_{12}, C_{13}) achieves the highest classification accuracy (92.59%) using an ensemble classifier with the C4.5 decision tree as the weak learner. The results also show that the RFRS method has superior performance compared to three common classifiers in terms of ACC, sensitivity, and specificity. In addition, the performance of the proposed system is superior to that of existing methods in the literature. Based on empirical analysis, the results indicate that the proposed classification system can be used as a promising alternative tool in medical decision making for heart disease diagnosis.

However, the proposed method also has some weaknesses. The number of the nearest neighbors (k) and the weight threshold (θ) are not stable in the ReliefF algorithm [20]. One solution to this problem is to compute estimates for all possible numbers and take the highest estimate of each feature as the final result [20]. We need to perform more experiments to find the optimal parameter values for the ReliefF algorithm in the future.

Table 6: Comparison of our results with those of other studies.

Author	Method	Classification accuracy (%)
Our study	RFRS classification system	92.59
Lee [4]	Graphical characteristics of BSWFM combined with Euclidean distance	87.4
Tomar and Agarwal [5]	Feature selection-based LSTSVM	85.59
Buscema et al. [6]	TWIST algorithm	84.14
Subbulakshmi et al. [7]	ELM	87.5
Karegowda et al. [8]	GA + Naïve Bayes	85.87
Srinivas et al. [9]	Naïve Bayes	83.70
Polat and Güneş [10]	RBF kernel F-score + LS-SVM	83.70
Özşen and Güneş [11]	GA-AWAIS	87.43
Helmy and Rasheed [12]	Algebraic Sigmoid	85.24
Wang et al. [13]	Linear kernel SVM classifiers	83.37
Özşen and Güneş [14]	Hybrid similarity measure	83.95
Kahramanli and Allahverdi [15]	Hybrid neural network method	86.8
Yan et al. [16]	ICA + SVM	83.75
Şahan et al. [17]	AWAIS	82.59
Duch et al. [18]	*K*NN classifier	85.6

BSWFM: bounded sum of weighted fuzzy membership functions; LSTSVM: Least Square Twin Support Vector Machine; TWIST: Training with Input Selection and Testing; ELM: Extreme Learning Machine; GA: genetic algorithm; SVM: support vector machine; ICA: imperialist competitive algorithm; AWAIS: attribute weighted artificial immune system; *K*NN: *k*-nearest neighbor.

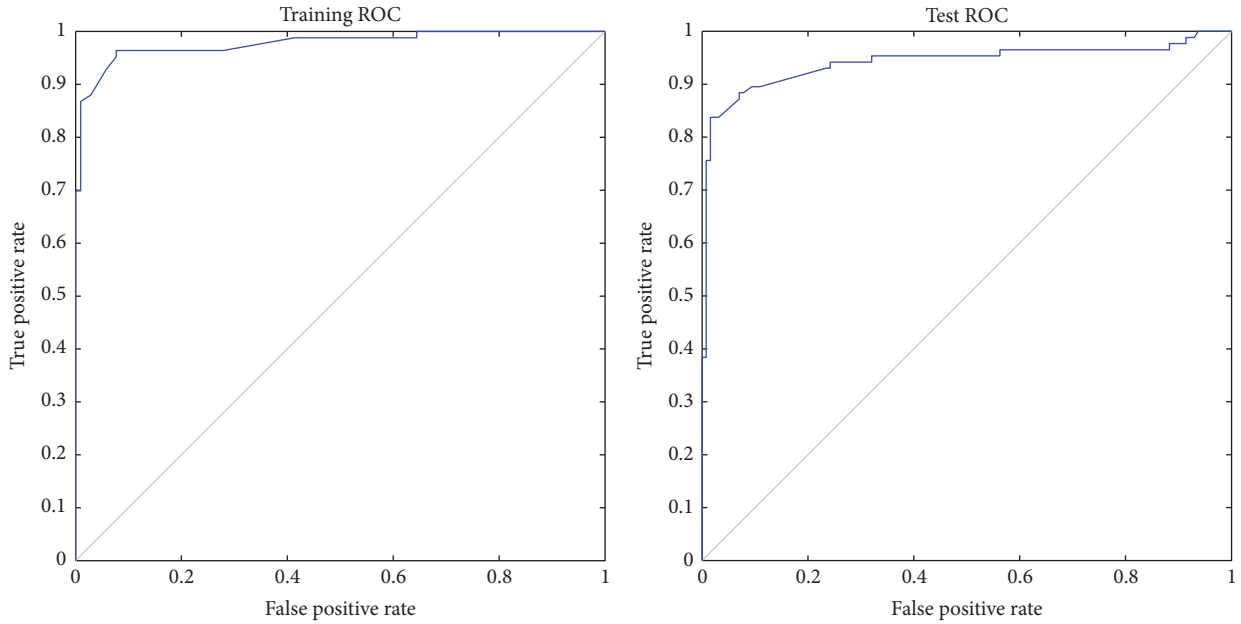

Figure 3: ROC curves for training and test sets.

Competing Interests

The authors declare that there is no conflict of interests regarding the publication of this paper.

Acknowledgments

This study was supported by the National Natural Science Foundation of China (Grant no. 71432007).

References

[1] K. D. Kochanek, J. Xu, S. L. Murphy, A. M. Miniño, and H.-C. Kung, "Deaths: final data for 2009," *National Vital Statistics Reports*, vol. 60, no. 3, pp. 1–116, 2011.

[2] H. Temurtas, N. Yumusak, and F. Temurtas, "A comparative study on diabetes disease diagnosis using neural networks," *Expert Systems with Applications*, vol. 36, no. 4, pp. 8610–8615, 2009.

[3] UCI Repository of Machine Learning Databases, http://archive.ics.uci.edu/ml/datasets/Statlog+%28Heart%29.

[4] S.-H. Lee, "Feature selection based on the center of gravity of BSWFMs using NEWFM," *Engineering Applications of Artificial Intelligence*, vol. 45, pp. 482–487, 2015.

[5] D. Tomar and S. Agarwal, "Feature selection based least square twin support vector machine for diagnosis of heart disease," *International Journal of Bio-Science and Bio-Technology*, vol. 6, no. 2, pp. 69–82, 2014.

[6] M. Buscema, M. Breda, and W. Lodwick, "Training with Input Selection and Testing (TWIST) algorithm: a significant advance in pattern recognition performance of machine learning," *Journal of Intelligent Learning Systems and Applications*, vol. 5, no. 1, pp. 29–38, 2013.

[7] C. V. Subbulakshmi, S. N. Deepa, and N. Malathi, "Extreme learning machine for two category data classification," in *Proceedings of the IEEE International Conference on Advanced Communication Control and Computing Technologies (ICACCCT '12)*, pp. 458–461, Ramanathapuram, India, August 2012.

[8] A. G. Karegowda, A. S. Manjunath, and M. A. Jayaram, "Feature subset selection problem using wrapper approach in supervised learning," *International Journal of Computer Applications*, vol. 1, no. 7, pp. 13–17, 2010.

[9] K. Srinivas, B. K. Rani, and A. Govrdhan, "Applications of data mining techniques in healthcare and prediction of heart attacks," *International Journal on Computer Science and Engineering*, vol. 2, pp. 250–255, 2010.

[10] K. Polat and S. Güneş, "A new feature selection method on classification of medical datasets: kernel F-score feature selection," *Expert Systems with Applications*, vol. 36, no. 7, pp. 10367–10373, 2009.

[11] S. Özşen and S. Güneş, "Attribute weighting via genetic algorithms for attribute weighted artificial immune system (AWAIS) and its application to heart disease and liver disorders problems," *Expert Systems with Applications*, vol. 36, no. 1, pp. 386–392, 2009.

[12] T. Helmy and Z. Rasheed, "Multi-category bioinformatics dataset classification using extreme learning machine," in *Proceedings of the IEEE Congress on Evolutionary Computation (CEC '09)*, pp. 3234–3240, Trondheim, Norway, May 2009.

[13] S.-J. Wang, A. Mathew, Y. Chen, L.-F. Xi, L. Ma, and J. Lee, "Empirical analysis of support vector machine ensemble classifiers," *Expert Systems with Applications*, vol. 36, no. 3, pp. 6466–6476, 2009.

[14] S. Özşen and S. Güneş, "Effect of feature-type in selecting distance measure for an artificial immune system as a pattern recognizer," *Digital Signal Processing*, vol. 18, no. 4, pp. 635–645, 2008.

[15] H. Kahramanli and N. Allahverdi, "Design of a hybrid system for the diabetes and heart diseases," *Expert Systems with Applications*, vol. 35, no. 1-2, pp. 82–89, 2008.

[16] G. Yan, G. Ma, J. Lv, and B. Song, "Combining independent component analysis with support vector machines," in *Proceedings of the in 1st International Symposium on Systems and Control in Aerospace and Astronautics (ISSCAA '06)*, pp. 493–496, Harbin, China, January 2006.

[17] S. Şahan, K. Polat, H. Kodaz, and S. Günes, "The medical applications of attribute weighted artificial immune system (AWAIS): diagnosis of heart and diabetes diseases," *Artificial Immune Systems*, vol. 3627, pp. 456–468, 2005.

[18] W. Duch, R. Adamczak, and K. Grabczewski, "A new methodology of extraction, optimization and application of crisp and fuzzy logical rules," *IEEE Transactions on Neural Networks*, vol. 12, no. 2, pp. 277–306, 2001.

[19] M. P. McRae, B. Bozkurt, C. M. Ballantyne et al., "Cardiac ScoreCard: a diagnostic multivariate index assay system for predicting a spectrum of cardiovascular disease," *Expert Systems with Applications*, vol. 54, pp. 136–147, 2016.

[20] M. Robnik-Šikonja and I. Kononenko, "Theoretical and empirical analysis of ReliefF and RReliefF," *Machine Learning*, vol. 53, no. 1-2, pp. 23–69, 2003.

[21] D. Wettschereck, D. W. Aha, and T. Mohri, "A review and empirical evaluation of feature weighting methods for a class of lazy learning algorithms," *Artificial Intelligence Review*, vol. 11, no. 1–5, pp. 273–314, 1997.

[22] I. Kononenko, E. Šimec, and M. R. Šikonja, "Overcoming the myopia of inductive learning algorithms with RELIEFF," *Applied Intelligence*, vol. 7, no. 1, pp. 39–55, 1997.

[23] K. Kira and L. Rendell, "A practical approach to feature selection," in *Proceedings of the International Conference on Machine Learning*, pp. 249–256, Morgan Kaufmann, Aberdeen, Scotland, 1992.

[24] I. Kononenko, "Estimating attributes: analysis and extension of ReliefF," in *Machine Learning: ECML-94: European Conference on Machine Learning Catania, Italy, April 6–8, 1994 Proceedings*, vol. 784 of *Lecture Notes in Computer Science*, pp. 171–182, Springer, Berlin, Germany, 1994.

[25] R. Ruiz, J. C. Riquelme, and J. S. Aguilar-Ruiz, "Heuristic search over a ranking for feature selection," in *Proceedings of 8th International Work-Conference on Artificial Neural Networks (IWANN '05), Barcelona, Spain, June 2005*, vol. 3512 of *Lectures Notes in Computer Science*, pp. 742–749, Springer, Berlin, Germany, 2005.

[26] N. Spolaôr, E. A. Cherman, M. C. Monard, and H. D. Lee, "Filter approach feature selection methods to support multi-label learning based on ReliefF and information gain," in *Advances in Artificial Intelligence—SBIA 2012: 21th Brazilian Symposium on Artificial Intelligence, Curitiba, Brazil, October 20–25, 2012. Proceedings*, vol. 7589 of *Lectures Notes in Computer Science*, pp. 72–81, Springer, Berlin, Germany, 2012.

[27] R. Ruiz, J. C. Riquelme, and J. S. Aguilar-Ruiz, "Fast feature ranking algorithm," in *Proceedings of the Knowledge-Based Intelligent Information and Engineering Systems (KES '03)*, pp. 325–331, Springer, Berlin, Germany, 2003.

[28] V. Jovanoski and N. Lavrac, "Feature subset selection in association rules learning systems," in *Proceedings of Analysis, Warehousing and Mining the Data*, pp. 74–77, 1999.

[29] J. J. Liu and J. T. Y. Kwok, "An extended genetic rule induction algorithm," in *Proceedings of the Congress on Evolutionary Computation*, pp. 458–463, LA Jolla, Calif, USA, July 2000.

[30] L.-X. Zhang, J.-X. Wang, Y.-N. Zhao, and Z.-H. Yang, "A novel hybrid feature selection algorithm: using ReliefF estimation for GA-Wrapper search," in *Proceedings of the International Conference on Machine Learning and Cybernetics*, vol. 1, pp. 380–384, IEEE, Xi'an, China, November 2003.

[31] Z. Zhao, L. Wang, and H. Liu, "Efficient spectral feature selection with minimum redundancy," in *Proceedings of the 24th AAAI Conference on Artificial Intelligence*, AAAI, Atlanta, Ga, USA, 2010.

[32] F. Nie, H. Huang, X. Cai, and C. H. Ding, "Efficient and robust feature selection via joint $\ell_{2,1}$-norms minimization," in *Advances in Neural Information Processing Systems*, pp. 1813–1821, MIT Press, 2010.

[33] S.-Y. Jiang and L.-X. Wang, "Efficient feature selection based on correlation measure between continuous and discrete features," *Information Processing Letters*, vol. 116, no. 2, pp. 203–215, 2016.

[34] M. J. Kearns and U. V. Vazirani, *An Introduction to Computational Learning Theory*, MIT Press, Cambridge, Mass, USA, 1994.

[35] R. Bellman, *Adaptive Control Processes: A Guided Tour, RAND Corporation Research Studies*, Princeton University Press, Princeton, NJ, USA, 1961.

[36] Z. Pawlak, "Rough set theory and its applications to data analysis," *Cybernetics and Systems*, vol. 29, no. 7, pp. 661–688, 1998.

[37] A.-E. Hassanien, "Rough set approach for attribute reduction and rule generation: a case of patients with suspected breast cancer," *Journal of the American Society for Information Science and Technology*, vol. 55, no. 11, pp. 954–962, 2004.

[38] A. Skowron and C. Rauszer, "The discernibility matrices and functions in information systems," in *Intelligent Decision Support-Handbook of Applications and Advances of the Rough Sets Theory, System Theory, Knowledge Engineering and Problem Solving*, R. Słowinski, Ed., vol. 11, pp. 331–362, Kluwer Academic, Dordrecht, Netherlands, 1992.

[39] Z. Pawlak, "Rough set approach to knowledge-based decision support," *European Journal of Operational Research*, vol. 99, no. 1, pp. 48–57, 1997.

[40] X. Wang, J. Yang, X. Teng, W. Xia, and R. Jensen, "Feature selection based on rough sets and particle swarm optimization," *Pattern Recognition Letters*, vol. 28, no. 4, pp. 459–471, 2007.

[41] C. Ma, J. Ouyang, H.-L. Chen, and X.-H. Zhao, "An efficient diagnosis system for Parkinson's disease using kernel-based extreme learning machine with subtractive clustering features weighting approach," *Computational and Mathematical Methods in Medicine*, vol. 2014, Article ID 985789, 14 pages, 2014.

[42] A. H. El-Baz, "Hybrid intelligent system-based rough set and ensemble classifier for breast cancer diagnosis," *Neural Computing and Applications*, vol. 26, no. 2, pp. 437–446, 2015.

[43] J.-H. Eom, S.-C. Kim, and B.-T. Zhang, "AptaCDSS-E: a classifier ensemble-based clinical decision support system for cardiovascular disease level prediction," *Expert Systems with Applications*, vol. 34, no. 4, pp. 2465–2479, 2008.

[44] Y. Ma, *Ensemble Machine Learning: Methods and Applications*, Springer, New York, NY, USA, 2012.

[45] S. A. Etemad and A. Arya, "Classification and translation of style and affect in human motion using RBF neural networks," *Neurocomputing*, vol. 129, pp. 585–595, 2014.

[46] Z. Pawlak, "Rough sets," *International Journal of Computer & Information Sciences*, vol. 11, no. 5, pp. 341–356, 1982.

[47] Z. Pawlak, "Rough sets and intelligent data analysis," *Information Sciences*, vol. 147, no. 1–4, pp. 1–12, 2002.

[48] Y. Huang, P. J. McCullagh, and N. D. Black, "An optimization of ReliefF for classification in large datasets," *Data and Knowledge Engineering*, vol. 68, no. 11, pp. 1348–1356, 2009.

[49] J. Sun, M.-Y. Jia, and H. Li, "AdaBoost ensemble for financial distress prediction: an empirical comparison with data from Chinese listed companies," *Expert Systems with Applications*, vol. 38, no. 8, pp. 9305–9312, 2011.

[50] R. Kohavi and F. Provost, "Glossary of terms," *Machine Learning*, vol. 30, no. 2-3, pp. 271–274, 1998.

[51] W. Chen and H. Lin, "Prediction of midbody, centrosome and kinetochore proteins based on gene ontology information," *Biochemical and Biophysical Research Communications*, vol. 401, no. 3, pp. 382–384, 2010.

[52] K.-C. Chou and C.-T. Zhang, "Prediction of protein structural classes," *Critical Reviews in Biochemistry and Molecular Biology*, vol. 30, no. 4, pp. 275–349, 1995.

[53] W. Chen and H. Lin, "Identification of voltage-gated potassium channel subfamilies from sequence information using support vector machine," *Computers in Biology and Medicine*, vol. 42, no. 4, pp. 504–507, 2012.

[54] K.-C. Chou and H.-B. Shen, "Recent progress in protein subcellular location prediction," *Analytical Biochemistry*, vol. 370, no. 1, pp. 1–16, 2007.

[55] P. Feng, H. Lin, W. Chen, and Y. Zuo, "Predicting the types of J-proteins using clustered amino acids," *BioMed Research International*, vol. 2014, Article ID 935719, 8 pages, 2014.

[56] K.-C. Chou and H.-B. Shen, "ProtIdent: a web server for identifying proteases and their types by fusing functional domain and sequential evolution information," *Biochemical and Biophysical Research Communications*, vol. 376, no. 2, pp. 321–325, 2008.

[57] K.-C. Chou and Y.-D. Cai, "Prediction of membrane protein types by incorporating amphipathic effects," *Journal of Chemical Information and Modeling*, vol. 45, no. 2, pp. 407–413, 2005.

[58] F. Tom, "ROC graphs: notes and practical considerations for researchers," *Machine Learning*, vol. 31, pp. 1–38, 2004.

[59] J. Huang and C. X. Ling, "Using AUC and accuracy in evaluating learning algorithms," *IEEE Transactions on Knowledge and Data Engineering*, vol. 17, no. 3, pp. 299–310, 2005.

[60] F. D. Foresee and M. T. Hagan, "Gauss-Newton approximation to Bayesian learning," in *Proceedings of the International Conference on Neural Networks*, vol. 3, pp. 1930–1935, Houston, Tex, USA, 1997.

Hindawi Publishing Corporation
Computational and Mathematical Methods in Medicine
Volume 2016, Article ID 6930482, 8 pages
http://dx.doi.org/10.1155/2016/6930482

Research Article

Computational Analysis of Pumping Efficacy of a Left Ventricular Assist Device according to Cannulation Site in Heart Failure with Valvular Regurgitation

Aulia Khamas Heikhmakhtiar and Ki Moo Lim

Department of IT Convergence Engineering, Kumoh National Institute of Technology, Gumi-si, 39253, Republic of Korea

Correspondence should be addressed to Ki Moo Lim; kmlim@kumoh.ac.kr

Received 23 June 2016; Revised 4 November 2016; Accepted 5 December 2016

Academic Editor: Yoichiro Mori

Mitral valve regurgitation (MR) causes blood to flow in two directions during contraction of the left ventricle (LV), that is, forward into the aorta and backward into the left atrium (LA). In aortic valve regurgitation (AR), leakage occurs from the aorta into the LV during diastole. Our objective is to analyze the contribution of a left ventricular assist device (LVAD) to MR and AR for the following two different cannulation sites: from the LA to the aorta (LAAO) and from the LV to the aorta (LVAO). Using a computational method, we simulated three ventricular conditions (normal [HF without valvular regurgitation], 5% MR, and 5% AR) in three groups (control [no LVAD], LAAO, and LVAO). The results showed that LVAD with LAAO cannulation is appropriate for recovery of the MR heart, and the LVAD with LVAO cannulation is appropriate for treating the AR heart.

1. Introduction

Worldwide, heart failure (HF) is the major cause of death, according to data from the American Heart Association [1]. HF is characterized by progressive inability of the heart to pump the appropriate amount of blood through the body [2]. In HF, the structure (from molecular level to organ level) and function of the heart are considerably altered, resulting in reduced cardiac performance. The heart becomes dilated and cardiac cells develop abnormal ion channel gates, leading to abnormal electrical activation, slow electrical conduction, and disarranged calcium activation, which causes ineffective contraction, dyssynchrony of depolarization, and myofiber shortening, among several other effects. Severe HF develops without prompt and appropriate treatment. HF can have several causes, such as an unhealthy lifestyle with inappropriate nutrition and/or drug use, smoking, and lack of exercise. Genetic or congenital diseases, birth defects, age-related changes, and infections can also result in HF [3]. One of the factors that can lead to severe HF is valvular regurgitation [4].

In valvular regurgitation, valve(s) do not close completely during the ejection and/or diastolic phase. This creates backflow of blood into the atrium and/or the ventricle, decreasing blood flow in the body [3, 5]. The most common type is mitral valve regurgitation (MR). A mitral valve leak can cause blood to flow in two directions during contraction of the left ventricle (LV), that is, forward into the aorta and backward into the left atrium (LA). This increases the pressure and volume in the LA, which leads to increased pressure in the pulmonary vein. Severe regurgitation can result in fluid accumulation in the lung [6]. In aortic valve regurgitation (AR), leakage from the aorta into the LV during diastole leads to increased pressure and volume in the LV. As a result, the heart works harder with each beat. This can cause thickening in the heart wall and eventually leads to HF [3]. AR is commonly caused by weakening of valve tissue owing to the aging process.

A left ventricular assist device (LVAD) can be used to support heart function as a bridge or as a treatment for patients with HF [7]. The LVAD increases cardiac output, unloads the ventricle, and improves coronary circulation

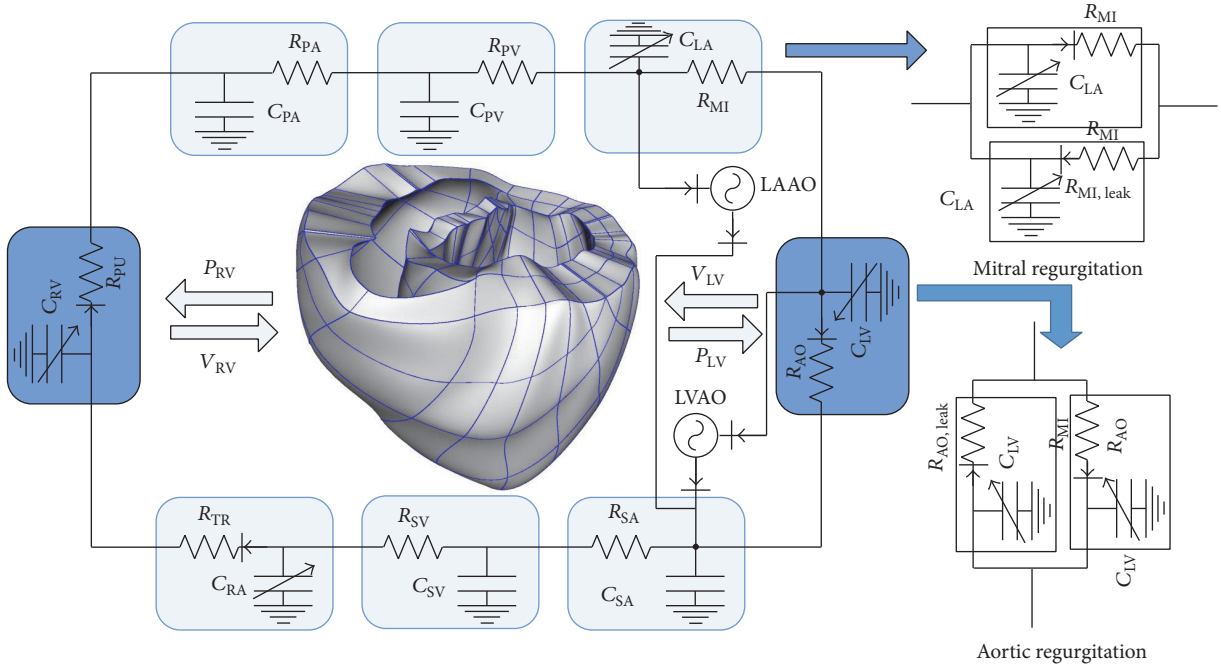

FIGURE 1: Schematic diagram of the finite-element ventricular electromechanical model coupled with the circulatory, valvular regurgitation, and LVAD models (LAAO and LVAO). P_{RV}: RV pressure, V_{RV}: RV volume, P_{LV}: LV pressure, V_{LV}: LV volume, R_{PA}: pulmonary artery resistance, C_{PA}: pulmonary artery compliance, R_{PV}: pulmonary vein resistance, C_{PV}: pulmonary vein compliance, R_{MI}: mitral valve resistance, C_{LA}: left atrium compliance, R_{AO}: aortic valve resistance, R_{SA}: systemic artery resistance, C_{SA}: systemic artery compliance, R_{SV}: systemic vein resistance, C_{SV}: systemic vein compliance, R_{TR}: tricuspid valve resistance, C_{RA}: right atrium compliance, and R_{PU}: pulmonary valve resistance.

[8, 9]. Timms et al. performed an experimental study of the ventricular unloading effect of an LVAD for the following two cannulation sites: from LV to ascending aorta (LVAO) and from LA to ascending aorta (LAAO) [10]. They concluded that LVAO is appropriate for a class IV patient who uses an LVAD as a bridge to transplantation or as a destination therapy. However, for a class III patient, alternative cannulations, such as LAAO and ascending aorta to descending aorta (AODA), are applied for recovery, as these cannulations do not alter the damaged ventricle invasively. The drawback of using LAAO or AODA is that it causes a serious problem in the long term, such as valve stenosis and blood thrombosis, owing to low ejection fraction (EF) [11]. Previously, using computational methods, we developed several cannulation methods for LVAD support as a bridge to recovery [12]. The cannulation sites were AODA, LAAO, and LVAO. The results showed that LAAO is more advantageous than AODA in terms of ventricular unloading and coronary perfusion.

The purpose of this study is to analyze the effect of an LVAD on AR and MR for different cannulation sites. Using a computational method similar to the numerical method used for developing previously reported cardiac electromechanical models [12, 13], we simulated a failing canine ventricular model under the following three conditions: HF without valvular regurgitation (normal), HF with 5% AR, and HF with 5% MR. We applied these conditions to the following three groups based on the LVAD cannulation site: control, LAAO, and LVAO. In the control group, the conditions (normal, AR, and MR) were modeled without the use of the LVAD. In the LAAO group, the LVAD was used for all conditions, with the cannulation site placed between the LA and aorta. In the LVAO group, the LVAD was used for all conditions, with the cannulation site placed between the LV and aorta

2. Materials and Methods

2.1. Mechanical Ventricular Method. We used a previously developed canine electromechanical model based on magnetic resonance imaging [14, 15]. Then, we combined a three-dimensional (3D) image-based failing canine ventricle with a lumped model of the circulatory system and an LVAD model, as shown in Figure 1. The LVAD was modeled as a flow generator. The flux of the LVAD was set to have a constant value of 40 mL/s. For the simulation protocol, we used electromechanical coupling model. The electromechanical model consisted of two compartments, that is, electrical and mechanical. Each compartment was coupled using Ca^{2+} activation. For electrical simulation, we implemented a sinus rhythm by applying the electrical activation time proposed by Durrer et al. [16] with a basic cycle length of 600. We obtained intracellular Ca concentration profiles at all computation nodes from the electrical simulation. Then, these profiles were applied to the mechanical simulation as input parameters. For the mechanical simulation, we performed simulation until 20 seconds, until a steady state response was obtained. The myocardial filament model developed by Rice et al. [17] was used for the mechanical compartment. To mimic the HF model, the passive scale factor of the strain

energy function was increased by five times [18], and the normal myocardial cell calcium transient was reduced by 70% [19]. The schematic diagram in Figure 1 shows the combination of LAAO and LVAO in the model; however, we simulated each condition separately. The schematic diagram represents the blood circulatory system in the human body. It consists of a 3D ventricular diagram and a nondimensional lumped model. Each compartment of the system exchanges information about the pressure and volume in the LV and right ventricle (RV). P, V, C, and R denote pressure, volume, capacitance, and resistance, respectively.

We analyzed several mechanical responses such as 3D adenosine triphosphate (ATP) consumption rate distribution, average ATP consumption rate, pressure waves of the LA, LV, and systemic artery, LV pressure and volume, and LV stroke work. The ATP consumption rate was calculated by integrating the ATP consumption of each node, which represents the myofilament model in one cycle proposed by Rice et al. [17]. In the single myofilament model, the ATP consumption rate (E) per unit volume is the product of cross-bridge detachment rate (g_{xbT}) and the single overlap fraction of thick filaments ($\mathrm{SOVF}_{\mathrm{Thick}}$):

$$E = g_{\mathrm{xbT}} \times \mathrm{SOVF}_{\mathrm{Thick}}. \tag{1}$$

2.2. Valvular Regurgitation Model. To model AR and MR, we added two additional branches parallel to the compartments of the LA and systemic arteries, which contained flow resistances and one-way valves in the lumped model of the circulatory system. $R_{\mathrm{MI,Leak}}$ and $R_{\mathrm{AO,Leak}}$ represent backward flow resistances through the mitral and aortic valves, respectively, in Figure 1. The flow mechanics of AR and MR are represented by the following equations:

$$Q_{\mathrm{MI}} = \begin{cases} \dfrac{P_{\mathrm{LA}} - P_{\mathrm{LV}}}{R_{\mathrm{MI}}} & \text{when } P_{\mathrm{LA}} > P_{\mathrm{LV}} \\ \dfrac{P_{\mathrm{LA}} - P_{\mathrm{LV}}}{R_{\mathrm{MI,Leak}}} = \dfrac{P_{\mathrm{LA}} - P_{\mathrm{LV}}}{R_{\mathrm{MI}}} \times \dfrac{\mathrm{SF}}{100} & \text{when } P_{\mathrm{LA}} \le P_{\mathrm{LV}}, \end{cases} \tag{2}$$

$$Q_{\mathrm{AO}} = \begin{cases} \dfrac{P_{\mathrm{LV}} - P_{\mathrm{AO}}}{R_{\mathrm{AO}}} & \text{when } P_{\mathrm{LV}} > P_{\mathrm{AO}} \\ \dfrac{P_{\mathrm{LV}} - P_{\mathrm{AO}}}{R_{\mathrm{AO,Leak}}} = \dfrac{P_{\mathrm{LV}} - P_{\mathrm{AO}}}{R_{\mathrm{AO}}} \times \dfrac{\mathrm{SF}}{100} & \text{when } P_{\mathrm{LV}} \le P_{\mathrm{AO}}. \end{cases} \tag{3}$$

Equation (2) represents the flux direction of the mitral valve for two different conditions. The first condition represents the LA contraction phase, in which the LA pressure is higher than the LV pressure. The flux direction is from the LA to the LV. The second condition represents the LV contraction phase, in which the LV pressure is higher than the LA pressure. In this condition, the flux direction is from the LV to the aorta and LA. The flux flows back to the LA owing to 5% leak in the mitral valve. SF is the scale factor of the leakage from the valve. SF was set as 5 to represent 5% leak in the mitral valve. Equation (3) represents the leak in the aortic valve. Q, P, and R denote flow rate (mL/min), pressure (mmHg), and resistance (mmHg min/L), respectively, and subscripts MI, AO, LV, LA, and Leak denote mitral valve, aortic valve, left ventricle, left atrium, and regurgitation, respectively.

3. Results

Figure 2 shows the ATP contour distribution (Figure 2(a)) and the average ATP consumption rate (Figure 2(b)) for the normal (HF without valvular regurgitation), AR, and MR conditions for all groups. Under the normal condition, the LAAO and LVAO groups consumed 4.4% and 31% less ATP, respectively, as compared to the control group. The AR heart of the control group consumed 91 s^{-1} ATP. The AR heart with the LAAO cannulation site consumed 47% more ATP, and the AR heart with the LVAO cannulation site consumed slightly less ATP, as compared to the AR heart of the control group. The MR heart of the control group consumed 80 s^{-1} ATP. The MR heart consumed 45% less ATP with LVAD with the LAAO and LVAO cannulation sites, as compared to the control group. The LVAD with LVAO cannulation reduced ATP consumption for all heart conditions.

Figure 3 shows a comparison of the LA, LV, and aortic pressures for the normal, AR, and MR conditions in terms of the waveform (Figures 3(a)–3(c)), LA peak pressure (LAPP) (Figure 3(d)), and LV peak pressure (LVPP) (Figure 3(e)). A comparison between the mechanical responses for the normal, AR, and MR conditions was obtained from one cycle in steady state, which was from 18.6 seconds to 19.2 seconds. In Figure 3(a), the aortic pressure for the normal condition increased by up to 30% using the LVAD with both cannulation sites (LAAO and LVAO). This is due to the continuous flux pumped by the LVAD, which distributes blood continuously to the outlet of the cannulation (aorta). The peak pressure of the inlet chamber decreased by 44% and 25% for the LA with LAAO and LV with LVAO, respectively. In addition, the LV pressure for the normal condition with LAAO cannulation did not exceed the aortic pressure, which created isovolumic contraction and trapped the blood in the LV. This condition was also observed in the experimental study on severe HF by Timms et al. They showed that the use of LAAO in severe HF trapped blood in the LV during systole [10]. This trapped blood is the primary cause of blood thrombosis [11].

Figure 3(b) shows the LV, LA, and aortic pressures for the AR condition. The LV pressure for the control group under this condition was 16% lower compared to that under the normal condition. This is due to the leak from the aortic valve that reduces systolic efficacy. In addition, the LA pressure for the control group increased by 20% compared to that under the normal condition. The LVAD with LAAO cannulation increased the LV pressure for the control group by 34% under the AR condition, as compared to that under the normal condition. Increase in the LV and aortic pressures under the AR condition with LAAO cannulation was due to increase in the volume of the LV. The LAAO cannulation absorbed blood from the LA and sent it to the aorta. However, blood leaked to the LV from the aortic valve, which increased the LV volume. In addition, the LA pressure decreased owing to

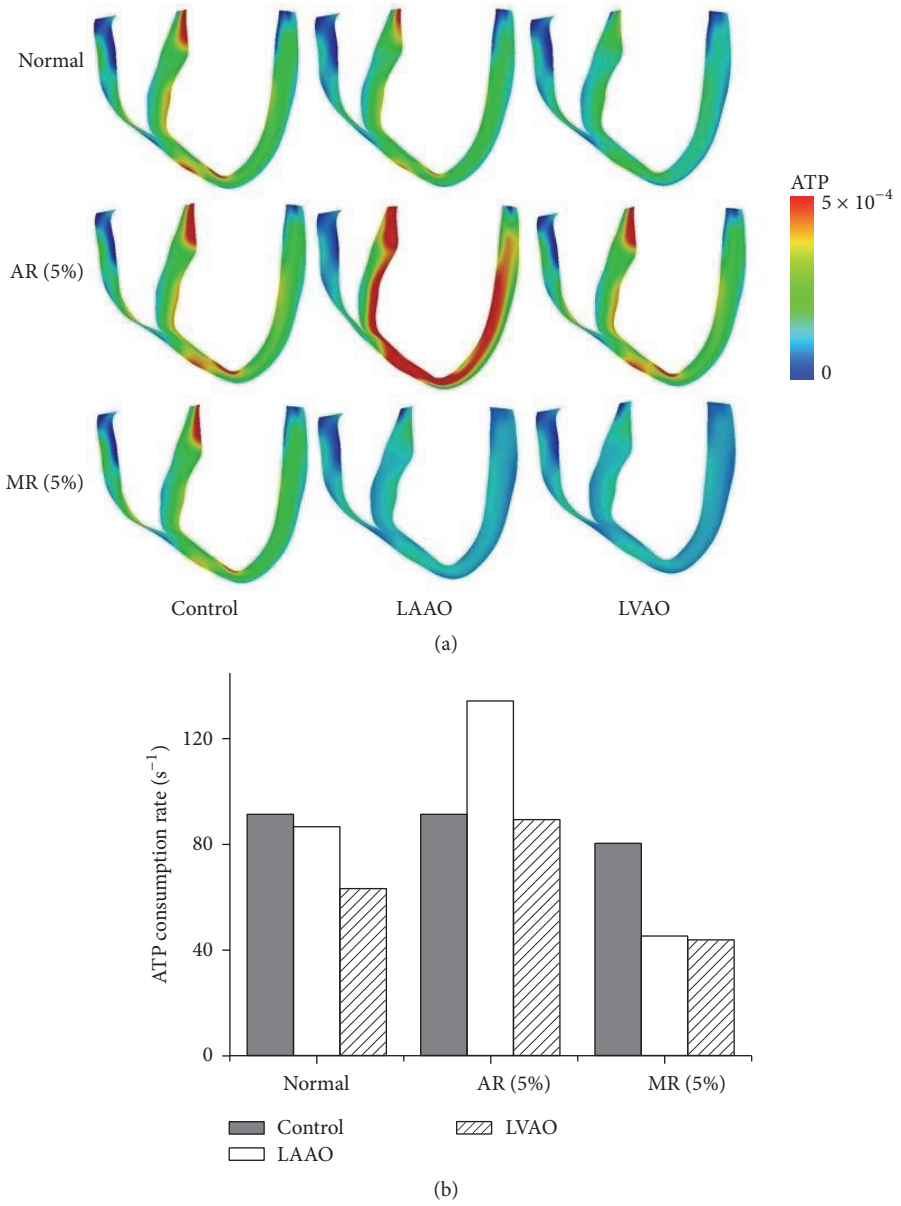

Figure 2: ATP consumption under normal, AR, and MR conditions for all groups.

the unloading from LAAO cannulation. On the other hand, the use of LVAO cannulation did not affect the AR condition significantly. Even though the LVAD distributed the load to the aorta, the pressure of the systemic artery/aorta for coronary perfusion could not be maintained because of the leak.

In Figure 3(c), the LA pressure for the control group under the MR condition increased during the systolic phase owing to the mitral valve leak. Furthermore, the LV and aorta pressures could not be maintained. The use of the LVAD with LAAO and LVAO cannulations increased the systemic artery pressure, which resulted in high perfusion in coronary arteries. Additionally, both cannulations succeeded in unloading the blood from each chamber (LA for LAAO and LV for LVAO).

Figures 3(d) and 3(e) show the comparison between the LAPP and LVPP for all conditions and groups. It can be observed that the LAPP for the control group increased by 28% and 72% under the AR and MR conditions, respectively. On the other hand, the LVPP for the control group under the AR and MR conditions decreased by 16% and 31%, respectively.

Figure 4 shows the pressure-volume (PV) loop diagram for the normal (Figure 4(a)), 5% AR (Figure 4(b)), and 5% MR (Figure 4(c)) conditions, and the stroke work (Figure 4(d)) for all conditions. In Figure 4(a), the stroke volume of the control group under the normal condition was 20 mL, which implies it has 20% EF. The peak pressure was lower than that for the normal heart condition, and the end diastolic volume was higher than that for the normal

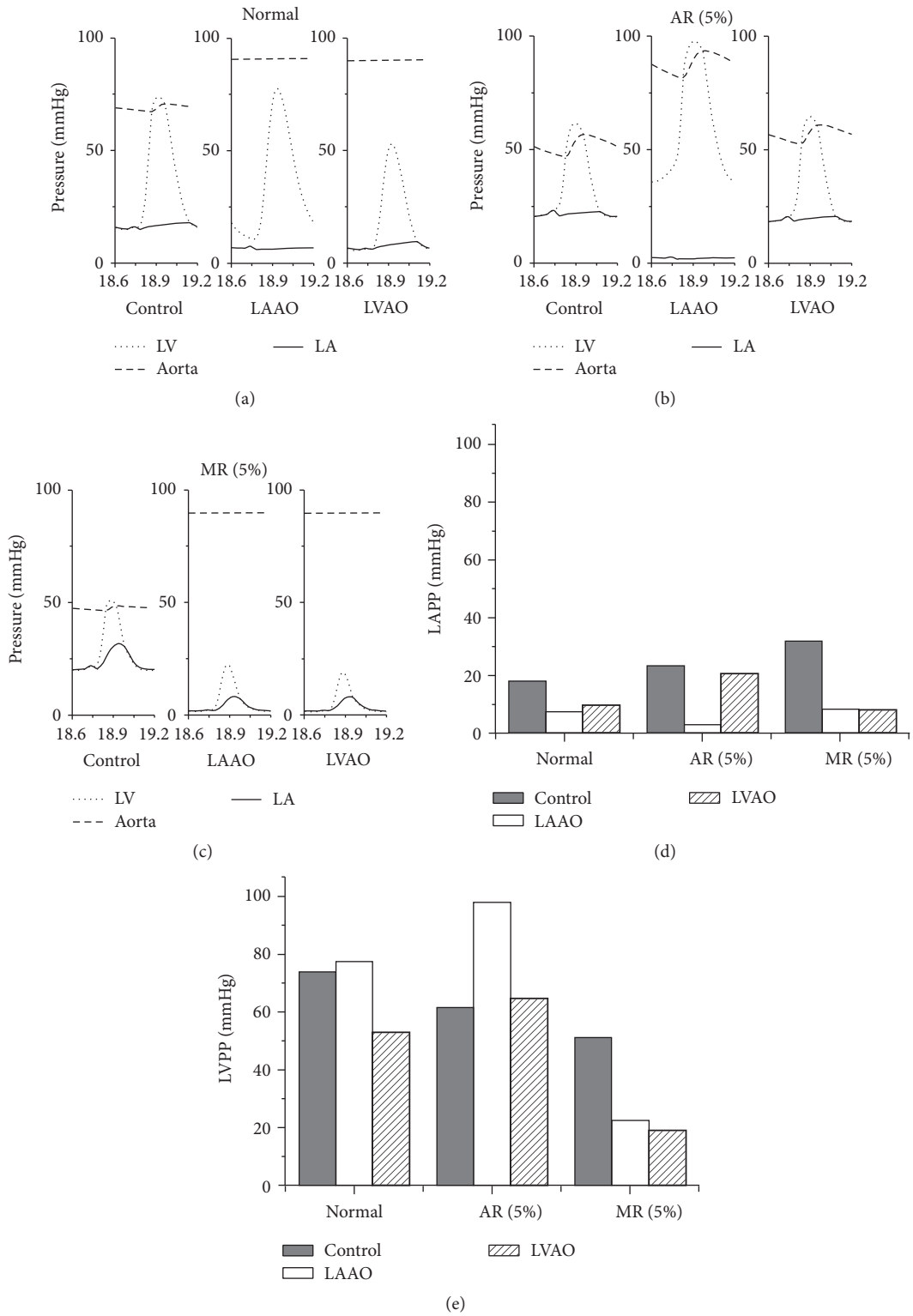

Figure 3: (a) LA, (b) LV, and (c) aortic pressures; (d) LAPP; and (e) LVPP under all conditions for all groups.

condition. The normal condition of the control group was categorized as severe HF. Isovolumic contraction occurred under LVAD treatment with the LAAO cannulation site in the normal condition because of direct cannulation from the LA to the aorta, which completely distributed the blood, resulting in no change in the LV volume. The blood that remained in the LV could not flow through the aortic valve because the LV pressure under this condition is less than the aortic pressure. Thus, the blood was trapped in the LV.

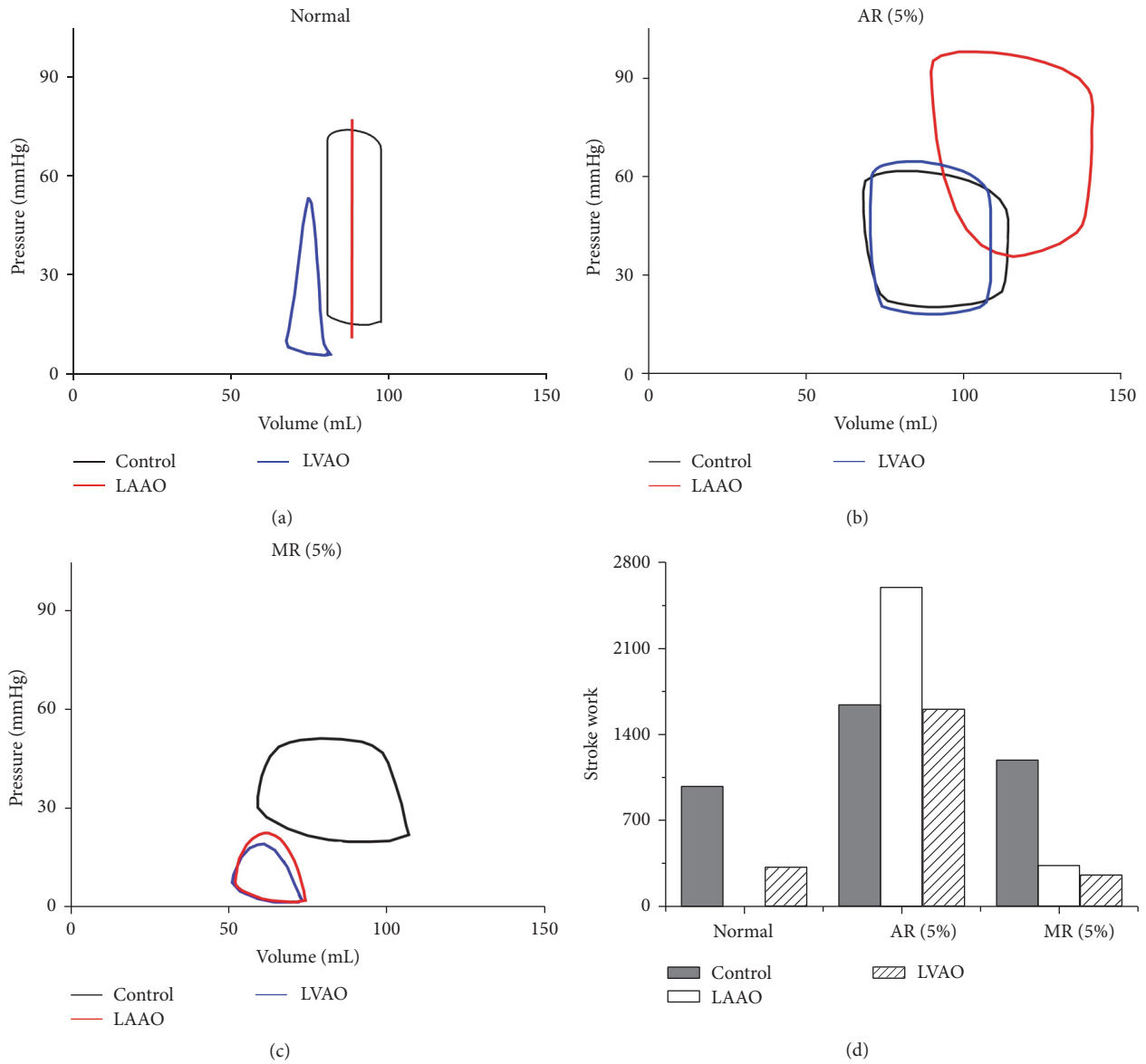

Figure 4: (a, b, c) Pressure-volume loops and (d) stroke work for all conditions.

In Figure 4(b), the LV under the AR condition exhibits a higher pressure and volume loop compared to the normal condition under control group when the LVAD with LAAO cannulation is implemented because of the leak in the aortic valve, which increases the volume and pressure of the LV. On the other hand, the PV loop for the AR condition is restored by implementing the LVAD with LVAO cannulation.

Figure 4(c) shows that the LVAD with LAAO and LVAO cannulation sites succeeded in unloading the blood and reduced the stroke work under the MR condition (Figure 4(d)). This implies that both cannulation sites distributed the blood appropriately and maintained the aortic pressure to increase coronary perfusion. Hence, LAAO or LVAO cannulation is suitable for treating a patient suffering from MR. However, as LAAO does not alter the LV structure and anatomy, we propose that LAAO cannulation is the most suitable for cardiac recovery of the MR heart. Stroke work exhibits similar pattern for the ATP consumption rate, except for the LAAO cannulation site under the normal condition. The stroke work for this condition was zero owing to 0% EF.

4. Discussion

We simulated a realistic 3D failing canine heart model under normal (HF without valvular regurgitation), 5% AR, and 5% MR conditions with two cannulation sites for an LVAD, that is, LAAO and LVAO. We analyzed mechanical responses such as ATP contour distribution, average ATP consumption rates, pressures of LV, LA, and aorta, PV loop diagram, and stroke work. The difference between the ATP consumption rates for the control groups was insignificant for the normal, 5% AR, and 5% MR conditions. The LVAD with LAAO and

LVAO cannulations reduced the ATP consumption by 45% under the MR condition. Even though LAAO reduced the ATP consumption under the MR condition, it increased the ATP consumption by up to 47% under the AR condition, as compared to that for the control group under the AR condition.

In terms of the LV PV loop, isovolumic contraction was observed under the normal condition for the LVAD with LAAO cannulation. LAAO worsened pumping efficacy, in which the heart consumed considerable energy and the EF was zero. Even though the blood circulates with the assistance of the LVAD, the blood trapped in the LV causes thrombosis. In addition, LAAO cannulation under the AR condition is not applicable based on the simulation result because it increased the ATP consumption rate, LV pressure, and stroke work above normal values under the AR condition. In contrast, the LVAD with LVAO cannulation is more appropriate for treating an AR patient because it restores the ATP consumption and maintains the LV PV loop.

In the MR heart, the LVAD with LAAO and LVAO cannulation sites succeeded in restoring cardiac functions, which reduced ATP consumption, increased the aortic pressure for coronary perfusion, and provided sufficient cardiac output to the body. Nonetheless, the LVAD with LAAO cannulation is more appropriate for treating the MR heart. This option is suitable for a patient who uses LVAD solely for recovery and not as a bridge to transplantation or as a destination therapy. This is because LAAO cannulation does not alter the diseased LV directly, which is necessary for restoring cardiac functions.

5. Conclusions

The effect of the LVAD with LAAO and LVAO cannulation sites was predicted theoretically under the normal (HF without valvular regurgitation), 5% AR, and 5% MR heart conditions. The results showed that the LVAD with LVAO cannulation restored the hemodynamics of the heart under the AR and MR conditions. For the LVAD with LAAO cannulation, even though this cannulation restored the cardiac hemodynamics under the MR condition, it worsened the cardiac hemodynamics under the AR condition by increasing the ATP consumption, LV pressure/hypertension, and LV stroke work. In conclusion, the LVAD with LAAO cannulation is appropriate for recovery of the MR heart, and the LVAD with LVAO cannulation is appropriate for treating the AR heart.

Competing Interests

The authors declare that they have no competing interests.

Acknowledgments

This research was partially supported by the MSIP, Korea, under the CITRC support program (IITP-2015-H8601-15-1011) supervised by the IITP and NRF (2016R1D1A1B0101440 and 2016M3C1A6936607).

References

[1] D. Lloyd-Jones, R. Adams, M. Carnethon et al., "Heart disease and stroke statistics—2009 update: a report from the American Heart Association Statistics Committee and Stroke Statistics Subcommittee," *Circulation*, vol. 119, no. 3, pp. e21–e181, 2009.

[2] A. H. A. S. Committee and S. S. Subcommittee, "About heart failure," http://www.heart.org/HEARTORG/Conditions/HeartFailure/AboutHeartFailure/About-Heart-Failure_UCM_002044_Article.jsp.

[3] American Heart Association, "Problem: Heart valve regurgitation," http://www.heart.org/HEARTORG/Conditions/More/HeartValveProblemsandDisease/Problem-Heart-Valve-Regurgitation_UCM_450736_Article.jsp.

[4] M. Enriquez-Sarano, H. V. Schaff, T. A. Orszulak, K. R. Bailey, A. J. Tajik, and R. L. Frye, "Congestive heart failure after surgical correction of mitral regurgitation: a long-term study," *Circulation*, vol. 92, no. 9, pp. 2496–2503, 1995.

[5] T. Irvine, G. D. Stetten, V. Sachdev et al., "Quantification of aortic regurgitation by real-time 3-dimensional echocardiography in a chronic animal model: computation of aortic regurgitant volume as the difference between left and right ventricular stroke volumes," *Journal of the American Society of Echocardiography*, vol. 14, no. 11, pp. 1112–1118, 2001.

[6] A. H. Association, "Problem: Mitral valve regurgitation," http://www.heart.org/HEARTORG/Conditions/More/HeartValveProblemsandDisease/Problem-Mitral-Valve-Regurgitation_UCM_450612_Article.jsp.

[7] National Heart, Lung, and Blood Institute, "What is a ventricular assist device?" http://www.nhlbi.nih.gov/health/health-topics/topics/hvd.

[8] D. Casarotto, T. Bottio, A. Gambino, L. Testolin, and G. Gerosa, "The last to die is hope: prolonged mechanical circulatory support with a Novacor left ventricular assist device as a bridge to transplantation," *The Journal of Thoracic and Cardiovascular Surgery*, vol. 125, no. 2, pp. 417–418, 2003.

[9] D. J. Goldstein, "Worldwide experience with the Micromed DeBakey ventricular assist device® as a bridge to transplantation," *Circulation*, vol. 108, no. 10, supplement 1, pp. II-272–II-277, 2003.

[10] D. Timms, S. Gregory, P.-L. Hsu et al., "Atrial versus ventricular cannulation for a rotary ventricular assist device," *Artificial Organs*, vol. 34, no. 9, pp. 714–720, 2010.

[11] A. G. Rose and S. J. Park, "Pathology in patients with ventricular assist devices: a study of 21 autopsies, 24 ventricular apical core biopsies and 24 explanted hearts," *Cardiovascular Pathology*, vol. 14, no. 1, pp. 19–23, 2005.

[12] K. M. Lim, J. S. Lee, J.-H. Song, C.-H. Youn, J.-S. Choi, and E. B. Shim, "Theoretical estimation of cannulation methods for left ventricular assist device support as a bridge to recovery," *Journal of Korean Medical Science*, vol. 26, no. 12, pp. 1591–1598, 2011.

[13] K. M. Lim, I. S. Kim, S. W. Choi et al., "Computational analysis of the effect of the type of LVAD flow on coronary perfusion and ventricular afterload," *Journal of Physiological Sciences*, vol. 59, no. 4, pp. 307–316, 2009.

[14] V. Gurev, T. Lee, J. Constantino, H. Arevalo, and N. A. Trayanova, "Models of cardiac electromechanics based on individual hearts imaging data: image-based electromechanical models of the heart," *Biomechanics and Modeling in Mechanobiology*, vol. 10, no. 3, pp. 295–306, 2011.

[15] K. M. Lim, J. Constantino, V. Gurev, R. Zhu, E. B. Shim, and N. A. Trayanova, "Comparison of the effects of continuous and

pulsatile left ventricular-assist devices on ventricular unloading using a cardiac electromechanics model," *The Journal of Physiological Sciences*, vol. 62, no. 1, pp. 11–19, 2012.

[16] D. Durrer, R. T. van Dam, G. E. Freud, M. J. Janse, F. L. Meijler, and R. C. Arzbaecher, "Total excitation of the isolated human heart," *Circulation*, vol. 41, no. 6, pp. 899–912, 1970.

[17] J. J. Rice, F. Wang, D. M. Bers, and P. P. De Tombe, "Approximate model of cooperative activation and crossbridge cycling in cardiac muscle using ordinary differential equations," *Biophysical Journal*, vol. 95, no. 5, pp. 2368–2390, 2008.

[18] Y. Wu, S. P. Bell, K. Trombitas et al., "Changes in titin isoform expression in pacing-induced cardiac failure give rise to increased passive muscle stiffness," *Circulation*, vol. 106, no. 11, pp. 1384–1389, 2002.

[19] B. O'Rourke, D. A. Kass, G. F. Tomaselli, S. Kääb, R. Tunin, and E. Marbán, "Mechanisms of altered excitation-contraction coupling in canine tachycardia-induced heart failure, I: experimental studies," *Circulation Research*, vol. 84, no. 5, pp. 562–570, 1999.

Hindawi Publishing Corporation
Computational and Mathematical Methods in Medicine
Volume 2016, Article ID 4310634, 9 pages
http://dx.doi.org/10.1155/2016/4310634

Research Article

In Silico Investigation into Cellular Mechanisms of Cardiac Alternans in Myocardial Ischemia

Jiaqi Liu,[1] Yinglan Gong,[1] Ling Xia,[1] and Xiaopeng Zhao[2]

[1]*Department of Biomedical Engineering, Zhejiang University, Hangzhou 310027, China*
[2]*Department of Mechanical, Aerospace, and Biomedical Engineering, University of Tennessee, Knoxville, TN 37996, USA*

Correspondence should be addressed to Yinglan Gong; yinglangong@zju.edu.cn and Ling Xia; xialing@zju.edu.cn

Received 15 August 2016; Accepted 9 November 2016

Academic Editor: Michele Migliore

Myocardial ischemia is associated with pathophysiological conditions such as hyperkalemia, acidosis, and hypoxia. These physiological disorders may lead to changes on the functions of ionic channels, which in turn form the basis for cardiac alternans. In this paper, we investigated the roles of hyperkalemia and calcium handling components played in the genesis of alternans in ischemia at the cellular level by using computational simulations. The results show that hyperkalemic reduced cell excitability and delayed recovery from inactivation of depolarization currents. The inactivation time constant τ_f of L-type calcium current (I_{CaL}) increased obviously in hyperkalemia. One cycle length was not enough for I_{CaL} to recover completely. Alternans developed as a result of I_{CaL} responding to stimulation every other beat. Sarcoplasmic reticulum calcium-ATPase (SERCA2a) function decreased in ischemia. This change resulted in intracellular Ca (Ca_i) alternans of small magnitude. A strong Na^+-Ca^{2+} exchange current (I_{NCX}) increased the magnitude of Ca_i alternans, leading to APD alternans through excitation-contraction coupling. Some alternated repolarization currents contributed to this repolarization alternans.

1. Introduction

The mechanisms underlying ventricular arrhythmias are complex [1]. Ischemia is one of the main causes. Cardiac arrhythmias are produced by electrophysiological disturbances of the heart [1]. Three major pathophysiological conditions linked to acute myocardial ischemia have been identified, including elevated extracellular potassium, acidosis, and anoxia [2]. These conditions cause changes of electrical activities that produce the potent arrhythmia substrate.

T-wave alternans (TWA) can be used for predicting arrhythmogenesis in clinical practice [3]. TWA refers to beat-to-beat alternation in the morphology and amplitude of the ST-segment or T-wave magnitude [3]. Electrical instabilities in ischemia promote the occurrence of TWA. Animal experiments show that ischemia increases the magnitude of TWA [3]. Moreover, TWA alone can be identified as a strong indicator for ischemic cardiomyopathy [4]. It originates from action potential duration (APD) alternans at the cellular level [3].

To understand the mechanism of TWA, the study of APD alternans is necessary. APD alternans can be caused either by voltage instabilities (voltage-driven alternans) or by Ca^{2+} handling dynamics instabilities (Ca^{2+}-driven alternans) or their interactions [5]. Because of the bidirectional coupling between membrane voltage kinetics and Ca handling dynamics, it is difficult to identify the exact mechanism of APD alternans [6, 7]. Voltage instabilities or Ca^{2+} handling instabilities affect alternans occurring through changes of ionic currents. Thus, there must exist ionic basis in the genesis of alternans. In order to explore the role of ionic currents in the genesis of alternans, computational simulation methods are applied [8, 9]. Eleven factors have been experimentally reported to be related to cardiac alternans [8]. In order to find out the most relevant factors, investigators compared the differences of these factors between normal and alternans groups [8]. There are significant differences in the following 6 ionic currents between the two groups: the fast sodium current (I_{Na}), the L-type calcium current (I_{CaL}), the rapid delayed rectifier potassium current, the sodium calcium exchange current (I_{NCX}), the sarcoplasmic reticulum (SR) calcium release current (I_{rel}), and the SR calcium reuptake current (I_{up}) [8, 9]. These 6

currents play an important role in the development of alternans. Voltage-driven alternans is related to APD restitution properties [1, 9]. APD restitution curve results from collective effects of the recovery properties of all the ionic currents and their interactions with membrane voltage [1, 5]. Sarcolemmal K^+ and Ca^{2+} currents have an influence in the genesis of voltage-driven alternans. Transmembrane proteins such as Na^+-Ca^{2+} exchange and Na^+-K^+ pump also take an effect [8]. Ca_i alternans is subsequently induced by the effect of voltage-dependent I_{CaL} current [6, 7]. Ca^{2+}-driven alternans originates from steep fractional Ca^{2+} release relationship [10] or a generic mechanism of RyR properties, refractoriness, randomness, and recruitment [11]. I_{rel}, I_{up}, I_{CaL}, and I_{NCX} have an effect on the genesis of Ca^{2+}-driven alternans [6, 7]. A strong I_{NCX} can translate Ca_i alternans to voltage alternans [12].

Some of the 6 factors are related to instabilities of electrical activities in ischemia. Intracellular and extracellular acidosis affect ionic currents as channel proteins function like enzymes [13]. Conductibility of I_{Na} and I_{CaL} is decreased by acidosis. I_{rel} current is reduced significantly by acidosis [13]. SERCA2a is regulated by energy metabolism and its function is greatly decreased in ischemia [14]. A population-based study shows that the conductance g_{CaL} contributes most to the occurrence of APD alternans. Under ischemic conditions, there are also other currents such as I_{NCX}, I_{Kr}, and I_{Ks} that play a role [15].

Pathophysiological conditions in ischemia, such as hyperkalemia, acidosis, and hypoxia, promote alternans occurrence by affecting ionic currents at the cellular level. While many experimental and numerical studies reveal voltage- or Ca^{2+}-dependent cellular mechanism, how ischemic conditions cause alternans remains unclear. In this work, we aim to investigate how electrical changes in ischemia promote alternans using computer simulations.

2. Methods

2.1. Hyperkalemic Condition. The epicardial ten Tusscher model (TNNP) [16] was employed in this study. In the epicardial cell model, we simulated hyperkalemic condition by increasing the extracellular potassium concentration ($[K^+]_o$). We changed $[K^+]_o$ alone to investigate its independent role in the development of alternans. $[K^+]_o$ concentration was set to increase from 5.4 to 15 mM. Cycle length was applied at 400 ms.

2.2. SERCA2a Function Decreased in Ischemia. A thermodynamic model of the cardiac SERCA2a [17] was integrated into the TNNP model. The thermodynamic model based on biophysical kinetic is sensitive to metabolism compromised in ischemia.

$$2Ca_i^{2+} + MgATP + H_2O \Longleftrightarrow 2Ca_{sr}^{2+} + MgADP + Pi + H^+ \quad (1)$$

The process of Ca uptake from the cytoplasm to SR can be presented by the above reaction equation. The equation shows that translating two Ca^{2+} needs the hydrolysis of one ATP. At the same time, the products MgADP, Pi, and H^+ are released. This reversible reaction is modeled by E1-E2 model [18, 19] which consisted of two conformational changes of Ca^{2+}-binding sites.

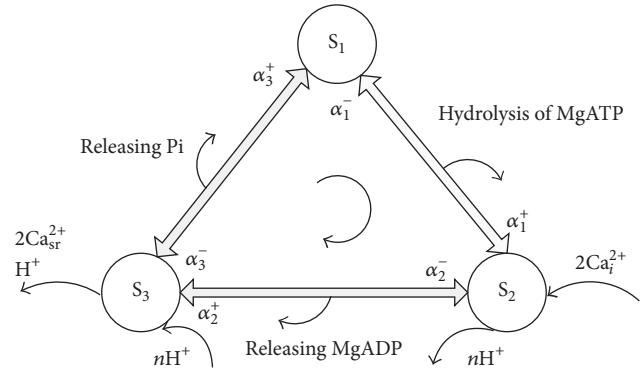

FIGURE 1: Schematic of the three-state model. S_1, S_2, and S_3 represent the state of SERCA pump in the reaction process. The rate constants are represented by $\alpha_i^{\pm}(1, 2, 3)$ and signs represent the forward or backward direction of reaction. Hydrolysis of MgATP and the release of MgADP/Pi occur in the positive direction during the transformation process. The reaction process is simplified from the E1-E2 model [18, 19].

The cardiac SERCA2a model applied in our study was a three-state model. The three-state model (Figure 1) is simplified from the E1-E2 model [18, 19] using rapid equilibrium assumption. In the positive direction, state S_1 transforms to S_2 via the hydrolysis of ATP. State S_2 indicates Ca^{2+}-binding sites binding Ca^{2+} and the Ca^{2+}/H^+ countertransport transporting H^+ from SR to the cytoplasm, state S_3 represents the Ca^{2+}-binding sites releasing Ca^{2+} to the SR and Ca^{2+}/H^+ countertransport binding H^+ to SERCA. The rate constants (α_i) are functions of intracellular Pi, ATP, ADP, and H^+ concentrations. See Appendix for formulas of these rate constants [17].

$$V_{cycle} = \frac{\alpha_1^+\alpha_2^+\alpha_3^+ - \alpha_1^-\alpha_2^-\alpha_3^-}{\Sigma}, \quad (2)$$

where V_{cycle} is clockwise cycle rate per pump at steady state. By modifying physiological parameters we could simulate metabolism compromised. In ischemia pH was decreased accompanied with a decrease of intracellular ATP. We set pH at 6 and ATP concentration at 4.2 mM. At the same time the concentrations of intracellular ADP and Pi [20] were simulated to increase to 100 nM and 30 mM [21], respectively. Values of other parameters in the formulas were the same as in the original three-state model [17].

$$I_{up} = N * V_{cycle}. \quad (3)$$

The value of I_{up} was in proportion to the whole-cell pump flux. The whole-cell pump flux was determined by V_{cycle} and the numbers of SERCA pumps on the SR membrane. In order to calculate I_{up} under compromised metabolism conditions, we multiplied V_{cycle} by the constant N as a scale factor. The value of N was the ratio of maximum I_{up} obtained by original TNNP model simulation and maximum V_{cycle} under normal conditions.

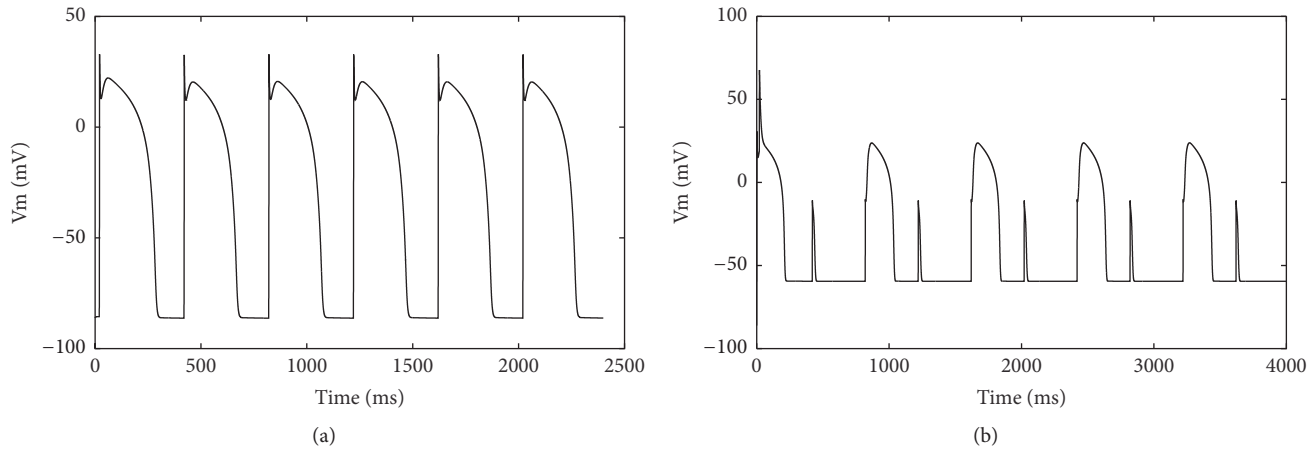

FIGURE 2: APD computed at the cycle length of 400 ms. (a) APs in control condition with $[K^+]_o$ = 5.4 mM. (b) Alternate APs in hyperkalemia with $[K^+]_o$ = 15 mM.

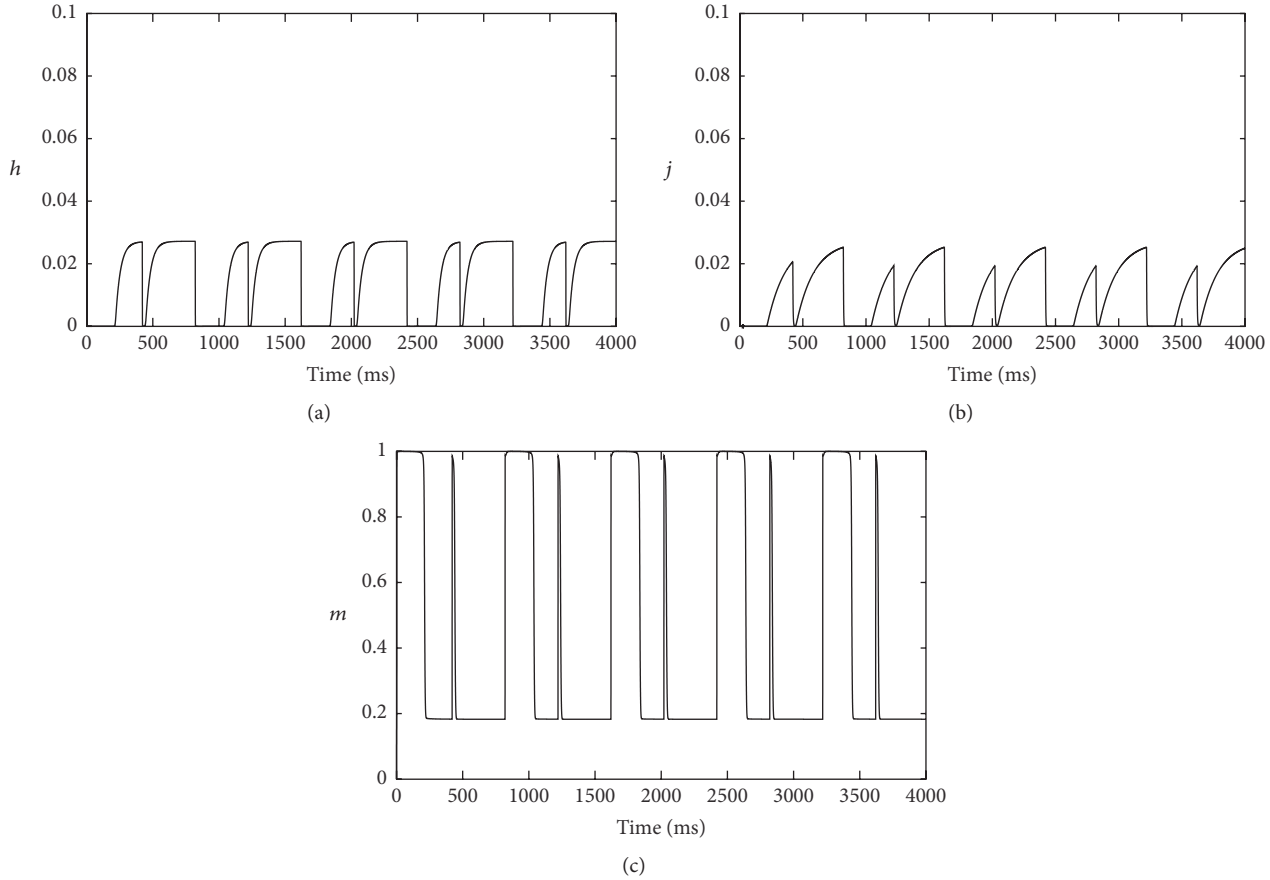

FIGURE 3: Gating variables of I_{Na} in hyperkalemia. (a) Fast inactivation gate h; (b) slow inactivation gate j; (c) activation gate m.

3. Results

3.1. The Effects of Hyperkalemia on APD and Ionic Currents. While the cycle length was applied at 400 ms, no APD alternans existed under normal conditions (Figure 2(a)). There existed no alternans except for the elevated resting potential and decreased amplitude of action potential when the $[K^+]_o$ values were in between 5 mM and 14.7 mM. APD alternans occurred in hyperkalemia with $[K^+]_o$ ranging from 14.7 to 15 mM. The $[K^+]_o$ values in this range correspond to severe hyperkalemia. Moreover, significantly elevated $[K^+]_o$ values may also occur in ischemic hearts as well as in isolated hearts in experiments. The longer AP manifested two depolarization phases. These two depolarization phases were

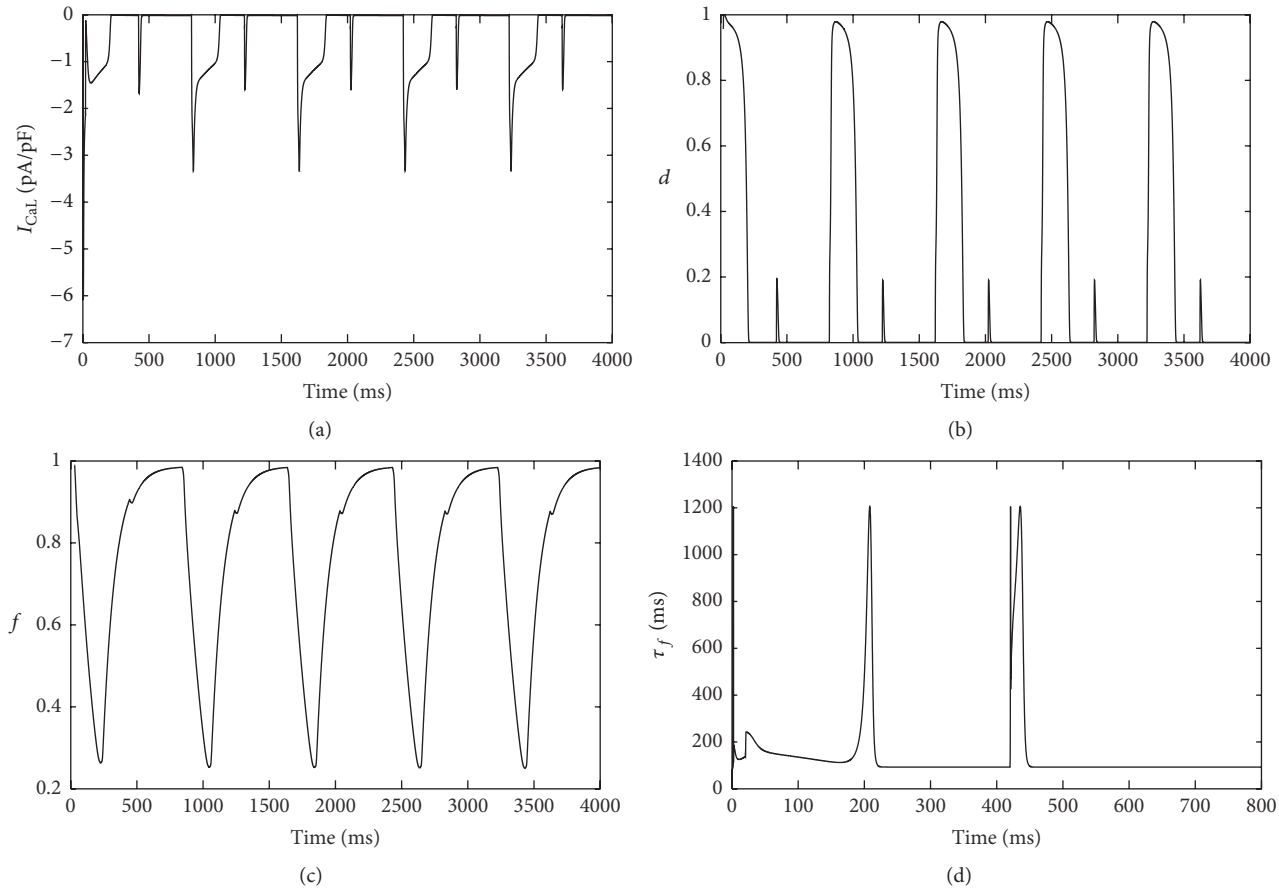

FIGURE 4: I_{CaL} and its gating variables in hyperkalemia. (a) I_{CaL} current; (b) voltage-dependent activation gate d; (c) voltage-dependent inactivation gate f; (d) inactivation time constant τ_f of the gate f during two consecutive beats.

maintained by I_{Na} and I_{CaL}. The availability of I_{CaL} in shorter APs was reduced, resulting in small depolarization phases during the next beats (Figure 2(b)).

To investigate the process of alternans occurring, depolarization currents were selected to be studied. I_{Na} decreased significantly in hyperkalemia. Open possibilities of inactivation gates, h and j, came near to be zero (Figures 3(a) and 3(b)). In contrast, the open possibility of activation gate m increased at depolarized resting voltage (Figure 3(c)).

The amplitude of I_{CaL} showed alternans (Figure 4(a)). Activation gate d was voltage-dependent and manifested alternans from beat to beat (Figure 4(b)). The intracellular calcium-dependent inactivation gate, f_{ca}, was nearly in closed state. Voltage-dependent inactivation gate f needed two cycle lengths to recover completely (Figure 4(c)). Moreover, the inactivation time constant τ_f of the gate f became larger during shorter APs (Figure 4(d)). That further verified the gate f could not recover instantly from inactivation, leading to decreased availability of I_{CaL} during shorter APs. While τ_f was decreased by 70 ms (Figure 5(a)), the gate f recovered instantly (Figure 5(b)) and alternans in APD disappeared (Figure 5(c)).

3.2. The Effects of I_{up} and I_{NCX} on Ca Transient and APD. As the component of cardiac Ca handling, I_{up} decreased under ischemic conditions. This change was simulated by modifying the physiological parameters of the SERCA pump model [17]. Thus the direct role of I_{up} in the onset of Ca_i alternans could be investigated. Decreased I_{up} slowed down the rate of SR Ca uptake and could not balance Ca^{2+} flux released from SR. As Figure 6(b) showed, Ca^{2+} transients alternated obviously during early beats and reached a steady state finally. In contrast to alternate Ca^{2+} transients, APD remained unchanged (Figure 6(a)).

I_{NCX} decreased under acidic conditions [13]. Decreased I_{NCX} was also added in the simulation after investigating the effect of I_{up} on Ca_i alternans. As Figure 7 showed, the magnitude of Ca^{2+} transient alternans decreased. The result suggested that decreased I_{NCX} could inhibit Ca_i alternans. Based on this observation, we expected that Ca_i alternans magnitude would increase as I_{NCX} current increased. Figure 8(b) confirmed the guess. Results showed that APD alternans was accompanied with Ca_i alternans of large magnitude (Figure 8(a)).

To compare the differences in the durations of repolarization between APs, we placed the 6 beats in the coordinate axes in Figure 9(a). Previous study suggested that I_{Kr} and I_{Ks} played a role in the occurrence of APD alternans. We selected I_{Ks} and I_{Kr} to investigate their roles in the process. I_{Kr} and I_{Ks} alternated from beat to beat as shown in Figures 9(b) and 9(c).

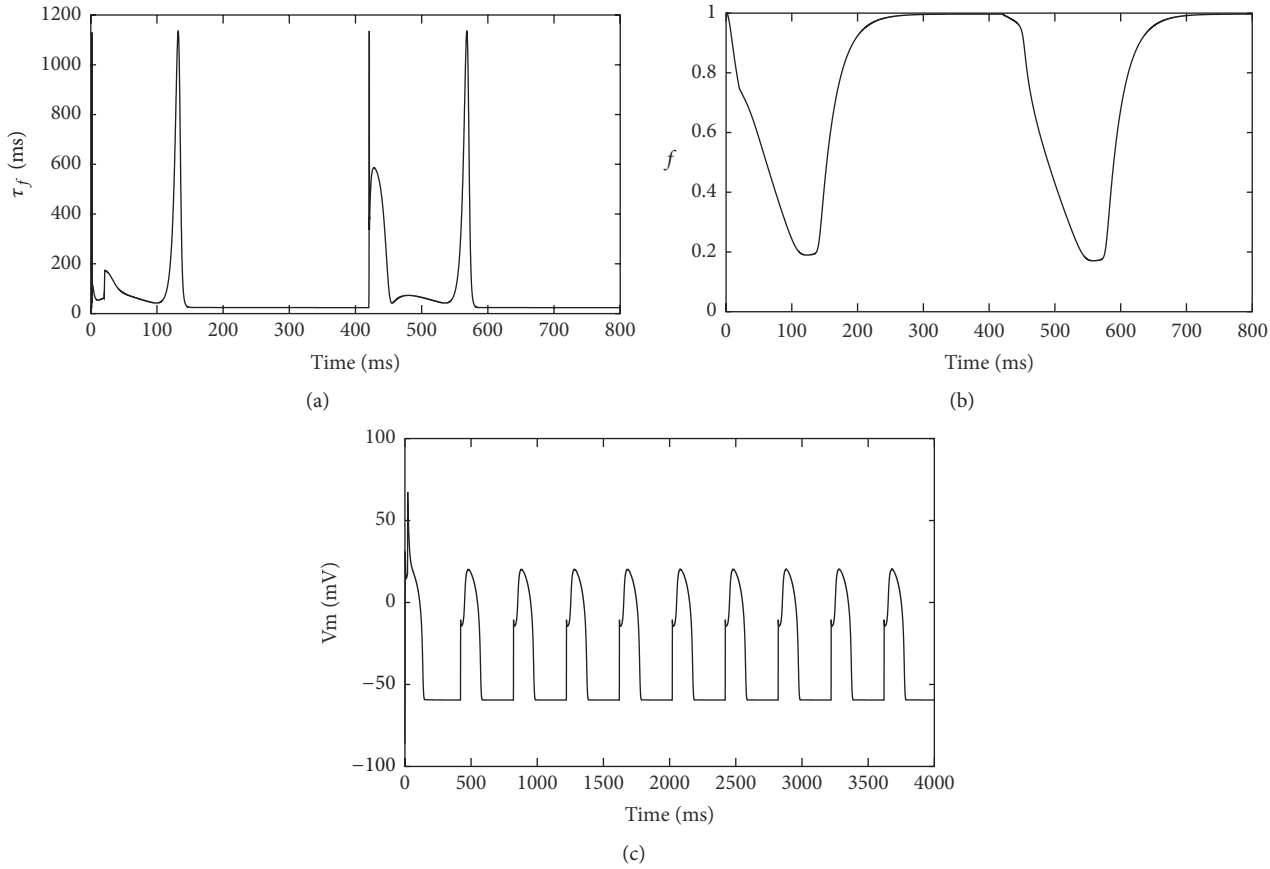

FIGURE 5: Simulations of the inactivation gate f and APD after decreasing inactivation time constant τ_f in hyperkalemia. (a) Decreased inactivation time constant τ_f of the gate f; (b) voltage-dependent inactivation gate f. Decreased τ_f made the gate f recover completely before the next APD. The gate f responded once during two consecutive beats in hyperkalemia without decreasing τ_f; (c) APs with no alternans.

4. Discussion

4.1. The Mechanism of Alternans in Hyperkalemia. Depolarization alternans in hyperkalemia arises from changes in depolarization currents. In order to find out the key factors relating to alternans occurring in hyperkalemia, we selected depolarization currents for analysis. Our simulation results suggest that I_{Na} is too small to affect the process of depolarization during both longer and shorter APs. I_{CaL} may be the key factor in the development of alternans. Cycle lengths are fixed and the longer AP is followed by the shorter duration. I_{CaL} cannot recover completely from inactivation in the shorter duration. Its availability decreases in the following depolarization phase. Thus the next depolarization phase maintained by I_{Na} alone is small. Small depolarization phase leads to shorter AP. Subsequently, the longer duration provides enough time for I_{CaL} to recover completely. Shorter APs are following longer APs and alternans develops. In order to further verify the role of I_{CaL}, τ_f of voltage-dependent inactivation gate f is decreased in simulation. Decreased τ_f indicates that the gate f needs shorter time to recover completely. Then the availability of I_{CaL} increases in APs. Alternans disappears due to complete response of I_{CaL} in every beat.

In contrast, some studies investigate alternans mechanisms in ischemia at the tissue level. Previous study supports that the depolarization alternans is linked to conduction abnormalities in the ischemia region [22]. The conduction block occurs under hyperkalemic conditions. Moreover, the depolarization phase is fragmented in the current simulation of hyperkalemia as is consistent with previous observations. Results show that depolarization alternans in ischemia region can be produced by hyperkalemic conditions [23].

Alternate conduction block induced by hyperkalemia leads to APD alternans [24]. The areas of conduction blocks become larger and alternans occurs at slower pacing frequency while increasing the inactivation time constant τ_f [24]. According to the observation, smaller areas are expected to be blocked if τ_f decreases and APD alternans will be depressed in the areas with no block any more. In other words, decreased τ_f can abolish alternans through eliminating conduction block. That is consistent with our observations. Hyperkalemia increases τ_f by depolarizing the resting voltage and thus promotes APD alternans.

4.2. The Direct Role of I_{up} in Ca_i Alternans. The slow rate of SR Ca uptake contributes to the occurrence of Ca_i alternans

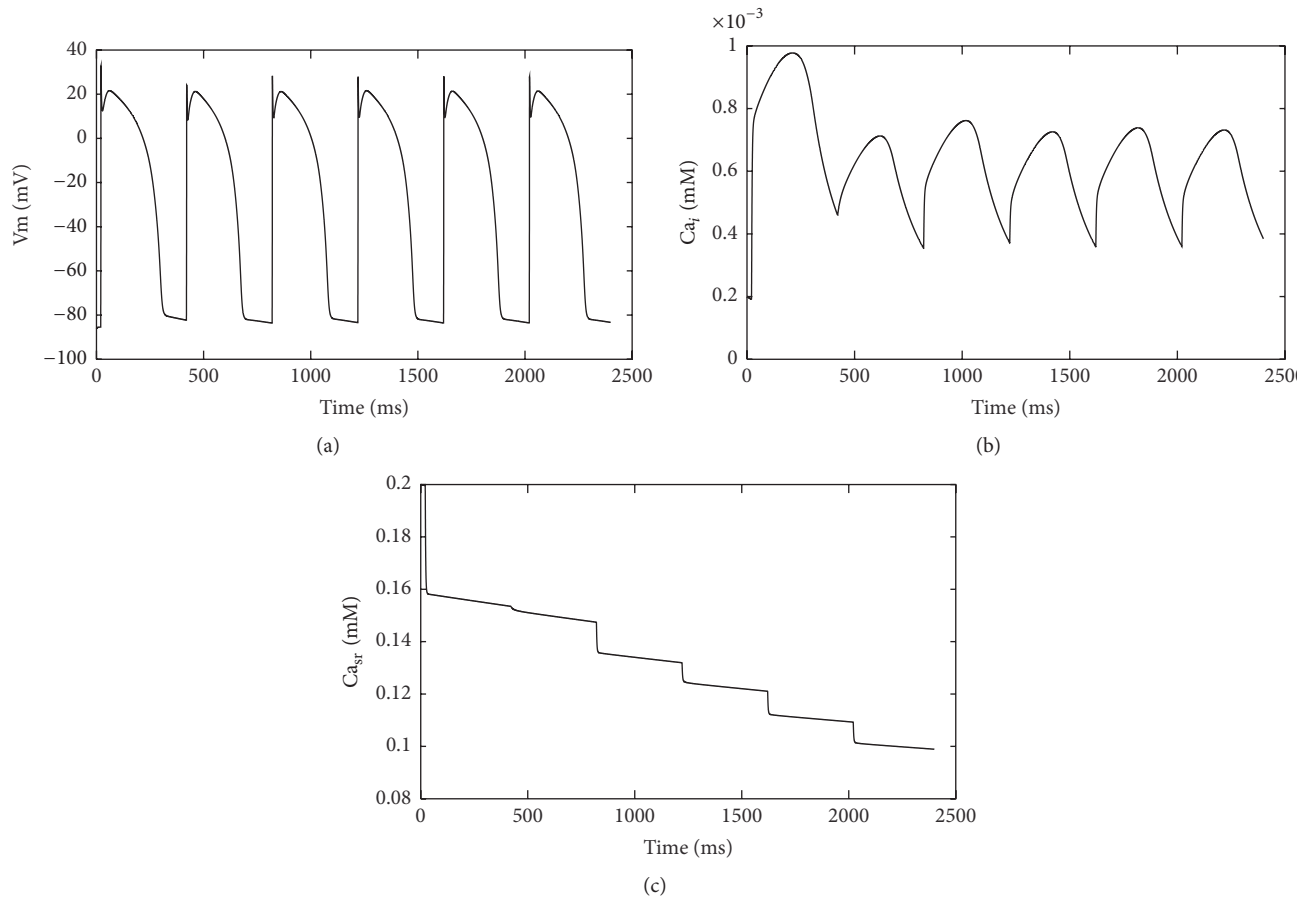

FIGURE 6: Ca transient, APs, and Ca^{2+} content in SR after decreasing I_{up} current. (a) APs with no alternans; (b) alternate Ca transient; (c) decreased Ca^{2+} content in SR from beat to beat.

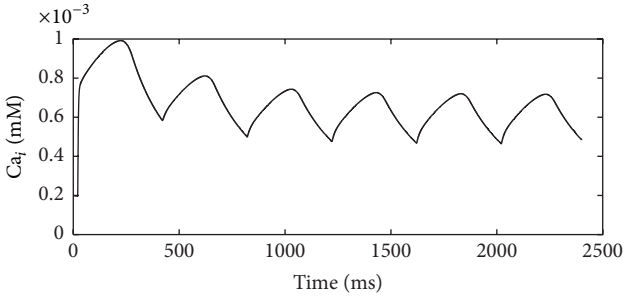

FIGURE 7: Ca transient after decreasing I_{up} and I_{NCX} currents. Ca_i alternans disappeared after decreasing I_{NCX}.

[25]. Qu et al. point out calcium alternans is determined by the interaction of the slopes of the fractional Ca^{2+} release curve, the SR Ca^{2+} uptake function, and properties of Ca^{2+} sparks [26]. The independent role of decreased I_{up} in the Ca_i alternans is investigated in our study. Decreased I_{up} has no ability to balance I_{up} current. The Ca content in diastole is affected. Subsequently, the release of Ca^{2+} from SR is depressed due to elevated Ca^{2+} in the cytoplasm. Then the Ca content in diastole decreases comparing to the last Ca transient. Fluctuations in cytoplasmic Ca content in diastole originate from unbalance in Ca^{2+} flux between I_{up} uptake and I_{rel} releasing. Transient Ca_i alternans are consequently caused by the fluctuations. According to the unified theory presented by Qu et al. [26], we could add ischemic changes of I_{rel} to the cell model to obtain stable calcium alternans. Ca content fluctuation in SR plays a role in producing Ca^{2+} transients alternans [10]. But our results show that SR load decreases from beat to beat (Figure 6(c)). That suggests SR load may not be the direct factor in the development of Ca_i alternans.

4.3. The Role of I_{NCX} in the Alternans Translation from Ca to APD. Larger I_{NCX} increases Ca_i alternans magnitude. Our results suggest that Ca_i alternans can lead to APD alternans while the Ca_i alternans magnitude is large enough. However, decreased I_{up} and increased I_{NCX} are not sufficient to produce stable alternans in our simulations. Previous study also shows that I_{NCX} is the key factor that translates alternans from Ca to APD [12]. More precisely, the balance of I_{NCX} and I_{Ca} determines coupling in phase of Ca_i alternans to APD alternans [27]. Alternans presented by Wan et al. can arise from the shifted balance of I_{NCX} and I_{Ca} at higher pacing

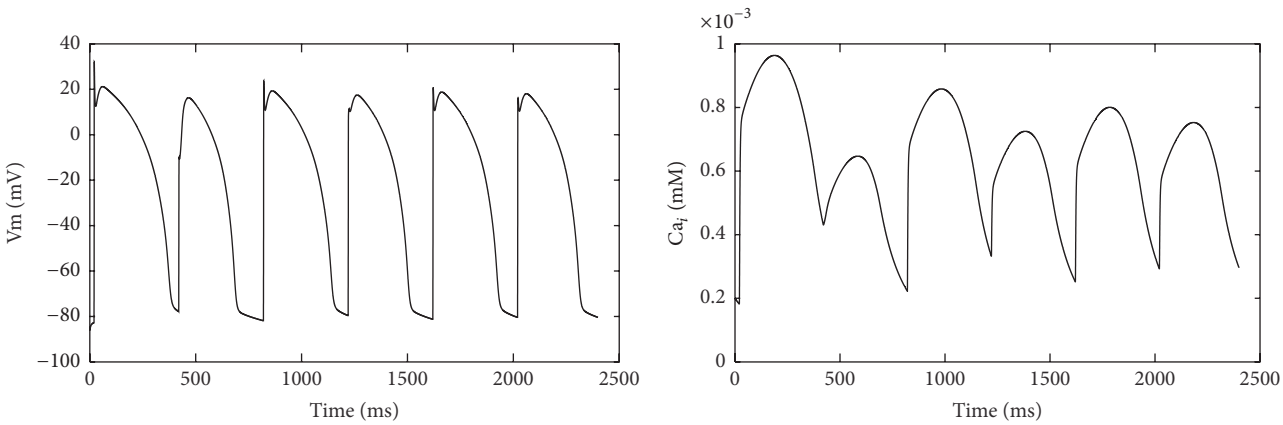

FIGURE 8: Ca transient and APs after decreasing I_{up} and increasing I_{NCX}. (a) Alternate APs; (b) Ca_i alternans. Decreased I_{up} produced Ca_i alternans; however, the magnitude of Ca_i alternans was larger after increasing I_{NCX}.

rates. In our simulation, the extent of unbalance between these currents shifted by increasing I_{NCX} at cycle length of 400 ms could be too small to produce stable alternans [27]. I_{Kr} and I_{Ks} contribute to the occurrence of APD alternans in ischemia [15]. I_{Kr} contributes most due to its larger amplitude.

5. Conclusion

In silico simulations have been carried out to investigate cellular mechanisms of cardiac alternans under pathological disorders including hyperkalemia, acidosis, and hypoxia. Pathophysiological changes in ischemia play a significant role in the development of cardiac alternans by affecting ionic currents. Hyperkalemic conditions delay the recovery of depolarization current I_{CaL}. Thus depolarization alternans occurs. Decreased I_{up} of Ca handling in ischemia promotes Ca_i alternans. A large I_{NCX} has the ability to translate alternans from Ca to APD. Studying changes of these ionic currents can help further understand cellular mechanisms of the genesis of alternans and form the basis of study of TWA in ischemia.

Appendix

The rate constants used in (2) are as follows:

$$\begin{aligned}
\alpha_1^+ &= k_1^+ \left[\mathrm{MgATP}\right], \\
\alpha_2^+ &= \frac{k_2^+ \widetilde{\mathrm{Ca}}_i^2}{\widetilde{\mathrm{Ca}}_i^{2+}\left(1+\widetilde{\mathrm{H}}_i\right)+\widetilde{\mathrm{H}}_i\left(1+\widetilde{\mathrm{H}}_1\right)}, \\
\alpha_3^+ &= \frac{k_3^+ \widetilde{\mathrm{H}}_{\mathrm{sr}}}{\widetilde{\mathrm{H}}\left(1+\widetilde{\mathrm{Ca}}_{\mathrm{sr}}^2\right)+\widetilde{\mathrm{H}}_{\mathrm{sr}}\left(1+\widetilde{\mathrm{H}}\right)}, \\
\alpha_1^- &= \frac{k_1^- \widetilde{\mathrm{H}}_i}{\widetilde{\mathrm{Ca}}_i^{2+}\left(1+\widetilde{\mathrm{H}}_i\right)+\widetilde{\mathrm{H}}_i\left(1+\widetilde{\mathrm{H}}_1\right)}, \\
\alpha_2^- &= \frac{k_2^- \left[\mathrm{MgADP}\right] \widetilde{\mathrm{Ca}}_{\mathrm{sr}}^2 \widetilde{\mathrm{H}}_{\mathrm{sr}}}{\widetilde{\mathrm{H}}\left(1+\widetilde{\mathrm{Ca}}_{\mathrm{sr}}^2\right)+\widetilde{\mathrm{H}}_{\mathrm{sr}}\left(1+\widetilde{\mathrm{H}}\right)}, \\
\alpha_3^- &= k_3^- \left[\mathrm{Pi}\right],
\end{aligned} \tag{A.1}$$

where

$$\begin{aligned}
\widetilde{\mathrm{Ca}}_i &= \frac{\left[\mathrm{Ca}^{2+}\right]_i}{K_{d,\mathrm{Ca}_i}}, \\
\widetilde{\mathrm{H}}_i &= \frac{\left[\mathrm{H}^+\right]}{K_{d,\mathrm{H}_i}}, \\
\widetilde{\mathrm{H}}_1 &= \frac{\left[\mathrm{H}^+\right]}{K_{d,\mathrm{H}_1}}, \\
\widetilde{\mathrm{Ca}}_{\mathrm{sr}} &= \frac{\left[\mathrm{Ca}^{2+}\right]_{\mathrm{sr}}}{K_{d,\mathrm{Ca}_{\mathrm{sr}}}}, \\
\widetilde{\mathrm{H}}_{\mathrm{sr}} &= \frac{\left[\mathrm{H}^+\right]}{K_{d,\mathrm{H}_{\mathrm{sr}}}}, \\
\widetilde{\mathrm{H}} &= \frac{\left[\mathrm{H}^+\right]}{K_{d,\mathrm{H}}}.
\end{aligned} \tag{A.2}$$

Competing Interests

The authors declare that there is no conflict of interests regarding the publication of this paper.

Acknowledgments

This project is supported in part by the National Natural Science Foundation of China (61527811), a key research grant for national fitness from General Administration of Sports

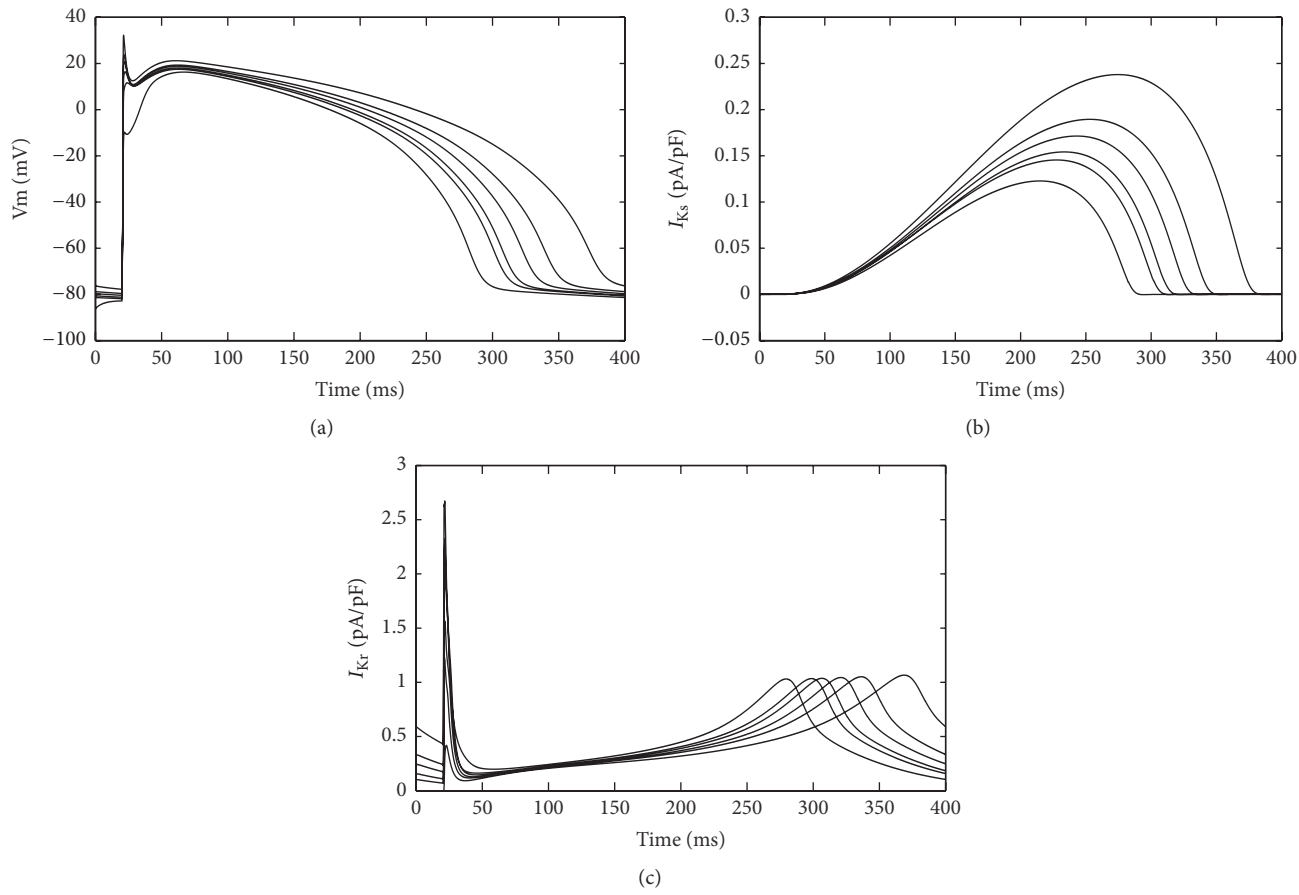

Figure 9: Alternate APs and two repolarization currents in consecutive beats after decreasing Iup and increasing I_{NCX}. (a) Consecutive APs in the same coordinate system. Repolarization alternans was obvious by comparing duration of action potentials; (b) beat-to-beat alternation in repolarization current I_{Ks}; (c) beat-to-beat alternation in repolarization current I_{Kr}.

of China (2015B043), and the National Science Foundation (CMMI-1234155).

References

[1] Z. Qu and J. N. Weiss, "Mechanisms of ventricular arrhythmias: from molecular fluctuations to electrical turbulence," *Annual Review of Physiology*, vol. 77, pp. 29–55, 2015.

[2] R. M. Shaw and Y. Rudy, "Electrophysiologic effects of acute myocardial ischemia: a theoretical study of altered cell excitability and action potential duration," *Cardiovascular Research*, vol. 35, no. 2, pp. 256–272, 1997.

[3] R. L. Verrier, T. Klingenheben, M. Malik et al., "Microvolt T-wave alternans: physiological basis, methods of measurement, and clinical utility—consensus guideline by international society for Holter and noninvasive Electrocardiology," *Journal of the American College of Cardiology*, vol. 58, no. 13, pp. 1309–1324, 2011.

[4] T. Chow, D. J. Kereiakes, C. Bartone et al., "Prognostic utility of microvolt T-wave alternans in risk stratification of patients with ischemic cardiomyopathy," *Journal of the American College of Cardiology*, vol. 47, no. 9, pp. 1820–1827, 2006.

[5] Z. Qu, Y. Xie, A. Garfinkel, and J. N. Weiss, "T-wave alternans and arrhythmogenesis in cardiac diseases," *Frontiers in Physiology*, vol. 1, article 154, 2010.

[6] D. Sato and C. E. Clancy, "Cardiac electrophysiological dynamics from the cellular level to the organ level," *Biomedical Engineering and Computational Biology*, vol. 5, pp. 69–75, 2013.

[7] Y.-L. Zang and L. Xia, "Cellular mechanism of cardiac alternans: an unresolved chicken or egg problem," *Journal of Zhejiang University: Science B*, vol. 15, no. 3, pp. 201–211, 2014.

[8] X. Zhou, A. Bueno-Orovio, M. Orini et al., "Population of human ventricular cell models calibrated with in vivo measurements unravels ionic mechanisms of cardiac alternans," in *Proceedings of the IEEE Computing in Cardiology Conference (CinC '13)*, Zaragoza, Spain, September 2013.

[9] M. L. Koller, S. K. G. Maier, A. R. Gelzer, W. R. Bauer, M. Meesmann, and R. F. Gilmour Jr., "Altered dynamics of action potential restitution and alternans in humans with structural heart disease," *Circulation*, vol. 112, no. 11, pp. 1542–1548, 2005.

[10] M. E. Díaz, S. C. O'Neill, and D. A. Eisner, "Sarcoplasmic reticulum calcium content fluctuation is the key to cardiac alternans," *Circulation Research*, vol. 94, no. 5, pp. 650–656, 2004.

[11] R. Rovetti, X. Cui, A. Garfinkel, J. N. Weiss, and Z. Qu, "Spark-induced sparks as a mechanism of intracellular calcium alternans in cardiac myocytes," *Circulation Research*, vol. 106, no. 10, pp. 1582–1591, 2010.

[12] X. Zhou, A. Bueno-Orovio, M. Orini et al., "In vivo and in silico investigation into mechanisms of frequency dependence of

repolarization alternans in human ventricular cardiomyocytes," *Circulation Research*, vol. 118, no. 2, pp. 266–278, 2016.

[13] E. Carmeliet, "Cardiac ionic currents and acute ischemia: from channels to arrhythmias," *Physiological Reviews*, vol. 79, no. 3, pp. 917–1017, 1999.

[14] S. Krause and M. L. Hess, "Characterization of cardiac sarcoplasmic reticulum dysfunction during short-term, normothermic, global ischemia," *Circulation Research*, vol. 55, no. 2, pp. 176–184, 1984.

[15] A. M. S. Dutta, J. Walmsley, and B. Rodriguez, "Ionic mechanisms of variability in electrophysiological properties in Ischemia: a population-based study," in *Proceedings of the IEEE Computing in Cardiology Conference (CinC '13)*, pp. 691–694, Zaragoza, Spain, September 2013.

[16] K. H. W. J. Ten Tusscher, D. Noble, P. J. Noble, and A. V. Panfilov, "A model for human ventricular tissue," *American Journal of Physiology—Heart and Circulatory Physiology*, vol. 286, no. 4, pp. H1573–H1589, 2004.

[17] K. Tran, N. P. Smith, D. S. Loiselle, and E. J. Crampin, "A thermodynamic model of the cardiac Sarcoplasmic/Endoplasmic Ca^{2+} (SERCA) pump," *Biophysical Journal*, vol. 96, no. 5, pp. 2029–2042, 2009.

[18] M. Makinose, "Possible functional states of the enzyme of the sarcoplasmic calcium pump," *FEBS Letters*, vol. 37, no. 2, pp. 140–143, 1973.

[19] L. D. Meis and A. L. Vianna, "Energy interconversion by the Ca^{2+}-dependent ATPase of the sarcoplasmic reticulum," *Annual Review of Biochemistry*, vol. 48, pp. 275–292, 1979.

[20] J. P. Ebus, Z. Papp, R. Zaremba, and G. J. M. Stienen, "Effects of MgATP on ATP utilization and force under normal and simulated ischaemic conditions in rat cardiac trabeculae," *Pflügers Archiv*, vol. 443, no. 1, pp. 102–111, 2001.

[21] A. F. De Castro, A. Giovanni, J. F. Rodriguez, and J. M. Ferrero, "Dynamic computational simulations of alternans in acute myocardial ischemia," in *Proceedings of the 41st IEEE Computing in Cardiology Conference (CinC '14)*, pp. 877–880, September 2014.

[22] I. Martišiene, J. Jurevičius, R. Vosyliute et al., "Evolution of action potential alternans in rabbit heart during acute regional ischemia," *BioMed Research International*, vol. 2015, Article ID 951704, 12 pages, 2015.

[23] J. Carro, J. F. Rodriguez, P. Laguna, and E. Pueyo, "A human ventricular cell model for investigation of cardiac arrhythmias under hyperkalaemic conditions," *Philosophical Transactions of the Royal Society of London, Series A: Mathematical, Physical and Engineering Sciences*, vol. 369, no. 1954, pp. 4205–4232, 2011.

[24] O. Bernus, C. W. Zemlin, R. M. Zaritsky, S. F. Mironov, and A. M. Pertsov, "Alternating conduction in the ischaemic border zone as precursor of reentrant arrhythmias: a simulation study," *Europace*, vol. 7, no. S2, pp. S93–S104, 2005.

[25] L.-H. Xie, D. Sato, A. Garfinkel, Z. Qu, and J. N. Weiss, "Intracellular Ca alternans: coordinated regulation by sarcoplasmic reticulum release, uptake, and leak," *Biophysical Journal*, vol. 95, no. 6, pp. 3100–3110, 2008.

[26] Z. Qu, M. B. Liu, and M. Nivala, "A unified theory of calcium alternans in ventricular myocytes," *Scientific Reports*, vol. 6, Article ID 35625, 2016.

[27] X. Wan, M. Cutler, Z. Song et al., "New experimental evidence for mechanism of arrhythmogenic membrane potential alternans based on balance of electrogenic INCX/ICa currents," *Heart Rhythm*, vol. 9, no. 10, pp. 1698–1705, 2012.

Hindawi Publishing Corporation
Computational and Mathematical Methods in Medicine
Volume 2016, Article ID 4576313, 8 pages
http://dx.doi.org/10.1155/2016/4576313

Research Article

Role of CaMKII and PKA in Early Afterdepolarization of Human Ventricular Myocardium Cell: A Computational Model Study

Ling Dai,[1] Yunliang Zang,[1] Dingchang Zheng,[2] Ling Xia,[1] and Yinglan Gong[1]

[1]*Department of Biomedical Engineering, Zhejiang University, Hangzhou, China*
[2]*Health and Wellbeing Academy, Faculty of Medical Science, Anglia Ruskin University, Chelmsford CM1 1SQ, UK*

Correspondence should be addressed to Ling Xia; xialing@zju.edu.cn and Yinglan Gong; yinglangong@zju.edu.cn

Received 11 June 2016; Accepted 31 October 2016

Academic Editor: Xiaopeng Zhao

Early afterdepolarization (EAD) plays an important role in arrhythmogenesis. Many experimental studies have reported that Ca^{2+}/calmodulin-dependent protein kinase II (CaMKII) and β-adrenergic signaling pathway are two important regulators. In this study, we developed a modified computational model of human ventricular myocyte to investigate the combined role of CaMKII and β-adrenergic signaling pathway on the occurrence of EADs. Our simulation results showed that (1) CaMKII overexpression facilitates EADs through the prolongation of late sodium current's (I_{NaL}) deactivation progress; (2) the combined effect of CaMKII overexpression and activation of β-adrenergic signaling pathway further increases the risk of EADs, where EADs could occur at shorter cycle length (2000 ms versus 4000 ms) and lower rapid delayed rectifier K^+ current (I_{Kr}) blockage (77% versus 85%). In summary, this study computationally demonstrated the combined role of CaMKII and β-adrenergic signaling pathway on the occurrence of EADs, which could be useful for searching for therapy strategies to treat EADs related arrhythmogenesis.

1. Introduction

Early afterdepolarizations (EADs) are triggered before the completion of repolarization [1] and associated with polymorphic ventricular tachyarrhythmia for long QT syndrome patients [2]. Prolongation of action potential duration (APD) and recovery of L-type Ca^{2+} current have been reported as two important factors for the occurrence of EADs [3]. It is also known that the increase of inward currents (e.g., I_{CaL} and late sodium current, I_{NaL}) or the decrease of outward currents (e.g., rapid delayed rectifier K^+ current, I_{Kr} and slow delayed rectifier K^+ current, I_{Ks}) at plateau membrane voltage could increase the probability of EADs events. Therefore, any factors that could change the intensity or time sequence of these currents may lead to the occurrence of EADs [4–8].

Ca^{2+}/calmodulin-dependent protein kinase II (CaMKII) is a key kinase in tuning cardiac excitation-contraction coupling. Its substrates include ion channels, transporters, and accessory proteins [9]. It has been reported that CaMKII phosphorylates I_{CaL}, leading to increased amplitude and APD prolongation and facilitating the occurrence of EADs [10, 11]. CaMKII can also alter I_{NaL}, transient outward K current (I_{to}), SR Ca^{2+}-ATPase (SERCA) [12], and ryanodine receptor (RyR) channels [10]. It would therefore be useful to understand and quantify these regulatory roles. However, it is very difficult for the laboratory experiments to achieve this. Computer modelling approaches provide alternative ways, allowing us to distinguish the most effective phosphorylation target of arrhythmogenesis, which would ultimately provide useful tool in searching for antiarrhythmia therapy.

It has been known that β-adrenergic signaling pathway regulates Ca^{2+} cycling partly via phosphorylation of I_{CaL} and phospholamban (PLB) [13]. I_{CaL} elevates intracellular Ca^{2+} ($[Ca]_i$) and increases spontaneous Ca^{2+} release via the SERCA inhibition by PLB. The broken balance of Ca^{2+} cycling may contribute to the occurrence of EADs [14–16]. Volders et al. investigated the ionic mechanisms of β-adrenergic on the occurrence of EADs in canine ventricular myocyte and concluded that cellular Ca^{2+} overload and spontaneous SR Ca^{2+} release played important roles in EADs [17].

On the contrary, other studies reported that β-adrenergic agonists activate protein kinase A (PKA), which phosphorylates I_{CaL}, RyR, PLB, SERCA, and I_{Ks}, resulting in delayed afterdepolarization (DADs) [18]. These numerous targets and different temporal characteristics of phosphorylation effects complicate the mechanism analysis of β-adrenergic agonists in relation to EADs. Recently, different computational models have been used to investigate these complex interactions. Xie et al. developed a biophysically detailed rabbit model and found that the faster time course of I_{CaL} versus I_{Ks} increased ISO-induced transient EADs [19] and emphasized the importance of understanding the nonsteady state of kinetics in meditating β-adrenergic-induced EADs and arrhythmia. However, other targets including I_{NaL} have not been investigated thoroughly in their model. It is noted that, although the computational studies of EAD mechanisms have been widely taken, the majority of these published modelling studies have been developed based on nonhuman myocyte. Furthermore, to the best of our knowledge, there is no modelling study considering the combined effect of CaMKII overexpression and β-adrenergic agonists on EADs.

This study aimed to develop a modified computational model of human ventricular myocyte that integrates CaMKII and β-adrenergic signaling networks into a modified ORd's dynamic model [20], with which the combined role of CaMKII and β-adrenergic signaling pathway on the occurrence of EADs would be investigated.

2. Methods

2.1. Integration of CaMKII. Since there is a lack of experimental measurements of human ventricle CaMKII pathway, O'Hara et al. used the Hund-Decker-Rudy's dog model to describe CaMKII kinetics [21, 22]. Our model was developed from the O'Hara-Rudy dynamic model (ORd model) to integrate CaMKII pathway [20]. The following equations describe the CaMKII kinetic of human ventricle:

$$\begin{aligned}
\mathrm{CaMK}_{\mathrm{bound}} &= \mathrm{CaMK}_0 \cdot \frac{1 - \mathrm{CaMK}_{\mathrm{trap}}}{1 + \mathrm{K}_{m\mathrm{CaM}} / \left[\mathrm{Ca}^{2+}\right]_{\mathrm{ss}}},\\
\mathrm{CaMK}_{\mathrm{active}} &= \mathrm{CaMK}_{\mathrm{bound}} + \mathrm{CaMK}_{\mathrm{trap}},\\
\frac{d\mathrm{CaMK}_{\mathrm{trap}}}{dt} &= \alpha_{\mathrm{CaMK}} \cdot \mathrm{CaMK}_{\mathrm{bound}} \cdot \left(\mathrm{CaMK}_{\mathrm{bound}} + \mathrm{CaMK}_{\mathrm{trap}}\right) - \beta_{\mathrm{CaMK}} \cdot \mathrm{CaMK}_{\mathrm{trap}},\\
&\alpha_{\mathrm{CaMK}} = 0.05\,\mathrm{ms}^{-1},\ \beta_{\mathrm{CaMK}} = 0.00068\ \mathrm{ms}^{-1},\ \mathrm{CaMK}_0 = 0.05,\ K_{m\mathrm{CaM}} = 0.0015\,\mathrm{mM}.
\end{aligned} \tag{1}$$

The fraction of active CaMKII binding sites at equilibrium state (CaMK_0) was set to 0.05 at the control state. CaMK_0 of 0.12 was used to simulate CaMKII overexpression according to the study from Kohlhaas et al. [23].

2.2. Integration of β-Adrenergic Signaling Networks. The detailed description of β-adrenergic signaling networks could be found from the published study by Soltis and Saucerman [24]. PKA has been reported to phosphorylate I_{CaL}, PLB, troponin I, RyR, myosin binding protein-C, protein phosphates Inhibitor-I [25], and I_{Ks} [24]. I_{CaL}, PLB, and I_{Ks} were the three key factors in this study to model the inotropic effect of β-adrenergic related to potential EADs occurrence. Although the PKA phosphorylation of Na^+/K^+ ATPase current (I_{NaK}) has been previously described in the computational models [19, 26], its effect was not included in this study partially because there is a lack of direct measurements of I_{NaK} for the normal human ventricle [20]. The phosphorylation by PKA to the three targets (I_{CaL}, PLB, and I_{Ks}) is described as follows:

$$f_{\mathrm{avail}} = 0.017 \cdot \frac{\mathrm{LCC}_{b\mathrm{PKA}_P}}{\mathrm{fracLCC}_{bp0}} + 0.983, \tag{2}$$

$$\mathrm{dss} = \frac{1}{1.0 + \exp\left(-\left(V + v\mathrm{shift}\right)/4.230\right)}, \tag{3}$$

$$\begin{aligned}
I_{\mathrm{CaL}} = {} & \left(\overline{I_{\mathrm{CaL}}} \cdot d \cdot \left(1 - \phi_{I_{\mathrm{CaL,CaMK}}}\right)\right.\\
& \cdot \left(f \cdot (1 - n) + f_{\mathrm{Ca}} \cdot n \cdot j_{\mathrm{Ca}}\right) + \overline{I_{\mathrm{CaL,CaMK}}} \cdot d\\
& \left. \cdot \phi_{I_{\mathrm{CaL,CaMK}}} \cdot \left(f_{\mathrm{CaMK}} \cdot (1 - n) + f_{\mathrm{Ca,CaMK}} \cdot n \cdot j_{\mathrm{Ca}}\right)\right)\\
& \cdot f_{\mathrm{avail}},
\end{aligned} \tag{4}$$

$$\Phi_{I_{\mathrm{CaL,CaMK}}} = \frac{1}{1 + \mathrm{K}m, \mathrm{CaMK}/\mathrm{CaMK}_{\mathrm{active}}}, \tag{5}$$

$$\begin{aligned}
td = 1.2 \cdot \Bigg(0.6 & \\
& + \frac{1}{\exp\left(-0.05 \cdot (V + 6.0)\right) + \exp\left(0.09 \cdot (V + 14.0)\right)}\Bigg).
\end{aligned} \tag{6}$$

Equation (2) shows the coefficient that represents the effect of PKA on I_{CaL} phosphorylation. In (3), the value of "$v$shift" was increased from 3.94 (no ISO application) to 10.0 (for saturated ISO application), which means that the steady state activation curve of I_{CaL} was moved left by 6.06 mV. The permeability of ion Ca^{2+} was increased by 10% with saturated ISO application. Equation (4) describes the augmentation of I_{CaL} amplitude by multiplying "f_{avail}" with the value without PKA phosphorylation, and this represents how PKA regulates

Table 1: Current increment and EADs occurrence when different targets were phosphorylated by CaMKII independently.

Cycle length (ms)	I_{Kr} blockage level (%)	CaMKII target ($CaMK_0 = 0.12$)	Target current variation	Deactivation time (ms)	EADs
2000	85	I_{NaL}	Decreased by 24% (from 0.25 to 0.19 μA/μF)	1297 versus 761 ms	Alternated
		I_{CaL}	Increased by 4.2% (from 1.67 to 1.74 μA/μF)		No
		I_{CaK}	Increased by 6.5% (from 0.62 to 0.66 μA/μF)		No
		I_{CaNa}	Increased by 8.1% (from 0.37 to 0.40 μA/μF)		No
		I_{to}	Increased by 3.2% (from 0.95 to 0.98 μA/μF)		No

I_{CaL}. In (6), the time constant of activation gate (td) was extended by 20% with saturated ISO application

$$\mathrm{frac}I_{\mathrm{Ksavail}} = 0.49 \cdot \frac{I_{\mathrm{KsPKA}_p}}{\mathrm{frac}I_{\mathrm{Ks}p0}} + 0.51, \quad (7)$$

$$\mathrm{GKs} = \mathrm{frac}I_{\mathrm{Ksavail}} \cdot \mathrm{GKs}, \quad (8)$$

$$Xs05 = 11.60 \cdot \mathrm{frac}I_{\mathrm{Ksavail}}, \quad (9)$$

$$X_{S1,\infty} = \frac{1}{1 + \exp\left(-\left(V + Xs05\right)/8.932\right)}. \quad (10)$$

Equation (7) describes the factor of phosphorylation to I_{Ks} by PKA, which was used to alter maximum conductance of I_{Ks} (GKs) in (8). Meanwhile, I_{Ks} state steady activation curve was adjusted by time dependent gate value through the factor "$\mathrm{frac}I_{\mathrm{Ksavail}}$" in (9) and (10).

2.3. Combination of CaMKII and β-Adrenergic Signaling Networks.

$$f\mathrm{PKA}_{\mathrm{PLB}} = \left(\frac{\mathrm{PLB\_PKA}_n}{\mathrm{fracPKA}_{\mathrm{PLB}_0}}\right) \cdot \frac{1}{4} + \frac{3}{4}, \quad (11)$$

$$f\mathrm{Jupp} = \frac{1.0}{\left(1.0 + \mathrm{K}_{m,\mathrm{CaMK}} \cdot \left(f\mathrm{PKA}_{\mathrm{PLB}}/\mathrm{CaMK}_{\mathrm{active}}\right)\right)}, \quad (12)$$

$$\mathrm{Jup} = \left(1.0 - f\mathrm{Jupp}\right) \cdot \mathrm{Jupnp} + f\mathrm{Jupp} \cdot \mathrm{Jupp} - \mathrm{Jleak}. \quad (13)$$

$\mathrm{CaMK}_{\mathrm{active}}$ that is affected by CaMK_0 as shown in (1) would influence I_{CaL} in (4) via the fraction of I_{CaL} channels phosphorylated by CaMKII ($\Phi_{I_{\mathrm{CaL,CaMK}}}$). The fraction of SERCAs phosphorylated by CaMKII in (12) was affected by "$f\mathrm{PKA}_{\mathrm{PLB}}$" and "$\mathrm{CaMK}_{\mathrm{active}}$", representing the effects of PKA and CaMKII on SERCAs, respectively. As shown in (13), SERCAs were separated into nonphosphorylated populations and CaMKII phosphorylated populations. Therefore, the total Ca^{2+} uptake via SERCAs was adjusted by these two networks simultaneously.

2.4. Simulation Strategy. In order to determine the potential targets in CaMKII-induced EADs, CaMKII was solely overexpressed by assigning the CaMK_0 of 0.12 to specific targets (including I_{NaL}, I_{CaL}, I_{CaK}, I_{NaCa}, and I_{to}), respectively, while β-adrenergic signaling was maintained inactive. Next, CaMKII overexpression was applied with ISO administration. 1 μM ISO was applied in this study to simulate its effect on myocyte action potential and ion currents.

The cycle length of 2000 ms was used in this study since it was closer to normal human beat rhythm than the length of 4000 ms used in the experiments from Guo et al. [27]. In Guo et al.'s work, EADs appeared with I_{Kr} blockage of about 85% [27], which was used for comparison in this study. 500 cycles were performed when the simulation reached steady state. In each individual cycle length, the upper bound of solver step size was set 2 ms.

3. Results

3.1. Effect of CaMKII Overexpression on Ion Currents

3.1.1. Late Sodium Current (I_{NaL}). As shown in Table 1 and Figure 1, with the overexpressed CaMK_0 value to I_{NaL} of 0.12 and the normal CaMK_0 value of 0.05 to other targets, the alternated EADs occur from our simulation with the cycle length (CL) of 2000 ms and I_{Kr} blockage of 85%.

As shown in Figure 1, I_{NaL} amplitudes alternated with overexpressed CaMK_0. In beats with EADs, I_{NaL} amplitude was about 24% smaller (0.19 μA/μF versus 0.25 μA/μF) than these with normal CaMK_0 value to I_{NaL} and in beats without EADs, I_{NaL} amplitude was also reduced by 32% (0.17 μA/μF versus 0.25 μA/μF). In Figure 1(d), when EADs occurred, I_{NaL} deactivated, which was about 168% of normal beats (1297 ms versus 773 ms) and about 170% of the control situation in Figure 1(b) (1297 ms versus 761 ms), indicating that overexpressed CaMKII phosphorylation level of I_{NaL} reduces its amplitude and prolongs I_{NaL} deactivation process. Furthermore, the results also indicate that the delayed deactivation of I_{NaL}, rather than its amplitude variation, contributes to the formation of EADs.

3.1.2. L-Type Calcium Current (I_{CaL}). Similarly, as shown in Table 1, with the overexpressed CaMK_0 to I_{CaL} of 0.12 and

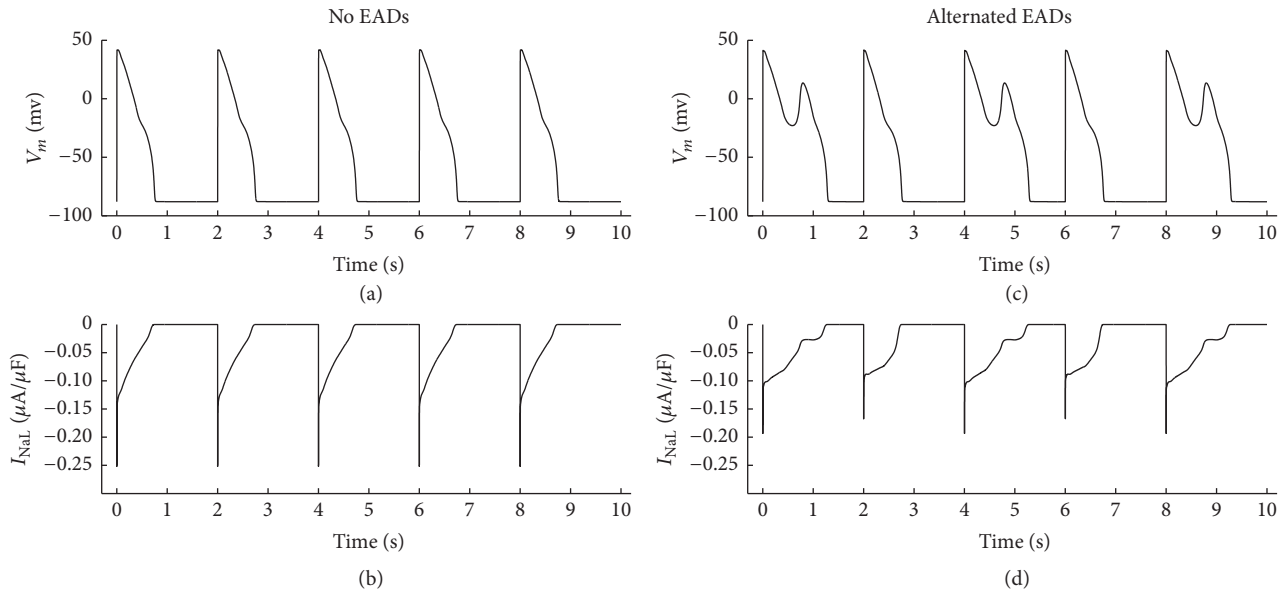

Figure 1: (a) No EAD was produced when CaMKII phosphorylation level was in control ($CaMK_0 = 0.05$). (b) Corresponding I_{NaL} when no EADs occurred in (a). (c) Alternated EADs were produced when I_{NaL} phosphorylation by CaMKII was enhanced with $CaMK_0$ of 0.12 and other targets' phosphorylation levels were in control ($CaMK_0 = 0.05$). (d) Corresponding I_{NaL} when alternated EADs occurred in (c). Under these conditions, CL was 2000 ms and I_{Kr} was blocked by 85%.

Table 2: Combined effect of CaMKII overexpression and β-adrenergic agonist on EADs.

Cycle length (ms)	ISO application	CaMKII target ($CaMK_0$ = 0.12)	I_{Kr} blockage level (%)	EADs
2000	None	None	85	None
		None	85	Yes
		None	77	No
	1 μM	I_{NaL}	85	Yes
		I_{NaL}	77	Yes
		I_{CaL}	85	Yes
		I_{CaL}	77	No

the normal $CaMK_0$ value of 0.05 to other targets, no EADs occur at CL of 2000 ms and I_{Kr} blockage of 85%, suggesting that the probability of EADs might have little relation with amplitude of I_{CaL}. With the enhanced $CaMK_0$ value to I_{CaL}, the amplitudes of I_{CaL} only increased by 4.2% (1.74 μA/μF versus 1.67 μA/μF).

3.1.3. K^+ Current through the L-Type Ca^{2+} Channel (I_{CaK}), Na^+ Current through the L-Type Ca^{2+} Channel (I_{CaNa}), and Transient Outward K^+ Current (I_{to}). As above, CL was set to 2000 ms and I_{Kr} was blocked by 85%. As shown in Table 1, with enhanced CaMKII phosphorylation level ($CaMK_0$ = 0.12) to different targets, I_{CaK} increased only by 6.5% (0.66 μA/μF versus 0.62 μA/μF), I_{CaNa} by 8.1% (0.40 μA/μF versus 0.37 μA/μF), and I_{to} by 3.2% (0.98 μA/μF versus 0.95 μA/μF). No EADs occurred under all these conditions.

3.2. Combined Effect of CaMKII Overexpression and β-Adrenergic Agonist

3.2.1. Normal CaMKII and 1 μM ISO. The action potentials with different I_{Kr} blockage level are shown in Figure 2. A fixed CL =2000 ms was used and CaMKII phosphorylation level to all targets was kept control ($CaMK_0 = 0.05$). In Figure 2(a), with I_{Kr} blocked by 85%, stable EADs occurred with the application of ISO, indicating that β-adrenergic agonist facilitates EADs. The I_{Kr} blockage level decreased gradually from 85%, and, when it was decreased to 77%, as shown in Figure 2(b), these EADs disappeared, indicating that 77% was the threshold value for EADs disappearance in this setting. Therefore, 77% was used in following simulation to compare with previously published level of 85% [20]. These results are listed from row 2 to row 3 in Table 2.

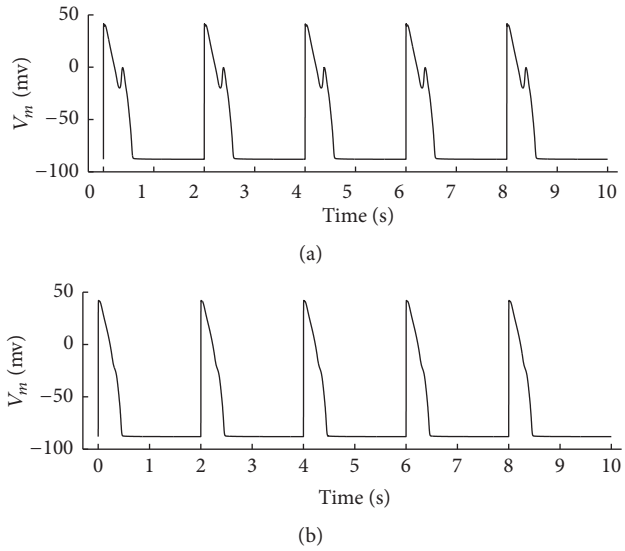

Figure 2: (a) EADs were induced when 1 μM ISO was applied and I_{Kr} was blocked by 85%. In (b), EADs disappeared when I_{Kr} blockage was reduced to 77%. Cycle length was set 2000 ms and CaMKII phosphorylation level to all targets was kept control ($CaMK_0 = 0.05$).

3.2.2. Enhanced CaMKII to I_{NaL} and 1 μM ISO. As shown in Figure 3, with enhanced CaMKII to I_{NaL} and 1 μM ISO, when I_{Kr} was blocked by 85%, EADs were induced. The EADs were still observed when I_{Kr} was blocked by 77%, suggesting that I_{NaL} phosphorylation by CaMKII and ISO application together increased the probability of EADs. These results are listed from row 4 to row 5 in Table 2.

3.2.3. Enhanced CaMKII to I_{CaL} and 1 μM ISO. As shown in Figure 4, with enhanced CaMKII to I_{CaL} and 1 μM ISO, when I_{Kr} was blocked by 85%, EADs were induced, but when I_{Kr} blockage was reduced to 77%, EADs disappeared. These results are listed from row 6 to row 7 in Table 2.

4. Discussion

This study developed a modified computational model of human ventricular myocardium cell based on the ORd human model with the integration of regulation mechanism by CaMKII and PKA [20], with which their effects on EADs have been investigated.

EADs often occur during bradycardia under the condition of reduced repolarization reserve. O'Hara's group successfully elicited EADs with cycle length reduced to 4000 ms and I_{Kr} blocked by 85% [20]. In our simulation, with the cycle length halved (2000 ms) and I_{Kr} blocked by 85%, alternated EADs occurred with the sole effect of CaMKII overexpression to I_{NaL}, suggesting that ventricular myocardial cell with CaMKII overexpression is more susceptible to EADs in normal HR range (CL = 2000 ms). Additionally, previous work has shown that I_{CaL} plays an important role in the occurrence of EADs [6]. Our simulation showed that CaMKII overexpression slightly increased I_{CaL} amplitude, but this effect alone did not induce EADs, and CaMKII did not alter the overlap region of I_{CaL} steady state activation and reactivation curves. Zaza et al. reported that [28], when repolarization is suitably slow, channel reactivation within the overlap region may break the current balance and support the possibility of autoregenerative depolarization. Other inward currents such as Na^+-Ca^{2+} exchange current (I_{NaCa}) may play certain roles in triggering EADs if amplitude is augmented and falls into the overlap region. Our simulation results suggest that CaMKII enhances these currents but does not induce EADs via this effect individually. Therefore, when CaMKII is overexpressed, the susceptibility to EADs is mainly originated from I_{NaL} variation.

Our study also demonstrated the behavior of ventricular myocardial cell with the integration of CaMKII overexpression and ISO application. With the ISO application, cyclic AMP (cAMP) is formed through β-adrenergic mediated activation of adenylyl cyclase, which activates PKA, a well-described mediator with targets that promote myocardial performance. In the case where PKA took effect independently, EADs occurred with shorter cycle length (2000 ms versus 4000 ms), indicating that the precondition of EADs is relaxed. Our results were different from that from Xie et al.'s study, where the APD shortening after ISO application was observed without EADs in steady state [19]. Xie et al.'s results could be caused by the simulation of transient I_{CaL} recovery and the prevented spontaneous SR Ca^{2+} release, limiting the I_{NaCa} in forward mode. Therefore, when the cells step into steady state with small inward I_{NaCa}, the shortening of APD could be reasonable. In our work, SR Ca^{2+} release was enhanced by I_{CaL} amplification. With the integration with I_{Kr} blockage, I_{NaCa} was more likely to work as inward current, contributing to the prolongation of APD and occurrence of EADs. Additionally, the shortening of APD was also obtained without I_{Kr} blockage when β-adrenergic pathway was activated. Simulation results showed that when cycle length was chosen at 500 ms, 1000 ms, 1500 ms, 2000 ms, and 4000 ms, the corresponding APD90 shortening was 31.6 ms (233.0 versus 201.4 ms), 30.5 ms (268.6 versus 238.1 ms), 22.3 ms (282.6 versus 260.3 ms), 17.3 ms (289.1 versus 271.8 ms), and 18.6 ms (305.6 versus 287.0 ms). These results were consistent with the experiment measurements from Volders et al. [29]. In the case that CaMKII overexpression acted on I_{NaL} alone with ISO application, EADs occur at CL = 2000 ms and I_{Kr} blockage by 77%, suggesting that the combination of PKA and CaMKII overexpression on I_{NaL} relaxes the precondition further (I_{Kr} blockage 77% versus 85%) and increases the probability of EADs. With the CaMKII overexpressed on I_{CaL} alone, PKA induced EADs occurrence with 85% I_{Kr} blockage, not 77% I_{Kr} blockage, suggesting that, with the ISO application, I_{NaL} phosphorylation by CaMKII has more effect on EADs than I_{CaL}. The steady state of $CaMK_{active}$ was simulated with and without ISO application when CL = 2000 ms, and their corresponding maximum values were 0.0469 and 0.0421, respectively. This suggests that CaMKII activation increased with the application of ISO.

Our simulation results have shown that our proposed model is useful for exploring the interaction of β-adrenergic receptor signaling and CaMKII in formation of EADs; some

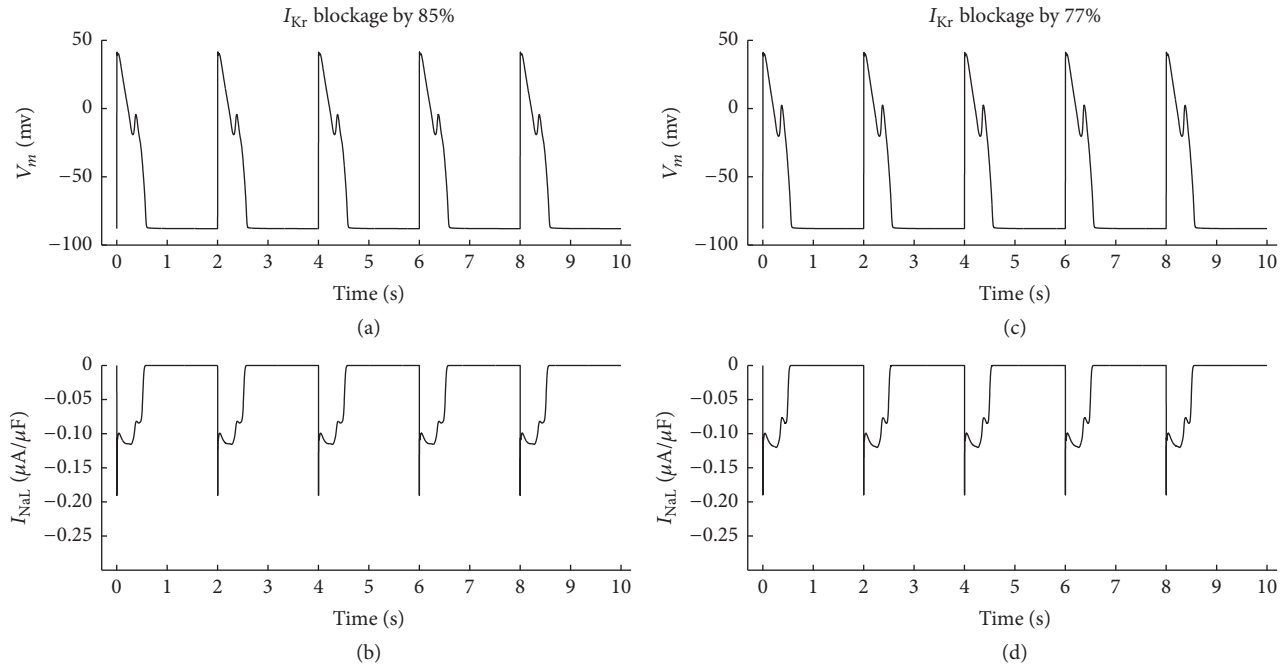

Figure 3: EADs occurred when I_{Kr} was blocked by 85% (a) and 77% (c); corresponding I_{NaL} when I_{Kr} was blocked by 85% (b) and 77% (d). CL was set 2000 ms, 1 μM ISO was applied and $CaMK_0$ for I_{NaL} was set 0.12 independently.

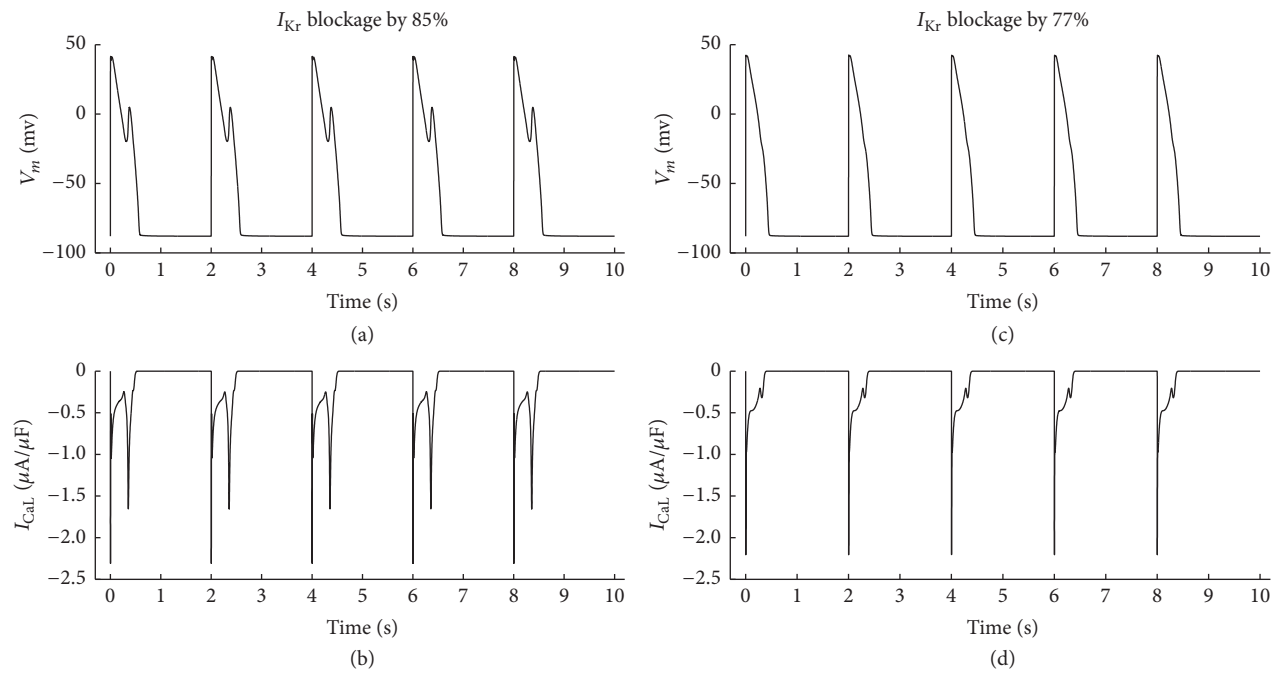

Figure 4: 1 μM ISO was applied and cycle length was 2000 ms. $CaMK_0$ for I_{CaL} was 0.12 but $CaMK_0$ for other targets was 0.05. EADs occurred when I_{Kr} was blocked by 85% in (a), but when I_{Kr} blockage was reduced to 77%, EADs vanished in (c). (b) I_{CaL} figures when EADs existed. (d) I_{CaL} figures when EADs vanished.

potential limitations need to be addressed. Firstly, the role of CaMKII on RyR function has not been considered. There is growing evidence about its role in modulating RyR function. Increasing Ca^{2+} leak via RyR would limit SR Ca^{2+} load and disturb Ca^{2+} cycling. This should be incorporated into an improved model in a future study. Secondly, CaMKII overexpression may downregulate inward rectifier potassium current (I_{K1}) and increase baseline I_{K1} amplitude [30]. We did not include any CaMKII effect on I_{K1} in our model. Thirdly, our model only describes the short-term effect of CaMKII

on different current targets. It has been suggested that short-term and chronic effects of CaMKII are different [30–33]. Short-term (milliseconds to hours) CaMKII overexpression may slow I_{to} inactivation and accelerate recovery, but chronic overexpression may downregulate $I_{to,fast}$ and upregulate $I_{to,slow}$ [34]. Therefore, there is a scope to improve our model by taking chronic effects of CaMKII into consideration in future. Fourthly, there is a lack of an accurate measurement about how ISO regulates I_{NaK} with dynamic calcium change during the beat cycle, although it has been published by Gao et al. [35] that ISO regulated I_{NaK} increased (when calcium is 1.4 μM) or decreased in pump current (when calcium is 0.15 μM) depending on the intracellular Ca^{2+} concentrations. In our model the resting calcium concentration was 0.12 μM and the peak calcium concentration was 1.1 μM. Similar to the simulation work of Heijman et al. [26], by simply increasing the pump current from 17% to 33%, no significant change of I_{NaK} in triggering EADs (results not shown here) has been observed. However, when the continuous experimental data from human ventricular cells is available, the regulation of ISO on I_{NaK} could be incorporated into the model to reconfirm this nonsignificant effect. Fifthly, it has been reported that local regulation of cAMP and substrate phosphorylation play important roles in β-adrenergic receptor signaling [26, 36–38], so it could be useful to incorporate local control mechanism in a future study. Lastly, there are four CaMKII isoforms ($\alpha, \beta, \gamma, \delta$) with different distributions, kinetics, and roles in physiological and pathological adjustments. Until now, these differences have not been fully understood. Developing a model with detailed CaMKII isoforms information could be useful when experiment data are available.

In conclusion, our simulation results computationally demonstrated a better understanding of the combinational effect of CaMKII and ISO stimulus on the occurrence of EADs in human ventricular myocyte, which may provide useful tool to research therapeutic methods for the treatment of arrhythmia.

Competing Interests

The authors declare that there is no conflict of interests regarding the publication of this paper.

Acknowledgments

This project is supported by the National Natural Science Foundation of China (61527811).

References

[1] P. F. Cranefield and R. S. Aronson, *Cardiac Arrhythmias: The Role of Triggered Activity and Other Mechanisms*, Futura Publishing Company, New York, NY, USA, 1988.

[2] J. N. Weiss, A. Garfinkel, H. S. Karagueuzian, P.-S. Chen, and Z. Qu, "Early afterdepolarizations and cardiac arrhythmias," *Heart Rhythm*, vol. 7, no. 12, pp. 1891–1899, 2010.

[3] J. Zeng and Y. Rudy, "Early afterdepolarizations in cardiac myocytes: mechanism and rate dependence," *Biophysical Journal*, vol. 68, no. 3, pp. 949–964, 1995.

[4] C. Antzelevitch, Z.-Q. Sun, Z.-Q. Zhang, and G.-X. Yan, "Cellular and ionic mechanisms underling erythromycin-induced long QT intervals and Torsade de Pointes," *Journal of the American College of Cardiology*, vol. 28, no. 7, pp. 1836–1848, 1997.

[5] W. Shimizu and C. Antzelevitch, "Sodium channel block with mexiletine is effective in reducing dispersion of repolarization and preventing torsade de pointes in LQT2 and LQT3 models of the long-QT syndrome," *Circulation*, vol. 96, no. 6, pp. 2038–2047, 1997.

[6] C. T. January, J. M. Riddle, and J. J. Salata, "A model for early afterdepolarizations: Induction with the Ca^{2+} channel agonist Bay K 8644," *Circulation Research*, vol. 62, no. 3, pp. 563–571, 1988.

[7] C. T. January and J. M. Riddle, "Early afterdepolarizations: mechanism of induction and block. A role for L-type Ca2+ current," *Circulation Research*, vol. 64, no. 5, pp. 977–990, 1989.

[8] R. V. Madhvani, Y. Xie, A. Pantazis et al., "Shaping a new Ca^{2+} conductance to suppress early afterdepolarizations in cardiac myocytes," *The Journal of Physiology*, vol. 589, no. 24, pp. 6081–6092, 2011.

[9] P. J. Mohler and T. J. Hund, "Role of CaMKII in cardiovascular health, disease, and arrhythmia," *Heart Rhythm*, vol. 8, no. 1, pp. 142–144, 2011.

[10] Y. Wu, J. Temple, R. Zhang et al., "Calmodulin kinase II and arrhythmias in a mouse model of cardiac hypertrophy," *Circulation*, vol. 106, no. 10, pp. 1288–1293, 2002.

[11] Y. L. Hashambhoy, J. L. Greenstein, and R. L. Winslow, "Role of CaMKII in RyR leak, EC coupling and action potential duration: a computational model," *Journal of Molecular and Cellular Cardiology*, vol. 49, no. 4, pp. 617–624, 2010.

[12] P. D. Swaminathan, A. Purohit, T. J. Hund, and M. E. Anderson, "Calmodulin-dependent protein kinase II: linking heart failure and arrhythmias," *Circulation Research*, vol. 110, no. 12, pp. 1661–1677, 2012.

[13] D. M. Bers, *Excitation-Contraction Coupling and Cardiac Contractile Force*, Kluwer/Academic Publishers, Boston, Mass, USA, 2nd edition, 2001.

[14] S. C. Verduyn, M. A. Vos, A. P. Gorgels, J. Van der Zande, J. D. M. Leunissen, and H. J. Wellens, "The effect of flunarizine and ryanodine on acquired torsades de pointes arrhythmias in the intact canine heart," *Journal of Cardiovascular Electrophysiology*, vol. 6, no. 3, pp. 189–200, 1995.

[15] L. Carlsson, L. Drews, and G. Duker, "Rhythm anomalies related to delayed repolarization in vivo: Influence of sarcolemmal Ca^{2+} entry and intracellular Ca^{2+} overload," *Journal of Pharmacology and Experimental Therapeutics*, vol. 279, no. 1, pp. 231–239, 1996.

[16] Z. Song, C. Y. Ko, M. Nivala, J. N. Weiss, and Z. Qu, "Complex darly and delayed afterdepolarization dynamics caused by voltage-calcium coupling in cardiac myocytes," *Biophysical Journal*, vol. 108, no. 8, pp. 261A–262A, 2015.

[17] P. G. A. Volders, A. Kulcsár, M. A. Vos et al., "Similarities between early and delayed afterdepolarizations induced by isoproterenol in canine ventricular myocytes," *Cardiovascular Research*, vol. 34, no. 2, pp. 348–359, 1997.

[18] C. T. January and H. A. Fozzard, "Delayed afterdepolarizations in heart muscle: mechanisms and relevance," *Pharmacological Reviews*, vol. 40, no. 3, pp. 219–227, 1988.

[19] Y. Xie, E. Grandi, J. L. Puglisi, D. Sato, and D. M. Bers, "β-Adrenergic stimulation activates early afterdepolarizations

transiently via kinetic mismatch of PKA targets," *Journal of Molecular and Cellular Cardiology*, vol. 58, no. 1, pp. 153–161, 2013.

[20] T. O'Hara, L. Virág, A. Varró, and Y. Rudy, "Simulation of the undiseased human cardiac ventricular action potential: model formulation and experimental validation," *PLoS Computational Biology*, vol. 7, no. 5, Article ID e1002061, 2011.

[21] K. F. Decker, J. Heijman, J. R. Silva, T. J. Hund, and Y. Rudy, "Properties and ionic mechanisms of action potential adaptation, restitution, and accommodation in canine epicardium," *American Journal of Physiology—Heart and Circulatory Physiology*, vol. 296, no. 4, pp. H1017–H1026, 2009.

[22] T. J. Hund and Y. Rudy, "Rate dependence and regulation of action potential and calcium transient in a canine cardiac ventricular cell model," *Circulation*, vol. 110, no. 20, pp. 3168–3174, 2004.

[23] M. Kohlhaas, T. Zhang, T. Seidler et al., "Increased sarcoplasmic reticulum calcium leak but unaltered contractility by acute CaMKII overexpression in isolated rabbit cardiac myocytes," *Circulation Research*, vol. 98, no. 2, pp. 235–244, 2006.

[24] A. R. Soltis and J. J. Saucerman, "Synergy between CaMKII substrates and β-adrenergic signaling in regulation of cardiac myocyte Ca^{2+} handling," *Biophysical Journal*, vol. 99, no. 7, pp. 2038–2047, 2010.

[25] M. J. Lohse, S. Engelhardt, and T. Eschenhagen, "What is the role of β-adrenergic signaling in heart failure?" *Circulation Research*, vol. 93, no. 10, pp. 896–906, 2003.

[26] J. Heijman, P. G. A. Volders, R. L. Westra, and Y. Rudy, "Local control of β-adrenergic stimulation: effects on ventricular myocyte electrophysiology and Ca^{2+}-transient," *Journal of Molecular and Cellular Cardiology*, vol. 50, no. 5, pp. 863–871, 2011.

[27] D. Guo, Q. Liu, T. Liu et al., "Electrophysiological properties of HBI-3000: a new antiarrhythmic agent with multiple-channel blocking properties in human ventricular myocytes," *Journal of Cardiovascular Pharmacology*, vol. 57, no. 1, pp. 79–85, 2011.

[28] A. Zaza, L. Belardinelli, and J. C. Shryock, "Pathophysiology and pharmacology of the cardiac 'late sodium current'," *Pharmacology and Therapeutics*, vol. 119, no. 3, pp. 326–339, 2008.

[29] P. G. A. Volders, M. Stengl, J. M. Van Opstal et al., "Probing the contribution of IKs to canine ventricular repolarization: key role for β-adrenergic receptor stimulation," *Circulation*, vol. 107, no. 21, pp. 2753–2760, 2003.

[30] S. Wagner, E. Hacker, E. Grandi et al., "Ca/calmodulin kinase II differentially modulates potassium currents," *Circulation: Arrhythmia and Electrophysiology*, vol. 2, no. 3, pp. 285–294, 2009.

[31] S. Tessier, P. Karczewski, E.-G. Krause et al., "Regulation of the transient outward K+ current by Ca2+/calmodulin- dependent protein kinases II in human atrial myocytes," *Circulation Research*, vol. 85, no. 9, pp. 810–819, 1999.

[32] O. Colinas, M. Gallego, R. Setién, J. R. López-López, M. T. Pérez-García, and O. Casis, "Differential modulation of Kv4.2 and Kv4.3 channels by calmodulin-dependent protein kinase II in rat cardiac myocytes," *American Journal of Physiology—Heart and Circulatory Physiology*, vol. 291, no. 4, pp. H1978–H1987, 2006.

[33] G. P. Sergeant, S. Ohya, J. A. Reihill et al., "Regulation of $K_v4.3$ currents by Ca^{2+}/calmodulin-dependent protein kinase II," *American Journal of Physiology—Cell Physiology*, vol. 288, no. 2, pp. C304–C313, 2005.

[34] M. E. Anderson, J. H. Brown, and D. M. Bers, "CaMKII in myocardial hypertrophy and heart failure," *Journal of Molecular and Cellular Cardiology*, vol. 51, no. 4, pp. 468–473, 2011.

[35] J. Gao, R. Wymore, R. T. Wymore et al., "Isoform-specific regulation of the sodium pump by α- and β-adrenergic agonists in the guinea-pig ventricle," *The Journal of Physiology*, vol. 516, no. 2, pp. 377–383, 1999.

[36] V. O. Nikolaev, A. Moshkov, A. R. Lyon et al., "β_2-Adrenergic receptor redistribution in heart failure changes cAMP compartmentation," *Science*, vol. 327, no. 5973, pp. 1653–1657, 2010.

[37] P. T. Wright, V. O. Nikolaev, T. O'Hara et al., "Caveolin-3 regulates compartmentation of cardiomyocyte beta2-adrenergic receptor-mediated cAMP signaling," *Journal of Molecular and Cellular Cardiology*, vol. 67, pp. 38–48, 2014.

[38] R. V. Iancu, S. W. Jones, and R. D. Harvey, "Compartmentation of cAMP signaling in cardiac myocytes: a computational study," *Biophysical Journal*, vol. 92, no. 9, pp. 3317–3331, 2007.

Hindawi Publishing Corporation
Computational and Mathematical Methods in Medicine
Volume 2016, Article ID 7861653, 17 pages
http://dx.doi.org/10.1155/2016/7861653

Research Article

In Silico Evaluation of the Potential Antiarrhythmic Effect of Epigallocatechin-3-Gallate on Cardiac Channelopathies

Maroua Boukhabza,[1] Jaouad El Hilaly,[1,2,3] Nourdine Attiya,[2] Ahmed El-Haidani,[4] Younes Filali-Zegzouti,[2] Driss Mazouzi,[1,2] and Mohamed-Yassine Amarouch[1,2]

[1]*Materials, Natural Substances, Environment and Modeling Laboratory, Multidisciplinary Faculty of Taza, University Sidi Mohamed Ben Abdellah, Fez, Morocco*
[2]*Biology, Environment & Health Team, Department of Biology, Faculty of Sciences and Techniques Errachidia, University of Moulay Ismaïl, Meknes, Morocco*
[3]*Department of Life and Earth Sciences, Regional Institute of Education and Training Careers, Fez, Morocco*
[4]*Team of Nutritional Physiology and Endocrine Pharmacology, Department of Biology, Faculty of Sciences and Techniques Errachidia, University of Moulay Ismaïl, Meknes, Morocco*

Correspondence should be addressed to Mohamed-Yassine Amarouch; mohamed.amarouch@usmba.ac.ma

Received 11 August 2016; Revised 21 September 2016; Accepted 29 September 2016

Academic Editor: Sharon Zlochiver

Ion channels are transmembrane proteins that allow the passage of ions according to the direction of their electrochemical gradients. Mutations in more than 30 genes encoding ion channels have been associated with an increasingly wide range of inherited cardiac arrhythmias. In this line, ion channels become one of the most important molecular targets for several classes of drugs, including antiarrhythmics. Nevertheless, antiarrhythmic drugs are usually accompanied by some serious side effects. Thus, developing new approaches could offer added values to prevent and treat the episodes of arrhythmia. In this sense, green tea catechins seem to be a promising alternative because of the significant effect of Epigallocatechin-3-Gallate (E3G) on the electrocardiographic wave forms of guinea pig hearts. Thus, the aim of this study was to evaluate the benefits-risks balance of E3G consumption in the setting of ion channel mutations linked with aberrant cardiac excitability phenotypes. Two gain-of-function mutations, $Na_{v1.5}$-p.R222Q and $Na_{v1.5}$-p.I141V, which are linked with cardiac hyperexcitability phenotypes were studied. Computer simulations of action potentials (APs) show that 30 μM E3G reduces and suppresses AP abnormalities characteristics of these phenotypes. These results suggest that E3G may have a beneficial effect in the setting of cardiac sodium channelopathies displaying a hyperexcitability phenotype.

1. Introduction

Ion channels are transmembrane proteins that allow the passage of ions according to the direction of their electrochemical gradients across cell membranes. They are pore-forming membrane proteins whose normal function is critical for several physiological processes in cells. In excitable cells, such as cardiac cells, the activity of these proteins maintains the resting membrane potential and generates action potentials that are essential for excitation-contraction coupling process.

Ion channel dysfunction is the principal pathophysiological mechanism underlying various inherited forms of arrhythmic disorders, also called channelopathies [1]. In cardiac cells, mutations in more than 30 genes encoding ion channels have been associated with an increasingly wide range of inherited cardiac arrhythmias [1]. Examples of genetic cardiac disorders include congenital ectopic Purkinje-related premature contractions (MEPPC) and exercise induced polymorphic ventricular tachycardia (EPVT) which have been linked to the presence of the $Na_{v1.5}$-p.R222Q and $Na_{v1.5}$-p.I141V mutations [2–4].

The ECG of the $Na_{v1.5}$-p.R222Q carriers displayed atrial fibrillation, narrow junctional, and rare sinus beats competing with numerous premature ventricular contractions. The observed arrhythmia disappears under exercise [2, 3]. For $Na_{v1.5}$-p.I141V carriers, the ECG is characterized by

Table 1: Formulation of WT and mutated sodium channels ($Na_{v1.5}$-p.R222Q and $Na_{v1.5}$-p.I141V) in the presence or absence of 30 μM of E3G. The bold font corresponds to mutations effect and the bold-italic font to E3G effects.

	TNNP/SANNBZ models, p.R222Q.I_{Na}	TNNP/SANNBZ models, p.I141V.I_{Na}	TNNP/SANNBZ models, I_{CaL}	TNNP/SANNB models, I_{Ks}
WT	m_∞, WT (V_m) = m_∞, WT (V_m) α_m, WT (V_m) = α_m, WT (V_m) β_m WT (V_m) = β_m, WT (V_m) h_∞, WT (V_m) = h_∞, WT (V_m) β_hWT (V_m) = β_m, WT (V_m)	m_∞, WT (V_m) = m_∞, WT (V_m) α_m, WT (V_m) = α_m, WT (V_m) β_m WT (V_m) = β_m, WT (V_m) h_∞, WT (V_m) = h_∞, WT (V_m) β_h WT (V_m) = β_m, WT (V_m)	100% of I_{CaL}	100% of I_{Ks}
WT + 30 μM E3G	m_∞, WT (V_m) = m_∞, WT (V_m) α_m, WT (V_m) = α_m, WT (V_m) β_m WT (V_m) = β_m, WT (V_m) h_∞, WT (V_m) = h_∞, WT (V_m + ***6***) β_hWT (V_m) = β_h, WT (V_m)	m_∞, WT (V_m) = m_∞, WT (V_m) α_m, WT (V_m) = α_m, WT (V_m) β_m WT (V_m) = β_m, WT (V_m) h_∞, WT (V_m) = h_∞, WT (V_m + ***6***) β_hWT (V_m) = β_h, WT (V_m)	***80***% of I_{CaL}	***50***% of I_{Ks}
Mutants	m_∞, p.I141V (V_m) = m_∞, WT (V_m − **6.3**) α_m, p.I141V (V_m) = α_h, WT (V_m) β_m, p.I141V (V_m) = β_h, WT (V_m) h_∞, p.I141V (V_m) = h_∞, WT (V_m + **6.2**) β_hWT (V_m) = β_h, WT (V_m)	m_∞, p.I141V (V_m) = m_∞, WT (V_m − **7**) α_m, p.I141V (V_m) = α_h, WT (V_m − **7**) β_m, p.I141V (V_m) = β_h, WT (V_m + **7**) h_∞, p.I141V (V_m) = h_∞, WT (V_m) β_hWT (V_m) = β_h, WT (V_m + **7**)	100% of I_{CaL}	100% of I_{Ks}
Mutants + 30 μM E3G	m_∞, p.I141V (V_m) = m_∞, WT (V_m − **6.3**) α_m, p.I141V (V_m) = α_h, WT (V_m) β_m, p.I141V (V_m) = β_h, WT (V_m) h_∞, p.I141V (V_m) = h_∞, WT (V_m + **6.2** + ***6***) β_hWT (V_m) = β_h, WT (V_m)	m_∞, p.I141V (V_m) = m_∞, WT (V_m − **7**) α_m, p.I141V (V_m) = α_h, WT (V_m − **7**) β_m, p.I141V (V_m) = β_h, WT (V_m + **7**) h_∞, p.I141V (V_m) = h_∞, WT (V_m + ***6***) β_hWT (V_m) = β_h, WT (V_m + **7**)	***80***% of I_{CaL}	***50***% of I_{Ks}

an increased sinus rate, atrial tachyarrhythmias, and an increased number of ventricular complexes during exercise [4]. On the molecular level, these mutations affect the biophysical properties of $Na_{v1.5}$ by shifting its voltage dependence of steady state of activation towards more negative potentials and accelerating its activation and inactivation kinetics [2–6].

Ion channels become one of the most important molecular targets for several classes of drugs including antiarrhythmics and local anesthetic molecules [7]. In this sense, green tea flavonoids could offer a natural promising alternative. Indeed, Epigallocatechin-3-Gallate (E3G), as a major flavanol of green tea, has shown significant effects on the electrocardiographic wave forms in guinea pig. This compound has been demonstrated to exhibit inhibitory action on several cardiac ion channels [8].

Tea is manufactured from the dried leaves of *Camellia sinensis* in three basic forms of nonoxidized (green), semioxidized (oolong), and oxidized (black). Green tea is one of the most widely consumed beverages in North Africa and exhibits high content in polyphenolic flavanols known as catechins which may constitute up to 36% of the dry leaf weight [9, 10]. Catechins represent 80% to 90% of green tea total flavonoids, where epigallocatechin gallate appears to be the major predominant catechin (48–55%) followed by epigallocatechin (9–12%), epicatechin gallate (9–12%), epicatechin (5–7%), and a small proportion of catechin (0.3–0.6%) [11].

Most flavonoids affect vascular system insofar to normalize blood pressure by either inhibiting calcium channels or activating potassium channels or both. But contrary to the clear-cut pathophysiological benefit of flavonoids on vascular system, the impact of these compounds on cardiac channelopathies is yet somewhat unclear [12]. Previous investigation using patch clamp technique showed that flavonoids act as multichannel inhibitors, thereby triggering generally unexpected pharmacological effects. Therefore, the reported effects on cardiac ion channels of most flavonoids remain largely unknown whether they are anti- or proarrhythmic [12, 13]. In this sense, voltage gated sodium channel (VGSC) inhibition by polyphenols is well documented as cardioprotective and antiarrhythmic pathways. Catechins, like other polyphenols, share the common structural feature of one or more phenolic rings with several antiarrhythmic VGSC inhibitors such as lidocaine and mexiletine. These polyphenolic compounds may also inhibit peak and/or late I_{Na}, leading to beneficial impact on the parameters associated with arrhythmias.

In this context, the aim of this study was to evaluate the benefits-risks balance of E3G effect on the setting of cardiac channelopathies.

2. Materials and Methods

2.1. Models. The action potentials were simulated using the updated mathematical model of the human atrial action potential of Maleckar-Greenstein-Trayanova-Giles (MGTG) [14], Stewart–Aslanidi–Noble–Noble–Boyett–Zhang (SANNBZ) Purkinje cell model [15], and Tusscher–Noble–Noble–Panfilov (TNNP) human ventricular cell models [16].

Table 2: Formulation of WT and mutated sodium channels ($Na_{v1.5}$-p.R222Q and $Na_{v1.5}$-p.I141V) in the presence or absence of 30 μM of E3G in the Maleckar-Greenstein-Trayanova-Giles atrial cell model. The bold font corresponds to mutations effect and the bold-italic font to E3G effects.

	MGTG atrial model, p.R222Q.I_{Na}	MGTG atrial model, p.I141V.I_{Na}	MGTG atrial model, I_{CaL}	MGTG atrial model, I_{Ks}
WT	m_∞, WT (V_m) = m_∞, WT (V_m) m factor, WT (V_m) = m factor, WT (V_m) τ_m = $4.2e-5$ (s) $*$ exp($-m_{factor} * m_{factor}$) + $2.4e-5$ (s) h_∞, WT (V_m) = h_∞, WT (V_m) h factor, WT (V_m) = h factor, WT (V_m) τ_{h1} = 0.03 (s) $*h_{factor}$ + 0.0003 (s)	m_∞, WT (V_m) = m_∞, WT (V_m) m factor, WT (V_m) = m factor, WT (V_m) τ_m = $4.2e-5$ (s) $*$ exp($-m_{factor} * m_{factor}$) + $2.4e-5$ (s) h_∞, WT (V_m) = h_∞, WT (V_m) h factor, WT (V_m) = h factor, WT (V_m) τ_{h1} = 0.03 (s) $*$ h_{factor} + 0.0003 (s)	100% of I_{CaL}	100% of I_{Ks}
WT + 30 μM E3G	m_∞, WT (V_m) = m_∞, WT (V_m) m factor, WT (V_m) = m factor, WT (V_m) τ_m = $4.2e-5$ (s) $*$ exp($-m_{factor} * m_{factor}$) + $2.4e-5$ (s) h_∞, WT (V_m) = h_∞, WT (V_m + ***6***) h factor, WT (V_m) = h factor, WT (V_m) τ_{h1} = 0.03 (s) $*$ h_{factor} + 0.0003 (s)	m_∞, WT (V_m) = m_∞, WT (V_m) m factor, WT (V_m) = m factor, WT (V_m) τ_m = $4.2e-5$ (s) $*$ exp($-m_{factor} * m_{factor}$) + $2.4e-5$ (s) h_∞, WT (V_m) = h_∞, WT (V_m + ***6***) h factor, WT (V_m) = h factor, WT (V_m) τ_{h1} = 0.03 (s) $*$ h_{factor} + 0.0003 (s)	***80***% of I_{CaL}	***50***% of I_{Ks}
Mutants	m_∞, WT (V_m) = m_∞, WT (V_m + **6.3**) m factor, WT (V_m) = m factor, WT (V_m) τ_m = $4.2e-5$ (s) $*$ exp($-m_{factor} * m_{factor}$) + $2.4e-5$ (s) h_∞, WT (V_m) = h_∞, WT (V_m + **6.2**) h factor, WT (V_m) = h factor, WT (V_m) τ_{h1} = 0.03 (s) $*$ h_{factor} + 0.0003 (s)	m_∞, WT (V_m) = m_∞, WT (V_m + **7**) m factor, WT (V_m) = m factor, WT (V_m + **7**) τ_m = $4.2e-5$ (s) $*$ exp($-m_{factor} * m_{factor}$) + $2.4e-5$ (s) h_∞, WT (V_m) = h_∞, WT (V_m) h factor, WT (V_m) = h factor, WT (V_m + **7**) τ_{h1} = 0.03 (s) $*$ h_{factor} + 0.0003 (s)	100% of I_{CaL}	100% of I_{Ks}
Mutants + 30 μM E3G	m_∞, WT (V_m) = m_∞, WT (V_m + **6.3**) m factor, WT (V_m) = m factor, WT (V_m) τ_m = $4.2e-5$ (s) $*$ exp($-m_{factor} * m_{factor}$) + $2.4e-5$ (s) h_∞, WT (V_m) = h_∞, WT (V_m + **6.2** + ***6***) h factor, WT (V_m) = h factor, WT (V_m) τ_{h1} = 0.03 (s) $*$ h_{factor} + 0.0003 (s)	m_∞, WT (V_m) = m_∞, WT (V_m + **7**) m factor, WT (V_m) = m factor, WT (V_m + **7**) τ_m = $4.2e-5$ (s) $*$ exp($-m_{factor} * m_{factor}$) + $2.4e-5$ (s) h_∞, WT (V_m) = h_∞, WT (V_m + ***6***) h factor, WT (V_m) = h factor, WT (V_m + **7**) τ_{h1} = 0.03 (s) $*$ h_{factor} + 0.0003 (s)	***80***% of I_{CaL}	***50***% of I_{Ks}

2.2. Formulation of Fast Sodium Current. In TNNP and SANNBZ models, the sodium current I_{Na} is represented according to a Hodgkin–Huxley formalism: $I_{Na} = g_{Na} m^3 hj(V_m - E_{Na})$, where g_{Na} is the maximal conductance of I_{Na}. m^3, h, and j are the activation gate, fast inactivation gate, and slow inactivation gate, respectively. V_m represents the membrane potential, and E_{Na} is the Nernst potential of sodium.

For the MGTG atrial model, the sodium current I_{Na} is represented according to the following equation:

$$I_{Na} = P_{Na} m^3 \left(0.9h_1 + 0.1h_2\right) \left[Na^+\right]_c V \frac{F^2}{RT} \frac{e^{(V-E_{Na})F/RT} - 1}{e^{VF/RT} - 1}, \quad (1)$$

where P_{Na} represents the permeability to the sodium and m^3, h_1, and h_2 are the activation gate, fast inactivation gate, and slow inactivation gate, respectively. V represents the membrane potential, and E_{Na} is the Nernst potential of sodium.

2.3. Computer Modeling of $Na_{v1.5}$-p.R222Q and $Na_{v1.5}$-p.I141V Mutants. The same strategy was used for all models of the atrial, human Purkinje cells, and left-ventricular myocytes [15–18]. As reported by Mann et al., 2012, and Swan et al., 2014, [3, 4], the equations corresponding to the I_{Na} current were modified to reproduce the relative variation of biophysical properties of the sodium current due to the $Na_{v1.5}$-p.R222Q and $Na_{v1.5}$-p.I141V mutations.

The effects of the $Na_{v1.5}$-p.R222Q and $Na_{v1.5}$-p.I141V mutations were simulated as previously described by Mann et al., 2012, and Swan et al., 2014, for the ventricular and Purkinje models [3, 4]. m_∞, h_∞, α_m, β_m, and β_h were modified to reproduce the shift in the voltage dependencies of steady

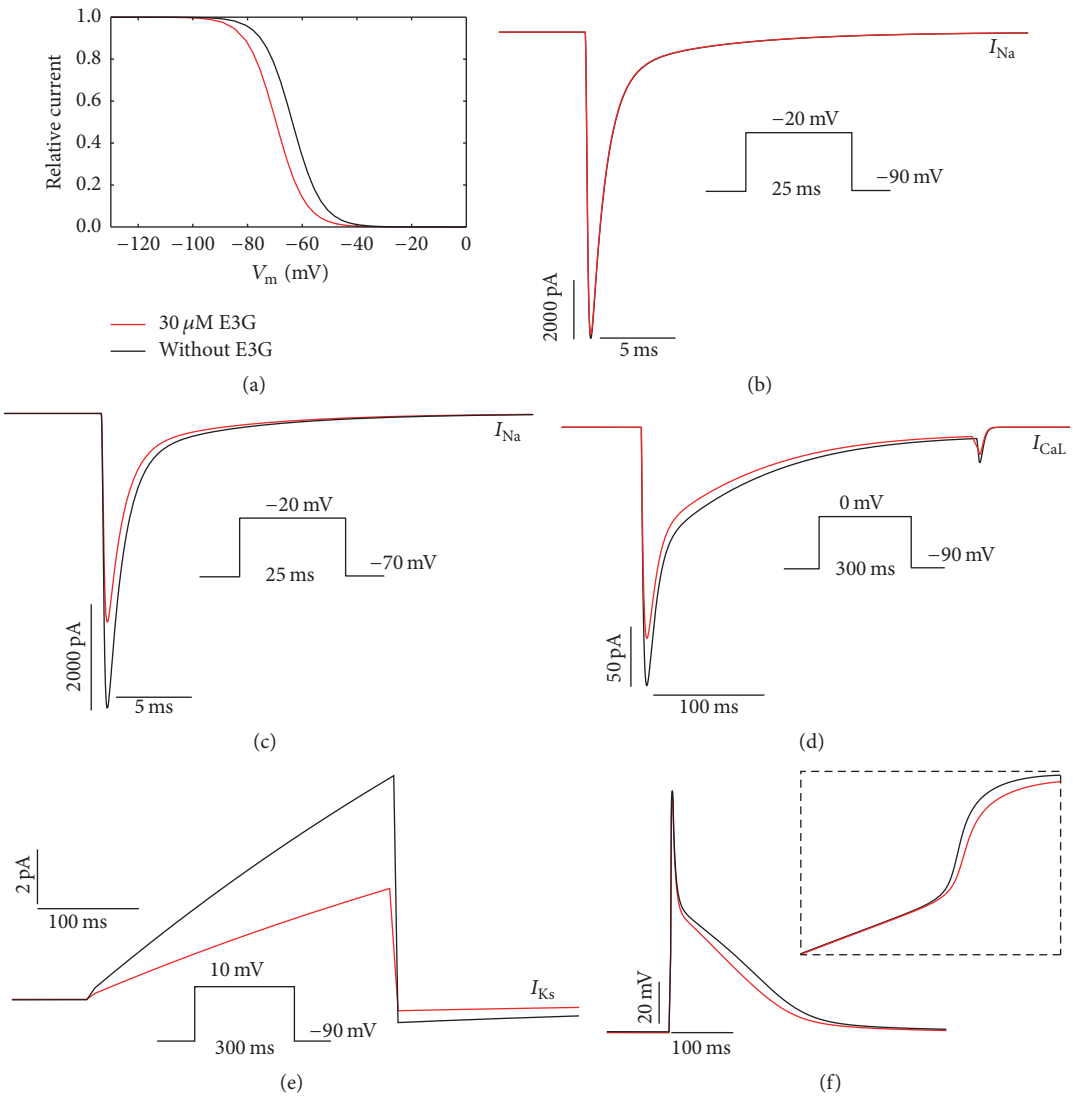

Figure 1: Simulated effects of 30 μM E3G in the human atrial model (MGTG (Maleckar-Greenstein-Trayanova-Giles)). (a) Steady state inactivation curves (h_∞) in the presence or absence of E3G. (b) and (c) Inhibitory effect of E3G on the sodium current at −90 mV and −70 mV resting potentials. (d) Inhibitory effect of E3G on the calcium current (20% inhibition). (e) Inhibitory effect of E3G on the I_{Ks} current (50% inhibition). (f) E3G effect on the atrial action potential (intensity of stimulus = 15 μA/μF, duration: 6 ms; inset, zoom of the rapid depolarization phase). For all panels, black lines: without E3G; red lines: 30 μM E3G.

state of activation and inactivation and their kinetics. For the MGTG atrial model, m_∞, m factor, h_∞, and h factor were modified to reproduce the shift of the activation and inactivation curves as well as the changes observed in the sodium current kinetics. In all conditions, the heterozygous states were reproduced by the summation of half the WT current and half the mutant current.

2.4. Computer Modeling of Epigallocatechin-3-Gallate Effect on Ion Channels. For all models and conditions (WT and mutants), the effects of E3G on ion channels were reproduced based on the experimental work of Kang et al. [8].

Table 1 summarizes the modifications of the cardiac ion currents that were introduced in all models to match the experimental Data.

Table 3: A summary of the parameters used for the calculation of conduction velocity in the atrial, ventricular, and Purkinje models.

Model	Cell number (n)	Intercellular conductance (mS/μF)	Step size (ms)
MGTG	100	17	0.01
SANNBZ	100	17	0.01
TNNP	100	7	0.001

2.5. Conduction Velocity. Conduction velocity was investigated in fibers of MGTG, TNNP, and SANNBZ cell models (pacing rates: 1 Hz for the atrial and ventricular models and 2.5 Hz for the Purkinje model). Table 3 summarizes the parameters used for the calculation of conduction velocity.

All simulations were performed by Myokit v.1.20.5 [19].

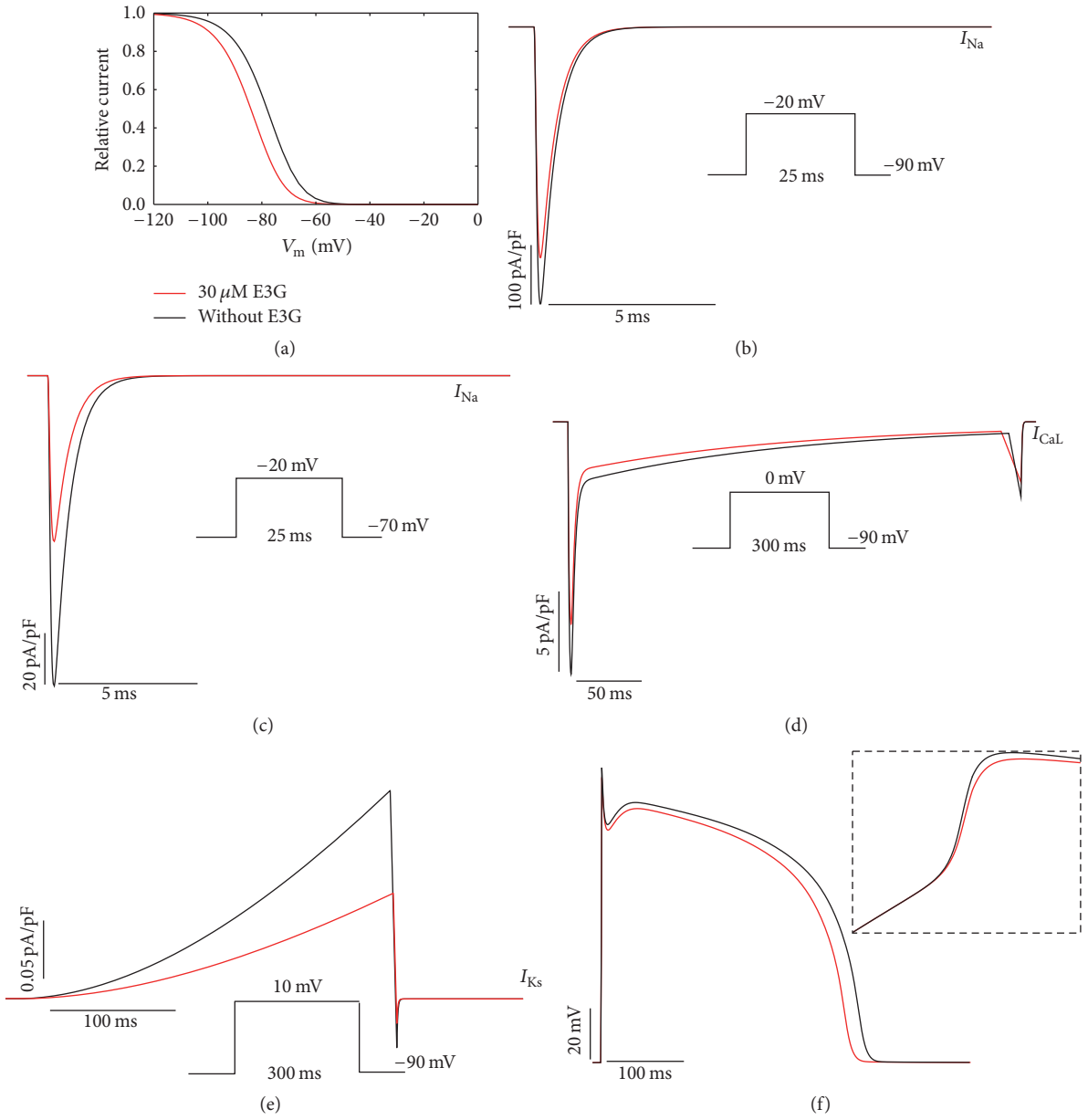

FIGURE 2: Simulated effects of 30 μM E3G in the human ventricular model (TNNP [Tusscher–Noble–Noble–Panfilov]). (a) Steady state inactivation curves (h_∞) in the presence or absence of E3G. (b) and (c) Inhibitory effect of E3G on the sodium current at −90 mV and −70 mV resting potentials. (d) Inhibitory effect of E3G on the calcium current (20% inhibition). (e) Inhibitory effect of E3G on the I_{Ks} current (50% inhibition). (f) E3G effect on the midmyocardial action potential (intensity of stimulus = 52 μA/μF, duration: 1 ms; inset, zoom of the rapid depolarization phase). For all panels, black lines: without E3G; red lines: 30 μM E3G.

3. Results

3.1. Simulated Effect of E3G on the Electrical Activity of Cardiac Cells. To investigate the functional consequences of 30 μM E3G on the electrical activity of atrial, Purkinje, and ventricular cells, we used MGTG, SANNBZ, and human epicardial, midmyocardial, and endocardial ventricular TNNP cell models. Using these models, the observed changes in cardiac ion channels function such as voltage dependencies and current amplitudes were implemented (see Section 2, Figures 1–3).

In the I_{Na} formulations of MGTG, SANNBZ, and TNNP cell models, the effects of E3G on the sodium channel function were simulated by shifting the voltage dependence of the steady state equilibrium h_∞ of h gate by −6 mV (Figures 1(a), 2(a), and 3(a)). The m and j gates were left unchanged.

The introduction of a negative shift in the inactivation curve, related to the presence of E3G, allowed us to reproduce the inhibitory effect of this compound on the sodium current amplitude for the ventricular and Purkinje cell models (Figures 2(b), 2(c), 3(b), and 3(c)). Indeed, as reported by

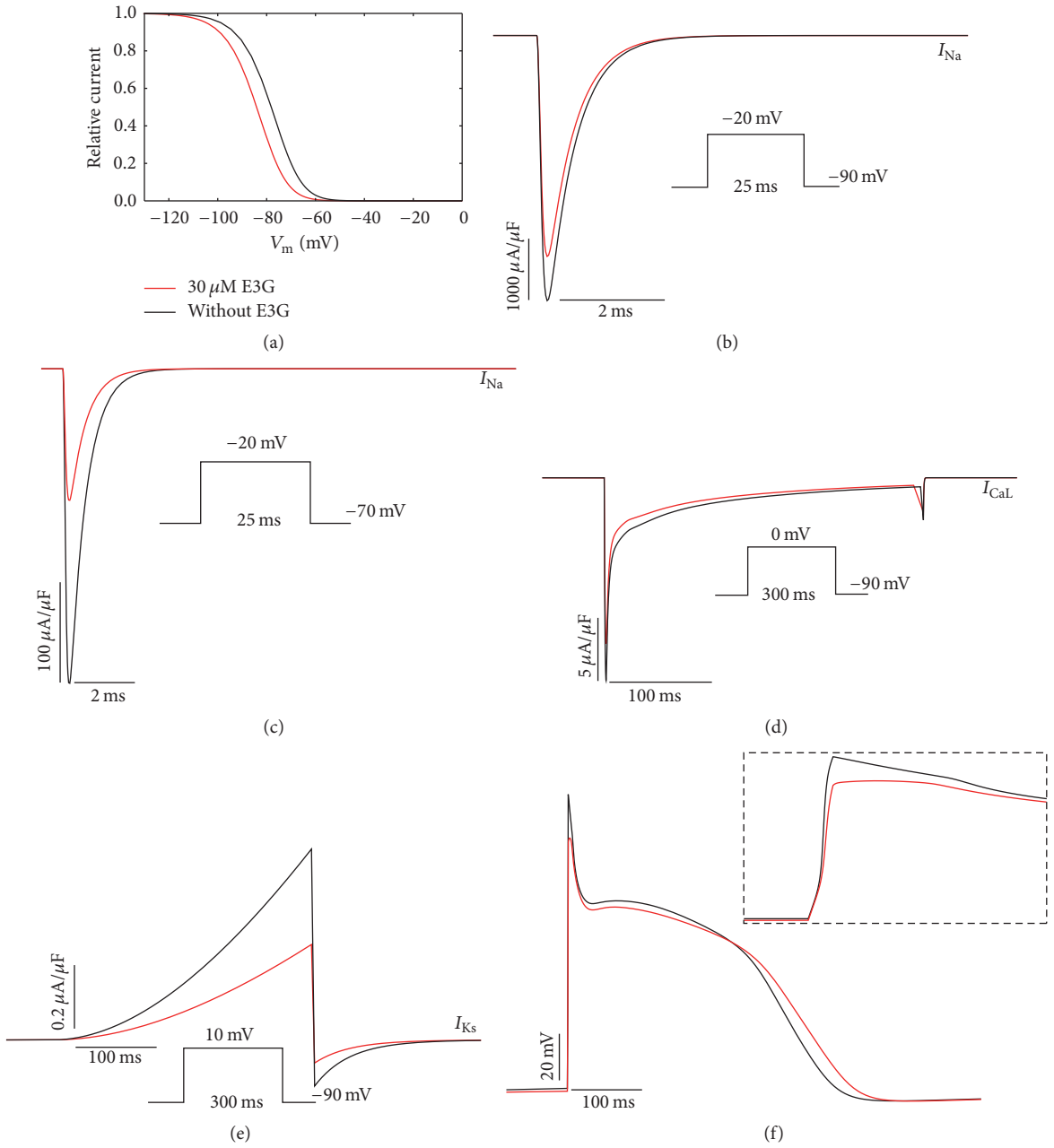

Figure 3: Simulated effects of 30 μM E3G in the human Purkinje model (SANNBZ (Stewart–Aslanidi–Noble–Noble–Boyett–Zhang Purkinje cell model)). (a) Steady state inactivation curves (h_∞) in the presence or absence of E3G. (b) and (c) Inhibitory effect of E3G on the sodium current at −90 mV and −70 mV resting potentials. (d) Inhibitory effect of E3G on the calcium current (20% inhibition). (e) Inhibitory effect of E3G on the I_{Ks} current (25% inhibition: dashed line; 50% inhibition: solid line). (f) E3G effect on the Purkinje action potential (intensity of stimulus = 52 μA/μF, duration: 1 ms; inset, zoom of the rapid depolarization phase). For all panels, black lines: without E3G; red lines: 30 μM E3G.

Kang et al. [8], the inhibitory effect of E3G is higher at depolarized resting potentials. However, for the atrial cell model, we observed that 30 μM E3G decreases the sodium current amplitude only when the resting potential is maintained at −70 mV (Figures 1(b) and 1(c)). There is no E3G effect when the resting potential is maintained at −90 mV. This is due to the biophysical properties of inactivation at basal condition. In fact, as shown in Figure 1(a), there is no difference in the sodium channel availability with or without E3G at −90 mV. Thus, an equal number of sodium channels were available in both conditions when the membrane was maintained at this potential.

Moreover, by using the same voltage protocols described by Kang et al., the inhibitory effect of 30 μM E3G on I_{CaL} and I_{Ks} currents was reproduced via decreasing the amplitude of these currents to 80% and 50% of WT amplitude, respectively

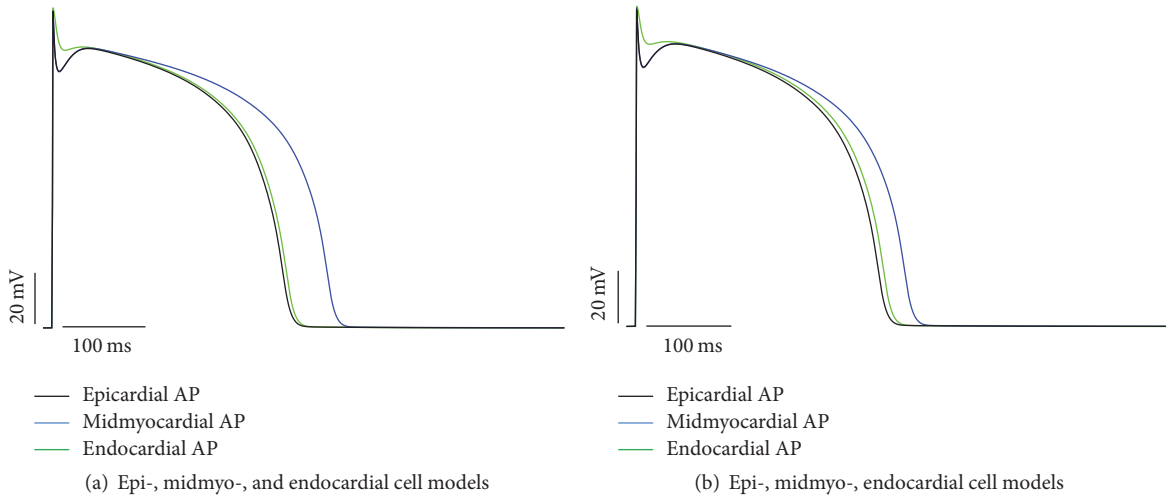

(a) Epi-, midmyo-, and endocardial cell models (b) Epi-, midmyo-, endocardial cell models

Figure 4: Repolarization dispersion across the ventricular wall. (a) Superimposition of the epi-, midmyo-, and endocardial action potentials (TNNP cells models) in absence of E3G. (b) Superimposition of the epi-, midmyo-, and endocardial action potentials in the presence of 30 μM E3G.

Table 4: The effect of E3G on conduction velocity investigations in the presence of p.R222Q and p.I141V in heterozygous states.

Model	Atrial cells		Ventricular cells		Purkinje cells	
Condition	CV (cm/s) control	CV (cm/s) 30 μM E3G	CV (cm/s) control	CV (cm/s) 30 μM E3G	CV (cm/s) control	CV (cm/s) 30 μM E3G
$Na_{v1.5}$ WT	55.07	50.84	49.91	45.72	67.68	37.20
$Na_{v1.5}$ p.I141V	57.44	53.93	53.63	49.11	72.43	42. 92
$Na_{v1.5}$ p.R222Q	60.93	56.23	51.93	45.56	62.72	—

(Figures 1(d), 1(e), 2(d), 2(e), 3(d), and 3(e)). All used formulations are summarized in Tables 1 and 2 (see Section 2). Simulations were run for 60 s with a cycle length of 1 Hz to stabilize the model. Then, supplementary run was started for another 5 s and then the last AP of each supplementary run was analyzed.

The combined effects of 30 μM E3G on cardiac ion channels slightly decreased the AP amplitudes and maximum upstroke velocities of atrial, Purkinje, and ventricular cells (Figures 1(f), 2(f), and 3(f)). In addition, the plateau phase of atrial AP was reduced (Figure 1(f)). However, E3G increased AP duration in Purkinje cell model (Figure 2(f)).

For midmyocardial cells, E3G shortened the AP duration (Figure 3(f)). On the other hand, the superimposition of the epi-, midmyo-, and endocardial APs predicted a small decrease of the repolarization dispersion across the ventricular wall (Figure 4).

3.2. The p.R222Q and p.I141V Effects on Cardiac Excitability. According to the experimental work of Kang et al. [8], the E3G antiarrhythmic effect, in the sitting of MEPPC and EPVT cardiac disorders, was evaluated. First, we incorporated the biophysical modifications that are induced by the $Na_{v1.5}$-p.R222Q and $Na_{v1.5}$-p.I141V mutations and got insight on their effects on atrial, ventricular, and Purkinje APs using MGTG, TNNP, and SANNBZ models (Figures 5, 6, and 7).

Interestingly, the introduction of equations mimicking the heterozygous state into the atrial and ventricular cell models induced minor changes in their AP morphologies (Figures 8(a), 8(b), 9(a), 9(b), 10(a), 10(b), 11(a), and 11(b)). Conversely, Mann et al. and Swan et al. [3, 4] reported a drastic effect when these equations are introduced in the Purkinje cell model. Indeed, for the $Na_{v1.5}$-p.R222Q and $Na_{v1.5}$-p.I141V mutants, the model showed an accelerated rate of spontaneous activity of Purkinje cells leading to the occurrence of ectopic beats during the diastolic interval at 1 Hz (Figures 12(a), 12(b), 13(a), and 13(b)). These abnormalities disappeared at higher pacing rates (Data not shown).

On the other hand, using MGTG, TNNP, and SANNBZ models, strength-duration curves were constructed. In the presence of $Na_{v1.5}$-p.R222Q and $Na_{v1.5}$-p.I141V mutations, a lower excitation threshold for action potential generation (pacing rates: 1 Hz for atrial and ventricular models and 2.5 Hz for the Purkinje model) was observed in the p.R222Q and p.I141V mutations in homozygous and heterozygous genotypes compared with the WT ((d) in Figures 8–13).

Conduction velocity was investigated in fibers of MGTG, TNNP, and SANNBZ cell models (pacing rates, as described above). The presence of the $Na_{v1.5}$-p.I141V mutation, in homozygous and heterozygous states, accelerated atrial and ventricular conduction at 1 Hz and Purkinje conduction at 2.5 Hz. Similar variations were observed in $Na_{v1.5}$-p.R222Q mutation, whereas the conduction velocity was lower than WT condition in Purkinje cell model at 2.5 Hz pacing rate (Table 4).

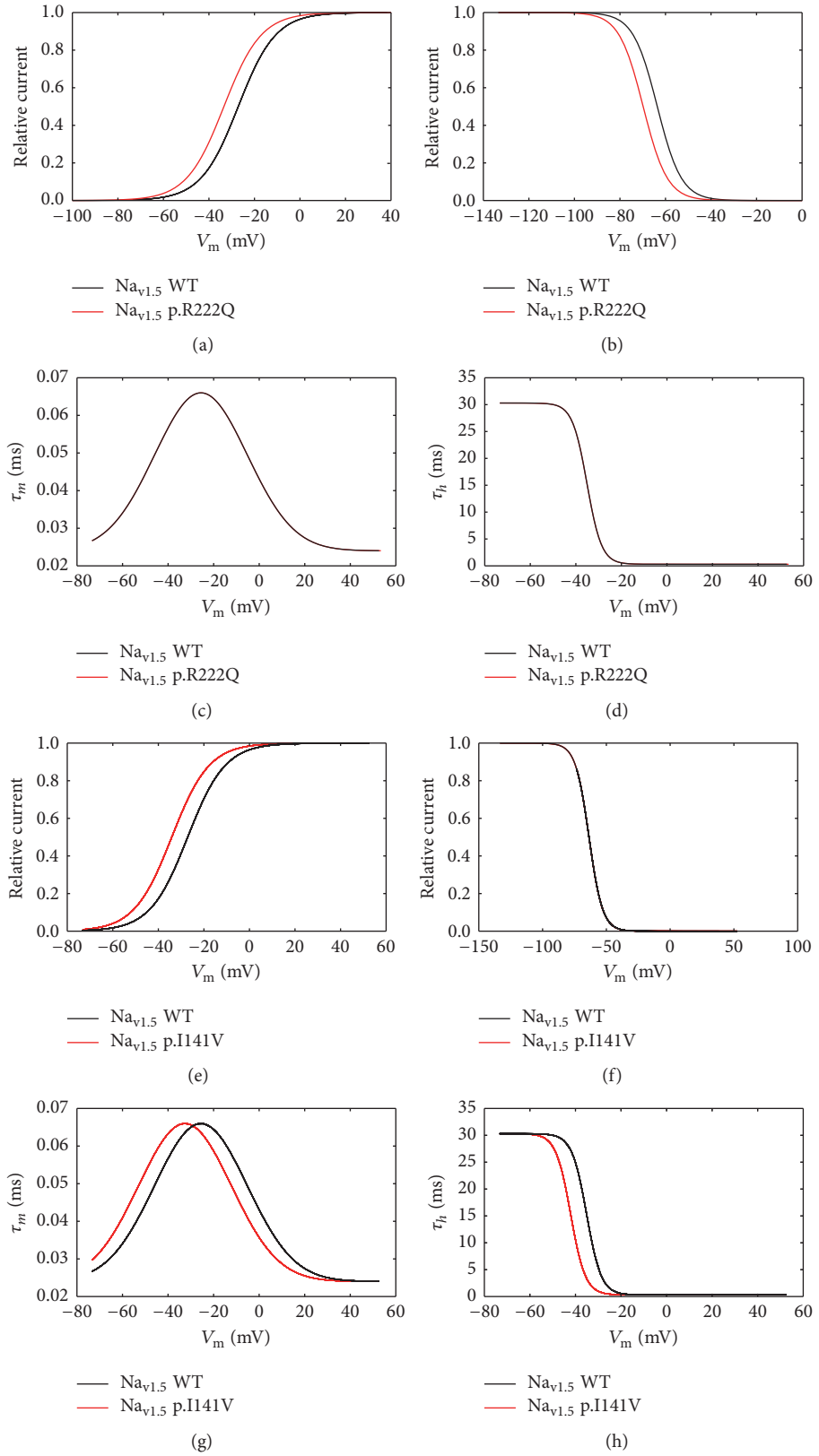

Figure 5: Effects of the p.R222Q and p.I141V mutations on I_{Na} properties in the human atrial cell model (MGTG cell model). (a) and (b) Effect of the p.R222Q mutation on the voltage dependence of steady state of activation and inactivation. (c) and (d) Effect of the p.R222Q mutation on the activation and inactivation kinetics. (e) and (f) Effect of the p.I141V mutation on the voltage dependence of steady state of activation and inactivation. (g) and (h) Effect of the p.I141V mutation on the activation and inactivation kinetics. For all panels, black lines: WT condition; red lines: mutant conditions.

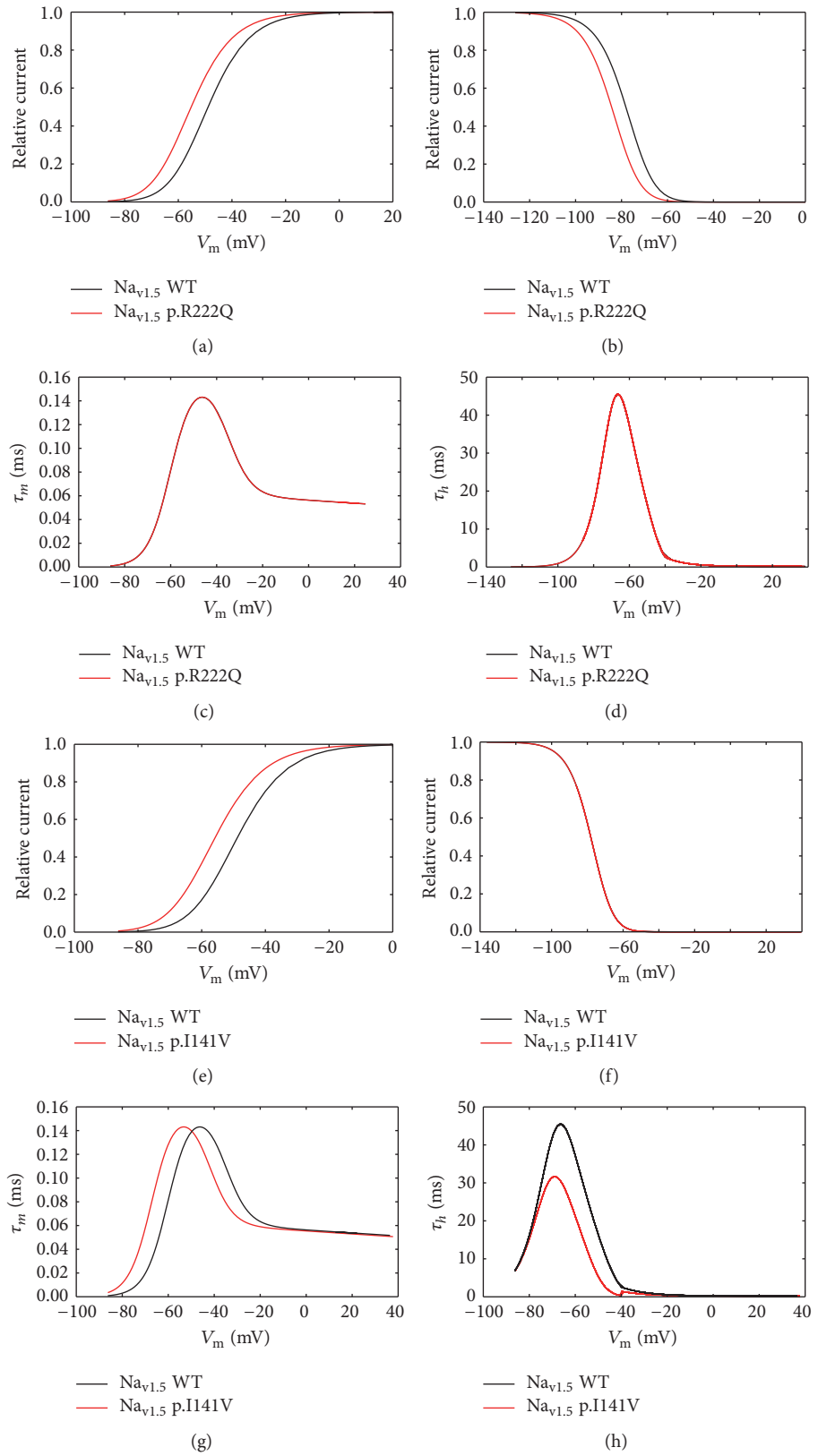

Figure 6: Effects of the p.R222Q and p.I141V mutations on I_{Na} properties in the human ventricular cell model (TNNP cell model). (a) and (b) Effect of the p.R222Q mutation on the voltage dependence of steady state of activation and inactivation. (c) and (d) Effect of the p.R222Q mutation on the activation and inactivation kinetics. (e) and (f) Effect of the p.I141V mutation on the voltage dependence of steady state of activation and inactivation. (g) and (h) Effect of the p.I141V mutation on the activation and inactivation kinetics. For all panels, black lines: WT condition; red lines: mutant conditions.

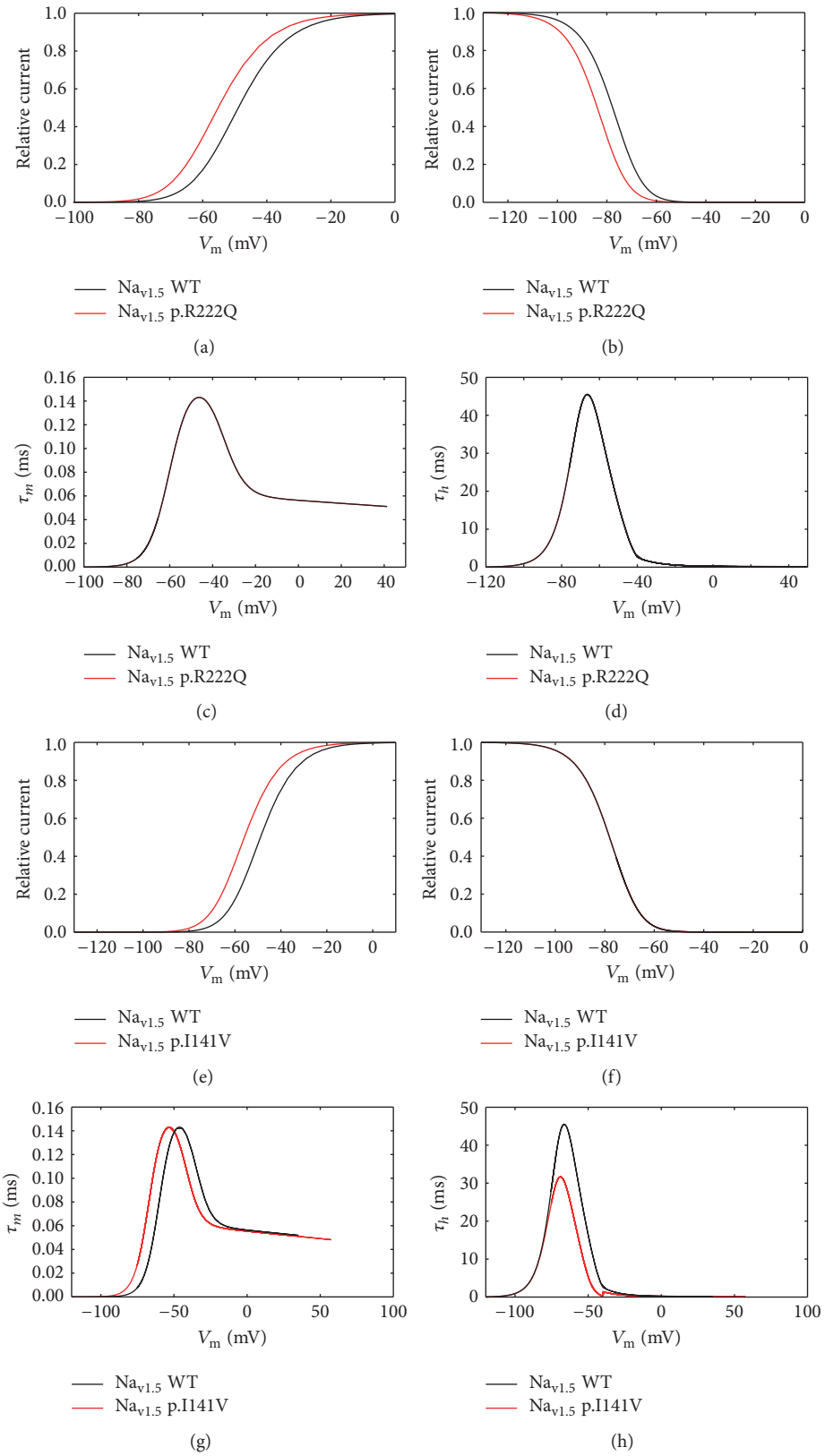

FIGURE 7: Effects of p.R222Q and p.I141V mutations on I_{Na} properties in the human Purkinje cell model (SANNBZ cell model). (a) and (b) Effect of the p.R222Q mutation on the voltage dependence of steady state of activation and inactivation. (c) and (d) Effect of the p.R222Q mutation on the activation and inactivation kinetics. (e) and (f) Effect of the p.I141V mutation on the voltage dependence of steady state of activation and inactivation. (g) and (h) Effect of the p.I141V mutation on the activation and inactivation kinetics. For all panels, black lines: WT condition; red lines: mutant conditions.

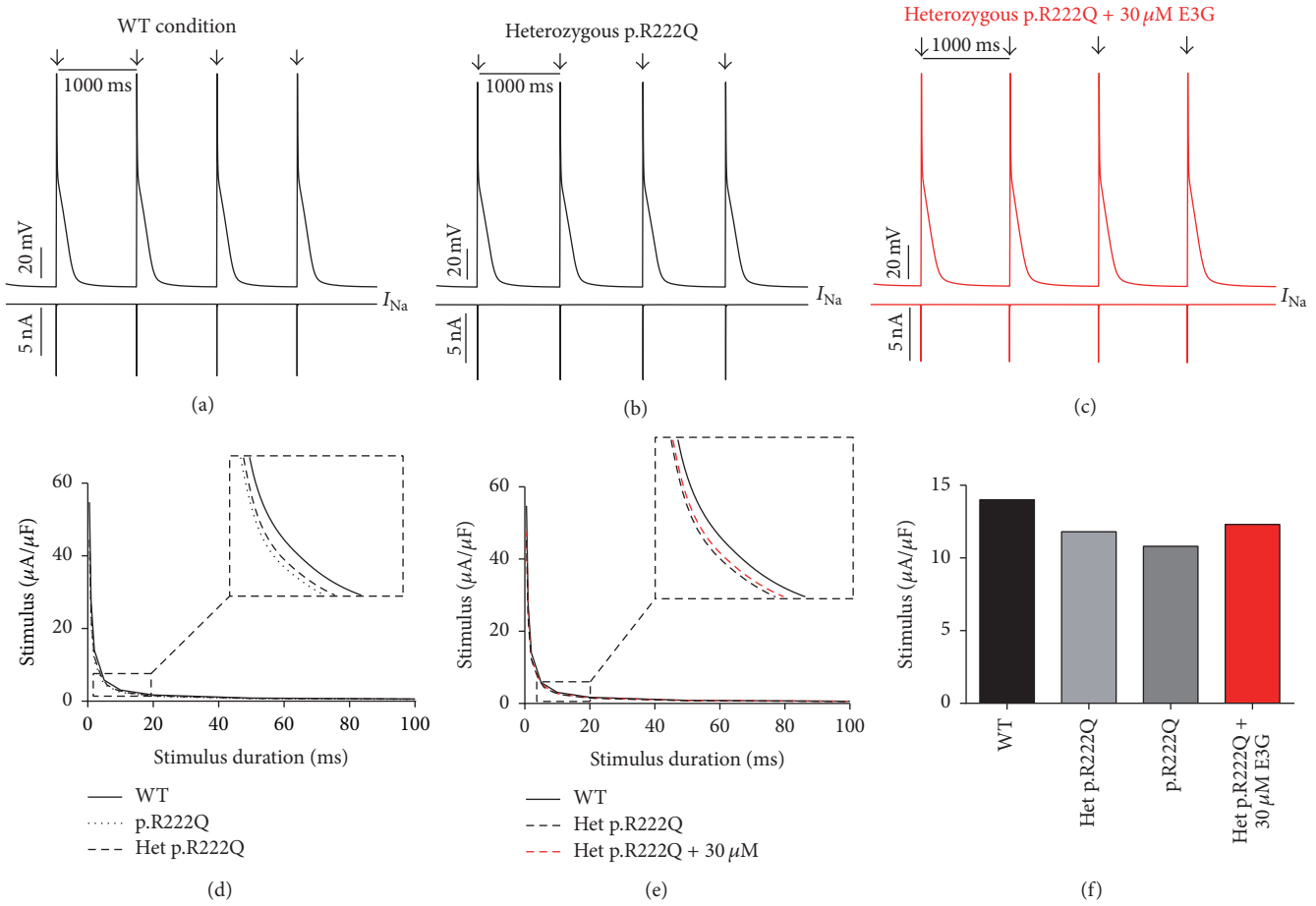

FIGURE 8: Effects of 30 μM E3G on atrial cell action potentials for $Na_{v1.5}$-WT and $Na_{v1.5}$-p.R222Q conditions (MGTG cell model). (a), (b), and (c) Simulated APs (Top of the panels) and the cardiac sodium currents (Bottom of the panels) in WT, heterozygous $Na_{v1.5}$-p.R222Q, and heterozygous $Na_{v1.5}$-p.R222Q + 30 μM conditions at 1 Hz cycle length. Arrows: external stimulus. (d) and (e) Strength-duration curves in the MGTG cell model for $Na_{v1.5}$-WT and heterozygous $Na_{v1.5}$-p.R222Q conditions with or without 30 μM E3G (inset, zoom on the strength-duration curves). (f) Excitation thresholds at 2 ms stimulus duration in the MGTG atrial AP or without 30 μM E3G.

Of note, strength-duration curves and conduction velocities could not be established at 1 Hz in the Purkinje model because of the accelerated spontaneous rhythm caused by p.R222Q and p.I141V mutations.

3.3. Antiarrhythmic Effect of E3G on SCN5A-Related Cardiac Syndrome, MEPPC, and EPVT. To investigate the potential antiarrhythmic effect of E3G on $Na_{v1.5}$-p.R222Q and $Na_{v1.5}$-p.I141V-related cardiac syndromes, the reported experimental effects of E3G were tested on these mutants. As shown in (a), (b), and (c) in Figures 8–11, 30 μM E3G does not affect the shape of action potentials in atrial and ventricular cells compared to the WT, $Na_{v1.5}$-p.R222Q, and $Na_{v1.5}$-p.I141V heterozygous conditions. However, this compound suppressed the ectopic APs observed in the presence of $Na_{v1.5}$-p.R222Q mutation in Purkinje cell model (Figure 12(c)). Similar effects were obtained for $Na_{v1.5}$-p.I141V mutation. Indeed, E3G decreased the number of ectopic beats associated with the presence of this mutation in Purkinje cells (Figure 13(c)). Of note, for these simulations, the models were stabilized during 60 s, then supplementary run was started for another 60 s, and finally the last 5 s of each supplementary run was analyzed.

Moreover, simulations were run using MGTG, TNNP, and SANNBZ cell models, and the strength-duration curves were constructed. In these models, the addition of 30 μM E3G decreased the excitability of the atrial, ventricular, and Purkinje cells by increasing the excitation threshold for action potential generation ((e) and (f) in Figures 8–13).

Finally, the effect of E3G on conduction velocity was investigated in the presence of p.R222Q and p.I141V mutations using fibers of atrial, ventricular, and Purkinje cell models. The presence of 30 μM E3G attenuates the effect of p.R222Q and p.I141V mutations by decreasing atrial, ventricular, and Purkinje conductions. Of note, the conduction velocity was calculated at 1 Hz for the atrial and ventricular models and at 2.5 Hz for the Purkinje cells (Table 4).

4. Discussion

The aim of this study was to evaluate the benefits-risks balance of E3G consumption on the setting of cardiac

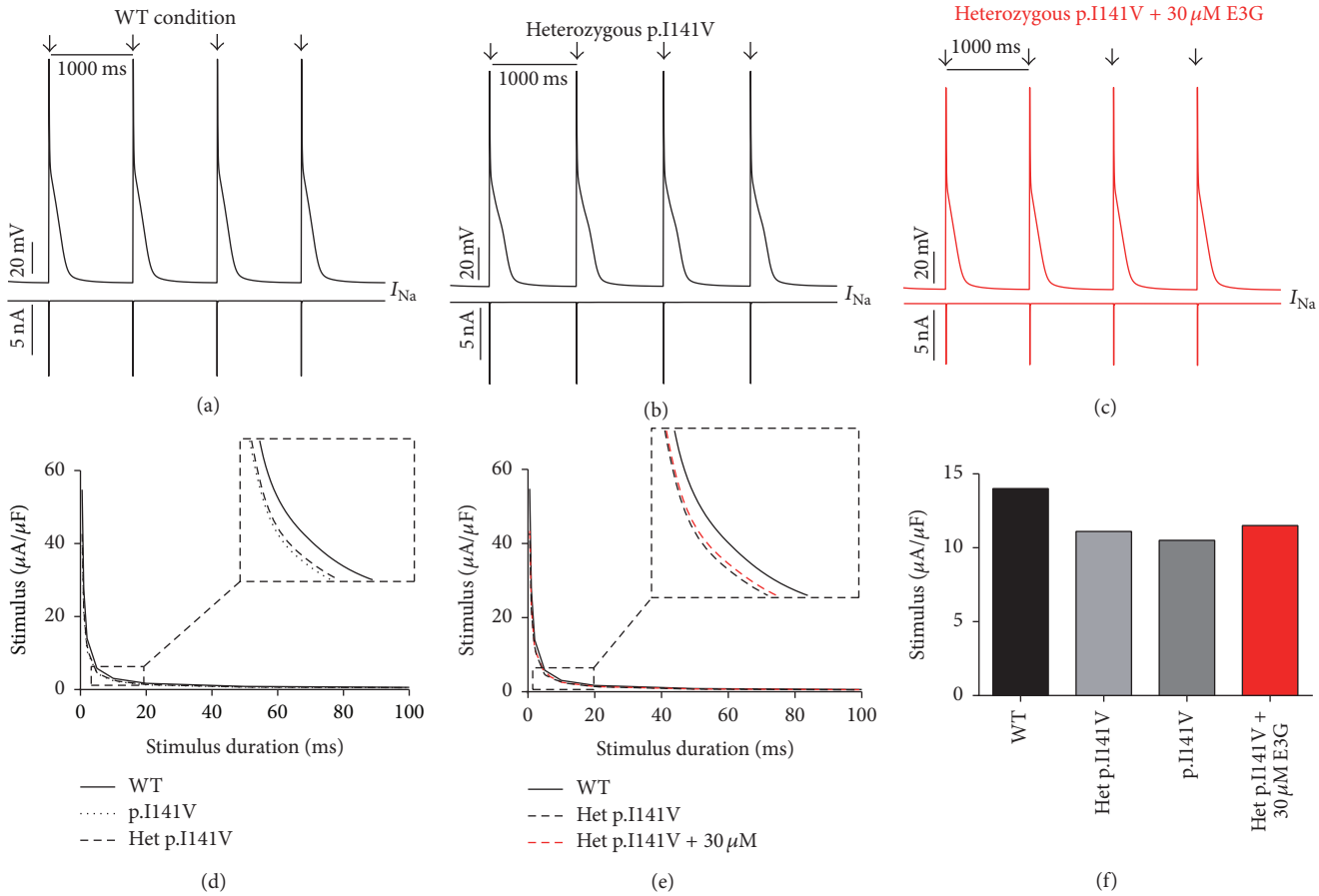

FIGURE 9: Effects of 30 μM E3G on atrial cell action potentials for $Na_{v1.5}$-WT and $Na_{v1.5}$-p.I141V conditions (MGTG cell model). (a), (b), and (c) Simulated APs (Top of the panels) and the cardiac sodium currents (Bottom of the panels) in WT, heterozygous $Na_{v1.5}$-p.I141V, and heterozygous $Na_{v1.5}$-p.I141V + 30 μM conditions at 1 Hz cycle length. Arrows: external stimulus. (d) and (e) Strength-duration curves in the MGTG cell model for $Na_{v1.5}$-WT and heterozygous $Na_{v1.5}$-p.I141V conditions with or without 30 μM E3G (inset, zoom on the strength-duration curves). (f) Excitation thresholds at 2 ms stimulus duration in the MGTG atrial AP or without 30 μM E3G.

channelopathies. Two gain-of-function mutations, $Na_{v1.5}$-p.R222Q and $Na_{v1.5}$-p.I141V, linked, respectively, with MEPPC and EPVT have been studied. Computer simulations of action potentials showed that 30 μM E3G reduced the excitability of Purkinje cells for the EPVT and suppressed the AP abnormalities characteristic of the MEPPC phenotype.

4.1. Simulated Effect of E3G on the Electrophysiological Properties of Cardiac Cells. Epigallocatechin-3-Gallate is the major catechin found in green tea. Tested at a dose of 30 μM, E3G modulates several voltage gated ion channels such as sodium, L-type calcium, and KCNQ1 channels [8]. Thus, the perfusion of this catechin induces several electrocardiographic modifications in Langendorff-perfused guinea pig hearts [8]. Indeed, E3G prolonged PR and QRS intervals, slightly shortened the QT interval, and altered the shape of the ST-T-wave segment [8]. To explain the link between these effects, *in silico* E3G effects were reproduced as described by Kang et al. [8]. Then, the effect of these modifications was evaluated on cardiac action potentials. Either for atrial, ventricular, or Purkinje cell models, our simulations showed delayed action potentials upstrokes, decreased APs amplitudes, and reduced conduction velocity in these cell models. These effects are likely related to the inhibition of the cardiac sodium channel by E3G. In fact, these parameters result mainly from the passage of sodium ions through these channels. Therefore, E3G effects are reflected on the whole heart activity by the prolongation of the PR and QRS intervals.

On the other hand, the experimental work of Kang et al. showed a slight decrease of the QT interval when E3G is perfused [8]. These findings are consistent with our results showing a slight diminution of ventricular AP duration in presence of E3G. However, our simulations failed to explain the increase of the interval from the peak of the T wave to the end of the T wave (T_p-T_e) on the resting guinea pig ECG. This interval reflects the transmural dispersion of repolarization in the ventricle [20, 21]. Accordingly, it was shown that the increase of this interval could be associated with an increase of the repolarization heterogeneity across the ventricular wall with an increased risk of sudden cardiac death [22]. In contrast to these evidences, our results predicted a slight decrease of this heterogeneity.

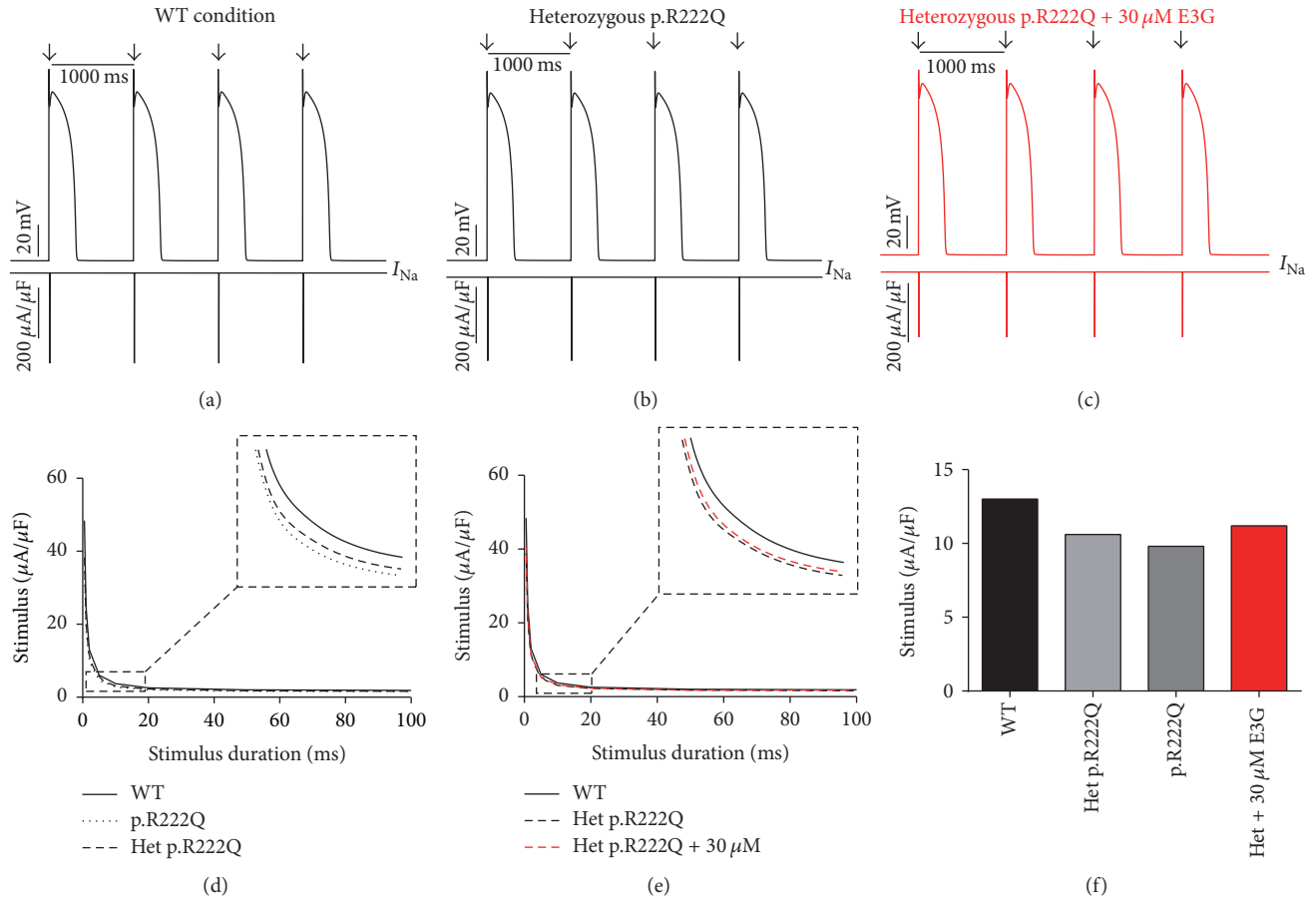

FIGURE 10: Effects of 30 μM E3G on ventricular cell action potentials for $Na_{v1.5}$-WT and $Na_{v1.5}$-p.R222Q conditions (TNNP cell model). (a), (b), and (c) Simulated APs (Top of the panels) and the cardiac sodium currents (Bottom of the panels) in WT, heterozygous $Na_{v1.5}$-p.R222Q, and heterozygous $Na_{v1.5}$-p.R222Q + 30 μM conditions at 1 Hz cycle length. Arrows: external stimulus. (d) and (e) Strength-duration curves in the TNNP cell model for $Na_{v1.5}$-WT and heterozygous $Na_{v1.5}$-p.R222Q conditions with or without 30 μM E3G (inset, zoom on the strength-duration curves). (f) Excitation thresholds at 2 ms stimulus duration in the TNNP atrial AP or without 30 μM E3G.

4.2. The p.R222Q and p.I141V Effects on Cardiac Excitability. In order to evaluate the possible antiarrhythmic effect of E3G in the sitting of MEPPC and EPVT cardiac disorders, the biophysical modifications induced by the $Na_{v1.5}$-p.R222Q and $Na_{v1.5}$-p.I141V mutants were incorporated as previously described by Mann et al. and Swan et al. [3, 4]. As shown by these groups, the introduction of these modifications into the atrial and ventricular cell models does not affect their AP morphologies. In contrast, the incorporation of the $Na_{v1.5}$-p.R222Q and $Na_{v1.5}$-p.I141V biophysical effects in the Purkinje cell model strongly affects the normal activation of these cells. Indeed, for these mutants, the model showed an accelerated rate of spontaneous activity of Purkinje cells leading to the occurrence of ectopic beats during the diastolic interval. In relevance to the disappearance of clinically observed premature contractions during exercise, the Purkinje ectopic APs induced by $Na_{v1.5}$-p.R222Q mutation disappear at high pacing rates (Data not shown).

On the other hand, in atrial, ventricular, and Purkinje models, the presence of $Na_{v1.5}$-p.R222Q and $Na_{v1.5}$-p.I141V mutations lowers the excitation thresholds for action potential generation compared with the WT. Thus, threshold potential could be rapidly reached during the diastolic depolarization phase and consequently fire more action potentials in the Purkinje fiber compared to the WT condition. In contrast, atrial and ventricular cells do not show any spontaneous or ectopic activity in the presence of $Na_{v1.5}$-p.R222Q and $Na_{v1.5}$-p.I141V mutations. The biophysical modification induced by these mutations may promote the onset of arrhythmias by increasing the excitability of atrial and ventricular cells but cannot induce a spontaneous activation of these cells. Thus, as described by Laurent et al., the premature ventricular contraction observed in the affected patients may be triggered via the abnormal activity of the Purkinje fibers in the presence of p.R222Q and p.I141V mutations [2].

Moreover, the investigation of conduction velocity in fibers of MGTG, TNNP, and SANNBZ cell models shows an accelerated atrial, ventricular, and Purkinje conduction in the presence of $Na_{v1.5}$-p.I141V mutation. Similar variations were observed in $Na_{v1.5}$-p.R222Q mutation, whereas the conduction velocity was lower than WT condition in Purkinje cell model. The difference between the two mutations is related to

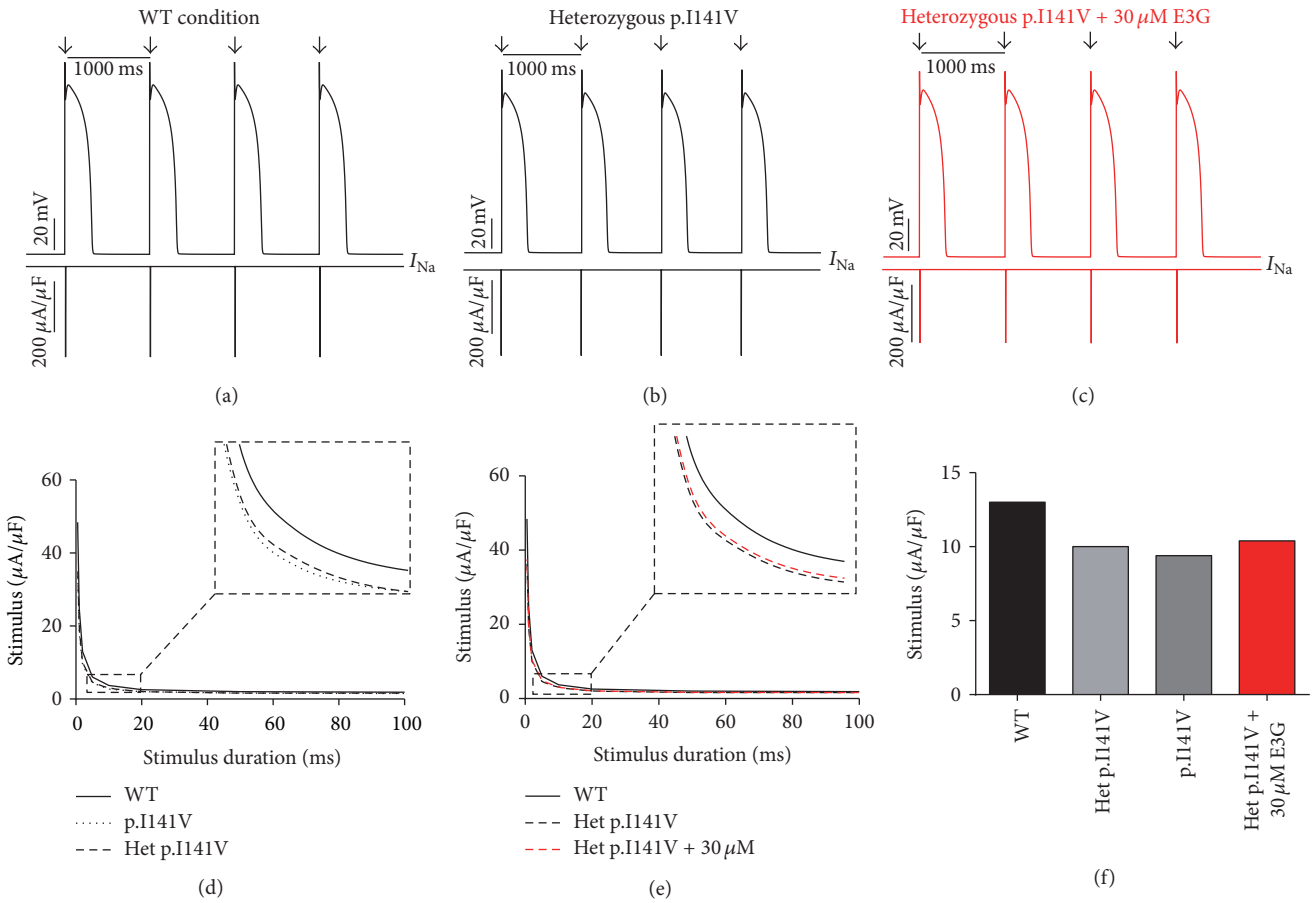

Figure 11: Effects of 30 μM E3G on ventricular cell action potentials for $Na_{v1.5}$-WT and $Na_{v1.5}$-p.I141V conditions (TNNP cell model). (a), (b), and (c) Simulated APs (Top of the panels) and the cardiac sodium currents (Bottom of the panels) in WT, heterozygous $Na_{v1.5}$-p.I141V, and heterozygous $Na_{v1.5}$-p.I141V + 30 μM conditions at 1 Hz cycle length. Arrows: external stimulus. (d) and (e) Strength-duration curves in the TNNP cell model for $Na_{v1.5}$-WT and heterozygous $Na_{v1.5}$-p.I141V conditions with or without 30 μM E3G (inset, zoom on the strength-duration curves). (f) Excitation thresholds at 2 ms stimulus duration in the TNNP atrial AP or without 30 μM E3G.

the left shift of the steady state of inactivation shown by the $Na_{v1.5}$-p.R222Q mutant. Indeed, when the $Na_{v1.5}$-p.R222Q effect on the steady state of inactivation was suppressed, an increase of the conduction velocity was observed (Data not shown).

4.3. Antiarrhythmic Effect of E3G on the MEPPC and EPVT Syndromes. By implementing the experimental functional effects of E3G on the cardiac ion channels, we investigated whether E3G had an antiarrhythmic effect on $Na_{v1.5}$-p.R222Q and $Na_{v1.5}$-p.I141V-related cardiac syndromes.

Regarding the $Na_{v1.5}$-p.R222Q mutation, the application of 30 μM E3G suppressed the ectopic APs characteristic of the MEPPC phenotype. However, at the same dose, E3G partially reduced the frequency of ectopic beats observed in Purkinje cells for the EPVT. These effects could be related to the inhibitory action of this compound on cardiac sodium channels, as was described in some antiarrhythmic drugs such as Quinidine and flecainide [2, 23]. In addition, the increase of excitation threshold for action potential generation and the decrease of conduction velocities, in the presence of 30 μM E3G, may also limit the cardiac cells hyperexcitability that is related to gain of functions mutations of the cardiac sodium channels.

On the other hand, a clear difference in E3G effect was observed between the MEPPC and EPVT disorders. This difference could be explained by the biophysical properties of $Na_{v1.5}$-p.R222Q and $Na_{v1.5}$-p.I141V mutants. Indeed, in contrast to the $Na_{v1.5}$-p.I141V mutation, known by the sole modification of the activation process of $Na_{v1.5}$, the $Na_{v1.5}$-p.R222Q mutation shifted the activation and inactivation processes towards more negative potentials [2, 3]. Therefore, E3G generated a more pronounced loss of function in the $Na_{v1.5}$-p.R222Q mutant than the $Na_{v1.5}$-p.I141V one. This is presumably due to the magnification of the negative shifts of $Na_{v1.5}$ steady state inactivation induced in presence of both E3G and $Na_{v1.5}$-p.R222Q.

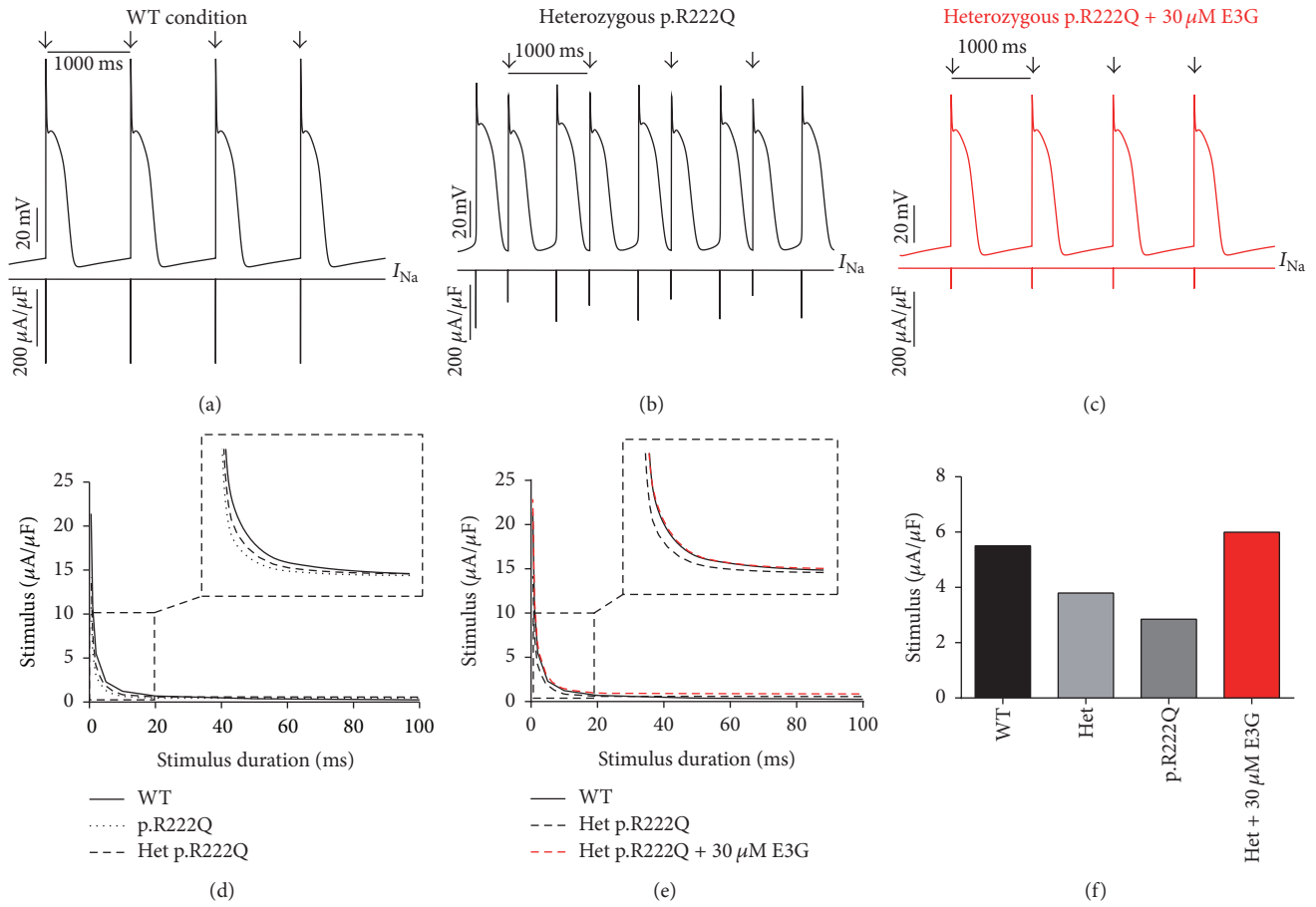

FIGURE 12: Effects of 30 μM E3G on Purkinje cell action potentials for $Na_{v1.5}$-WT and $Na_{v1.5}$-p.R222Q conditions (SANNBZ cell model). (a), (b), and (c) Simulated APs (Top of the panels) and the cardiac sodium currents (Bottom of the panels) in WT, heterozygous $Na_{v1.5}$- p.R222Q, and heterozygous $Na_{v1.5}$-p.R222Q + 30 μM conditions at 1 Hz cycle length. Arrows: external stimulus. (d) and (e) Strength-duration curves in the SANNBZ cell model for $Na_{v1.5}$-WT and heterozygous $Na_{v1.5}$-p.R222Q conditions with or without 30 μM E3G at 2.5 Hz (inset, zoom on the strength-duration curves). (f) Excitation thresholds at 2 ms stimulus duration in the SANNBZ atrial AP or without 30 μM E3G.

5. Conclusion

The present simulations suggest that E3G consumption may have a beneficial effect in the setting of cardiac sodium channelopathies displaying hyperexcitability phenotypes. Thus, this compound may offer a new promising alternative to prevent and treat the episodes of arrhythmia.

Additional Points

Limitations of the Study. The current study has several limitations: (i) the used cellular models did not incorporate the effects of adrenergic stimulation. (ii) Any biological variability was incorporated in these simulations. (iii) We assumed that WT and mutants ions channels have similar affinity to E3G. (iv) Kinetic effects of E3G were not considered in this study. (v) Cell-level arrhythmias such as early after depolarization and delayed after depolarization, or reentry, are not investigated in the current study. (vi) Any comparison of E3G effects was realized in the used action potential models.

Competing Interests

The authors declare that they have no competing interests.

Authors' Contributions

Professors Mohamed-Yassine Amarouch and Driss Mazouzi contributed equally to this work as senior authors.

Acknowledgments

The authors would like to thank (i) Professor Jan P. Kucera, Department of Physiology, University of Bern, Switzerland, for his comments on this manuscript and (ii) Michael Clerx, Maastricht University, Netherlands, for his technical help with Myokit software.

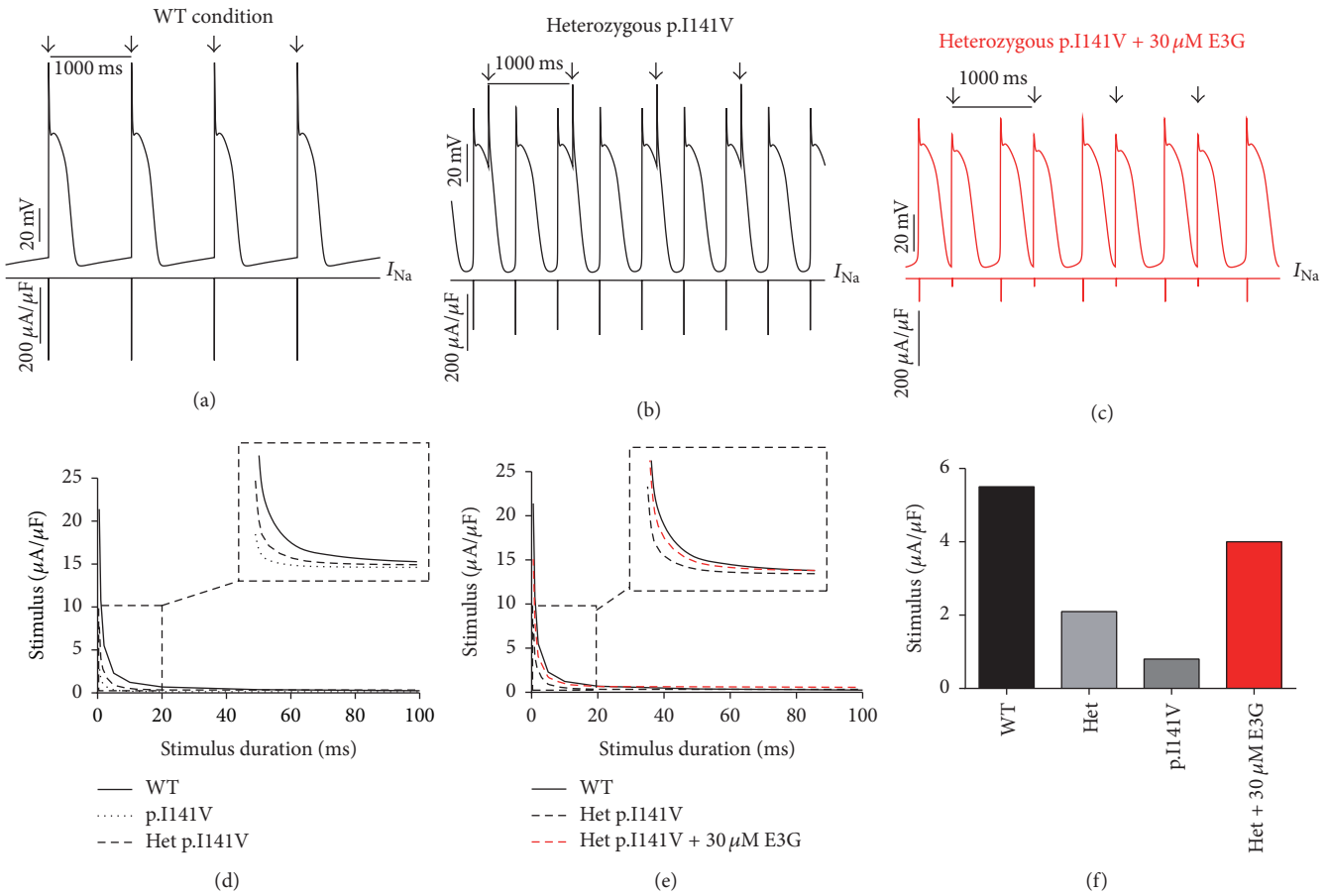

FIGURE 13: Effects of 30 μM E3G on Purkinje cell action potentials for $Na_{v1.5}$-WT and $Na_{v1.5}$-p.I141V conditions (SANNBZ cell model). (a), (b), and (c) Simulated APs (Top of the panels) and the cardiac sodium currents (Bottom of the panels) in WT, heterozygous $Na_{v1.5}$-p.I141V, and heterozygous $Na_{v1.5}$-p.I141V + 30 μM conditions at 1 Hz cycle length. Arrows: external stimulus. (d) and (e) Strength-duration curves in the SANNBZ cell model for $Na_{v1.5}$-WT and heterozygous $Na_{v1.5}$-p.I141V conditions with or without 30 μM E3G at 2.5 Hz (inset, zoom on the strength-duration curves). (f) Excitation thresholds at 2 ms stimulus duration in the SANNBZ atrial AP or without 30 μM E3G.

References

[1] H. Abriel and E. V. Zaklyazminskaya, "Cardiac channelopathies: genetic and molecular mechanisms," *Gene*, vol. 517, no. 1, pp. 1–11, 2013.

[2] G. Laurent, S. Saal, M. Y. Amarouch et al., "Multifocal ectopic Purkinje-related premature contractions: a new SCN5A-related cardiac channelopathy," *Journal of the American College of Cardiology*, vol. 60, no. 2, pp. 144–156, 2012.

[3] S. A. Mann, M. L. Castro, M. Ohanian et al., "R222Q SCN5A mutation is associated with reversible ventricular ectopy and dilated cardiomyopathy," *Journal of the American College of Cardiology*, vol. 60, no. 16, pp. 1566–1573, 2012.

[4] H. Swan, M. Y. Amarouch, J. Leinonen et al., "Gain-of-function mutation of the SCN5A gene causes exercise-induced polymorphic ventricular arrhythmias," *Circulation: Cardiovascular Genetics*, vol. 7, no. 6, pp. 771–781, 2014.

[5] M.-Y. Amarouch, M. A. Kasimova, M. Tarek, and H. Abriel, "Functional interaction between S1 and S4 segments in voltage-gated sodium channels revealed by human channelopathies," *Channels*, vol. 8, no. 5, pp. 414–420, 2014.

[6] M.-Y. Amarouch and H. Abriel, "Cellular hyper-excitability caused by mutations that alter the activation process of voltage-gated sodium channels," *Frontiers in Physiology*, vol. 6, article 45, 2015.

[7] H. A. Fozzard, M. F. Sheets, and D. A. Hanck, "The sodium channel as a target for local anesthetic drugs," *Frontiers in Pharmacology*, vol. 2, article 68, 2011.

[8] J. Kang, H. Cheng, J. Ji, J. Incardona, and D. Rampe, "In vitro electrocardiographic and cardiac ion channel effects of (−)-epigallocatechin-3-gallate, the main catechin of green tea," *The Journal of Pharmacology and Experimental Therapeutics*, vol. 334, no. 2, pp. 619–626, 2010.

[9] P. V. A. Babu and D. Liu, "Green tea catechins and cardiovascular health: an update," *Current Medicinal Chemistry*, vol. 15, no. 18, pp. 1840–1850, 2008.

[10] H. N. Graham, "Green tea composition, consumption, and polyphenol chemistry," *Preventive Medicine*, vol. 21, no. 3, pp. 334–350, 1992.

[11] F. Shahidi, "Antioxidants in food and food antioxidants," *Die Nahrung*, vol. 44, no. 3, pp. 158–163, 2000.

[12] E. P. Scholz, E. Zitron, H. A. Katus, and C. A. Karle, "Cardiovascular ion channels as a molecular target of flavonoids," *Cardiovascular Therapeutics*, vol. 28, no. 4, pp. e46–e52, 2010.

[13] K. Kelemen, C. Kiesecker, E. Zitron et al., "Green tea flavonoid epigallocatechin-3-gallate (EGCG) inhibits cardiac hERG potassium channels," *Biochemical and Biophysical Research Communications*, vol. 364, no. 3, pp. 429–435, 2007.

[14] M. M. Maleckar, J. L. Greenstein, N. A. Trayanova, and W. R. Giles, "Mathematical simulations of ligand-gated and cell-type specific effects on the action potential of human atrium," *Progress in Biophysics and Molecular Biology*, vol. 98, no. 2-3, pp. 161–170, 2008.

[15] P. Stewart, O. V. Aslanidi, D. Noble, P. J. Noble, M. R. Boyett, and H. Zhang, "Mathematical models of the electrical action potential of Purkinje fibre cells," *Philosophical Transactions of the Royal Society A: Mathematical, Physical and Engineering Sciences*, vol. 367, no. 1896, pp. 2225–2255, 2009.

[16] K. H. W. J. Ten Tusscher, D. Noble, P. J. Noble, and A. V. Panfilov, "A model for human ventricular tissue," *American Journal of Physiology-Heart and Circulatory Physiology*, vol. 286, no. 4, pp. H1573–H1589, 2004.

[17] M. Courtemanche, R. J. Ramirez, and S. Nattel, "Ionic mechanisms underlying human atrial action potential properties: insights from a mathematical model," *The American Journal of Physiology—Heart and Circulatory Physiology*, vol. 275, no. 1, pp. H301–H321, 1998.

[18] D. DiFrancesco and D. Noble, "A model of cardiac electrical activity incorporating ionic pumps and concentration changes," *Philosophical Transactions of the Royal Society of London. Series B: Biological Sciences*, vol. 307, no. 1133, pp. 353–398, 1985.

[19] M. Clerx, P. Collins, E. de Lange, and P. G. A. Volders, "Myokit: a simple interface to cardiac cellular electrophysiology," *Progress in Biophysics and Molecular Biology*, vol. 120, no. 1–3, pp. 100–114, 2016.

[20] T. Opthof, R. Coronel, and M. J. Janse, "Is there a significant transmural gradient in repolarization time in the intact heart?: Repolarization gradients in the intact heart," *Circulation: Arrhythmia and Electrophysiology*, vol. 2, no. 1, pp. 89–96, 2009.

[21] P. Taggart, P. M. I. Sutton, T. Opthof et al., "Transmural repolarisation in the left ventricle in humans during normoxia and ischaemia," *Cardiovascular Research*, vol. 50, no. 3, pp. 454–462, 2001.

[22] R. Panikkath, K. Reinier, A. Uy-Evanado et al., "Prolonged tpeak-to-tend interval on the resting ECG is associated with increased risk of sudden cardiac death," *Circulation: Arrhythmia and Electrophysiology*, vol. 4, no. 4, pp. 441–447, 2011.

[23] M. Y. Amarouch, H. Swan, J. Leinonen et al., "Antiarrhythmic action of flecainide in polymorphic ventricular arrhythmias caused by a gain-of-function mutation in the Nav1.5 sodium channel," *Annals of Noninvasive Electrocardiology*, vol. 21, no. 4, pp. 343–351, 2016.

Hindawi Publishing Corporation
Computational and Mathematical Methods in Medicine
Volume 2016, Article ID 9567294, 9 pages
http://dx.doi.org/10.1155/2016/9567294

Research Article

Endoleak Assessment Using Computational Fluid Dynamics and Image Processing Methods in Stented Abdominal Aortic Aneurysm Models

Yueh-Hsun Lu,[1,2] Karthick Mani,[3] Bivas Panigrahi,[3] Wen-Tang Hsu,[3] and Chia-Yuan Chen[3]

[1]*Department of Radiology, Taipei City Hospital, Zhongxing Branch, Taipei 103, Taiwan*
[2]*National Yang-Ming University, Taipei 112, Taiwan*
[3]*Department of Mechanical Engineering, National Cheng Kung University, Tainan 701, Taiwan*

Correspondence should be addressed to Chia-Yuan Chen; chiayuac@mail.ncku.edu.tw

Received 1 April 2016; Revised 2 July 2016; Accepted 9 August 2016

Academic Editor: Xiaopeng Zhao

Endovascular aortic aneurysm repair (EVAR) is a predominant surgical procedure to reduce the risk of aneurysm rupture in abdominal aortic aneurysm (AAA) patients. Endoleak formation, which eventually requires additional surgical reoperation, is a major EVAR complication. Understanding the etiology and evolution of endoleak from the hemodynamic perspective is crucial to advancing the current posttreatments for AAA patients who underwent EVAR. Therefore, a comprehensive flow assessment was performed to investigate the relationship between endoleak and its surrounding pathological flow fields through computational fluid dynamics and image processing. Six patient-specific models were reconstructed, and the associated hemodynamics in these models was quantified three-dimensionally to calculate wall stress. To provide a high degree of clinical relevance, the mechanical stress distribution calculated from the models was compared with the endoleak positions identified from the computed tomography images of patients through a series of imaging processing methods. An endoleak possibly forms in a location with high local wall stress. An improved stent graft (SG) structure is conceived accordingly by increasing the mechanical strength of the SG at peak wall stress locations. The presented analytical paradigm, as well as numerical analysis using patient-specific models, may be extended to other common human cardiovascular surgeries.

1. Introduction

Patients with abdominal aortic aneurysm (AAA) have a significantly high risk of suffering from destructive aneurysm rupture, which is a major source of morbidity and mortality in human [1]. AAA affects 8.8% of the population over the age of 65 [2]. This condition has an 11% risk of rupturing, and this rate exponentially increases when the transverse aneurysmal diameter exceeds 5 cm [3]. To prevent sudden aneurysm rupture, the mean enlargement rate and the occurrence of sudden change in the size of AAA are also important check points for subsequent follow-up medical care [4]. AAA is characterized by the degradation of elastinous constituents, the adaptive growth and remolding of collagen, the loss of smooth muscle cells with thinning of the medial wall, the infiltration of lymphocytes and macrophages, and neovascularization [5–8]. The major root cause of AAA is unclear, but abnormal flow-induced mechanical stress that is acting on the vessel wall in blood circulation is a known critical factor that contributes to AAA formation and pathological evolution [8, 9]. An in-depth investigation from the hemodynamic aspect can therefore provide invaluable insights to unveil the convoluted factors that lead to AAA formation and propagation.

Patients aged over 60 years with an aneurysm diameter exceeding 5.5 cm are commonly advised to undergo endovascular aneurysm repair (EVAR) or open AAA repair; however, these patients should be anesthetically and medically prepared for the procedures [10]. Clinical trials show that EVAR reduces the 30-day operative mortality of patients with large AAA by two-thirds compared with open AAA repair [10]. EVAR could be an ideal alternative for AAA treatment, but long-term clinical results are necessary to support the validity of EVAR. In EVAR, a stent graft (SG) is guided

from the femoral artery to the aneurysm bulge to shield the aneurysm from the blood flow. This SG can serve as a blood flow conduit through the aneurysm sac [11] to eliminate the blood in the intrasac of aneurysm and therefore reduce the risk of aneurysm rupture [12]. However, the complexity of hemodynamics and biomechanics in the aneurysm region may cause several complications in post-EVAR patients; such complications include an aneurysm expansion and rupture even in a successful EVAR [11], blood seepage into the cavity between the aneurysm wall and the SG wall (termed as endoleak) [12], SG migration, and SG failure [13].

Endoleak formation is associated with the failure of SG implantation and is used as an endpoint in clinical trials [14]. Endoleaks can be divided into five types based on the source of blood flow into the intrasac of aneurysm [11]. Type I endoleaks have a blood flow that originates from a SG attachment site, including the aortic neck and distal iliac attachment sites [15]. With this type, separation occurs between the SG and the native arterial wall, and the direction communication between the aneurysm sac and the systemic circulation is created; this condition can lead to SG failure [11]. Type II endoleaks are those in which blood flows into the aneurysm sac in the retrograde direction through the branch from the portion of the aorta that has not received a SG. Typical sources of Type II endoleaks include the inferior mesenteric and lumbar arteries [11]. Type III endoleaks occur when the structure of a SG fails [15]. Type IV endoleaks are caused by graft porosity and usually identified on the completion of angiography during implantation when the patient is fully anticoagulated [15]. Aneurysm expansion without endoleaks is referred to as endotension or a Type V endoleak [11]. However, whether or not Type I endoleaks are associated with a continued risk of aneurysm rupture and require immediate attention of medical treatments remains controversial [16]. Accordingly, the current study focused on Type I endoleaks to provide direct clinical impacts.

Computed tomographic angiography (CTA) is widely used to detect endoleaks because of the high sensitivity and specificity of this method [17]. However, CTA is less effective than conventional angiography in classifying endoleak types because of the difficulty in determining the direction of a blood flow from a routine CTA process. Another concern for CTA imaging is radiation exposure. High radiation doses of CTA administered during EVAR pose a potential risk of radiation-induced skin damage and later malignancy [18]. Patients who underwent EVAR should detect the damage early to prevent additional endoleak formation. Early endoleak detection reduces the need for unremitting follow-up through CTA examination and thus minimizes radiation exposure. The current study employed a three-dimensional (3D) computational fluid dynamics (CFD) method combined with a series of image processing methods to assess endoleak formation from the hemodynamic perspective.

A high degree of physiological relevance is necessary for a CFD analysis to simulate human cardiovascular flows with high accuracy. In addition to the physiological consistency of the imposed boundary and initial conditions, a direct match of the vascular geometrical features between numerical modeling and patient data is required. Papaharilaou et al. (2007) evaluated the AAA wall stress in an anatomically identical 3D patient-specific AAA model. They used 3D reconstruction software and developed the patient-specific AAA model from the CT images [19]. A similar concept was also adopted to create patient-specific AAA models for in vitro flow dynamic assessment and the wall stress evaluation through an experimental flow visualization technique [8]. Li and Kleinstreuer (2006) studied the effect of Type I endoleak on the stented AAA model through a numerical simulation technique. Their study reveals that there is an increase in the cavity pressure due to the endoleak which increases the probability of aneurysm rupture [20]. The consequences of various types of endoleak in a silicon rubber based AAA model were experimented on by Lu et al. under the maintained physiological conditions, and their study reveals that the presence of endoleak elevates the mean sac pressure to the aortic pressure. These patient-specific models provide useful insight towards the pathological aspect of AAA under the influence of endoleak. Though many researchers highlight the effect of endoleak on the aneurysm, very few researches have been reported till date which can predict either position or formation of the endoleak in post-EVAR patients [21]. To address this issue, as a first step, in the present work, six patient-specific models were constructed from the patients' CT images in order to provide a global view on the relationship between endoleak and its surrounding flow to draw a conclusion on identifying possible endoleak position with a high degree of statistical significance based on hemodynamics. Furthermore, the compliance nature of the aneurysm wall should be considered in AAA flow modeling to study the hemodynamics in AAA patients [22–25]. A fluid-structure interaction (FSI) method was developed to couple the wall effect into the simulation of AAA hemodynamics. This method was first implemented in AAA modeling in 2001 [22], where the complex mechanical interaction between blood flow and wall dynamics in a 3D custom model of an AAA patient was calculated through the FSI method. Several researchers also validated the importance of incorporating the FSI method compared with simple computational models using finite element modeling [23, 25, 26] in the AAA simulation. The FSI method underestimates the peak stress by 9% [23], which can increase to 12.5% if only a homogeneous pressure finite element model is used [19]. An open debate currently exists on whether or not a compliant wall should be considered in fluid dynamic experiments and simulations of AAAs [27]. The coupling of complete FSI in hemodynamic simulations provides a new insight into the examination of AAA-related complications, such as intraluminal thrombus [19], and its relationship with flows in the AAA lumen. In the present work, the FSI method was selected to provide a comprehensive flow assessment with high accuracy for blood dynamic flow behavior in SG.

2. Materials and Methods

2.1. Clinical Summary. Clinical information of six patients was included in this study. All the patients were of old age (81.5 ± 9.04 years) and had a history of atherosclerosis.

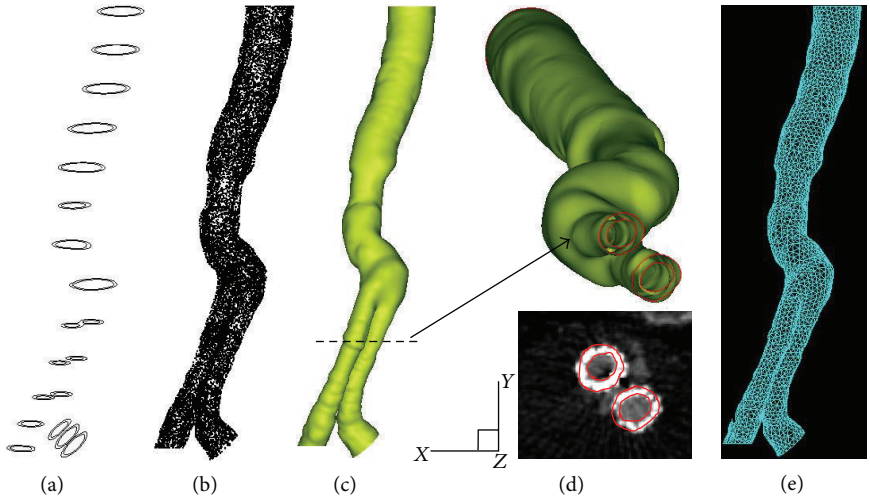

Figure 1: Snapshots of critical steps in 3D reconstruction of a patient-specific AAA with SG model. (a) Lumen segmentation; (b) geometry interpolation; (c) surface spline fitting; (d) selected reconstructed SG features and the corresponding in-plane CT slice in the region of interest; and (e) finite element meshing for CFD analysis.

Maximum diameter of the aneurysm sac for all the patients was found to be 6.96 ± 1.39 cm. Moreover, dynamic CT angiography scan suggests the presence of either Type I or Type II endoleak. CT scans were available for all the patients and were acquired at Taipei Veterans General Hospital (Taipei, Taiwan) through a CT scanner (Aquilion 64, Toshiba, Tokyo, Japan) with a 64-slice imaging capability and each scanned image had a voxel size of 5 mm in all the spatial directions. Each patient received 120 cc of contrast material before scanning via injection at a rate of 4.5 cc/s. This dose was administered into the cubital vein of the right arm. A bolus-tracking technique was applied in an arterial phase at 1.5 mm intervals for image recoding.

2.2. 3D Patient-Specific Anatomical Models. To provide hemodynamic assessment results with a high degree of clinical relevance, six computational models with patient-specific SG geometry were reconstructed from CT images of AAA patients with SG implants. A series of image processing methods were employed for the reconstruction and smoothing of the 3D surface. In particular, three software programs, namely, Simpleware (Simpleware Ltd., Exeter, UK), Geomagic (Geomagic Inc., NC, USA), and Pro/Engineer (Parametric Technology Corp., MA, USA), were used for the 3D reconstruction as well as smoothing surface of the patient-specific models. CT images were segmented through an intensity threshold method to extract the geometrical features of the implanted SG. Then, image smoothing using a recursive Gaussian filter was conducted to further filter background noise. A 3D anatomical model was subsequently produced in stereolithography format, in which a mesh of triangles was applied to form the shell of the reconstructed SG. Once the 3D model of the SG was constructed, a surface refinement algorithm was applied, and the surfaces and boundaries of the model were subsequently created through the nonuniform rational basis spline method. Detailed 3D reconstruction can be found in the literature [8, 9, 21, 28]. Figure 1 shows a selected schematic of the reconstructed AAA with SG model. In the present work, the patient data were all acquired a few months after SG implantation. Fully grown connective cells and tissues attached to the implants. Therefore, the SG was assumed to have a similar material property to the aneurysm wall. The SG wall was constructed by circumferentially dilating the SG perimeter outward; this wall was modeled as a hyperelastic homogeneous incompressible isotropic material with a uniform thickness of 2 mm [19], a density of 2000 kg/m^3, Young's modulus of 2.7 MPa, and a Poisson ratio of 0.45 [29].

2.3. Computational Fluid Dynamics (CFD) Analysis. The FSI method was coupled with the incompressible Navier–Stokes equations to provide detailed flow patterns, specifically for fluid flows in the SG vicinity and enhance the accuracy of stress distribution calculation on the SG wall structure. In the FSI simulation, fluid forces (blood) were applied onto the structure (SG), and then the structural deformation changed the fluid domain. Dominant fluid variables (pressure and velocity) and wall displacement were selected as solution variables of the fluid flow [30]. The imposing boundary and initial flow conditions were assumed to be identical for the six patient-specific models to provide a systemic investigation unveiling the interactions between the geometrical feature of the implanted SG and the encompassed blood flow dynamics. Blood pulsatility and SG properties were also determined in a similar manner. Blood was treated as a homogeneous, incompressible, and Newtonian fluid with a dynamic viscosity of 0.004 Pa s and a density of 1,055 kg/m^3 [29]. Physiologically representative inflow velocity and outflow pressure waveforms were applied in the modeling with a pulse period of 1.2 s [12], and the Reynolds number (Re)

was set as 2234 [9, 31]. To demonstrate grid independence, cell *Re* was calculated, and a convergence was reached for the approximate element number of 155,000. The total element number selected in the modeling for each patient slightly varied because of the different geometric natures of all tested patients. Commercially available software Adina (Adina, Watertown, MA) was used for finite element analysis. The von-Mises stress (wall stress) distribution was calculated and analyzed for each simulation case to represent the complex stress distribution in the wall of each virtual AAA. The von-Mises stress was derived from the distortion energy used in studies of material failure and was calculated from the six components of the stress tensor [32]. Studying the von-Mises stress allows significant interpretation of the hemodynamic flow impact to the SG structure, as evidenced by a previous study where the wall stress was several orders of magnitude larger than the wall shear stress in AAA models [1].

2.4. Image Processing of CT Images for Quantification of Endoleak Geometry. A series of image processing steps was employed to characterize the geometrical features of endoleak in AAA with SG-implanted models. Endoleak positions, with respect to the SG centroid, were quantified through the presented image processing flow. The results are shown in Figure 2. In addition to image binarization, region-of-interest (ROI) cropping from the raw CT image was performed. Cropping segmentation was performed to enhance and isolate the ROI. This step was followed by a series of image filtering techniques, such as noise reduction to sharpen the edges and ROI deblurring. Noise reduction is crucial to avoid artifacts and preserve anatomical details. This operation was achieved by replacing each pixel with the average pixels in a square window surrounding this pixel. Canny edge detection was performed through a 2D spatial gradient measurement on an image, and regions that corresponded to edges were highlighted. This method is usually applied to determine the approximate absolute gradient magnitude at each point in an imported grayscale image. After the edges of endoleaks and SG structures were located, an image morphological operation was applied to close all voids in the ROI. Subsequently, the centroids of each segmented structure were calculated. The entire process was conducted with an in-house imaging processing Matlab (MathWorks, Natick, MA, USA) programming code.

2.5. Matching Index. Six patient-specific models of AAA with SG were reconstructed carefully because of their high geometrical irregularity. The wall stress distribution along the height of each SG structure was obtained through FSI calculation. To provide significant clinical relevance, endoleak CT image slices were selected and compared with the corresponding wall stress distribution slices to determine the possible correlation between the endoleak and the local wall stress peak. Slices with location matching between the wall stress peak and the endoleak appearance on the SG structure are highlighted in Figures 3 and 4. The degree of

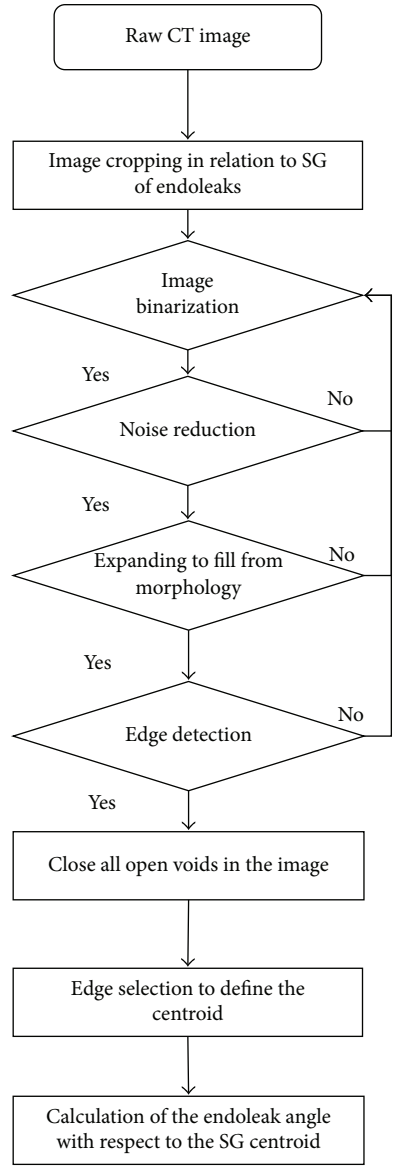

Figure 2: Illustration of the applied image processing algorithms describing the process flow for endoleak geometrical characterization.

the reported location agreement was further quantified and presented as a matching index using

$$\text{Matching index (\%)} = \frac{\left|\text{Angle}_{\text{Endoleak to SGC}} - \text{Angle}_{\text{Ws to SGC}}\right|}{\text{Angle}_{\text{Ws to SGC}}}, \quad (1)$$

where SGC denotes the centroid of SG.

3. Results and Discussion

3.1. Wall Stress Distribution in Patient-Specific Models. The wall stress distribution on the six patient-specific models was calculated (Figure 3). The distribution was complex with

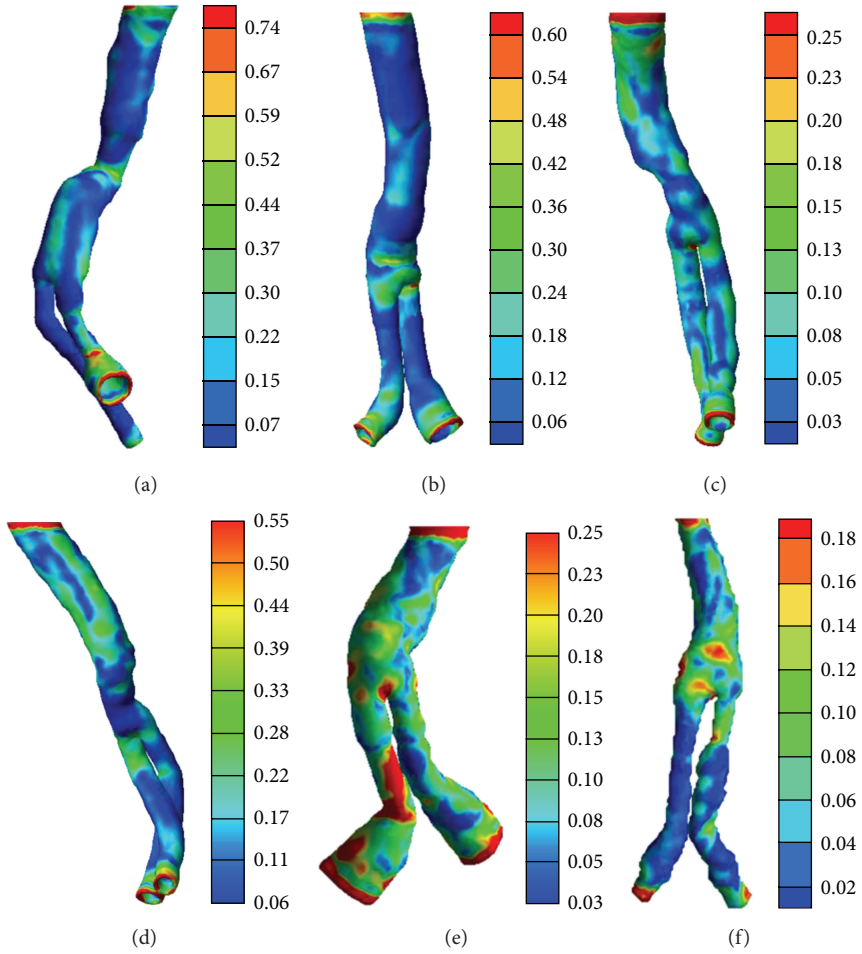

Figure 3: Wall stress distribution of six patient-specific models. (a)–(f) correspond to models I–VI, respectively. The color bar unit is in MPa.

large regional variations along the length of each model. In general, the peak wall stress was concentrated in regions with relatively high degrees of kinking and curved bifurcations, as well as in the vicinity of the model inlet and outlets. These findings well agreed with the results of the previously published researches where higher wall shear stress was evidenced in these aforementioned regions [12, 33]. The maximum calculated wall stress ranged from 0.81 MPa in model I to 0.2 MPa in model VI because of variations in the model structure even under identical imposed boundary conditions. Moreover, the calculated wall shear stress value has a magnitude similarity with the results of previous researches [20], where the authors have evidenced an elevated wall stress of 0.3 MPa near the bifurcating point of the SG model. In model I, the local maximum wall stress was located at the posterior wall of a daughter branch region. The peak magnitude was comparable with that close to the branch outlet and was relatively larger than that in the necking region (anterior region) of the SG. Notably, this stress peak appeared only in one daughter branch. This result indicates that the stress distribution is not symmetrical in both daughter branches. The symmetric outlet pressure boundary conditions were applied to both branches; thus, this asymmetrical wall stress distribution was contributed mainly by the SG geometry differences between them. Further analysis of the wall distribution in model II showed that the peaks were concentrated not only on the SG inlet and outlets but also on the anterior wall of the bifurcation. The peak wall stress was calculated up to 0.66 MPa. The distributed wall stress is concentrated in these aforementioned locations; hence, additional attention should be given to these regions in terms of mechanical strength reinforcement of the SG. Consistent wall stress distribution was found in models III, IV, V, and VI. Aside from the wall stress concentrated on the previously referred locations, local peak wall stress was also found along the length of one daughter branch in model V. This result can be attributed to the fact that the SG was significantly oriented out of the plane in the posterior end of this daughter branch with respect to the anterior side. The flow was diverted significantly, which resulted in high local wall stress distribution due to the pronounced flow impingement on the posterior wall.

3.2. Correlation between Endoleak and Peak Wall Stress through Location Comparison. Li and Kleinstreuer (2006) [20] computationally simulated the type I endoleak in a

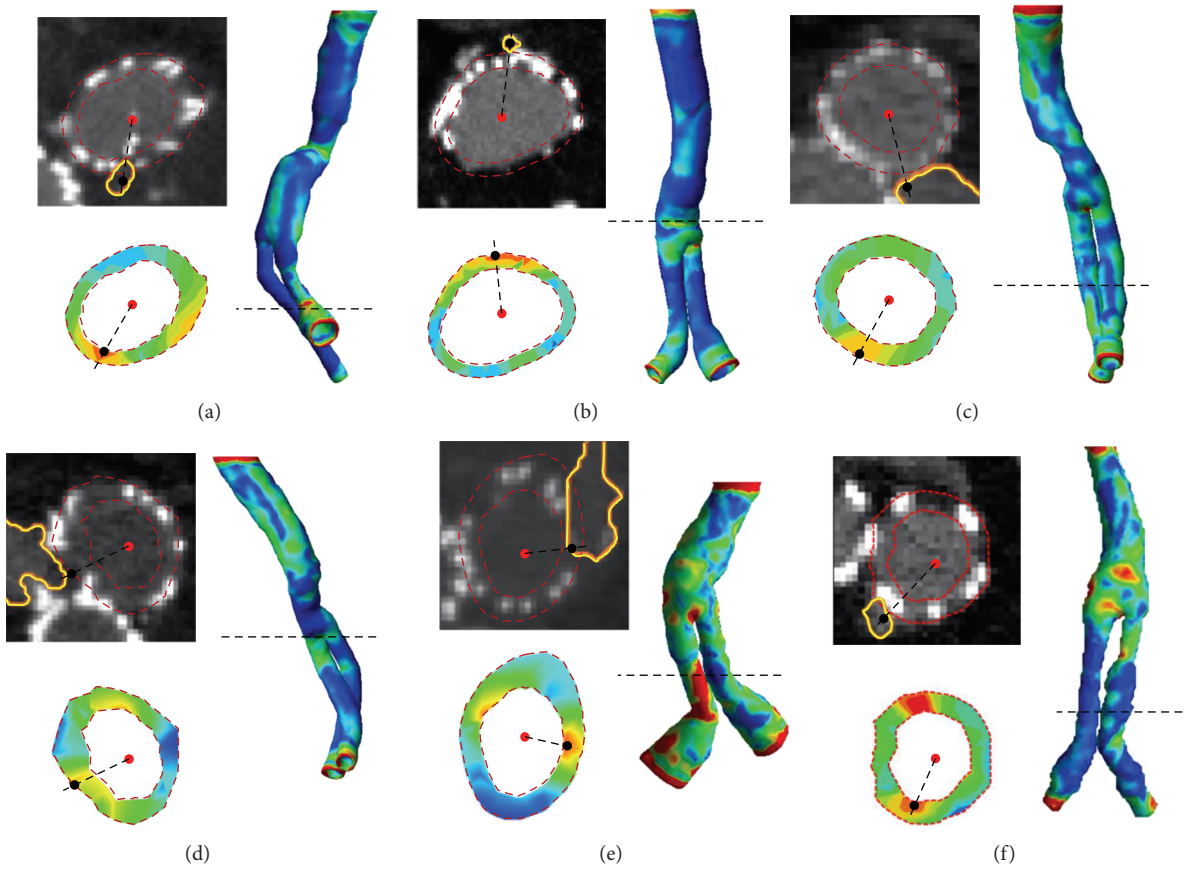

Figure 4: Location comparison between the endoleak (CT image) and the wall stress peak (color 3D and slicing plots) of six patient-specific models. Panels (a)–(f) correspond to models I–VI, respectively. SG and endoleak boundaries were outlined as red dotted and yellow solid lines, respectively. Each slice plot was extracted from the corresponding 3D plot at the level outlined as a black dashed line.

stented AAA model and indicated that the presence of endoleak maximizes the EVG wall shear stress near the bifurcating point while reducing its magnitude, which certainly differs to our hypothesis that there is an elevation in the EVG wall shear stress corresponding to endoleak position. To delve into possible mechanism underlying the onset of endoleak formation, the location of endoleak and peak wall stress were quantified. Thus, each patient CT image slice that matched the peak wall stress location from the corresponding 3D simulation model was reviewed and quantified through image processing. The obtained endoleak position was compared with the peak wall stress location, and the results are shown in Figure 4. In Figure 4(a), where the first clinical patient data and the modeling results are shown, an endoleak appeared on the distal region of the SG. We measured from the 2D CT image that the endoleak (outlined in yellow) was located at 265° with respect to the SG daughter branch centroid (indicated as red solid dot). This location was very close to the 230.9° wall stress peak with respect to the SG daughter branch centroid in the modeling results. This location agreement (with a matching index of 14.8%) reveals a possible correlation between endoleak formation and the locally concentrated wall stress. However, more than one wall stress peaks were found on the wall stress distribution slice. Another wall stress peak was located on the right hand side of the SG centroid with no endoleak appearance. These results suggest that endoleak formation may possibly occur when the local wall stress is high.

Further investigation of the second patient data set shows that endoleak location agrees well with the peak wall stress location, with a matching index of only 4.4% (Figure 4(b)). Inconsistent with the previous first patient data set where the endoleak was identified in one of the daughter branch regions, the endoleak appeared before the apex of the branches on the second patient data set. A narrowing SG diameter was found at the local geometry in the surrounding endoleak area. This distorted geometry may increase the local wall stress and subsequently induce endoleak formation because of the high mechanical loading acting on the SG structure. Patient-specific boundary conditions, such as the local hydrodynamics and SG strength, should be considered to verify the convoluted effects that contribute to endoleak formation. The third patient data set is shown in Figure 4(c). The exact leaking site from the SG is difficult to identify in the CT image because the endoleak spread over both SG branches. Alternatively, the middle point of the endoleak boundary that was in contact with both SG branch boundaries was selected as the leaking site. The

Table 1: Summary of the position correlation between the endoleak and the local wall stress peak through the presentation of the matching index calculation.

	Angle of endoleak to SGC	Angle of WS to SGC	Matching index (%)
Model I	265.1	230.9	14.8
Model II	87.8	91.9	4.4
Model III	275.2	244.7	12.5
Model IV	203.1	214.3	5.2
Model V	8.5	336.9	9.4
Model VI	234.6	249.7	6.0

matching index was calculated to be 12.5%, which is still within the acceptable range. Similar endoleak geometry was found with the boundary elongated through both daughter branches of the SG (Figure 4(d)). The middle point was again identified, and its location was compared with that of the wall stress peak of a SG daughter branch. The matching index in this case was measured to be 5.2%, which shows a high degree of position matching between the endoleak and the wall stress peak. The fifth patient data set is shown in Figure 4(e) with a position match occurring in the SG daughter branch between the endoleak and the wall stress peak. Specifically, the endoleak site was identified by an experienced radiologist (the leading author of the presented study) through examination of the sequential CT slices. A secondary wall stress peak again appeared on the opposite side of the investigated wall stress peak site. However, no endoleak was found in the vicinity of this secondary wall stress peak. Therefore, the matching index was calculated on the wall stress peak that was close to the verified endoleak with a value of 9.4%. Another patient data set is shown in Figure 4(f), where both the endoleak and the wall stress peak were found in one of the daughter branches of the SG. The matching index in this case was calculated to be 6.0%, indicating a high matching degree between the locations of the endoleak and the wall stress peak. The patient data sets suggest that a good agreement in location exists between the endoleak appearance and the local wall stress peak.

Table 1 presents a summarized position comparison evaluated through the matching index calculation from the six patient data sets. The conclusive points of view are described in the following. First, the calculated matching index values from these data sets were in a high level of agreement ranging from 4.4% to 14.8%. These consistent results support the idea that endoleak formation occurs because of the local high wall stress contributed by the local flow and SG structure interactions. This finding can be beneficial for a better SG design to reduce the chances of a secondary incision caused by the failure of previously implanted SG. The effects of radiation exposure during the typical long-term follow-up care using CT imaging can therefore be omitted. However, intensive investigation should focus on patient-specific hemodynamics. The precision of the obtained results can be increased by considering the flow boundary conditions of patients in modeling the wall stress analysis. Second, endoleak formation may occur in the daughter branches of the SG, where the wall stress is usually high because of the distorted geometry in these two branches. Therefore, the SG design phase should be given a major consideration to reduce the possibility of endoleak formation. Third, a significant barrier was posed while searching for the exact leaking point from the SG for the endoleak angle calculation. A well-trained radiologist or clinic physician should assist with the endoleak identification. An efficient imaging-based method that can capture the dynamic blood flow behavior nonintrusively is necessary to accurately identify the endoleak position. Moreover, the image processing steps, such as image segmentation and 3D reconstruction, are labor intensive. Thus, future advances in automatic imaging software development are warranted to reduce processing time and human errors in this regard. Experimental flow visualization tools, such as particle image velocimetry, can be used to provide a validation test case as a follow-up study in revealing the causes of endoleak formation.

3.3. Limitations. A major limitation to the current study is that mechanical properties of thrombus were not taken into account during the computational analysis. An aneurysm thrombus load substantially affects the hemodynamics inside the stent graft and may develop endoleak [34, 35]. Still, these biomechanical properties vary from person to person making it difficult to consider these properties for computation which were therefore excluded. Additional studies in this aspect will be carried out once the aforementioned issue is resolved.

4. Conclusions

The matching index values in the six patient data sets were all calculated to be lower than 15%. This finding indicates a high degree of correlation between the locations of the endoleak and the local wall stress. This investigation was achieved by performing a series of imaging processing methods to analyze the CT images of patients in a nonintrusive manner in conjunction with patient-specific models for wall stress calculation. The presented analytical paradigm is reliable and robust with high clinical relevance. The results of this study may be used as a basis for future improvement in terms of SG designs to reduce the possibility of SG reoperations. Despite some limitations, the presented technique can be extended to other local hemodynamics of interest.

Competing Interests

The authors declare that they have no competing interests.

Acknowledgments

The study was supported through Ministry of Science and Technology of Taiwan under Contracts nos. MOST 105-2628-E-006-006-MY3 and 104-2221-E-006-169 (to Chia-Yuan Chen). The authors would like to thank Kuang-Ting Liu, Hsing-Hung Lin, and Yen-Heng Liu for their support in imaging analysis and modeling validation. The research

was in part supported by the Ministry of Education, Taiwan, through the Aim for the Top University Project to National Cheng Kung University (NCKU).

References

[1] Z.-Y. Li, U. Sadat, J. U-King-Im et al., "Association between aneurysm shoulder stress and abdominal aortic aneurysm expansion: A Longitudinal Follow-Up Study," *Circulation*, vol. 122, no. 18, pp. 1815–1822, 2010.

[2] A. B. Newman, A. M. Arnold, G. L. Burke, D. H. O'Leary, and T. A. Manolio, "Cardiovascular disease and mortality in older adults with small abdominal aortic aneurysms detected by ultrasonography: the cardiovascular health study," *Annals of Internal Medicine*, vol. 134, no. 3, pp. 182–190, 2001.

[3] L. W. W. Reed, J. W. Hallett Jr., M. A. Damiano, and D. J. Ballard, "Learning from the last ultrasound—a population-based study of patients with abdominal aortic aneurysm," *Archives of Internal Medicine*, vol. 157, no. 18, pp. 2064–2068, 1997.

[4] A. V. Sterpetti, R. D. Schultz, R. J. Feldhaus, S. E. Cheng, and D. J. Peetz Jr., "Factors influencing enlargement rate of small abdominal aortic aneurysms," *Journal of Surgical Research*, vol. 43, no. 3, pp. 211–219, 1987.

[5] A. López-Candales, D. R. Holmes, S. Liao, M. J. Scott, S. A. Wickline, and R. W. Thompson, "Decreased vascular smooth muscle cell density in medial degeneration of human abdominal aortic aneurysms," *American Journal of Pathology*, vol. 150, no. 3, pp. 993–1007, 1997.

[6] G. Ailawadi, J. L. Eliason, and G. R. Upchurch Jr., "Current concepts in the pathogenesis of abdominal aortic aneurysm," *Journal of Vascular Surgery*, vol. 38, no. 3, pp. 584–588, 2003.

[7] P. N. Watton, N. B. Raberger, G. A. Holzapfel, and Y. Ventikos, "Coupling the hemodynamic environment to the evolution of cerebral aneurysms: computational framework and numerical examples," *Journal of Biomechanical Engineering*, vol. 131, no. 10, Article ID 101003, 2009.

[8] C.-Y. Chen, R. Anton, M.-Y. Hung et al., "Effect of intraluminal thrombus on patient-specific abdominal aortic aneurysm hemodynamics via stereoscopic PIV and CFD modeling," *Journal of Biomechanical Engineering*, vol. 136, no. 3, Article ID 031001, 2014.

[9] R. Anton, C. Y. Chen, M. Y. Hung, E. A. Finol, and K. Pekkan, "Experimental and computational investigation of the patient-specific abdominal aortic aneurysm pressure field," *Computer Methods in Biomechanics and Biomedical Engineering*, vol. 8, no. 9, pp. 981–992, 2014.

[10] R. M. Greenhalgh, L. C. Brown, G. P. Kwong et al., "Comparison of endovascular aneurysm repair with open repair in patients with abdominal aortic aneurysm (EVAR trial 1), 30-day operative mortality results: randomised controlled tria," *The Lancet*, vol. 364, no. 9437, pp. 843–848, 2004.

[11] S. W. Stavropoulos and S. R. Charagundla, "Imaging techniques for detection and management of endoleaks after endovascular aortic aneurysm repair," *Radiology*, vol. 243, no. 3, pp. 641–655, 2007.

[12] Z. Li and C. Kleinstreuer, "Analysis of biomechanical factors affecting stent-graft migration in an abdominal aortic aneurysm model," *Journal of Biomechanics*, vol. 39, no. 12, pp. 2264–2273, 2006.

[13] J. Charonko, S. Karri, J. Schmieg, S. Prabhu, and P. Vlachos, "*In vitro*, time-resolved PIV comparison of the effect of stent design on wall shear stress," *Annals of Biomedical Engineering*, vol. 37, no. 7, pp. 1310–1321, 2009.

[14] M. Desai, J. Eaton-Evans, C. Hillery et al., "AAA stent-grafts: past problems and future prospects," *Annals of Biomedical Engineering*, vol. 38, no. 4, pp. 1259–1275, 2010.

[15] M. A. Heikkinen, F. R. Arko, and C. K. Zarins, "What is the significance of endoleaks and endotension," *Surgical Clinics of North America*, vol. 84, no. 5, pp. 1337–1352, 2004.

[16] M. M. M. D. Lawrence-Brown, Z. Sun, J. B. Semmens, K. Liffman, I. D. Sutalo, and D. B. Hartley, "Type II endoleaks: when is intervention indicated and what is the index of suspicion for types I or III?" *Journal of Endovascular Therapy*, vol. 16, supplement 1, pp. I106–I118, 2009.

[17] A. M. Rozenblit, M. Patlas, A. T. Rosenbaum et al., "Detection of endoleaks after endovascular repair of abdominal aortic aneurysm: value of unenhanced and delayed helical CT acquisitions," *Radiology*, vol. 227, no. 2, pp. 426–433, 2003.

[18] R. A. Weerakkody, S. R. Walsh, C. Cousins, K. E. Goldstone, T. Y. Tang, and M. E. Gaunt, "Radiation exposure during endovascular aneurysm repair," *British Journal of Surgery*, vol. 95, no. 6, pp. 699–702, 2008.

[19] Y. Papaharilaou, J. A. Ekaterinaris, E. Manousaki, and A. N. Katsamouris, "A decoupled fluid structure approach for estimating wall stress in abdominal aortic aneurysms," *Journal of Biomechanics*, vol. 40, no. 2, pp. 367–377, 2007.

[20] Z. Li and C. Kleinstreuer, "Effects of major endoleaks on a stented abdominal aortic aneurysm," *Journal of Biomechanical Engineering*, vol. 128, no. 1, pp. 59–68, 2006.

[21] Y.-H. Lu, C.-Y. Chen, P. G. Menon, K.-T. Liu, and H.-H. Lin, "Hemodynamic effects of endoleak formation in abdominal aortic aneurysm patients with stent-graft implants," *Journal of Medical and Biological Engineering*, vol. 34, no. 6, pp. 554–558, 2014.

[22] E. S. Di Martino, G. Guadagni, A. Fumero et al., "Fluid-structure interaction within realistic three-dimensional models of the aneurysmatic aorta as a guidance to assess the risk of rupture of the aneurysm," *Medical Engineering and Physics*, vol. 23, no. 9, pp. 647–655, 2001.

[23] C. M. Scotti, A. D. Shkolnik, S. C. Muluk, and E. A. Finol, "Fluid-structure interaction in abdominal aortic aneurysms: effects of asymmetry and wall thickness," *BioMedical Engineering Online*, vol. 4, article 64, 2005.

[24] C. M. Scotti, J. Jimenez, S. C. Muluk, and E. A. Finol, "Wall stress and flow dynamics in abdominal aortic aneurysms: finite element analysis vs. fluid-structure interaction," *Computer Methods in Biomechanics and Biomedical Engineering*, vol. 11, no. 3, pp. 301–322, 2008.

[25] K. H. Fraser, M.-X. Li, W. T. Lee, W. J. Easson, and P. R. Hoskins, "Fluid-structure interaction in axially symmetric models of abdominal aortic aneurysms," *Proceedings of the Institution of Mechanical Engineers, Part H: Journal of Engineering in Medicine*, vol. 223, no. 2, pp. 195–209, 2009.

[26] C. M. Scotti and E. A. Finol, "Compliant biomechanics of abdominal aortic aneurysms: A Fluid-Structure Interaction Study," *Computers and Structures*, vol. 85, no. 11–14, pp. 1097–1113, 2007.

[27] J. Biasetti, T. C. Gasser, M. Auer, U. Hedin, and F. Labruto, "Hemodynamics of the normal aorta compared to fusiform and saccular abdominal aortic aneurysms with emphasis on a potential thrombus formation mechanism," *Annals of Biomedical Engineering*, vol. 38, no. 2, pp. 380–390, 2010.

[28] M. Lara, C.-Y. Chen, P. Mannor et al., "Hemodynamics of the hepatic venous three-vessel confluences using particle image velocimetry," *Annals of Biomedical Engineering*, vol. 39, no. 9, pp. 2398–2416, 2011.

[29] J. H. Leung, A. R. Wright, N. Cheshire et al., "Fluid structure interaction of patient specific abdominal aortic aneurisms: a comparison with solid stress models," *BioMedical Engineering Online*, vol. 5, article 33, 2006.

[30] K.-J. Bathe, H. Zhang, and S. H. Ji, "Finite element analysis of fluid flows fully coupled with structural interactions," *Computers and Structures*, vol. 72, no. 1–3, pp. 1–16, 1999.

[31] C. Chen, R. Antón, M. Hung, P. Menon, E. A. Finol, and K. Pekkan, "Effects of intraluminal thrombus on patient-specific abdominal aortic aneurysm hemodynamics via stereoscopic particle image velocity and computational fluid dynamics modeling," *Journal of Biomechanical Engineering*, vol. 136, no. 3, Article ID 031001, 2014.

[32] P. G. Menon, N. Teslovich, C.-Y. Chen, A. Undar, and K. Pekkan, "Characterization of neonatal aortic cannula jet flow regimes for improved cardiopulmonary bypass," *Journal of Biomechanics*, vol. 46, no. 2, pp. 362–372, 2013.

[33] Z. Li and C. Kleinstreuer, "Blood flow and structure interactions in a stented abdominal aortic aneurysm model," *Medical Engineering and Physics*, vol. 27, no. 5, pp. 369–382, 2005.

[34] S. M. Sampaio, J. M. Panneton, G. I. Mozes et al., "Proximal type I endoleak after endovascular abdominal aortic aneurysm repair: predictive factors," *Annals of Vascular Surgery*, vol. 18, no. 6, pp. 621–628, 2004.

[35] M. P. Armon, S. W. Yusuf, S. C. Whitaker, R. H. S. Gregson, P. W. Wenham, and B. R. Hopkinson, "Thrombus distribution and changes in aneurysm size following endovascular aortic aneurysm repair," *European Journal of Vascular and Endovascular Surgery*, vol. 16, no. 6, pp. 472–476, 1998.